

THERMAL TRANSPORT IN URANIUM DIOXIDE AND DIAMOND  
BY ATOMIC LEVEL SIMULATIONS

By

TAKU WATANABE

A DISSERTATION PRESENTED TO THE GRADUATE SCHOOL  
OF THE UNIVERSITY OF FLORIDA IN PARTIAL FULFILLMENT  
OF THE REQUIREMENTS FOR THE DEGREE OF  
DOCTOR OF PHILOSOPHY

UNIVERSITY OF FLORIDA

2008

© 2008 Taku Watanabe

To my family

## ACKNOWLEDGMENTS

Since the time I arrived at the University of Florida, I have been fortunate to meet many people for whom I am deeply thankful. These people have made my experience at the University of Florida extraordinary. I cannot sufficiently thank supervisory committee chair, Prof. Phillipot, for his enthusiasm of science and education and patience to guide his student. I respect him as a scientist, educator, and individual. He has been always willing to discuss about almost anything with a great sense of humor. He had a positive effect on my character. I also thank to Prof. Schelling in the University of Central Florida for helping me carrying out some of the key work I have done during my Ph.D program. He was always willing to help and I have learned so much from his deep insight of the subject. I am also grateful to Prof. Sinnott, Prof. Tulenko, Prof. Nino, Prof. Jones, and Prof. Anghaie for their guidance and willingness to help students.

I was fortunate to have the experience of visiting Los Alamos National Laboratory in summer of 2006. The people in MST-8 impressed me as scientists, mentors, and friends. Drs. Srivilliputhr, Uberuaga, and Stanek were especially helpful and made my time there productive and enjoyable.

It has been a great pleasure working with the people in our computational group in the Materials Science Department in the University of Florida. The group has been very active and supportive of each other, and it had positive impact on my research and life outside of the school. Finally, I thank to my family in Japan for their support and giving me the opportunity for the education and experience.

Part of this work was supported by DOE-NERI Award DE-FC07-05ID14649.

## TABLE OF CONTENTS

	<u>page</u>
ACKNOWLEDGMENTS .....	4
LIST OF TABLES .....	8
LIST OF FIGURES .....	9
ABSTRACT .....	14
CHAPTER	
1 GENERAL INTRODUCTION .....	15
Challenges in the Materials Science of Heat Transfer.....	15
Defects in Crystalline Solids .....	17
Uranium Dioxide .....	20
Diamond .....	23
Objective and Scope of Study.....	24
2 INTRODUCTION TO THERMAL TRANSPORT IN MATERIALS .....	34
Basic Concepts of Thermal Transport .....	34
Three Modes of Heat Transfer - Conduction, Radiation, Convection.....	35
Phonon Heat Transfer in Electronic Insulators.....	37
Point Imperfections.....	43
GBs and Surfaces.....	45
Thermal Transport in Disordered Solids .....	46
3 SIMULATION METHODS .....	52
Introduction.....	52
Numerical Integration.....	53
Periodic Boundary Condition .....	53
Interatomic Potentials .....	54
Long-range Interaction .....	54
Ewald sum .....	55
Direct summation .....	56
Short-range Interactions .....	57
Thermostat .....	58
Constant Pressure Algorithm.....	59
Nonequilibrium Thermal Conductivity Simulations .....	61
4 THERMAL TRANSPORT IN SINGLE CRYSTAL UO <sub>2</sub> .....	68
Molecular Dynamics Simulation of UO <sub>2</sub> .....	68

Potential Models .....	68
Thermal Expansion .....	70
Thermal Conductivity of Single Crystal $\text{UO}_2$ .....	72
Discussion.....	75
<b>5 THERMAL TRANSPORT IN POLYCRYSTALLINE <math>\text{UO}_2</math>.....</b>	<b>84</b>
Introduction.....	84
Structure of Model Polycrystal.....	84
Thermal Conductivity of Polycrystalline $\text{UO}_2$ .....	86
Discussion.....	89
<b>6 THERMAL TRANSPORT IN <math>\text{UO}_{2\pm x}</math>.....</b>	<b>98</b>
Introduction.....	98
Point Defects in $\text{UO}_2$ .....	98
Thermal Transport in $\text{UO}_2$ with Point Defects .....	101
Molecular Dynamics Simulations.....	103
Preparation of the Structures .....	104
Chemical Expansion of $\text{UO}_{2\pm x}$ .....	105
Thermal Expansions of $\text{UO}_{2\pm x}$ .....	106
Thermal Conductivity of $\text{UO}_{2+x}$ .....	107
Thermal Conductivity of $\text{UO}_{2-x}$ .....	109
Isotopic Effect .....	109
Lattice Dynamics Calculations.....	110
Discussion.....	112
<b>7 METHODOLOGY FOR THE SIMULATION OF RADIATION DAMAGE IN <math>\text{UO}_2</math>.....</b>	<b>138</b>
Introduction.....	138
Background.....	139
Type of Radiation .....	139
Fission and Radiation .....	140
Fission Products and the Type of Stopping .....	141
Previous Experimental Studies on Radiation Damage in $\text{UO}_2$ .....	142
Previous Simulation Studies on Radiation Damage in $\text{UO}_2$ .....	144
Implementation of the Molecular Dynamics Simulation Code .....	145
Universal Ziegler-Biersak-Littmark Potential .....	145
Variable Time Step Algorithm .....	149
Thermostat.....	153
Defect Identification Method .....	156
Radiation Damage Simulations .....	157
Time Step Size.....	157
Berendsen Time Constant.....	159
Statistics.....	160
Active Volume Effect.....	161
Discussion.....	162

8	INTERFACIAL THERMAL TRANSPORT IN DIAMOND.....	187
	Introduction.....	187
	Single Crystal Diamond.....	187
	Interfacial Conductance of (001) Twist GBs.....	190
	Interfacial Thermal Conductance: Diamond vs. Silicon.....	196
	Extended Read-Shockley Model For Interfacial Thermal Conductance.....	197
	Discussion.....	200
9	SIMULATIONS OF THERMAL TRANSPORT IN NANOCRYSTALLINE DIAMOND AND COMPARISON WITH EXPERIMENTAL RESULTS.....	222
	Introduction.....	222
	Experimental Approach.....	224
	Experimental Results.....	225
	Simulation Results.....	227
	Discussion.....	229
10	CONCLUSIONS.....	236
	APPENDIX: LATTICE DYNAMICS.....	240
	LIST OF REFERENCES.....	243
	BIOGRAPHICAL SKETCH.....	269

## LIST OF TABLES

<u>Table</u>	<u>page</u>
2-1. Values of the Debye temperature and the maximum in the experimental thermal conductivities of selected materials. ....	49
4-1. Parameters of interatomic potentials .....	77
4-2. Lattice parameter and elastic constants at 300 K. ....	78
6-1. Experimental and DFT values of the formation energies. ....	115
6-2. Potential parameters for the short-range interactions in $\text{UO}_{2\pm x}$ . ....	116
7-1. Spline parameters and connection points for U-U, O-O, and U-O interactions. ....	164
7-2. The ZBL screening function parameters. ....	165
8-1. Summary of the diamond (001) GBs properties. ....	201
8-2. Comparison of the GB energies and coordination of the atoms of $\Sigma 29(001)$ $\theta=43.6^\circ$ GB in diamond and Si .....	202

## LIST OF FIGURES

<u>Figure</u>	<u>page</u>
1-1. Point defects in crystalline solid.....	25
1-2. Pure relaxed single twist grain boundary (GB) between two cubic lattices.....	26
1-3. An asymmetric tilt GB between two cubic lattices .....	27
1-4. GB energy as a function of rotation angle in $\langle 100 \rangle$ (a,b) and $\langle 110 \rangle$ (c,d) symmetric tilt GBs of aluminum.....	28
1-5. Illustration of the lattice structure in $\Sigma 5$ (001) $\theta=36.5^\circ$ GB. ....	29
1-6. Fluorite structure of $\text{UO}_2$ unit cell. Blue and red denote uranium and oxygen atoms, respectively. ....	30
1-7. Phase diagram of U-O system .....	31
1-8. Fission product yield as a function of atomic number in a pressurized water reactor (PWR) after 2.9 % burnup .....	32
1-9. Unit cell structure of diamond.....	33
2-1. Temperature dependence of the thermal conductivity of selected materials.....	50
2-2. Temperature dependence of the thermal conductivity of Ge .....	51
3-1. The root mean square of the total energy as a function of time for velocity Verlet (circles), 4 <sup>th</sup> order Gear (squares), 5 <sup>th</sup> order Gear (triangles), and 6 <sup>th</sup> order Gear (diamond) algorithms.....	63
3-2. Two dimensional periodic system in simulation .....	64
3-3. A system of point charges as a sum of screened point charges and smeared charge density with opposite sign.....	65
3-4. Electrostatic energy by the direct summation method.....	66
3-5. Simulation cell setup for the direct method for simulating thermal conductivity.....	67
4-1. Normalized lattice parameter as a function of temperature from experiment <sup>3</sup> , Busker and Yamada potentials.....	79
4-2. Specific heat of $\text{UO}_2$ from GULP, MD and experiment.....	80
4-3. Size dependence of thermal conductivity for both the Busker (a) and Yamada (b) potentials. ....	81

4-4. Thermal conductivity of $\text{UO}_2$ from the compilation of experimental data by Fink and simulations using the Busker and Yamada potentials (a) before and (b) after the anharmonic correction. ....	82
4-5. The same thermal conductivity data as in Figure. 4-4(b), but in log-log plot. ....	83
5-1. Pair distribution function of the polycrystalline structure .....	91
5-2. The final polycrystalline structure used in the thermal conductivity calculations .....	92
5-3. Thermal conductivity of 3.8 nm grain polycrystalline $\text{UO}_2$ from simulation for the two potentials. ....	93
5-4. Average thermal conductance for the [001] tilt GBs from 3.8 nm grain polycrystalline $\text{UO}_2$ . ....	94
5-5. Kapitza length from 3.8 nm grain polycrystalline $\text{UO}_2$ simulations. ....	95
5-6. Grain size dependence of the thermal conductivity of polycrystalline $\text{UO}_2$ using Yamada's potential. ....	96
5-7. Interfacial conductances of selected interfaces as function of temperature .....	97
6-1. Normalized Frenkel and anti-Frenkel pair formation energies by empirical potentials.....	117
6-2. The 2:2:2 defect cluster in $\text{UO}_2$ .....	118
6-3. Pair distribution function between U-O in $\text{UO}_{2.25}$ .....	119
6-4. Pair distribution function between U-O in $\text{UO}_{1.80}$ .....	120
6-5. Normalized lattice parameter of $\text{UO}_{2+x}$ as a function of defect concentration .....	121
6-6. Normalized lattice parameter of $\text{UO}_{2-x}$ as a function of defect concentration.....	122
6-7. Thermal expansion of $\text{UO}_{2+x}$ .....	123
6-8. Thermal expansion coefficient of $\text{UO}_{2+x}$ as a function of $x$ .....	124
6-9. Thermal expansion of $\text{UO}_{2-x}$ .....	125
6-10. Inverse thermal conductivity of $\text{UO}_{2+x}$ with various concentrations of oxygen interstitials as a function of simulation cell length at 800 K.....	126
6-11. Inverse thermal conductivity of $\text{UO}_{2+x}$ with various concentrations of oxygen interstitials as a function of simulation cell length at 1600 K.....	127
6-12. Bulk thermal conductivity of $\text{UO}_{2+x}$ as a function of degree of off-stoichiometry without anharmonic correction at 800 and 1600 K.....	128

6-13. Bulk thermal conductivity of $\text{UO}_{2+x}$ as a function of degree of off-stoichiometry with anharmonic correction at 800 and 1600 K.....	129
6-14. Inverse thermal conductivity of $\text{UO}_{2-x}$ with various concentrations of oxygen vacancies as a function of simulation cell length at 800 K.....	130
6-15. Inverse thermal conductivity of $\text{UO}_{2-x}$ with various concentrations of oxygen vacancies as a function of simulation cell length at 1600 K.....	131
6-16. Bulk thermal conductivity of $\text{UO}_{2-x}$ as a function of degree of off-stoichiometry at 800 K and 1600 K.....	132
6-17. Thermal conductivity of $\text{UO}_{2+x}$ as a function of degree of off-stoichiometry at 800 K (a) and 1600 K (b) for $x \leq 0.025$ .....	133
6-18. Phonon Density of states of $\text{UO}_{2+x}$ for $-0.020 \leq x \leq 0.125$ .....	134
6-19. Participation ratios of $\text{UO}_{2+x}$ for $-0.020 \leq x \leq 0.125$ .....	135
6-20. Projections of the polarization vectors of vibrational modes in $\text{UO}_{2+x}$ at 1.5 THz.....	136
6-21. Projections of the polarization vectors of vibrational modes in $\text{UO}_{2+x}$ at 10 THz.....	137
7-1. Potential, kinetic, and total energy per atom from radiation damage simulations with various fixed time step size.....	166
7-2. Potential energy of O-O interactions as a function of the interatomic distance. ....	167
7-3. Trajectory of the O atom placed at 0.1 Å away from another O atom at the origin.....	168
7-4. The calculation of the PKA trajectory in two ways: one large step and two half steps.....	169
7-5. Flow chart of the determination of the variable time step algorithm. ....	170
7-6. Trajectory of 1 keV U PKA atom along [100] direction in $10 \times 10 \times 10$ single crystal $\text{UO}_2$ .....	171
7-7. Trajectory of 80 keV U PKA along [100] direction in $10 \times 10 \times 10$ single crystal $\text{UO}_2$ .....	172
7-8. Evolution of the time step size in the 80 keV U PKA simulation.....	173
7-9. The configuration of the MD simulation cell used in our radiation damage simulations ...	174
7-10. Temperature evolution of $10 \times 10 \times 10$ unit cells single crystal $\text{UO}_2$ during equilibration with the Berendsen thermostat with $\tau = 400$ fs.....	175
7-11. Total energy per atom of the equilibrated single crystalline $\text{UO}_2$ at 300 K.....	176
7-12. Standard deviation of the kinetic, potential and total energies per atom as a function of time constant, $\tau$ , from the equilibrated single crystalline $\text{UO}_2$ at 300 K.....	177

7-13. Defect identification method in crystalline structures.....	178
7-14. Effect of the time step size on radiation damage simulation in NVE ensemble .....	179
7-15. Number of $V_U$ , $U_I$ , $V_O$ , and $O_I$ produced after the 1 keV U PKA radiation damage in a single crystal $UO_2$ .....	180
7-16. Effect of time step size in radiation damage simulation in pNVE .....	181
7-17. Temperature of the active region during the radiation damage simulations with different Berendsen time constants.....	182
7-18. Total energy per atom during the radiation damage simulations with different Berendsen time constant .....	183
7-19. Number of uranium (top) and oxygen (bottom) vacancies produced in radiation damage simulations as a function of the Berendsen time constant.....	184
7-20. Number of uranium (top) and oxygen (bottom) vacancies produced in radiation damage simulations with equivalent PKA directions. ....	185
7-21. The number of U and O vacancies produced by the radiation damage simulations in $20 \times 20 \times 20$ and $30 \times 30 \times 30$ unit cells active volume.....	186
8-1. Lattice parameter of a single crystal diamond as a function of temperature.....	203
8-2. Temperature profile of $4 \times 4 \times 400$ unit cells single crystal diamond after 4 ps.....	204
8-3. Time evolution of the temperature at the edge ( $L_z=0$ ) and center ( $z=L_z/2$ ) of the simulation cell.....	205
8-4. Slopes of the linear region of the temperature profile shown in Figure 8-2.....	206
8-5. Slopes of the linear region of the temperature profile shown in Figure 8-4.....	207
8-6. Thermal conductivity versus temperature in both linear and log-log plots.....	208
8-7. Bonding of atoms in diamond structure along (a) [111], (b) [100] and (c) [110] directions.....	209
8-8. Thermal conductivity as a function of heat current density. ....	210
8-9. GB energy as a function of the number of atoms removed.....	211
8-10. A typical temperature profile of a system with GBs, in this case (001) $\theta=43.60^\circ$ $\Sigma 29$ symmetric twist boundaries .....	212
8-11. Linear temperature gradient from the temperature profile of the $\Sigma 29$ (001) $\theta=43.60^\circ$ GB.....	214

8-12. Size dependence of the thermal conductance of the $\Sigma 29 \theta=43.60^\circ$ GB fitted to a shifted exponential .....	215
8-13. Temperature dependence of the thermal conductance of the (001) $\Sigma 29 \theta=43.60^\circ$ GB.....	216
8-14. Thermal conductance as a function of twist angle for diamond (001) symmetric twist GBs. ....	217
8-15. Kapitza length in units of their respective lattice parameters as a function of twist angle for both diamond and Si at 1000 K .....	218
8-16. Cross section of $\Sigma 29(001)$ GB in diamond (a) and Si (b).....	219
8-17. GB energy (symbols) and the fit to the extended Read-Shockley model (solid line) .....	220
9-1. Compilation of the diamond thermal conductivity versus grain size $d$ .....	232
9-2. UNCD thermal conductivity as a function of film thickness .....	233
9-3. Microstructure and temperature profile of polycrystallin diamond.....	234
9-4. Temperature profile through a diamond $\Sigma 29 (001) \theta=43.60^\circ$ twist GB determined by simulation.....	235

Abstract of Dissertation Presented to the Graduate School  
of the University of Florida in Partial Fulfillment of the  
Requirements for the Degree of Doctor of Philosophy

THERMAL TRANSPORT IN URANIUM DIOXIDE AND DIAMOND  
BY ATOMIC LEVEL SIMULATIONS

By

Taku Watanabe

May 2008

Chair: Simon R. Phillpot  
Major: Materials Science and Engineering

Thermal transport properties of  $\text{UO}_2$  and diamond are investigated using atomic level simulation techniques. In particular, the effects of point defects and GBs are investigated. A nonequilibrium molecular dynamics technique is used to calculate the thermal conductivities of  $\text{UO}_2$  and diamond. The correct treatment of anharmonicity is found to be important for accurate prediction of thermal transport in crystalline solid. The thermal transport properties of polycrystalline  $\text{UO}_2$  are investigated. Three effective medium approaches are compared and used to derive the interfacial conductance from our simulation results. The temperature and grain size dependence of the interfacial conductance is also characterized.

Defect concentration dependence of the thermal conductivity of  $\text{UO}_{2\pm x}$  is obtained. In the effort to understand the nature of vibrational modes in  $\text{UO}_2$  with point defects, the theory of highly disordered solid is applied. To address the defect production and annihilation mechanisms in  $\text{UO}_2$ , a radiation-damage simulation code has been developed and validated.

Thermal transport properties of diamond GBs are investigated and characterized. Connections to the experimental work or collaborators are made.

## CHAPTER 1 GENERAL INTRODUCTION

### **Challenges in the Materials Science of Heat Transfer**

Heat transfer is a fundamental mode of energy transport. It is so fundamental that it can be observed at the atomic and molecular levels and also at the astronomical scale. Controlling heat transfer has been technologically important for more than a century. Thus, relentless efforts have been made to tailor the thermal transport properties of materials for specific applications. This is often very challenging because of the complexity of the transport mechanisms. Heat can propagate by means of conduction, convection, and radiation, and any combinations of these three mechanisms. In addition, the range of thermal conductivities of materials is quite narrow. For instance, the electrical conductivity accessible in materials is roughly 20 orders of magnitude; however, the thermal conductivity of materials ranges only over about 5 orders of magnitude.<sup>1,2</sup>

Despite the challenge, the demand for better management of the heat transfer has been continuously intensifying. In the effort to gain better control, one must look at the materials on both ends of the spectrum; namely, very high and low thermal conductivity materials.  $\text{UO}_2$  is a good example of a low thermal conductivity ceramic material. It is also the standard nuclear fuel for light water reactors for power generation. Its thermal conductivity is roughly 2-7 W/mK depending on its temperature and microstructure<sup>3</sup>. In a nuclear reactor, the energy released from the fission reactions is converted to the thermal energy. For efficient transfer of the thermal energy, it is desirable for the fuel to have a high thermal conductivity. Improving the thermal conductivity of  $\text{UO}_2$  is a significant challenge; for example, see the literatures on cermet materials.<sup>4,5</sup>

An example of the other end of the spectrum is diamond. Diamond has the highest thermal conductivity among the naturally occurring materials at room temperature.<sup>2,6</sup> There are a number of applications which require very high thermal conductivity, including heat spreader in microelectronics, coating for high wear machining devices, and high power IR laser windows. Because of this and its other unique properties, diamond, is being used in numerous applications.<sup>6,7</sup>

Both  $\text{UO}_2$  and diamond are electronic insulators, with band gaps of  $\sim 2 \text{ eV}$ <sup>8,9</sup> and  $\sim 5.5 \text{ eV}$ <sup>10</sup>, respectively. Thus, the main mechanism of the transport of heat is by the vibration of the crystalline lattice. The quantized lattice vibrations are called phonons and they are the main carriers of thermal energy in these materials. Thermal conductivity in an electronic insulator is determined by the scattering of phonons with other phonons and with defects. Thus the means to control phonon mediated heat transfer is to control point defects, grains, and addition of other materials. The detailed scattering mechanisms of phonon with other phonons and defects are quite complicated. Although there are some analytical models available, there are severe approximations made and the results are often in poor agreement with the observed data. Difficulties are not only in the theoretical understanding, but also in experiments. In experiments, numerous effects coexist in a single sample, as a result not straightforward to separate the mechanisms in clear manner.

In order to provide the necessary background to the work discussed in this thesis, in the following sections, the fundamentals of the defects in crystalline solids are introduced. In addition, the basic properties of  $\text{UO}_2$  and diamond are presented. In particular, point defects and GBs present in these two materials are introduced.

## Defects in Crystalline Solids

Solid materials with crystalline structure can contain a number of structural defects including point defects, dislocations, GBs, pores, second phases, and surfaces. In the work discussed here, we describe the effect of point defects and GBs on the thermal transport properties. Thus in this section, the basic features of point defects and GBs are introduced.

Point defects in crystalline solid can be divided into two major categories: intrinsic and extrinsic point defects. Intrinsic point defects are defects of the original matrix material, including vacancies, interstitials, Frenkel pairs, and Schottky defects: see Figure 1-1 for an illustration of these defects.

The probability that a vacancy will form in thermal equilibration is proportional to the Boltzmann factor,  $\exp(-E_v/k_B T)$ , where  $E_v$  is the vacancy formation energy,  $k_B$  is the Boltzmann constant, and  $T$  is the temperature. Thus the equilibrium number,  $n_v$ , of vacancies in a crystal of  $N$  atoms is given by,

$$\frac{n_v}{N - n_v} = \exp(-E_v / k_B T). \quad (1-1)$$

A typical value of  $E_v$  is of the order of  $\sim 1$  eV. Assuming  $T=1000$  K and  $E_v=1$  eV, this yields  $n_v/N \approx 10^{-5}$ . The equilibrium number of interstitials, Frenkel pairs, and Schottky defects can be obtained in a similar fashion.

Extrinsic point defects are atom species different from the perfect solid itself and can take the form of interstitials and substitutional defects.

Intrinsic and extrinsic defects often coexist in the same solid and they are extremely useful in many applications, such as ion transport in doped oxides. Intrinsic defects such as vacancies and interstitials can be created by doping of extrinsic defect. For example, in  $\text{UO}_2$ , doping  $\text{Gd}_2\text{O}_3$  can create vacancies in the crystal:



Gd is commonly doped in UO<sub>2</sub> to control the activity of the fuel in boiling water reactors<sup>11, 12</sup>.

The vacancies created by the Gd<sub>2</sub>O<sub>3</sub> doping are known to increase the electrical conductivity of the UO<sub>2</sub> fuel<sup>13, 14</sup>, but the reduce thermal conductivity by enhanced phonon-defect scatterings<sup>15, 16</sup>. The theory of phonon scattering mechanisms is discussed in Chapter 2.

There are a number of models proposed to describe the structure and properties of GBs.<sup>17</sup> We will cover discuss only rather simple grain boundary (GB) structures, namely, twist and tilt GBs in some detail since they are the most relevant to the rest of this thesis. However, a grain boundary in general can also be a combination of tilt or twist. (For more details, see reference<sup>18</sup>.)

Twist GBs can be viewed simply as follows. Take a block of single crystal and cut into half. Twist one half of the block by  $\theta$  about an axis perpendicular to the interface; the bring the two half blocks back into contact. The resulting interface is a twist GB; see Figure 1-2 for an illustration. Twist GBs can also be viewed as a crystal with a number of screw dislocations aligned in an atomic plane. The illustration in Figure 1-2 is a relaxed twist GB between two simple cubic crystals. The plane of the interface is (100) in this case.

Tilt GBs can be constructed by the relative rotation of the two blocks forming the GB about a rotation axis along the plane of the interface. If the atomic planes parallel to the GB on either side are the same, then the GB is symmetric. If the atomic planes are not the same, it is an asymmetric GB. Figure 1-3 is an example of an asymmetric tilt GB. Just as twist GBs consist of screw dislocations, tilt GBs can be viewed as a series of edge dislocations situated in the plane of GB.

A useful physical quantity associated with a GB is the GB energy. The GB energy can be defined as the energy difference between the single crystal and crystal with the GB per area:

$$E_{GB}(\theta) = \frac{E(\theta) - E_0}{A}. \quad (1-3)$$

$E(\theta)$  is the energy of the structure with the GB,  $E_0$  is the energy of a single crystal with the same number of atoms, and  $A$  is the area of the GB. The GB energy is a function of the rotation angle about the rotation axis. Figure 1-4 is an example of the calculated and measured energies of tilt GBs in aluminum.<sup>17</sup> Some of the notable features are the rapid increase and decrease with the rotation angle near 0 degree and 90 degree. There are also cusps at certain angles, corresponding to particular small unit cells (the  $\Sigma$  values on each figure). Twist GBs generally have much shallower cusps than those of tilt GBs. Read and Shockley<sup>19</sup> first proposed a model of  $E_{GB}(\theta)$  for the low angle GBs based on the dislocation models. Later Wolf<sup>18</sup> extended the model to the higher angles using phenomenological model. This latter model is called the extended Read-Shockley model and will be used in Chapter 8 to analyze our results on heat transport in diamond GBs.

One of the useful models to describe the GB structures is the coincident site lattice (CSL) model. The CSL model utilizes the fact that the two overlapping two dimensional lattices form a periodic pattern of the coincident lattice points. See Figure 1-5 for an example. The open and closed symbols in the figure are the atoms at simple cubic lattice site in two adjacent planes. The squares are used to show the two dimensional unit cells in each lattice. Imagine that the lattice made of the filled symbol is above the plane consisting of the open symbols. When the top plane is rotated by certain angles  $\theta$  relative to the bottom plane, some atoms in the top and bottom plane coincide. In Figure 1-5 the rotation angle is  $36.5^\circ$  and the plane is (100). This interface is called the  $\Sigma 5$  (100) GB:  $\Sigma$  denotes the fact the area of the two dimensional repeat pattern has an

area that is 5 times larger than the original unit cell in the simple cubic lattice. This model is a very useful way to catalog different types of GBs. Tilt GBs can be cataloged in a similar manner. More detailed explanations are widely available in the literature.<sup>17, 18</sup>

### Uranium Dioxide

Uranium dioxide has been a technologically important material for more than half a century,<sup>11</sup> particularly as a nuclear fuel in fission reactors for electrical power generation. Uranium is a rather common element and is generally found in the form of  $U_3O_8$  ore. Major producers of uranium ore are Australia, Canada, Kazakhstan, the United States, South Africa, in order of decreasing amount of reserves.<sup>20</sup> Perhaps the single most important reason that uranium is used for the nuclear fission reactors is the natural occurrence of  $^{235}U$ .  $^{235}U$  is the only naturally occurring stable fissile elements. After physical and chemical processing of the ore, the  $UO_2$  form used in reactors, is obtained.<sup>11</sup>

The main reasons why uranium is used in the form of  $UO_2$  for fission reactor fuel are: i) its high melting point  $\sim 3000$  K, ii) its chemical stability with common cladding materials and coolant, iii) its fluorite structure, which can relatively easily accommodate fission products.<sup>11</sup>  $UO_2$  of course is not without disadvantages in nuclear fuel applications: i) low thermal conductivity ( $\sim 5$  W/mK at 800 K), ii) lower density of fissile elements than its metallic form, and iii) the relative difficulty of processing compared to its metallic form.<sup>11</sup> Other phases of uranium oxides were also used for colorants for glasses and glazes until the 1940s.<sup>21</sup>

The crystalline structure of  $UO_2$  is the cubic fluorite structure (space group of  $Fm\bar{3}m$ ) with the lattice parameter of  $5.4698 \text{ \AA}$  at 300 K.<sup>22-25</sup> Figure 1-6 is the unit cell of  $UO_2$ . Uranium atoms sit at the face centered cubic (FCC) sites (4a Wycoff positions), while oxygen atoms occupy the tetrahedral positions (8c sites) in the FCC U lattice. The ionic radii of  $U^{4+}$  and  $O^{2-}$  are  $r(U^{4+})=0.95 \text{ \AA}$  and  $r(O^{2-})= 1.35 \text{ \AA}$ .<sup>26</sup> Therefore the radius ratio,  $r(U^{4+})/r(O^{2-})$ , is 0.704. The

structure is consistent with Pauling's rule<sup>27</sup> since the oxygen sublattice forms a simple cubic structure around the cations. The electronegativities of U and O are 1.7 and 3.5,<sup>1</sup> thus the difference is 1.8. According to the Pauling's law of electronegativity<sup>28</sup>, this means that the bonding in  $\text{UO}_2$  is ~55 % ionic.

Figure 1-7 is the binary phase diagram of U-O system obtained from the thermodynamic calculation by Lewis *et al.*, based on available experimental data.<sup>29</sup> There is only a single phase in stoichiometric  $\text{UO}_2$  from room temperature to the melting point.<sup>29-31</sup> The  $\text{UO}_{2+x}$  phase is fairly wide especially at high temperature. With a high concentration of oxygen in  $\text{UO}_{2+x}$ , the  $\text{U}_4\text{O}_9$  phase can form, but the exact phase boundary is still under debate.<sup>29</sup> By contrast,  $\text{UO}_{2-x}$  phase is very limited.

$\text{UO}_2$  can accommodate a number of point defects, especially when it is used in the nuclear reactor fuel. Intrinsic defects are  $V_U$ ,  $U_I$ ,  $V_O$ , and  $O_I$  with various charge states. U itself can take a wide variety of oxidation states:  $\text{U}^{2+}$ ,  $\text{U}^{3+}$ ,  $\text{U}^{4+}$ ,  $\text{U}^{5+}$ , and  $\text{U}^{6+}$ .<sup>32, 33</sup>  $\text{U}^{2+}$ , however, is very rare. The predominant intrinsic point defects in  $\text{UO}_2$  are the anti-Frenkel pair.<sup>3, 34-36</sup> In addition to the intrinsic defects, a large number of extrinsic defects exists in the nuclear fuel, and many of them are produced during the nuclear reactions.<sup>11</sup> Figure 1-8 gives the yields of elements produced as extrinsic defects during the nuclear fission reactions in a typical pressurized water reactor (PWR).<sup>37</sup> The effects of these extrinsic defects on properties depend on the type and on their concentrations. The study of the effects of fission products themselves is a large area of research and is beyond the scope of this work.

Point defects in  $\text{UO}_2$  are known to affect its thermophysical properties. For instance, Ronchi and Hyland<sup>35</sup> analyzed the available heat capacity data of  $\text{UO}_2$ . They found that below 1000 K the heat capacity is determined by the harmonic lattice vibrations and that the Debye

model applies very well. Between 1000 and 1500 K, the anharmonic interactions play an important role and as a result the heat capacity continues to increase with increasing temperature. From 1500 to 2760 K, defect formation (mainly Frenkel defects -or is it anti-Frenkel?) increase the rate of rise in the heat capacity. Finally above 2760 K, other point defects such as Schottky defects also become important and the heat capacity increases further. Thus different types of defects operate in different range of temperature and influence the thermodynamic property.

In addition to the point defects in  $\text{UO}_2$ , electronic defects can be important. Electrons in dielectric materials like  $\text{UO}_2$ , in which the ions are highly polarizable, can propagate when strongly coupled with lattice vibrations.<sup>38</sup> The quasiparticles associated with this phenomenon are called polarons. In particular, so-called ‘small’ polarons, are common in  $\text{UO}_2$  and are involved in the charge transfer at high temperature. In the small polaron model, electrons hop from ion to ion, unlike the electrons in the conduction band. Small polarons also contribute to the thermal conductivity of  $\text{UO}_2$  at high temperature. However, the contribution is rather small (at 2000 K, the thermal conductivity by polaron is the 0.31 W/mK while by phonon is about 1.87 W/mK)<sup>39</sup> and will not be considered further.

GBs in  $\text{UO}_2$  also play very important roles in nuclear fuel. As mentioned earlier, GBs contribute to the thermal resistance of crystalline solids. However, there has been no systematic study of the grain size effect on the thermal transport of  $\text{UO}_2$ . The reason may be that the grain size in  $\text{UO}_2$  fuel at beginning of life is fairly large (size in a typical  $\text{UO}_2$  fuel pellet is of the order of  $10\ \mu\text{m}$ )<sup>3,40</sup> and the interfacial resistance is not a significant factor in thermal transport. However, it is known that the grain subdivision occurs in high burnup structures, and the grain size can decrease to  $\sim 150\ \text{nm}$  on average.<sup>40,41</sup> At this grain size, the interfacial thermal resistance may be significantly enhanced. Experimentally it is difficult to determine the effect

of grain size because the high burnup structures also contain a large number of point defects and pores which also decrease the thermal conductivity.<sup>40, 41</sup>

Other than the thermal transport, GBs also have a number of other effects. One such example is the segregation of fission products. Pores formed during the usage in the nuclear reactor are generally found at the GBs.<sup>42, 43</sup> Pores smaller than 2  $\mu\text{m}$  are removed in fine grain (<6 micron) sample, but pores are stable if the grain size is large (>20  $\mu\text{m}$ ).<sup>44-46</sup> The amount of fission gas release and the rate of swelling can be reduced by increasing grain size.<sup>47</sup> Mechanical properties such as hardness<sup>47</sup>, elastic<sup>44</sup>, and creep<sup>48</sup> properties are also affected by the presence and the size of the grains in the sample.

### **Diamond**

Diamond is an allotrope of carbon and has a number of unique properties. It is the hardest of known materials (hardness of roughly ~137-167 GPa).<sup>49</sup> It has the highest thermal conductivity of ~2200 W/mK at 300 K among naturally occurring materials<sup>6</sup>. The refractive index of diamond is 2.417 making it ideal for some optical applications<sup>7</sup>, and the brilliant refraction is appreciated for a gem stone.

In diamond, carbon atoms are covalently bonded in the diamond structure with the space group of  $Fd\bar{3}m$ . Figure 1-9 is the unit cell of the diamond structure. There are 8 carbon atoms in a unit cell at 8a sites, and each atom has 4 nearest neighbors. The lattice parameter determined by X-ray diffraction is 3.5673 Å.<sup>50</sup>

Naturally occurring diamond contains less than 1 % nitrogen impurities and possibly much lower concentrations of hydrogen and boron. These diamonds are categorized into type-Ia, Ib, IIa, IIb and other rare types, based on the concentration and the types of the impurities. Type IIa diamond is often used in technological applications,<sup>6</sup> for which most important and the naturally occurring impurity is nitrogen. Nitrogen atoms reside in diamond as substitutional defects, strain

the lattice and also modify the electronic structure. In addition to the impurities, natural diamond contains isotopic defects; in particular  $^{13}\text{C}$  appear at concentration of  $\sim 1.1\%$ .<sup>6, 51</sup> Synthetic methods such as chemical vapor deposition (CVD) are often used to prepare diamonds of high purity.<sup>52, 53</sup> Beside the single crystals, polycrystalline diamond is technologically important because of its unique physical properties. In particular, ultrananocrystalline diamond (UNCD) is a very promising multifunctional material.<sup>54</sup>

### **Objective and Scope of Study**

The objective of this thesis is to elucidate the mechanisms by which atomic level defect structures influence thermal transport properties in  $\text{UO}_2$  and diamond. Atomic level simulation techniques are used to accomplish this task. A methodology for the simulation of radiation damage in  $\text{UO}_2$  is also developed.

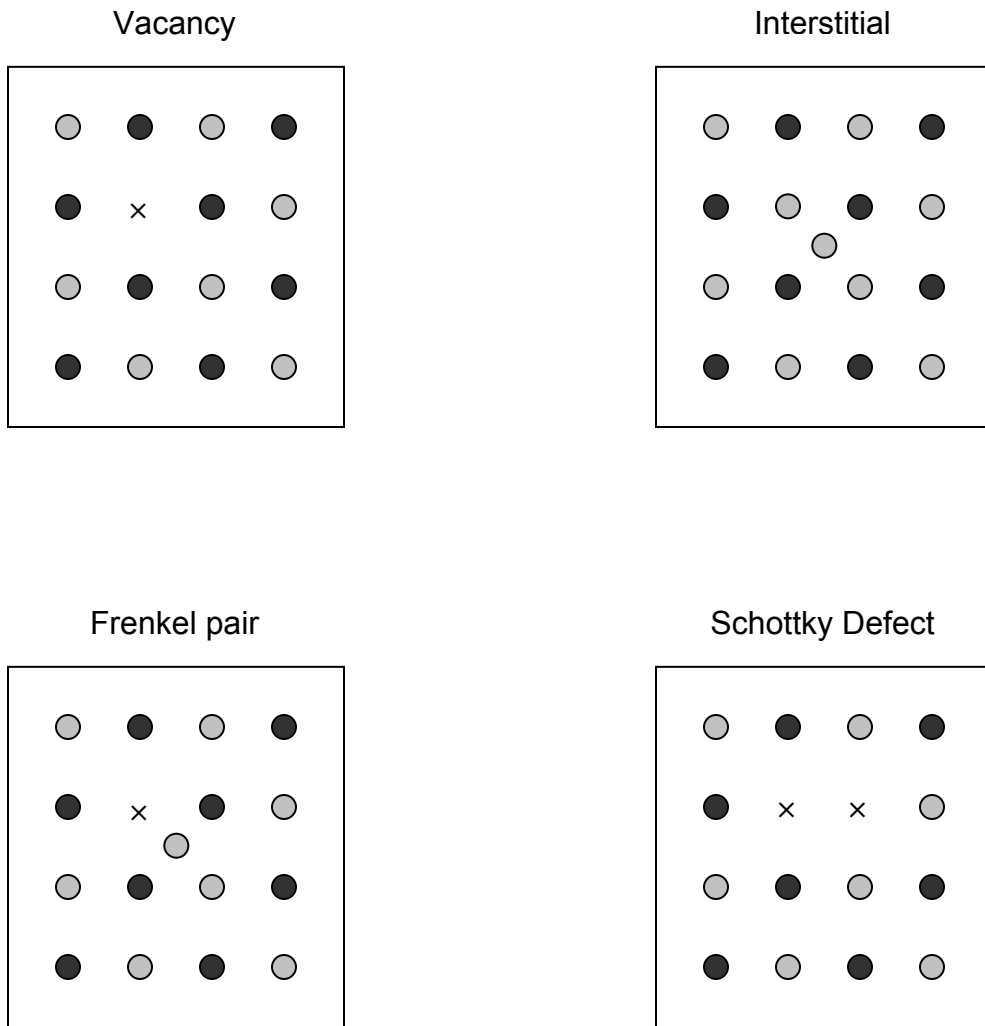


Figure 1-1. Point defects in crystalline solid. Black and grey symbols represent atoms of different types; × represents a vacant site.

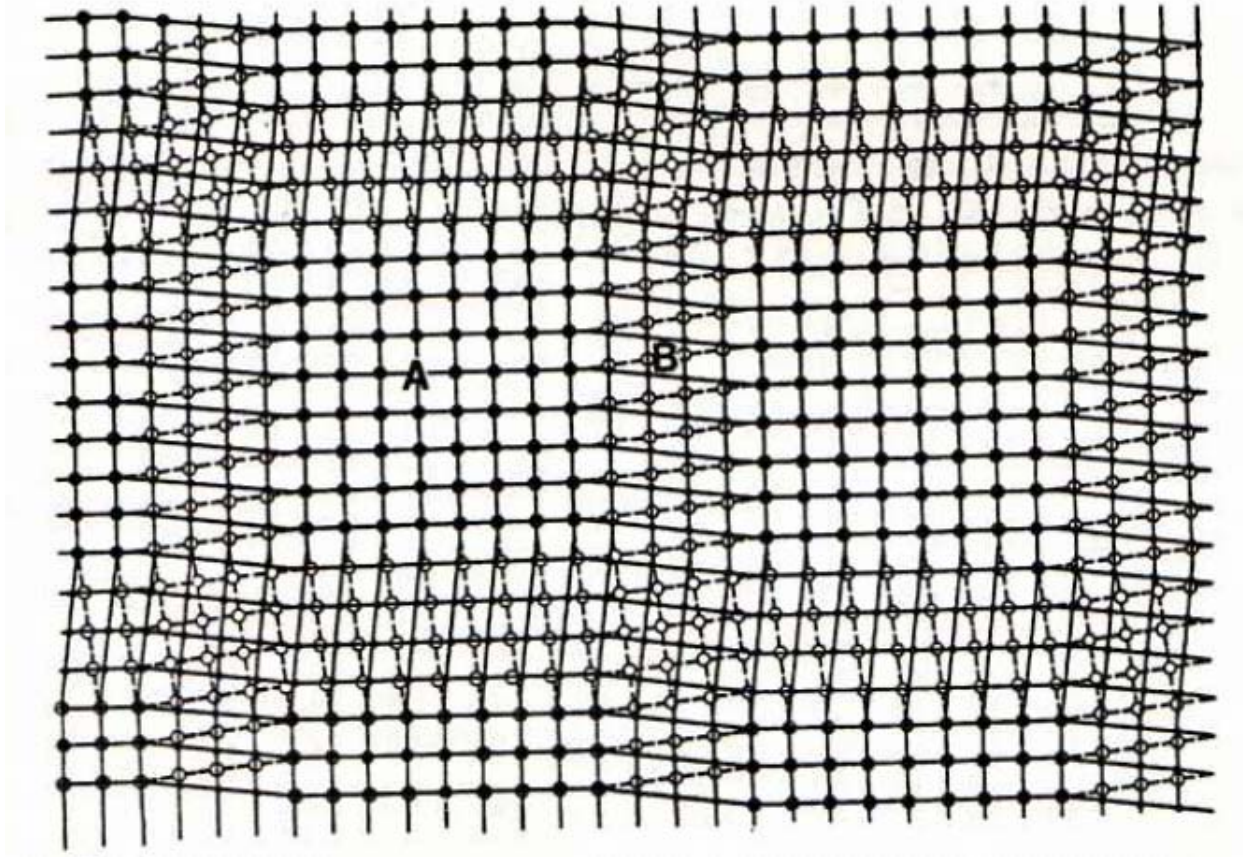


Figure 1-2. Pure relaxed single twist grain boundary (GB) between two cubic lattices. The GB is in the plane of the page. Region A and B are the region of coherent and incoherent interfaces, respectively. [Adapted from the reference 17 (Page 317, Figure 13.10).]

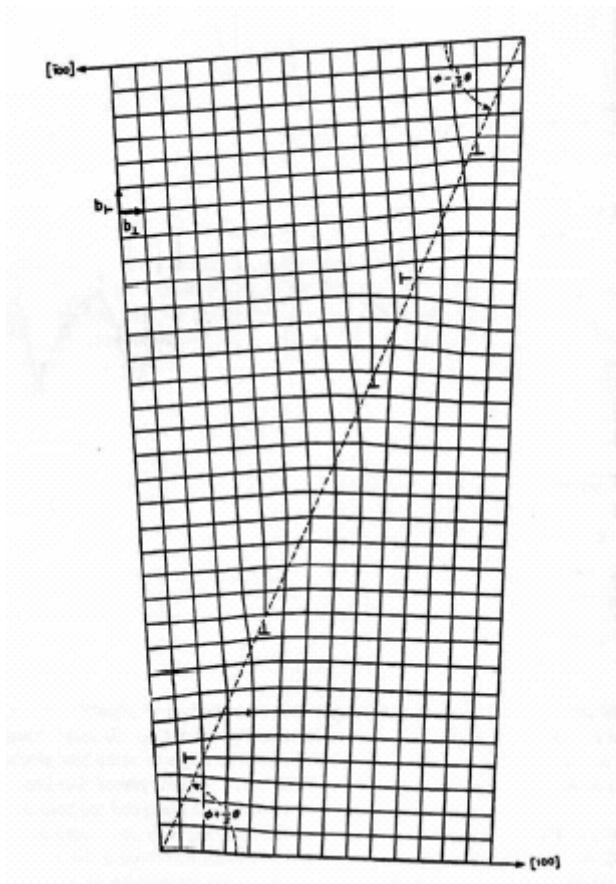


Figure 1-3. Asymmetric tilt GB between two cubic lattices. The GB is shown by the dashed line. Symbol  $\Upsilon$  is used to indicate the core of the edge dislocation. [Adapted from the reference 17 (Page 316, Figure 13.9).]

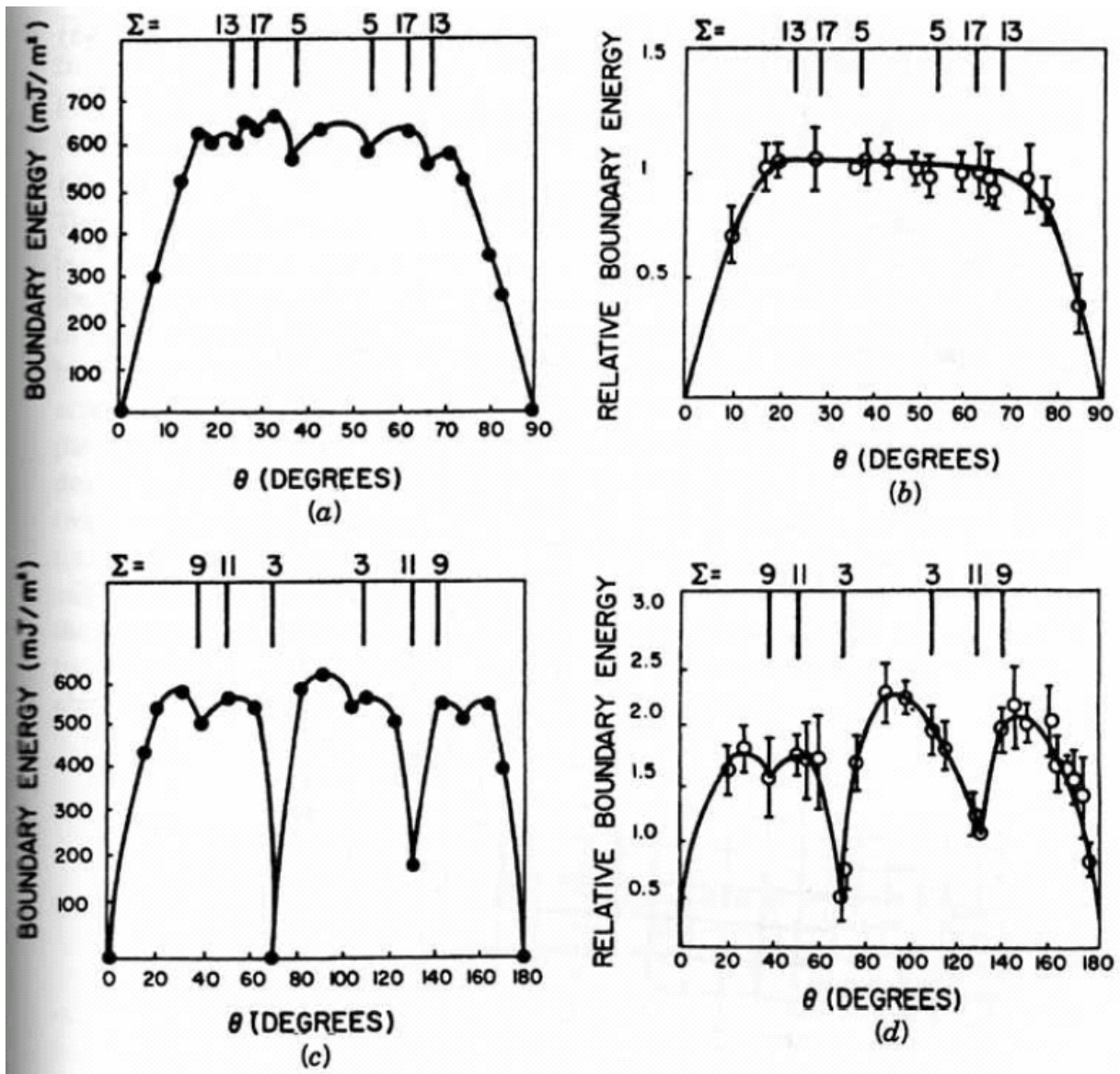


Figure 1-4. The GB energy as a function of rotation angle in  $\langle 100 \rangle$  (a,b) and  $\langle 110 \rangle$  (c,d) symmetric tilt GBs of aluminum. (a,c) are calculated values and (b,d) are measured data. [Adapted from reference 17 (Page 315, Figure 13.8).]

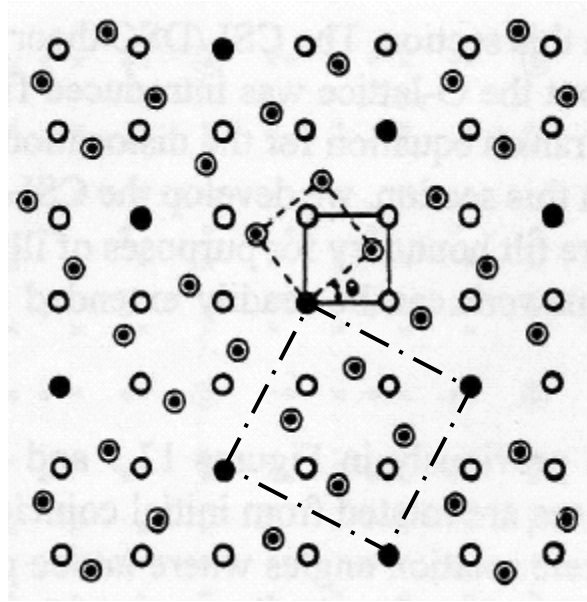


Figure 1-5. Lattice structure in  $\Sigma 5$  (001)  $\theta=36.5^\circ$  GB. Dotted circles ( $\odot$ ) and open circles ( $\circ$ ) represent atoms in two adjacent layers. Black dot ( $\bullet$ ) indicates the coincident sites of the two atomic layers. Black solid and dashed lines are used to indicate the cubic unit cell in each crystal. The dash-dot line shows the unit cell of  $\Sigma 5$  GB. [Adapted from reference 17 (Page 334, Figure 13.19) with minor modification.]

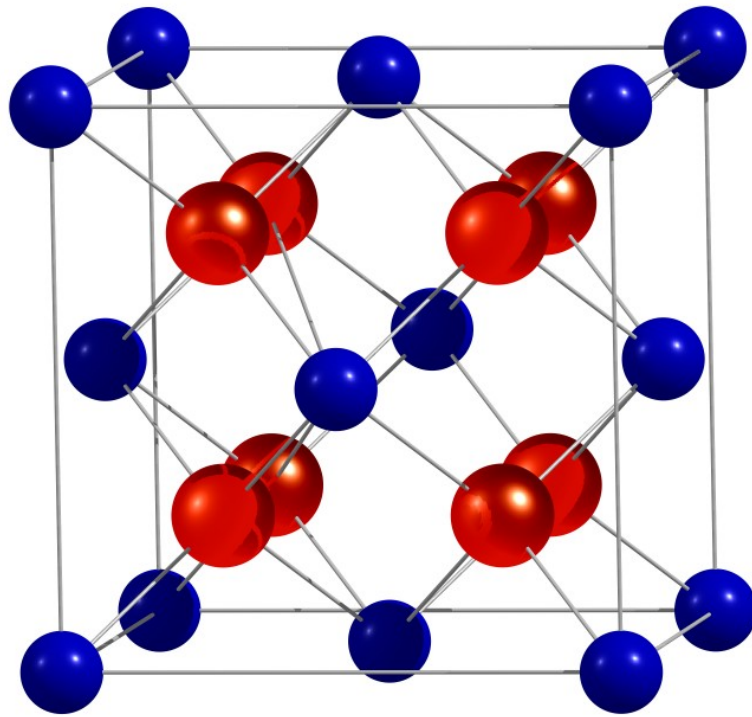


Figure 1-6. Fluorite structure of UO<sub>2</sub> unit cell. Blue and red denote uranium and oxygen atoms, respectively.

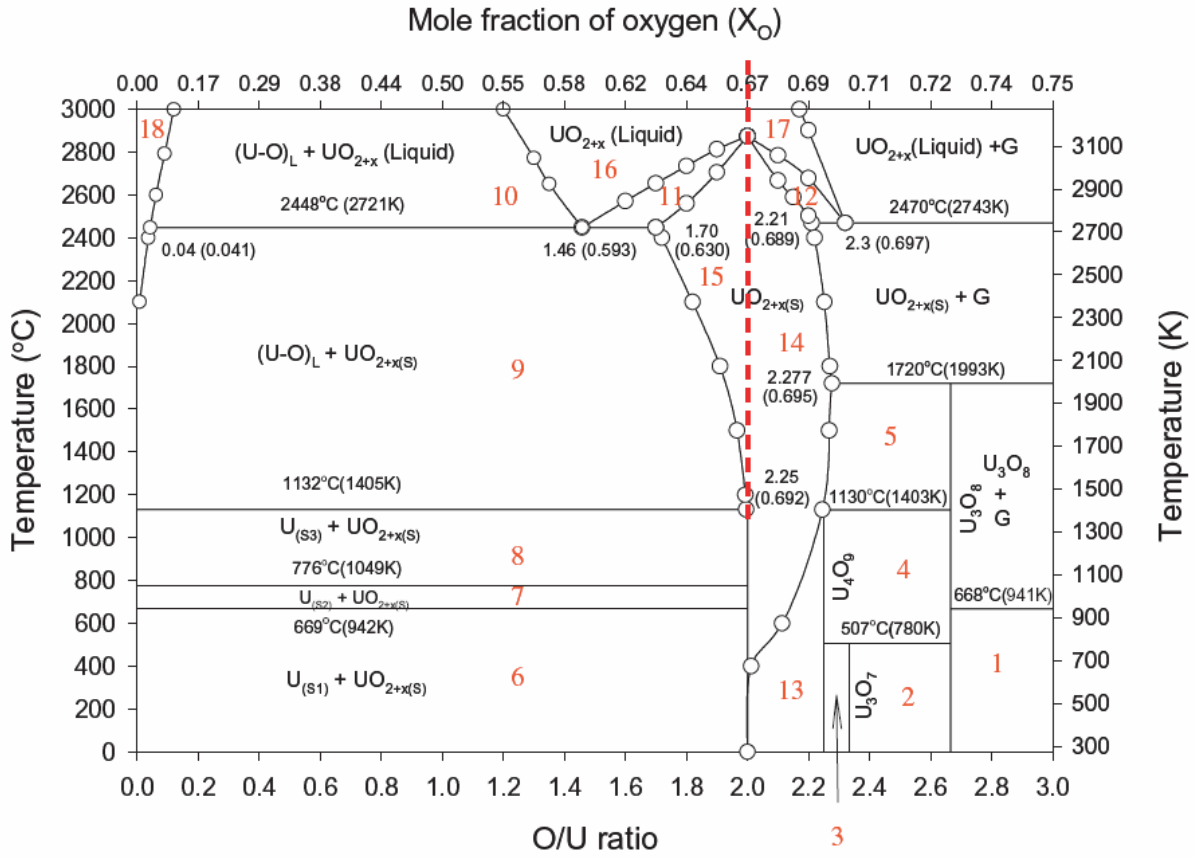


Figure 1-7. Phase diagram of U-O system. S and L in subscripts are used to indicate the solid and liquid phase. The numbers indicated in each phase are used in their reference for models of partial pressure of oxygen. [Adapted from reference 29 (Figure 4).]

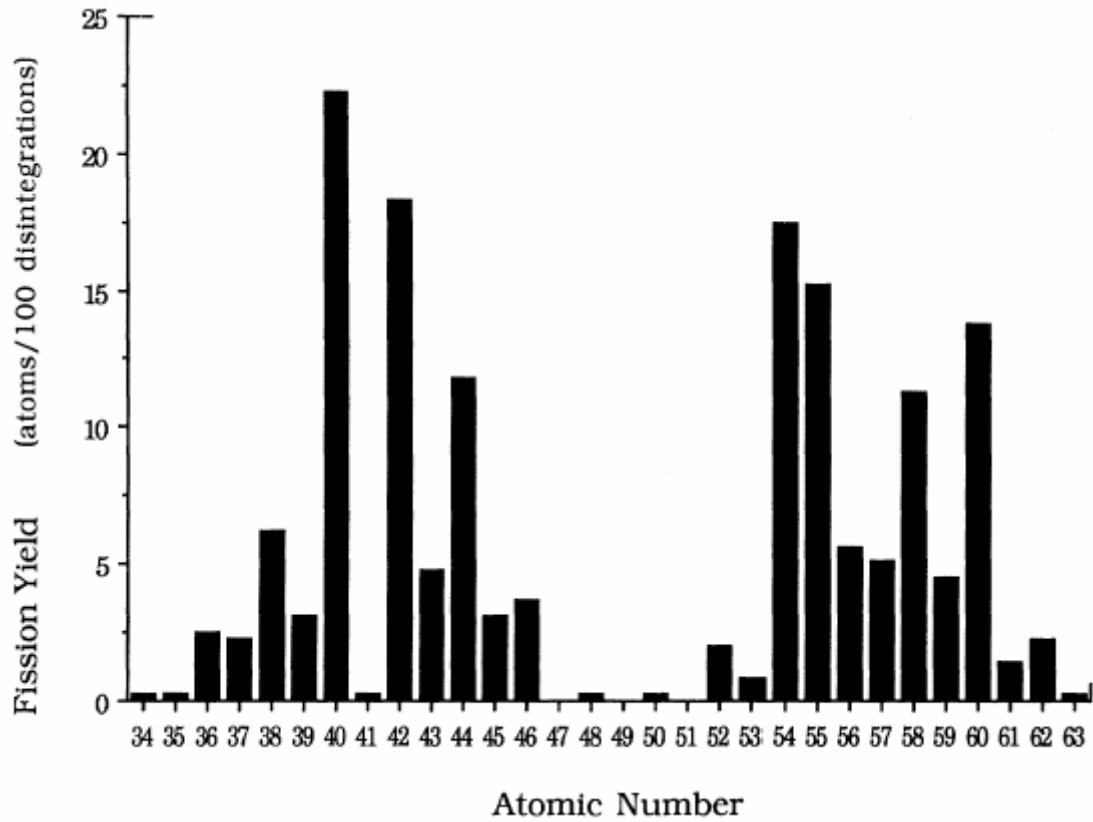


Figure 1-8. Fission product yield as a function of atomic number in a pressurized water reactor (PWR) after 2.9 % burnup. [Adapted from reference 37 (Figure 1).]

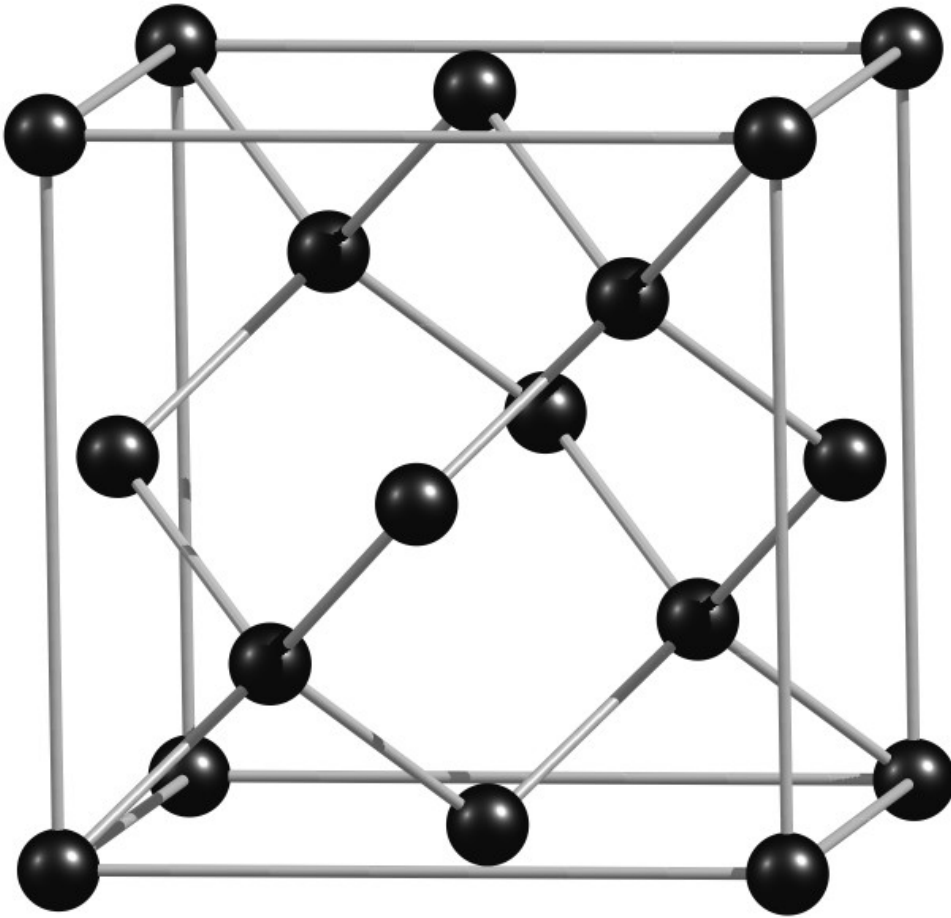


Figure 1-9. Unit cell structure of diamond. The bars are used to guide for the eyes.

## CHAPTER 2 INTRODUCTION TO THERMAL TRANSPORT IN MATERIALS

### **Basic Concepts of Thermal Transport**

Heat transfer is a fundamental mode of energy transport in nature. It is so fundamental that it exists everywhere from the interactions of molecules to the radiation of the cosmic microwave background of the universe. In today's world of technology, understanding the mechanism of heat transfer is more important than ever.

One example of the application of thermal energy management is in electronic devices. The size of logic circuits continues to shrink, and the length scale of a transistor is reaching ~45 nm today.<sup>55, 56</sup> Accordingly, the energy density of the device is also increasing. For example, chip level power densities as of Fall 2006 were estimated to be the order of  $100 \text{ W/cm}^2$ .<sup>57</sup> When the temperature of the transistor rises, the performance of the chip degrades: mobility and threshold voltage lowers and the leakage current increases.<sup>58, 59</sup> Therefore, such high power density electronic devices require better heat removal technologies.

Another example is in the generation of electrical power. Both scientific and technological advances today require an increasing supply of energy. In addition, the need for minimizing the dependence on foreign sources for energy production is naturally diversifying the field of power generation technologies. As a result nuclear energy is again receiving considerable attention. Nuclear power technology has the advantage of high power density per weight of the fuel, and no emission of the greenhouse gases. However, the concerns for the safety of radioactive waste have been a major issue. Therefore the continuous improvement of the technologies involved in the nuclear materials is imperative. Both fuel and structural materials used in nuclear power generation are under extreme conditions of radiation and temperature. For example, as discussed in Chapter 1,  $\text{UO}_2$  is the standard nuclear fuel material today. A typical ~1cm diameter fuel pin

in a PWR under operating conditions experiences a temperature of ~800 K at the surface and nearly 1600 K. Ideally, all the heat generated by the nuclear fission reactions is quickly released to the coolant so that the thermal energy can be converted to create the steam which drives the turbine and generates electricity. However, because of the high temperature of the material, the fuel pins experience physical and chemical changes in their properties that often result in undesirable effects such as deformation and cracking of fuel pellet, and possible chemical interaction with coolant.<sup>11</sup> Therefore, understanding the heat transfer mechanisms in nuclear fuel materials is particularly important.

In this chapter a general discussion on the types of heat transfer and mechanisms in solids is given, with particular emphasis on phonon-mediated thermal transport.

### **Three Modes of Heat Transfer - Conduction, Radiation, Convection**

Heat transfer in materials can occur through three distinct mechanisms: conduction, radiation and convection. Conduction occurs by the motion of the energy carriers such as electrons, lattice vibrations; radiation takes place via electromagnetic waves. By contrast, convection involves the mass transport of the constituent atoms. In solid materials, convection is therefore not relevant and will not be discussed further.

In electronic conductors, electrons are the major thermal energy carriers. The electronic contribution to thermal transport depends on the electrical conductivity and temperature. This is captured in the relation in Wiedemann-Franz law;

$$\frac{\kappa}{\sigma T} = \eta_L. \quad (2-1)$$

$\kappa$  and  $\sigma$  are the thermal and electrical conductivities, and  $T$  is the temperature.  $\eta_L$  on the right hand side is a constant called the Lorenz number,  $(3/2)(k_B/e)^2 = 1.11 \times 10^{-8} \text{ W}\Omega/\text{K}^2$ , where  $k_B$  is the

Boltzmann constant and  $e$  is the electron charge. This law holds to a good approximation if the collisions of the electrons are elastic.<sup>60</sup>

For intrinsic semiconductors and insulators, lattice vibrations (phonons) are the major carrier of thermal energy. This mechanism will be discussed in detail. It should be noted that the conduction through electrons and phonons can couple and operate simultaneously; they are not, however, relevant for the materials of interest here.

Whatever the carrier may be, once the system reaches steady state and the temperature distribution across the system is known, one can apply Fourier's law:

$$\vec{J} = -\kappa \nabla T. \quad (2-2)$$

$\vec{J}$  is the heat current,  $\kappa$  is the thermal conductivity of the medium, and  $T$  is the temperature.

Notice that  $\vec{J}$  and  $\nabla T$  are vectors; therefore,  $\kappa$  is a second-rank tensor. The negative sign indicates the fact that the heat flows from higher to lower temperature regions. The assumption here is that the medium is a continuum such that temperature can be defined every point within the volume of interest, and that the change of temperature is linear in space.

Radiation is another form of heat transfer involving the transmission of electromagnetic waves. Every material emits radiation at finite temperature because of the thermal oscillation of ions and electrons.<sup>61</sup> The oscillating charged particles emit electromagnetic waves of the corresponding energy.<sup>62</sup> The spectrum of the radiation follows the Planck distribution of a black body radiation.<sup>61</sup> The total emissive power is<sup>63</sup>,

$$J = \varepsilon_s \sigma_s T^4, \quad (2-3)$$

$\sigma_s$  is the Stefan-Boltzmann constant,  $5.670 \times 10^{-8} \text{ W/m}^2\text{K}^4$ , and  $\varepsilon_s$  is the emissivity of the material.

This mechanism is important at high temperature because of the  $T^4$  dependence. A good example is the thermal transport in thermal barrier coating. Yttria stabilized zirconia (YSZ) is a

commonly used for thermal barrier coating of gas turbine engine blade<sup>64,65</sup>. At the surface of YSZ layer, the temperature is ~2000 K or so, and at the inner interface with the bond coating it is above 1300 K depending on the way the coating is applied. Although heat transfer in YSZ is dominated by the conduction mechanism, the radiative component cannot be ignored at these high temperatures. For example, for a single layered 8 wt.% YSZ the radiation heat current density can be almost 25 % of the total heat flux for YSZ between the surface temperature of ~1700 K and bond coating temperature of 1400 K with 250 micron thick coating.<sup>66</sup> (The previous sentence is too complicated – please simplify) In the case of UO<sub>2</sub>, Hyland<sup>67</sup> estimated the radiation contribution to the thermal conductivity at very high temperature (>2900 K). His estimate suggests that the radiation component in the thermal conductivity is much less than other contributions. Bakker *et al.*<sup>68</sup> and Hayes *et al.*<sup>69</sup> also made estimates of the contribution of radiation to heat transfer in porous UO<sub>2</sub> using finite element methods. Their calculations gave ~1 % of the total thermal conductivity at 3000 K is due to radiation. Because of this reason, the radiative thermal transport in UO<sub>2</sub> is normally excluded from the analysis<sup>3</sup>.

In many situations, heat is transferred not only by a single mechanism but by more than one simultaneously. Effects of the individual modes must be taken into account to understand the entire processes.

### **Phonon Heat Transfer in Electronic Insulators**

As described above, in electronic insulators, phonons are the major carriers of the thermal energy. A model of phonon mediated heat transfer can be derived from the scattering of a phonon gas. The following discussion is based on standard discussions in solid state physics texts.<sup>38, 60, 70</sup>

To describe phonon-mediated heat transfer, the thermal conductivity of a solid can be considered as follows. Imagine phonons as particles behaving like gas molecules. Assume that

there is a container having a number of phonons with concentration,  $n$ . Suppose the system is in steady state between a temperature drop,  $\Delta T$ . If  $c$  is the specific heat per phonon, a phonon will lose energy  $c \Delta T$  by moving from the hot end to the cold end is,  $c \Delta T$ . If the local temperature gradient is  $dT/dx$  and  $l$  is the mean free path of the particles, then the temperature drop over distance  $l$  in direction  $i$  is  $\Delta T = (dT/dx_i)l_i$  (The Einstein summation convention is assumed on repeated indices from here on unless explicitly stated otherwise.) Then, the net flux of the energy carried by the phonons is,

$$J_i = -n v_i c \frac{\partial T}{\partial x_j} l_j = -c_v v_i v_j \tau \frac{\partial T}{\partial x_j}, \quad (2-4)$$

where  $v_i$  is the mean velocity of the particles,  $l_i$  is the mean free path,  $c_v$  is the volumetric specific heat, and  $\tau$  is the average time between two collision events of phonons, and is known as the relaxation time. By Fourier's law, the thermal conductivity is the given by,

$$\kappa_{ij} = c_v v_i l_j, \quad (2-5)$$

If the system is isotropic, the mean velocity of the phonons is  $v_i = \bar{v}/3$ . Therefore, the thermal conductivity is given by,

$$\kappa = \frac{1}{3} c_v \bar{v} l, \quad (2-6)$$

As discussed above, phonons, i.e. lattice vibrations, can be the major carrier of thermal energy. Despite the simplicity of the expression, this kinetic formula is very useful. Indeed, it will be the foundation for our phenomenological analyses of phonon-mediated thermal transport.

To understand the mechanisms of the thermal resistance to heat flow, two types of phonon scattering processes must be introduced. Phonons propagating in a crystalline lattice have wave vectors which are constrained by the periodic nature of the crystalline structure. A structure that is crystalline in a real space exhibits periodicity in the reciprocal (or momentum) space. This

periodicity in the momentum space is given by the reciprocal lattice vector,  $\vec{K}$ . For example, an FCC structure in real space has a BCC structure in reciprocal space, and vice versa. Just as a real space lattice structure has a primitive cell given by the Wigner-Seitz cell construction, a reciprocal space has a corresponding primitive cell given by the first Brillouin zone (BZ). The reciprocal lattice structure can be reproduced by replicating the first BZ and applying translational symmetry. The physical importance of the lattice structure in the reciprocal space is that it places constraints on the momentum conservation of phonons during the scattering processes. Consider a three-phonon scattering process:

$$\vec{p}_1 + \vec{p}_2 = \vec{p}_3 + \vec{K}. \quad (2-7)$$

This can be seen as two phonons with momenta,  $\vec{p}_1$  and  $\vec{p}_2$ , colliding to form a single phonon with momentum  $\vec{p}_3$ . Because of this conservation law of the crystal momentum, there are two possible processes: normal (N) and umklapp (U) processes. An N-process is a phonon scattering event in which the total phonon momentum is conserved, i.e.,  $\vec{K} = 0$ ; this is analogous to the scattering processes of particles such as gas molecules. A U-process, however, is a scattering process in which total phonon momentum changes by a reciprocal lattice vector, i.e.,  $\vec{K} \neq 0$ . Since the 1<sup>st</sup> BZ is defined by the reciprocal lattice vector, the sum of all the phonon momenta for a U-process must be outside of the first BZ. U-processes play distinct roles in the thermal transport. In N-processes, the total crystal momentum is conserved. This means that, if phonons are created on one end, the same number of phonons must disappear on the other end to conserve the net flow. Since phonon-phonon scattering conserves phonon energy, there cannot be any thermal resistance. Therefore, N-processes cannot contribute to the thermal resistance. On the other hand, in U-processes, the crystal momentum is not conserved, so that there can be a net heat flow and energy can dissipate.

As the thermal conductivity expression, Equation 2-6 include the specific heat, it is helpful to introduce the commonly used approximation to gain insight to its behavior.

The internal energy from the vibration of the atoms for each polarization is given by,

$$U = \int_0^{\infty} d\omega D(\omega) \langle n(\omega) \rangle, \quad (2-8)$$

where  $D(\omega)$  is the density of state (DOS) of phonons and  $\langle n(\omega) \rangle$  is the ensemble averaged number density of phonons, which follows Bose-Einstein statistics:

$$\langle n(\omega) \rangle = \frac{1}{\exp(\hbar\omega/k_B T) - 1}. \quad (2-9)$$

The internal energy can be used to calculate a number of thermodynamic quantities through the Maxwell's relations. However, this is not a straightforward task; the main complication being that  $D(\omega)$  is a rather complicated function of  $\omega$  and is singular. In order to gain physical insight through simpler analytic expression, there are two commonly used approximations: the Einstein approximation and Debye approximation.

The Einstein model assumes  $\omega(k) = \omega_0$ ; that is the atoms in the lattice all vibrate independently of each other with the same frequency. Thus  $D(\omega) = N\delta(\omega - \omega_0)$ , where  $\delta(\omega)$  is the Dirac delta function. Because of the simple expression of  $D(\omega)$ , Equation 2-8 can be directly integrated. From the simple thermodynamics relation  $c_v = (\partial U / \partial T)_v$ , we get,

$$c_v = 3Nk_B \frac{x^2 e^x}{(e^x - 1)^2}. \quad (2-10)$$

Here we introduced dummy variable  $x = \hbar\omega/k_B T$ . It is well known that the Einstein model underestimate the specific heat at low temperatures ( $T \ll \theta_D$ ).<sup>38, 60</sup> (Shouldn't there be an integral here – the Einstein model gives  $c_v$  vs T as the final result). At high temperature, ( $T \gg \theta_D$ ), it predict the Dulong-Petit law, as it must to be consistent with classical thermodynamics.

The Debye approximation assumes  $\omega = vk$ , where  $v$  is the speed of phonon assumed to be independent of  $k$ . Under the Debye approximation, the density of state is simply,

$$D(\omega) = \begin{cases} \frac{V\omega^2}{2\pi^2v^3}, & \omega < \omega_D, \\ 0, & \omega > \omega_D \end{cases}, \quad (2-11)$$

where  $V$  is the volume of the solid. The maximum frequency,  $\omega_D$  of phonons is limited by the size of the primitive cell, which is determined by the number density of atoms,  $n$ :

$$\omega_D = 2\pi^2v^3n. \quad (2-12)$$

Now the internal energy can be written as,

$$U = 9k_B T \left( \frac{\theta_D}{T} \right)^3 \int_0^{\theta_D/T} dx \frac{x^3}{e^x - 1}, \quad (2-13)$$

where,

$$\theta_D = \frac{\hbar\omega_D}{k_B} = \frac{2\pi^2\hbar}{k_B} v^3 n, \quad (2-14)$$

is the Debye temperature. Finally the volume specific heat can be given by the,

$$c_V = 9Nk_B \left( \frac{\theta_D}{T} \right)^3 \int_0^{\theta_D/T} dx \frac{x^4 e^x}{(e^x - 1)^2}. \quad (2-15)$$

The integral is called the Debye integral of 4<sup>th</sup> order, and in general it must be computed numerically. However, it is instructive to consider the limiting cases of low and high temperature relative to the Debye temperature:

$$c_V = \begin{cases} \frac{12\pi^4}{5} Nk_B \left( \frac{T}{\theta_D} \right)^3, & T \ll \theta_D, \\ 3Nk_B, & T \gg \theta_D \end{cases}. \quad (2-16)$$

The high temperature value is the same as the Dulong-Petit law.

Although both of these models are rather oversimplified, they are useful approximations that can be used to gain insight of the actual behavior of phonons of different modes.

Using the above results for the specific heat, the temperature dependence of thermal conductivity in solid can be described based on the phonon model. At high temperature ( $\theta_D \ll T$ ), the specific heat of a solid is constant, taking the Dulong-Petit value of  $c_v = 3k_B$ . The velocity of sound in a solid is not a strong function of temperature (unlike the classical gas) and does not control the temperature dependence of  $\kappa$ .<sup>70</sup> Therefore, the only temperature dependence of the thermal conductivity comes from the mean free path. A simple analysis based on Boltzmann equation of phonon transport, yields a  $1/T$  dependence of the mean free path at high temperature, although the exact solution cannot be obtained.<sup>71</sup> Using the Boltzmann equation, the scattering rate can be written in term of the change in occupation number of phonons, which can be given as a sum of all the scattering processes possible under given kinematics. The change in the occupation number turns out to be linear in the perturbation of the occupation numbers for three phonon processes. The perturbation is linear in temperature,  $T$ , of the system and therefore the scattering rate is also linear in  $T$ . Thus knowing that the mean free path is inversely proportional to the scattering rate,  $l$  is proportional to  $1/T$ . More sophisticated analysis shows that in fact the temperature dependence is quite generally,  $1/T^n$ , where  $n$  is between 1 and 2; this is confirmed experimentally<sup>60, 72</sup>. The precise value of  $n$  is determined by the competition between the cubic and quartic anharmonic phonon-phonon interactions<sup>72</sup>.

At the extreme of low temperature ( $\theta_D \gg T$ ), the phonon mean free path due to phonon-phonon scattering becomes extremely long. In fact, it can become so long that it is comparable to the dimensions of the solid; as a result the thermal conductivity is essentially independent of the mean free path. This limit of the mean free path is known as the Casimir limit<sup>73</sup>, and the scattering is dominated by the surfaces. In this limit, the mean free path is almost temperature independent. However, at low temperatures the specific heat has the temperature dependence of

$\sim T^3$  under the Debye approximation. As a result, the thermal conductivity thus also has the same  $T^3$  dependence. This behavior agrees with a number of experimental observations<sup>60</sup>.

In the intermediate range of temperature ( $T \sim \theta_D$ ), the situation is rather complicated and we have to resort to extending the behavior from the high and low temperature limits. When U-processes are the only source of the thermal resistivity,  $\kappa$  rises exponentially with decreasing  $T$ ,  $\sim \exp(\theta_D/T)$ , because of the quantization of the energy levels<sup>70</sup>. Since the specific heat rises as  $T^3$  at low temperature,  $\kappa$  is commonly expressed as,

$$\kappa = A \left( \frac{T}{\theta_D} \right)^n \exp\left( \frac{\theta_D}{bT} \right). \quad (2-17)$$

A, b, n are to be determined by fit. This function has the maximum at  $T = \theta_D/nb$ , where the value of  $nb$  is typically about 15-35. (Table 2-1.)

For summary, the temperature dependence the heat capacity of a pure crystalline solid is given by the Debye approximation. The temperature dependence of thermal conductivity varies from  $\sim T^3$  to  $T^n \exp(\theta_D/bT)$ , then  $\sim 1/T$ . Figure 2-2 illustrates this temperature dependence using data on Ge.

### Point Imperfections

A crystalline solid can contain a variety of point defects such as interstitials, vacancies, isotopic defects, and substitutional defects. These defects can differ from the ions in solid with regards to their mass, size, and interactions with other atoms. In order to understand the contribution to the thermal resistance from point defect scattering, we must return to the original expression of the thermal conductivity in Equation 2-6:

$$\kappa = \frac{1}{3} c_v \bar{v} l,$$

Here, it is useful to think the conductivity as a sum of the contribution from each mode of wave vector  $\vec{k}$ ,

$$\begin{aligned}\kappa &= \frac{1}{3} \sum_j \int c_{v,j}(k) v_j(k) l_j(k) d\vec{k} \\ &= \frac{1}{3} \sum_j \int c_{v,j}(k) v_j^2(k) \tau_j(k) d\vec{k},\end{aligned}\tag{2-18}$$

where  $\tau_j(k)$  is the relaxation time. The main problem one faces in calculation of  $\kappa$  is to calculate the relaxation time. This may be done by solving the Boltzmann transport equation. Exact solutions are generally unattainable due to mathematical complexity, and approximations must be used.

Klemens<sup>74</sup> applied second-order perturbation theory to the scattering of phonons by point imperfections. The point defect in this analysis is assumed to be a generic atomic defect with mass  $M_i$ , force constant  $f_i$ , and radius  $R_i$  such that the difference from the corresponding values of crystalline host material are given by,  $\Delta M_i = M_i - M_0$ ,  $\Delta f_i = f_i - f_0$  and  $\Delta R_i = R_i - R_0$ , where  $M_0$ ,  $f_0$  and  $R_0$ , are the mean values. The derivation of the formal expression is rather lengthy and the details are not central for this study. The basic procedure is following. Write the transition rate of phonon level by the phonon-defect scattering using the Fermi's golden rule<sup>75</sup>. Then give Hamiltonian in terms of the defect properties such as the differences in masses, radii, or force constants. Then the rate of the number of phonons created by the scattering can be obtained by integration the transition rate in momentum space. Finally the scattering rate can be written in terms of the change in the number of phonons. In the end, the scattering rate by the static point imperfections in the long wave length limit at low temperature ( $T \ll \theta_D$ ) is given by,

$$\frac{1}{\tau_j(\vec{k})} \sim \frac{\omega_j^4(\vec{k})}{v_j^3(\vec{k})} \sum_i x_i \left[ \frac{1}{12} \left( \frac{\Delta M_i}{M} \right)^2 + \left\{ \frac{\Delta f_i}{\sqrt{6}f} - 6 \sqrt{\frac{2}{3}} \frac{\Delta R_i}{R} \right\}^2 \right].\tag{2-19}$$

The overall numerical constants are suppressed since they are not relevant to the discussion. The summation is over the atomic species.  $x_i$  is the fraction of each defect species. Notice the mass, force constant, and radius difference comes into the scattering rate. Another important point is the dependence of the scattering rate on  $\omega^4$ . Since  $\omega = vk$ , and the original formal expression for the mean free path is proportional to the ratio of 4<sup>th</sup> order and 8<sup>th</sup> order Debye integrals, the mean free path is proportional to  $T^4$  at  $T \ll \theta_D$ . This in turn gives  $\kappa \sim 1/T$  dependence since the specific heat contribution gives  $T^3$  at  $T \ll \theta_D$ . Equation 2-19 also suggests that the thermal resistance is linear in the concentration of defects, but this dependence is rather artificial and introduced purely for the sake of mathematical convenience. A similar analysis shows that, at high temperature, the thermal resistance from point imperfections is independent of temperature<sup>70, 76</sup>.

### **GBs and Surfaces**

GBs and surfaces are also sources of thermal resistance for phonon mediated heat transfer. In order to quantify the thermal transport property of an interface, a phenomenological relationship analogous to Fourier's law is generally used:<sup>77, 78</sup>

$$J = G_k \Delta T. \tag{2-20}$$

$G_k$  is the interfacial thermal conductance, also known as Kapitza conductance.  $\Delta T$  is the temperature drop at the interface. There are two widely used phenomenological models for studying the interfacial resistance. The first is the acoustic mismatch model (AMM). In this model, the crystal is treated as a continuum while the interfacial resistance arises due to the acoustic impedance mismatch between the two solids on both side of the interface<sup>79</sup>. A key weakness of this approach is that this model does not take into the discrete lattice structure of ions consisting of solid. Thus, this approach cannot be justified if the phonon wavelength is comparable to the lattice parameter of the crystal. Furthermore, this model does not convey any

information of the effect of the interfacial structure on the thermal transport. Because of these limitations, AMM predicts zero interfacial resistance in GB structures, a result that is in qualitative disagreement with experiment. The second model is the diffuse mismatch model (DMM). DMM assumes independent scattering of phonons with the interface. In addition, all phonons are assumed to be randomly scattered at the interface such that they do not have any memory of their origin<sup>79, 80</sup>. Thus the fraction of energy transferred across the interface is given by the ratio of the phonon density of states (DOS) on either side of the GB. The DMM has been shown to work in some cases<sup>80</sup>, but predicts that the phonon transmission coefficient for all twist grain boundaries should be 50%, a result that disagrees with simulation results.<sup>77</sup>

There is also an analytical approach by Klemens for GB scattering<sup>76</sup>. However, this approach is severely limited by the approximations which are needed to make the calculation tractable. Klemens's model assumes that the GB consists of multiple edge dislocations. He has shown that the for low angle scattering of long wavelength phonon at low temperature, the scattering rate is proportional to the square of the phonon frequency,  $1/\tau \sim \omega^2$ . He argued that the thermal conductivity of a solid with GBs and surfaces should increase with  $T^3$  below  $\theta_D$  following the specific heat but should be constant at higher temperatures<sup>76</sup>. Based on the Klemens' work, Stoner and Maris gave the maximum limit to the Kapitza conductance in the form of the Debye integral<sup>81</sup>. However, their experimental data on heterogeneous interfaces were in poor agreement with their calculation.

Because of the lack of a satisfactory theoretical model, extensive work in the theory of interfacial thermal transport is still needed.

### **Thermal Transport in Disordered Solids**

In crystalline solids, the thermal transport is limited either by phonon-phonon scattering or phonon-defect (point defects, dislocations, GBs, surfaces) scattering. In highly disordered solids,

including amorphous materials, the thermal transport mechanism is fundamentally different from that in crystalline solids. In non-crystalline, the atomic arrangement is so disordered that the mean free paths of phonons are extremely short and are independent of temperature<sup>82, 83</sup>. However, the specific heat is almost linear in temperature at low temperature<sup>38</sup>. Above the Debye temperature,  $c_V$  increases slowly with  $T$  and eventually becomes almost temperature independent. Therefore, assuming the form of Equation (2-6), the thermal conductivity of disordered solid follows that of its specific heat. Slack<sup>83</sup> calculated the thermal conductivity of the Debye solid, assuming that the mean free path of the phonon is half of its wavelength for each mode. Under this assumption, he defined the minimum thermal conductivity of glasses. Cahill and Pohl<sup>84</sup> made the same assumption and gave the minimum thermal conductivity of amorphous solids in terms of a Debye integral. Although these models give reasonable agreement for the thermal conductivity of highly disordered solids, the physical basis of describing thermal transport in an amorphous solid using phonon gas model is questionable because the phonon mean free path in these materials is so short (on the order of the interatomic distance) that the concept of phonons itself seem inappropriate.

Allen *et al.*<sup>85, 86</sup> took a different approach to this problem, and developed a model for the thermal conductivity of amorphous materials at high temperatures. Their model is based on a harmonic approximation analysis of the vibrational modes of the system. They demonstrated that the majority of the thermal energy is transferred through diffusive modes termed “diffusons”. In their simulations of amorphous Si, approximately 93 % of the vibrational modes correspond to the diffuson modes. Other modes in the higher frequency bands are called “locons” due to the fact that they are truly spatially localized. At the other extreme of the phonon spectrum, the low frequency modes are similar to phonons, having well defined wave

vectors and polarization vectors. They are called “propagons” and constitute only about ~3 % of the entire vibrational modes for a-Si. Although the propagons are very efficient in transfer of thermal energy, their contribution to thermal conductivity is small because of the small population. Within this approach, the temperature dependence of the thermal conductivity mostly comes from the temperature dependence of specific heat. This in turn agrees with the temperature independent behavior at high temperature. The approach developed by Allen *et al.* is useful not only in analyzing amorphous solids, but in analyzing the thermal conductivity in heavily doped crystalline materials;<sup>87</sup> we will use this framework to understand the thermal conductivity of  $\text{UO}_{2\pm x}$ .

Table 2-1. Values of the Debye temperature and the maximum in the experimental thermal conductivities of selected materials.

	$\theta_D$ (K)	$T_{\max}$ (K)	$\theta_D/T_{\max}$
NaF	492 <sup>60</sup>	20 <sup>38</sup>	24.6
LiF	730 <sup>60</sup>	20 <sup>60</sup>	36.5
C (diamond)	2200 <sup>6</sup>	70 <sup>2</sup>	31.4
Si	625 <sup>60</sup>	40 <sup>88</sup>	15.6
Ge	360 <sup>60</sup>	15 <sup>89</sup>	24.0
MgO	940 <sup>90</sup>	30 <sup>2, 63</sup>	31.1
$\alpha$ -Al <sub>2</sub> O <sub>3</sub>	900 <sup>91</sup>	30 <sup>70</sup>	30.0

$T_{\max}$  is an estimate from the plot of  $\kappa(T)$ .

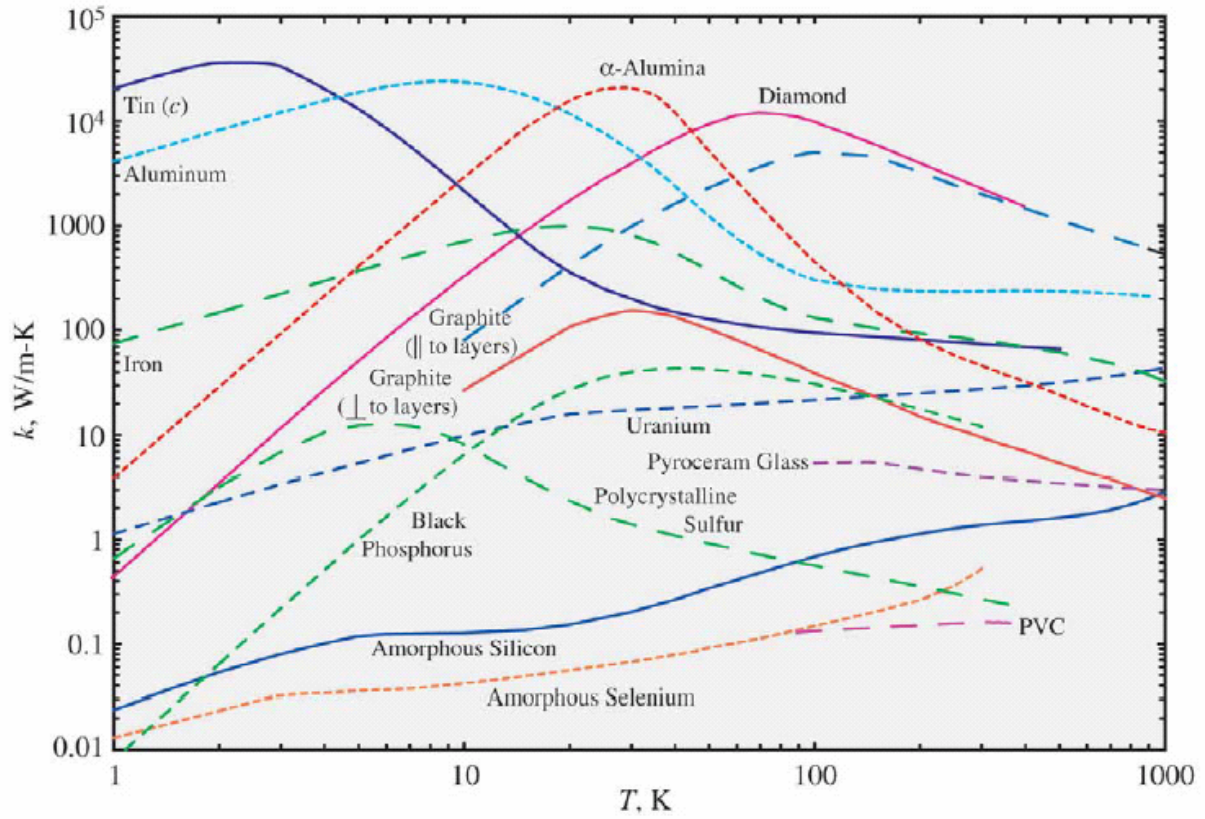


Figure 2-1. Temperature dependence of the thermal conductivity of selected materials.<sup>92</sup>

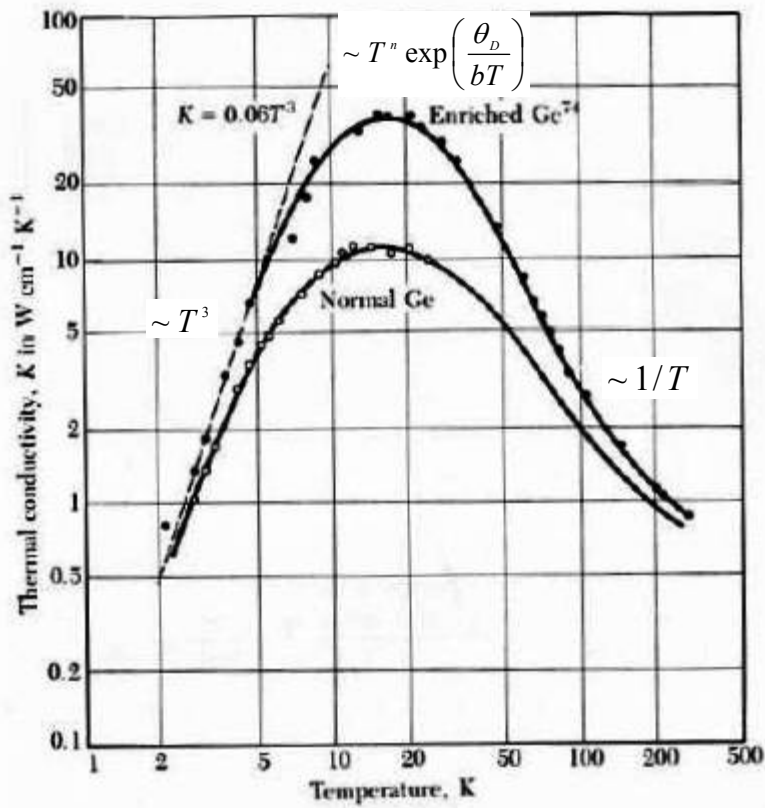


Figure 2-2. Temperature dependence of the thermal conductivity of Ge.<sup>38</sup> Temperature dependence given by the Debye approximation is shown in the figure. The two data sets are used to compare the effect of isotopic defects. The enriched Ge has 96 % <sup>74</sup>Ge. Normal Ge has 37 % <sup>74</sup>Ge and the rest consists of <sup>72</sup>Ge (27 %), <sup>70</sup>Ge (20 %), <sup>73</sup>Ge(8 %), and <sup>76</sup>Ge(8 %).

## CHAPTER 3 SIMULATION METHODS

### **Introduction**

There are a number of ways to simulate materials in condensed phases. There are several types of simulations which involve electronic structure calculations such as density functional theory (DFT) and Hartree-Fock method.<sup>93</sup> Molecular dynamics (MD) and Monte-Carlo (MC) treat atoms as the fundamental entities. Finite-element<sup>94</sup> and phase field<sup>95</sup> methods are continuum approaches that can handle  $>\mu\text{m}$  in size. The simulation method must be chosen based on the process of interest. For example, if one is interested in understanding the electronic structure of materials, DFT or HF may be appropriate. If equilibrium behavior is required, MC is a common choice.

MD is particularly useful in the study of nonequilibrium dynamic processes at the atomic level. MD treats atoms as point particles with no internal structure. For each atom, mass and charge are assigned. All atoms are treated classically and their dynamics are obtained by solving the Newton's equation of motion. Details of how to integrate the equation of motion are described in the following section. Since the electronic degrees of freedom of atoms are ignored, MD is capable of handling a large number of atoms and molecules. With today's computational power, MD can handle approximately  $10^7$  atoms on parallelized small workstation computers. With a super computer, simulation of  $10^9$  atoms is possible. The only physical input required by the MD simulation is the interatomic potential. This has a significant implication. It means that if the quality of interatomic potential is good, the calculated properties of the material as a whole should be reproduced to a reasonable extent. Unfortunately, while a given interatomic potential may describe well some aspects of the physical behavior of a material, no interatomic potential has been found to capture all the properties of a material in realistic manner.

## Numerical Integration

As mentioned in above, MD simulation requires integration of Newton's equation of motion, which is a second order ordinary differential equation. There are a variety of methods available to integrate such equation.<sup>96,97</sup> Here, we focus only on the Gear predictor-corrector method since it is the algorithm used in our in-house MD code.

The 5<sup>th</sup> order Gear predictor-corrector method<sup>96</sup> uses a high order Taylor expansion of atomic position about the current position,  $x(t)$ , up to the 5<sup>th</sup> derivative. Using the current velocity,  $v(t)$ , acceleration,  $a(t)$ , and higher order derivatives of  $x(t)$ , the next position of the atoms are predicted:

$$\vec{x}_p(t+dt) = \vec{x}(t) + \vec{v}(t)dt + \frac{1}{2}\vec{a}(t)dt^2 + \frac{1}{3!}\frac{d^3\vec{x}}{dt^3}(t)dt^3 + \frac{1}{4!}\frac{d^4\vec{x}}{dt^4}(t)dt^4 + \frac{1}{5!}\frac{d^5\vec{x}}{dt^5}(t)dt^5. \quad (3-1)$$

Once the next positions of the atoms are predicted, the force on each atom is calculated using the predicted positions. With the new predicted force, the atomic positions are corrected by the corrector step:

$$\vec{x}_c^{(i)}(t+dt) = \vec{x}_p^{(i)}(t+dt) + c_i \{ \vec{x}_p^{(2)}(t+dt) - \vec{x}_o^{(2)}(t+dt) \}. \quad (3-2)$$

The superscript ( $i$ ) is used to indicate the order of derivative of the trajectory. Thus,

$$\vec{x}_p^{(i)}(t) \equiv \frac{1}{n!} \frac{d^n \vec{x}_p}{dt^n}(t). \quad (3-3)$$

is implied.  $c_i$  is an array of numerical constants:  $c_0=3/20$ ,  $c_1=251/360$ ,  $c_2=1$ ,  $c_3=11/18$ ,  $c_4=1/6$ , and  $c_5=1/60$ .<sup>96</sup>  $\vec{x}_o^{(2)}(t+dt)$  is obtained by the plugging  $\vec{x}_p^{(2)}(t+dt)$  into the equation of motion.

$$\vec{x}_o^{(2)}(t+dt) \equiv \frac{1}{m} \vec{F}(\vec{x}_p^{(2)}(t+dt)). \quad (3-4)$$

## Periodic Boundary Condition

Although MD simulation technique can handle a large number of atoms, the number of atoms is quite small compared to that in real physical systems, which contain of the order of  $10^{24}$

atoms. Therefore in order to simulate a large bulk material, periodic boundary condition (PBCs) are used. Figure 3-2 illustrates PBCs in 2 dimensions. The actual simulation cell is the central shaded cell of size  $L \times L$ . Suppose, for simplicity, that the simulation cell contains only 5 molecules as shown in the figure. When molecule 1 crosses the boundary of the simulation box, its periodic image re-enters the cell from the other side. Clearly this is not what actually happens in a real materials; however but if there are a large number of atoms in the simulation cell, the environment any atom experience will resemble to that of an infinitely large system.

Another important effect of the PBCs is in the collective vibrations of atoms and molecules and pressure waves. If the PBC is not used, the simulation cell boundaries are terminated by the surfaces and only standing vibrational waves are allowed. Having PBCs actually allow traveling waves in the system allowing the material to behave like a large medium. It should be noted, however, that even if traveling waves are allowed in the simulation cell, their maximum wavelength is limited by the size of the cell, with longest wavelength being twice the length of the simulation cell size. As we shall see, these constraints are very important for thermal conductivity calculations.

### **Interatomic Potentials**

The interatomic potential is perhaps the most important piece in the MD simulation technique. As mentioned in the introduction to this chapter, the interatomic potentials are the only model input for MD simulations, and all the physical properties are determined by it. It is quite intriguing that even the rather crude models of interatomic interactions typically used can reproduce physical properties with reasonable accuracies.

### **Long-range Interaction**

Evaluation of the long-range  $1/r$  electrostatic interactions in ionic systems is one of the trickiest problems in MD simulations. We wish to compute the electrostatic energy by,

$$E_{ES} = \frac{1}{4\pi\epsilon_0} \sum_{i \neq j} \frac{q_i q_j}{r}, \quad (3-5)$$

where  $q_i$  and  $q_j$  are the charges of ions  $i$  and  $j$  separated by a distance  $r$ , and  $\epsilon_0$  is the electric permittivity of vacuum. The crux of the problem is that this sum is conditionally convergent. There have been several approaches proposed to get around this problem.<sup>96, 98</sup> In following, two methods used in our in-house MD code are described. The discussion focuses mainly on the idea behind the methodology rather than the details of derivation. Efficiency of the methods will also be discussed for the later purpose

### Ewald sum

The idea of Ewald sum is to rewrite the summation in Equation (3-2) in terms of the electric charge density and express these densities by a sum of delta functions. If we assume every point charge  $q_i$  is surrounded by a diffused charge of opposite sign,  $q_i$  cancels exactly (Figure 3-3). The potential energy due to charge  $q_i$  is the fraction of charge  $q_i$  that is not cancelled, and it goes to 0 rapidly at large distances. Using this approach, the conditionally convergent sum may be determined as:

$$E_{ES} = \frac{1}{2V} \sum_{\vec{k} \neq 0} \frac{4\pi}{k^2} |\rho(\vec{k})| \exp\left(-\frac{k^2}{4\alpha}\right) - \sqrt{\frac{\alpha}{\pi}} \sum_{i=1}^N q_i^2 + \frac{1}{2} \sum_{i \neq j}^N \frac{q_i q_j}{r_{ij}} \operatorname{erfc}(\sqrt{\alpha} r_{ij}). \quad (3-6)$$

The first term is the potential energy due the charge distribution  $\rho(r)$  given in reciprocal space. The second term is the correction for self-interaction. The third term is the electrostatic energy of the point charges screened by oppositely charged Gaussians given in real space.

Equation (3-6) is clearly complicated and the implementation of this in an MD code is not straightforward. Furthermore, for the application of this method to non-3D periodic system, further modifications are required.

In terms of efficiency, the time required for the evaluation of electrostatic interaction by Ewald summation scales as  $N^{3/2}$  where  $N$  is the number of atoms in the system. This is better than a straight forward evaluation of  $N^2$  scaling (Equation (3-5)); there are alternative methods which scale much better with the system size.<sup>96, 98, 99</sup>

### **Direct summation**

The  $1/r$  truncated summation method developed by Wolf *et al.* is a powerful alternative method to the Ewald summation.<sup>99</sup> From here on this method is referred to as direct summation. The idea is based on the two key observations:

1. The electrostatic energy by the double sum of Equation 3-5 depends strongly on the environment of the atoms.
2. The electrostatic energy of an ionic crystal (Madelung energy) is short-ranged.

Consider the case of NaCl crystal, for example. Imagine a sphere of radius  $R_c$  in the crystal. If one calculates the electrostatic energy using Equation 3-5, the values depends significantly on the choice of  $R_c$ . (Figure 3-4) Assuming that the net charge of the ions in the sphere is  $\Delta q$ , there is a clear linear dependence in the electrostatic energy on  $\Delta q$ . The Madelung energy of the crystal corresponds to the electrostatic energy for a charge neutral system. Thus, if it is possible to find the volume of the sphere such that  $\Delta q=0$ , a reasonably good value of the Madelung energy can be obtained. This can always be accomplished by smoothly compensating each charge in the sphere of  $R_c$  by equal and opposite charges at the surface of the volume. However, this itself is not sufficient for the direct application because of the slow oscillatory decay of the potential as a function of  $R_c$ . Additional damping of the pair potential is required for the method to be practically useful.

With all these in the consideration the electrostatic energy of the ionic crystal of  $N$  atoms can be written as,

$$E_{ES}(R_c) \approx \frac{1}{2} \sum_{i=1}^N \sum_{\substack{j \neq i \\ r_{ij} < R_c}} \left\{ \frac{q_i q_j}{r_{ij}} \operatorname{erfc}(\alpha r_{ij}) - \lim_{r_{ij} \rightarrow R_c} \left( \frac{q_i q_j}{r_{ij}} \operatorname{erfc}(\alpha r_{ij}) \right) \right\} - \left( \frac{\operatorname{erfc}(\alpha R_c)}{R_c} + \frac{\alpha}{\sqrt{\pi}} \right) \sum_{i=1}^N q_i^2 \quad (3-7)$$

where  $\alpha$  is the damping constant, whose value is chosen to produce the most efficient, yet accurate, results.. This method is also shown to work with highly disordered condensed phase such as liquid or amorphous solid.

The major advantage of this method is the computational efficiency. Because of the spherical truncation and fast convergence, the computation of the energy and forces is order  $N$ . This high efficiency is necessary for simulations of very large systems. The direction summation method is used in all of the simulations described in this thesis.

### Short-range Interactions

The short-range interaction is determined from the type of material. Two commonly used short-range interatomic potentials for ionic and covalent solids are the Buckingham<sup>100</sup> and Tersoff<sup>101, 102</sup> potentials. They are used here for the description of  $\text{UO}_2$  and diamond respectively.

The simplest form of the Buckingham potential is given by,

$$V(r_{ij}) = A_{ij} \exp(-r_{ij} / \rho_{ij}) - \frac{C_{ij}}{r_{ij}^6}. \quad (3-8)$$

Subscript  $i$  and  $j$  are used to indicate the type of interaction between atom  $i$  and  $j$ .  $A_{ij}$ ,  $\rho_{ij}$ ,  $C_{ij}$  are fitting parameters. The first term represents the repulsive potential from the overlap of the electron clouds of the two atoms. The second term is the Van der Waals attraction. There are a large number of the set of parameters for ionic solids; see the work of Lewis and Catlow<sup>103, 104</sup>, for instance. We will use a variant of this potential in Chapters 4-7.

The Tersoff potential was developed to describe covalent materials, taking into account the fact that the interatomic bonds depend on the environment of the atoms. The total energy  $E$  of a covalent solid is given by,

$$\begin{aligned}
 E &= \frac{1}{2} \sum_{i \neq j} V(r_{ij}) \\
 V(r_{ij}) &= f_c(r_{ij}) [A_{ij} \exp(-\lambda_1 r_{ij}) - B_{ij} \exp(-\lambda_2 r_{ij})] \\
 B_{ij} &= B_0 \exp(-z_{ij}/b) \\
 z_{ij} &= \sum_{k \neq i, j} \left[ \frac{w(r_{ik})}{w(r_{ij})} \right]^n [c + \exp(-d \cos \theta_{ijk})]^{-1} \\
 w(r_{ij}) &= f_c(r_{ij}) \exp(-\lambda_2 r_{ij})
 \end{aligned} \tag{3-9}$$

Here,  $A_{ij}$ ,  $B_0$ ,  $b$ ,  $c$ ,  $d$ ,  $n$ ,  $\lambda_1$ , and  $\lambda_2$  are parameters fitted to some bulk properties of the solid.  $\theta_{ijk}$  is the angle between the bond  $ij$  and  $jk$ .  $f_c(r_{ij})$  is given by,

$$f_c(r_{ij}) = \begin{cases} 1, & r < R - D \\ \frac{1}{2} - \frac{1}{2} \sin \left[ \frac{\pi}{2} \frac{(r_{ij} - R)}{D} \right], & R - D < r < R + D \\ 0, & r > R + D \end{cases} \tag{3-10}$$

$R$  and  $D$  are the fitting parameters. It is not easy to give physical meaning to all these terms except that  $A_{ij}$  and  $B_{ij}$  terms in  $V(r_{ij})$  are repulsive and attractive terms. The potential parameters for carbon are,  $A_{ij}=1393.6$  eV,  $B_0=346.74$  eV,  $b=$ ,  $c=38049$ ,  $d=4.3484$ ,  $\lambda_1= 3.4879$  Å,  $n=0.72751$ ,  $\lambda_2=2.2119$  Å,  $R=1.95$  Å, and  $D=0.15$  Å.<sup>101</sup> This potential is used to simulate diamond in Chapters 8 and 9.

### Thermostat

In order to simulate materials properties under realistic condition, it is necessary to control the temperature of the material. There are a several commonly used techniques for controlling the temperature. The simplest of all is the velocity rescaling thermostat. The idea of this method is to simply modify the velocity of all or a restricted number of atoms in the system such that

their mean temperature matches the target temperature. The kinetic energy of a solid consisting of  $N$  atoms in the system is related to the temperature by,

$$\sum_i \frac{1}{2} m_i \bar{v}_i^2 = \frac{3}{2} N k_B T, \quad (3-11)$$

where  $m_i$  and  $v_i$  are the mass and velocity of atom  $i$ ,  $T$  is the current temperature. To set the temperature of the thermostat to target temperature  $T_t$ , the velocity of the atom is scaled by,

$$\bar{v}_i(t) = \sqrt{\frac{T_t}{T}} \bar{v}_i(t). \quad (3-12)$$

A discussion of some of the issues associated with velocity rescaling thermostat is given in Chapter 7 in the context of our development of methodologies for simulations of radiation damage, along with a discussion of alternative methods.

### Constant Pressure Algorithm

Materials generally expand on heating. This implies that the size and shape of the simulation cell needs to be adjusted in realistic manner depending on the temperature and external pressure. In our MD simulations, this is done using a constant pressure algorithms.<sup>96, 98</sup> There are several available methods depending on the constraint on the pressure.

One of the methods called method of extended system first proposed by Andersen.<sup>105</sup> To understand this method, imagine a system of volume  $V$  to which a piston of mass  $Q$  is attached. Thus, with the motion of the piston, the volume of the system changes. If the volume of the simulation cell is  $V$ , then kinetic and potential energies of the piston are,

$$\begin{aligned} K.E. &= \frac{1}{2} Q \left( \frac{dV}{dt} \right)^2 \\ P.E. &= PV \end{aligned} \quad (3-13)$$

Here  $P$  is the pressure of the system. Now define variable,  $s_i(t)$ , for atom  $i$  in terms of atomic position  $x_i(t)$ :

$$\vec{x}_i(t) = V^{1/3} \vec{s}_i(t). \quad (3-14)$$

Thus,  $s_i(t)$  is reduced coordinate of atom  $i$ . Then the kinetic and potential energies of all the atoms in the simulation cell are,

$$\begin{aligned} K.E. &= \frac{1}{2} V^{2/3} \sum_i m_i \left( \frac{d\vec{s}_i}{dt} \right)^2. \\ P.E. &= U(V^{1/3} \vec{s}_i) \end{aligned} \quad (3-15)$$

Now using either Hamiltonian or Lagrangian formalism of classical mechanics, one can arrive at the two couple equations of motion:

$$\begin{aligned} \frac{d^2 \vec{s}_i}{dt^2} &= \frac{\vec{F}_i(t)}{mV^{1/3}} - \frac{2}{3V} \frac{d\vec{s}_i}{dt} \frac{dV}{dt}. \\ \frac{d^2 V}{dt^2} &= \frac{p - P}{Q}. \end{aligned} \quad (3-16)$$

Here  $F_i$  is the force on atom  $i$ .  $p$  is the instantaneous pressure, and it can be calculated from,

$$p = \frac{1}{3} \sum_i m_i \vec{v}_i^2 - \frac{1}{3V} \sum_i \vec{r}_i \cdot \vec{F}_i. \quad (3-17)$$

Notice that in this scheme the pressure is isotropic; it means that the pressure is hydrostatic.

However, it is easy to allow all the pressure components to evolve independently. To do so, we need to define matrix,  $H$ , such that,

$$x_i^a(t) = H_{ab} s_i^b(t), \quad (3-18)$$

instead of Equation (3-14).  $a$  and  $b$  here indicates the Cartesian directions. This expression implies that  $V = \det(H)$ . Now the equation of motion, Equation (3-16), can be rewritten in terms of  $H$  instead of  $V$ . This will give the constant stress simulation method developed by Parinello and Raman.<sup>106</sup> This method has no restriction in the evolution of the components of the pressure or the shape of the simulation cell. This Andersen (and Parinell-Rahman) methods are used throughout the work presented in this thesis.

## Nonequilibrium Thermal Conductivity Simulations

The thermal conductivity of a material can be obtained from the non-equilibrium MD simulation. This approach used here is called direct method and was first developed by Jund and Jullien.<sup>107</sup> The simulation cell used in this method is a square cylinder, long in the  $z$  direction, and narrow in the  $x$  and  $y$  directions: see Figure 3-5. Prior to the thermal-transport simulation, the system is heated to the temperature of interest using a constant temperature, constant pressure (NPT) simulation algorithm for thermal and strain equilibration. After the system has equilibrated, two regions in the simulation cell are designated for the heat source and heat sink. The simulation cell dimensions are then fixed, and the heat source and heat sink are turned on to create a steady state heat flow. Once the system reaches steady-state, the temperature gradient is determined from an average over some duration of simulation time. The thermal conductivity is then calculated from Fourier's law,  $J = -\kappa dT/dx$ , where  $J$  is the heat current,  $\kappa$  is thermal conductivity tensor, and  $dT/dx$  is the temperature gradient. Some specific setup and condition such as length of the simulation, heat current, simulation cell size, etc. may depend on the material of interest.

In a previous study on silicon, it was shown that the calculated thermal conductivity depends weakly on the cross sectional area<sup>108</sup>. The same study on Si also showed that the calculated thermal conductivity depends strongly on the length of the simulation box. In Chapter 2, using the elementary kinetic theory for a phonon gas, it was shown that, (Equation 2-6)

$$\kappa = \frac{1}{3} c_v \bar{v} l,$$

where  $c_v$  is the volumetric specific heat,  $\bar{v}$  is the mean sound velocity, and  $l$  is the effective mean free path of phonons. The appropriate specific heat above the Debye temperature is given by the Dulong-Petit value for a non-interacting gas:

$$c_v = (3/2)k_B n, \quad (3-19)$$

where  $k_B$  is the Boltzmann constant, and  $n$  is the number density of the ions. For a cubic lattice with  $N_c$  atoms in the unit cell,  $n=N_c/a^3$ .  $v_s$  can be estimated by  $v=(v_L+2v_T)/3$ , where  $v_L$  and  $v_T$  are the longitudinal and transverse sound velocities. These values are given by  $v_L = \sqrt{\rho/C_{11}}$  and  $v_T = \sqrt{\rho/C_{44}}$  for a cubic lattice. The effective mean free path can be written as, using Matthiessen's rule for the relaxation time<sup>108</sup> as,

$$l_{eff}^{-1} = l_{\infty}^{-1} + l_{BC}^{-1}, \quad (3-20)$$

where  $l_{\infty}^{-1}$  and  $l_{BC}^{-1}$  are the mean free path of phonon-phonon scattering in an infinite media and phonon-boundary scattering, respectively. If the length of the simulation cell is  $L_z$ ,  $l_{BC}$  is approximated by  $L_z/4$  since the heat source and sink are separated by  $L_z/2$ .

Finally the thermal conductivity can be written as a function of system length as:

$$\frac{1}{\kappa} = \frac{2a^3}{k_B N_c v} \left( \frac{1}{l_{\infty}} + \frac{4}{L_z} \right). \quad (3-21)$$

This means that the best estimate for the infinite size bulk thermal conductivity can be obtained from MD simulations by the extrapolation of the conductivity values to  $1/L_z=0$ . This approach was previously applied to Si and diamond single crystals<sup>108</sup>, and will be used here.

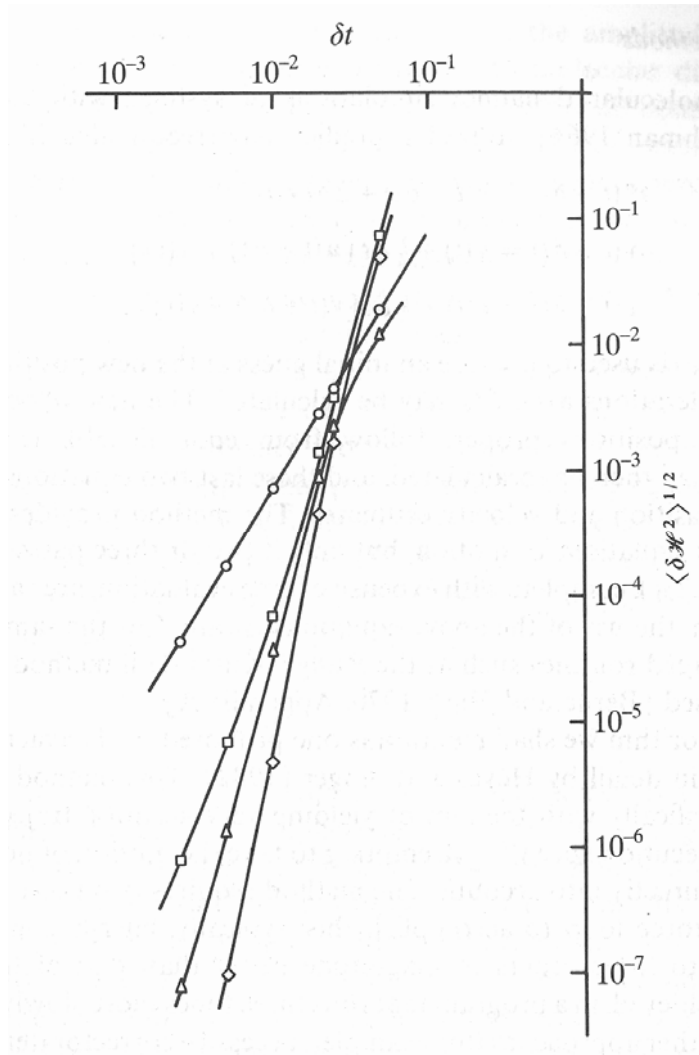


Figure 3-1. The root mean square of the total energy as a function of time for velocity Verlet (circles), 4<sup>th</sup> order Gear (squares), 5<sup>th</sup> order Gear (triangles), and 6<sup>th</sup> order Gear (diamond) algorithms. The steep slopes of the Gear method indicate that it has high accuracy is small time step size is used. [Adapted from reference 96 (Page 83, Figure 3.3).]

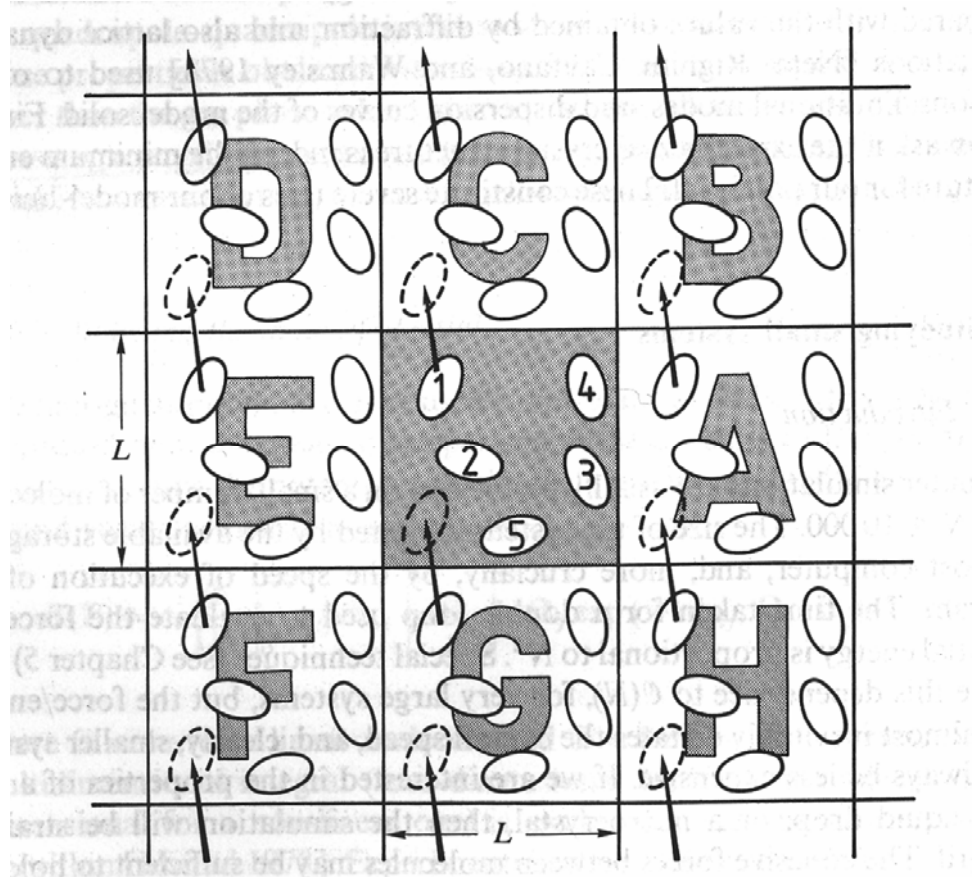


Figure 3-2. Two dimensional periodic system in simulation. The actual simulation cell is the central shaded cell of the size  $L \times L$ . All the other cells labeled A-H are its periodic image. The arrows indicate the molecule 1 is moving out of the simulation cell and coming in from the other side because of its periodic image. [Adapted from reference 96 (Page 24, Figure 1.9).]

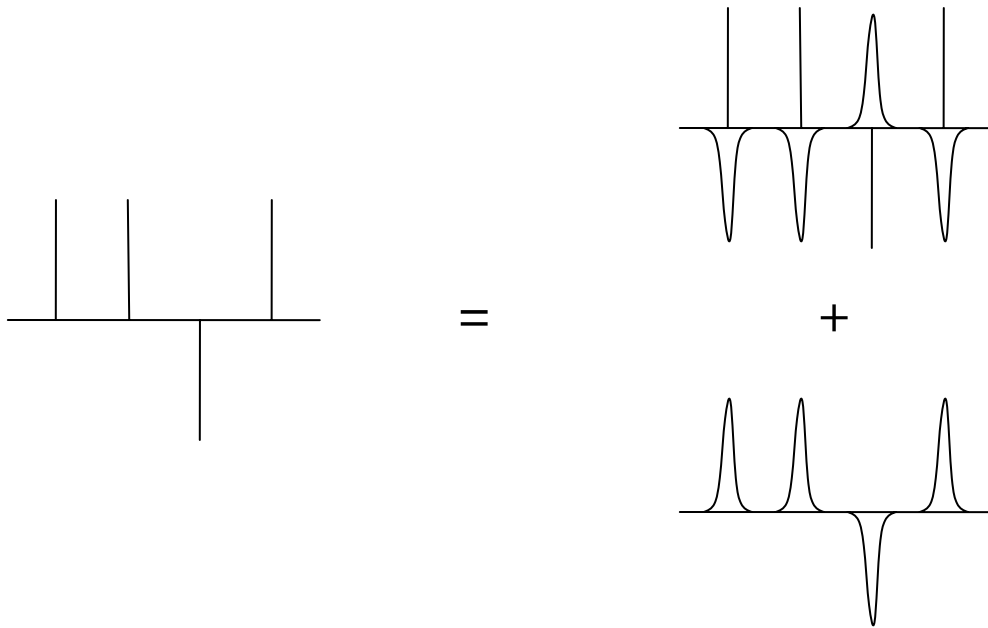


Figure 3-3. A system of point charges as a sum of screened point charges and smeared charge density with opposite sign. [Reproduction from reference 96 (Page 30, Figure 1).]

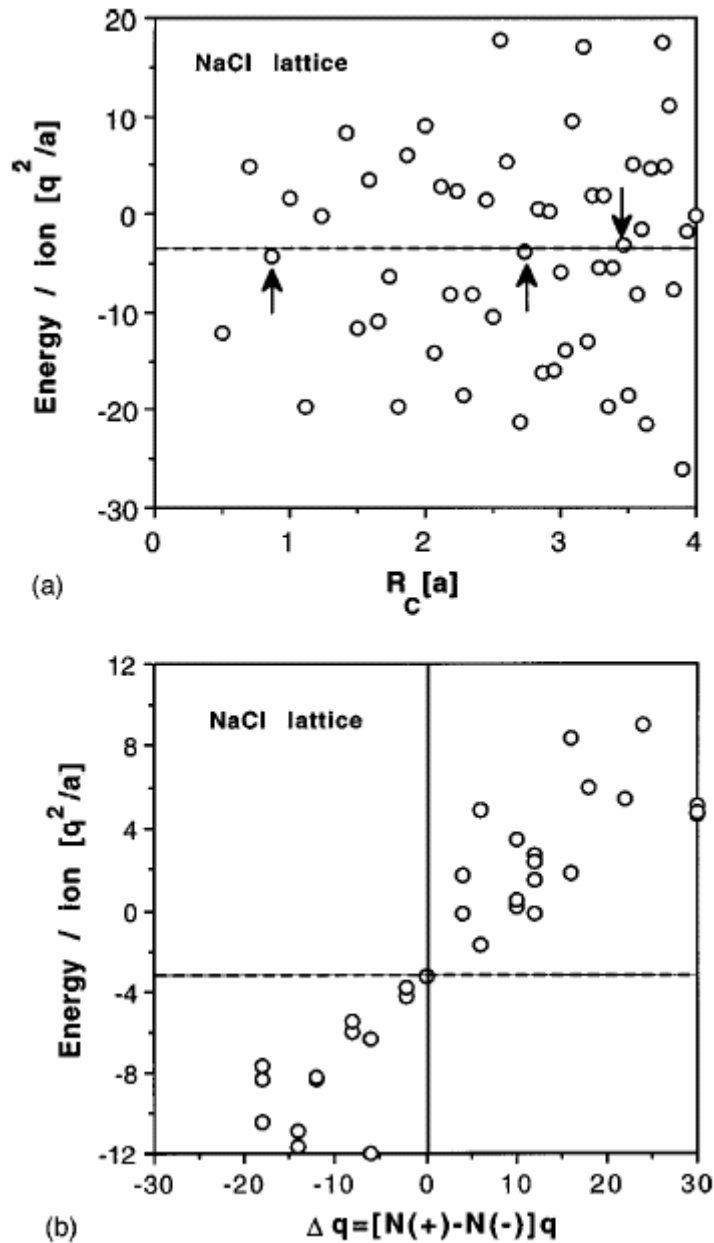


Figure 3-4. (a) Electrostatic energy per ion as a function of cutoff,  $R_c$ . Dash line is used to indicate the Madelung energy of NaCl. Electrostatic energy show no systematic convergence even at large  $R_c$ . However, there are a few value of  $R_c$  that gives near the Madelung energy. (b) Electrostatic energy per ion as a function of the net charge,  $\Delta q$ , in the sphere. Approximate linear relation is clear between the energy and the net charge of the sphere. The Madelung energy coincide with point,  $\Delta q=0$ . [Adapted from reference 99 (Figure 1).].

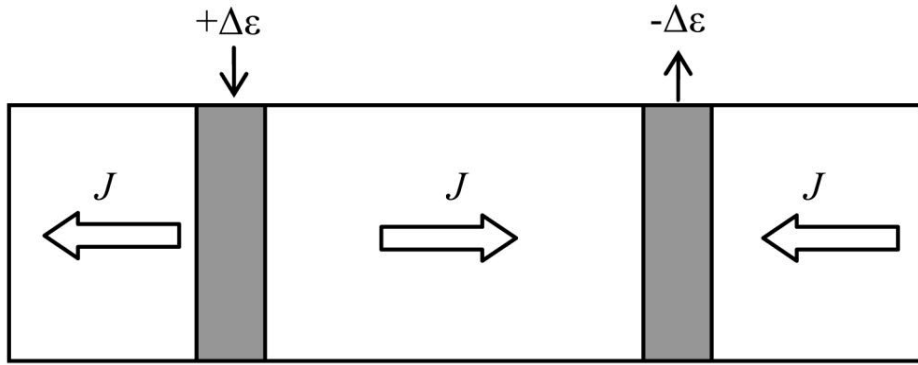


Figure 3-5. Simulation cell setup for the direct method for simulating thermal conductivity. The heat source and sink are located at a quarter of the cell length away from the center of the cell. The same amount of energy,  $\Delta\varepsilon$ , is added to the atoms in the heat source, and removed from those in the heat sink. This setup results in two equivalent heat currents  $J$  in opposite directions along the  $z$  axis.

CHAPTER 4  
THERMAL TRANSPORT IN SINGLE CRYSTAL UO<sub>2</sub>

**Molecular Dynamics Simulation of UO<sub>2</sub>**

As discussed in Chapter 1, the thermal conductivity is one of the most important performance metrics for a nuclear fuel material. UO<sub>2</sub> is used as the primary fuel in nuclear power reactors, and its thermal conductivity has been determined in a number of experiments. Therefore, it is an ideal material to test theoretical models. Once the validity of the model is established, simulations with point defects and GBs are possible.

**Potential Models**

The interatomic interactions (Chapter 3) consist of a long-range electrostatic component and short-range interactions which describe the materials specific largely-repulsive component. In this work, the results obtained from two short-range interaction models: those due to Yamada<sup>109</sup> and the Busker<sup>110, 111</sup>. The Busker potential<sup>110, 111</sup> is a traditional Buckingham potential (Equation 3-8),

$$V(r_{ij}) = A_{ij} \exp(-r_{ij} / \rho_{ij}) - \frac{C_{ij}}{r_{ij}^6}.$$

The values of the parameters are given in Table I. One of the advantages of Busker model is the transferability of the potential between a variety of elements<sup>110, 111</sup> – it also has parameters for U<sup>3+</sup> and U<sup>5+</sup>, thereby allowing the effects of off-stoichiometry to be studied. (Chapter 6) The Busker potential was originally developed to study defect properties in UO<sub>2</sub> and ZrO<sub>2</sub>. By contrast, the Yamada model is a Bushing-Ida type potential<sup>112</sup> given by<sup>109</sup>:

$$V(r_{ij}) = A_{ij} \exp(-r_{ij} / \rho) - \frac{C_{ij}}{r_{ij}^6} + D_{ij} [\exp(-2\beta(r_{ij} - r_{ij}^*)) - 2 \exp(-\beta(r_{ij} - r^*))]. \quad (4-1)$$

The first two terms are the same as in the Buckingham potential. The last two terms are the Morse term, which provides a “covalent” component. However, this term is not strictly

covalent in the sense that it does not have directionality. Due to the assumption of partial covalency, the charges of the ions are given by non-formal values intended to represent the partial charge transfer between ions (Table I). Unlike the Busker potential, the Yamada potential was fit specifically to the U-Pu-O system.

To avoid the prohibitive computational expense associated with the calculation of the electrostatic interaction through the Ewald method, particularly for systems with large numbers of ions, the electrostatic interactions are calculated using the direct summation method. (Chapter 3)

Table II summarizes the structural parameters and elastic properties determined using the two potentials. By construction, both give good values for the lattice parameters. The General Utility Lattice Program (GULP)<sup>113, 114</sup> is used to determine the elastic properties at 300K. GULP uses a static method based on the quasi-harmonic approximation<sup>113, 114</sup> and thus provides a slightly lower estimated value for the elastic constants<sub>1</sub> than does the direct MD simulation, which includes the dynamical motion of the ions. We can see that while the Busker potential reproduces the value of  $C_{12}$  rather well, it overestimates  $C_{11}$  and  $C_{44}$ . By contrast, the Yamada potential gives good estimates of  $C_{11}$  and  $C_{44}$ , but severely underestimates  $C_{12}$ . As a result one overestimates and the other underestimates the bulk modulus  $B = (C_{11} + 2C_{12})/3$ .

There are numerous other interatomic potentials for  $\text{UO}_2$  in the literature. Recently, Govers *et al.* undertook an extensive comparison of a number of empirical potentials for  $\text{UO}_2$ , including the two used in this study<sup>115</sup>. Their assessment included both rigid-ion and shell models, and they calculated the cohesive energy, lattice parameter, elastic constants, dielectric constants,  $\Gamma$  point phonon frequencies, and defect formation energies. While some potentials seemed to give a better physical description than others, their results showed that no single

potential faithfully reproduces all of the physical properties of  $\text{UO}_2$ . The two potentials used in here are thus representative of other  $\text{UO}_2$  potentials with regards to their materials fidelity.

### Thermal Expansion

Another metric of the fidelity of a potential is to compare the thermal expansion of the system with experiment. The simulations to determine the thermal expansion are performed using Andersen's constant pressure scheme<sup>105</sup>. The simulation cell contains  $6 \times 6 \times 6$  unit cells (2592 atoms), and the temperature of the system is controlled by velocity rescaling. In order to reach equilibrium, the simulations are run for 7.5 ps with 0.25 fs time steps. The temperature is varied from 0 K to 2000 K at 100 K intervals. The lattice parameter at each temperature is obtained by the simulation cell volume average of the last 5.5 ps of the simulation.

Figure 4-1 shows the normalized lattice parameter as a function of temperature; the experimental values are taken from Fink's critical assessment of the experimental data<sup>3</sup>. Yamada's potential shows good agreement with the experimental thermal expansion up to about 1000 K, above which it is systematically lower. The Busker potential gives a systematically lower thermal expansion at all temperatures. At low temperatures, the thermal expansions are essentially temperature independent with  $\alpha_{\text{Yamada}} = 8.4 \times 10^{-6} \text{ K}^{-1}$  and  $\alpha_{\text{Busker}} = 6.2 \times 10^{-6} \text{ K}^{-1}$ . The discrepancy between our calculated value for the Yamada potential and the previously published value of  $10.1 \times 10^{-6} \text{ K}^{-1}$ <sup>109</sup> is at least in part due to the Wigner-Kirkwood correction<sup>116</sup> to the free energy used in analyzing their simulations. The thermal expansion calculated with the two potentials are both smaller than the experimental value of  $\alpha_{\text{Expt}} = 11.8 \times 10^{-6} \text{ K}^{-1}$ .

The thermal expansion coefficient is a result of the anharmonicity of the interactions in the material. This is encapsulated in the Grüneisen relation:

$$\alpha = \frac{\gamma c_v}{3B}, \quad (4-2)$$

where  $c_v$  and  $B$  are the specific heat and bulk modulus respectively, and  $\gamma$  is the Grüneisen parameter, which measures the dependence of the phonon frequencies on system volume, and is thus a direct measure of the anharmonicity of the interactions in the system<sup>60</sup>. If the interatomic interactions were purely harmonic, then the Grüneisen parameter would be zero and there would be no thermal expansion. Thus the higher thermal expansion of the Yamada model can be interpreted as a result of higher anharmonicity in the potential compared to the Busker potential.

An estimate of the lattice thermal conductivity in terms of the Grüneisen parameter was first given by Leibfried and Schloemann<sup>117</sup>, and refined by Klemens<sup>118</sup>,

$$\kappa \sim \frac{24}{10} \frac{\sqrt{4}}{\gamma^2} \left( \frac{k_B}{h} \right)^3 Mv \frac{\theta^3}{T}. \quad (4-3)$$

Here  $k_B$  is the Boltzmann constant,  $h$  is the Planck constant,  $v$  and  $M$  are the volume and the mass per atom. The only two materials constants that enter into Equation 4-3 are  $\theta$ , the Debye temperature, and  $\gamma$  the frequency-averaged Grüneisen parameter. From this relation, it is clear that the thermal conductivity decreases with increasing anharmonicity.

Through their dependences on the Grüneisen parameter, we can use Equations 4-2 and 4-3 to give a simple relationship between the thermal conductivity and thermal expansion, in terms of the Debye temperature, the bulk modulus and the specific heat:

$$\alpha^2 \kappa = \chi \frac{\theta^3 c_v^2}{B}. \quad (4-4)$$

The constant  $\chi$  subsumes all of the non-materials constants in Equation 4-2 and 4-3. In classical simulations at temperatures above the Debye temperature (370K for UO<sub>2</sub>), the specific heat is

essentially equal to the Dulong-Petit value of  $3k_B$ . Also the Debye temperatures for the two potentials are assumed to be the same. Hence we find:

$$\kappa = \frac{\chi'}{\alpha^2 B}, \quad (4-5)$$

where  $\chi' = \chi \theta^3 C_v^2$ .

Using the values of  $\alpha$  and  $B$  determined above for the two potentials, we then predict the following:

$$\begin{aligned} \kappa_{\text{Busker}} &\sim 10.1 \times 10^{-2} \chi' \\ \kappa_{\text{Yamada}} &\sim 8.1 \times 10^{-2} \chi' \end{aligned} \quad (4-6)$$

Using the experimental values of  $B$  and  $\alpha$ , Equation (4-5) gives  $\kappa_{\text{Expt}} \sim 3.4 \times 10^{-2} \chi'$ , which is considerably smaller than the predictions for the Busker and Yamada potentials. Thus, based on this very naïve analysis, we expect the direct simulations with the two potentials to give thermal conductivities for the Busker and Yamada potentials that are 3.0 and 2.4 times larger respectively than the experimental values; as we shall see in the next section, these estimates are quite accurate..

### **Thermal Conductivity of Single Crystal $\text{UO}_2$**

The temperature dependence of the thermal conductivity of single crystal  $\text{UO}_2$  is calculated using the direct method (Chapter 2). In this approach a heat current is set up; the resulting temperature gradient is identified from which the thermal conductivity is calculated from Fourier's Law.

Using the description given in Chapter 3, the system is heated to the temperature of interest using a constant temperature, constant volume simulation algorithm before the thermal-transport simulation. We determined that 12.5 ps. is sufficient for thermal equilibration. The heat source and heat sink are then turned on, so as to create a steady state heat flow. Once the

system reaches steady-state, which takes about  $\sim 500$  ps, the temperature gradient is determined from an average over 250 ps.

Thermal conductivity depends weakly on the cross sectional area (Chapter 2).<sup>108</sup> Therefore the cross-section area is set to be  $4 \times 4$  unit cells, which is the smallest size that can be simulated with the cutoff values used in these potentials of  $R_c = 1.98a$ , where  $a$  is the lattice parameter.

Since our simulation cell size is limited by the number of atoms that the available computational resources can reasonably handle, an analysis of the finite size length of the simulation cell must be taken into account to obtain the bulk thermal conductivity (Chapter 3). The thermal conductivity of single crystal  $\text{UO}_2$  between 300 K and 2000 K is shown for the two potentials in Figure 4-3 as  $1/\kappa$  vs.  $1/L_Z$  plots, in accordance with Equation 3-21. The results for the two potentials are similar at all temperatures and system sizes.

The thermal conductivity for infinite system size is determined by linear fits to the data in Figure 4-3. These infinite size limit thermal conductivities, which are the best estimates of the intrinsic thermal conductivity of  $\text{UO}_2$  described by these potentials, are shown for the two potentials in Figure 4-4(a) as a function of temperature. Although the error bars overlap, it does appear that the Yamada potential gives a somewhat higher estimated thermal conductivity at low  $T$  than does the Busker potential, but has a somewhat stronger temperature dependence. This result is reasonably consistent with the only small difference in thermal conductivity predicted by our simple anharmonicity analysis.

The higher values for the estimated thermal conductivity derived using the Yamada potential compared to those previously published for this potential<sup>109</sup> mainly arise from the finite size effects which are particularly important at low temperatures when the phonon mean-free path is long, and which were not addressed in the earlier simulations. A secondary effect is that

in this study we have not used the Wigner-Kirkwood correction to the temperature, which has a significant effect below the Debye temperature.

As Figure 4-4(a) indicates, both potentials give significantly higher thermal conductivities at low temperatures than the experimental values. Figure 4-4(a) shows the thermal conductivity corrected according to the anharmonicity analysis in the previous section; as we can see the match between the simulation and experiment is now much better especially above 750K, the temperature range of interest for nuclear-fuel applications. It is worth stressing that this agreement is not the result of fitting the simulation results to the experiments, but comes from a physical analysis of the anharmonicity in the experimental and simulated systems, via quantities that are both computationally easy to calculate and generally experimentally available, even for materials in which thermal transport data are lacking. It thus attributes the majority of the difference between the experimental and simulation values as arising from the differences in the bulk modulus, which measures the harmonic properties of the system, and the thermal expansion, which measures the anharmonic properties of the system.

As discussed in Chapter 3, the anharmonic Umklapp processes lead to the temperature dependence of the thermal conductivity. Debye showed that  $\kappa \sim T^n$ , with  $n \sim 1-2$ .<sup>119</sup> Figure 4-4 is a log-log plot of the data in 4-4(b). In each case, the thermal conductivity shows power-law behavior with temperature. The experimental results are fitted by  $\alpha_{\text{Exp}} \sim 0.79$ , while the simulations yield  $n_{\text{Yamada}} \sim 1.14$  and  $n_{\text{Busker}} \sim 1.30$  respectively, which are consistent with the Debye analysis.

The systems simulated are structurally much simpler than the experimental systems; this also contributes to the discrepancy between the simulation and experimental results. In particular, in the simulations there are no isotopic defects, no off-stoichiometry, and no

microstructural defects (GBs, dislocations, second phases etc.) Characterization of the effects of polycrystalline microstructures is given in the next chapter; the effects of point defects are analyzed in Chapter 6.

### **Discussion**

The simulation approaches used here are well suited to the characterization of the thermal transport properties of electrically insulating materials such as  $\text{UO}_2$  in which heat is transported by atomic vibrations. However, even in a relatively poor thermal conductor such as  $\text{UO}_2$ , finite system size effects can lead to a significant underestimate of the thermal conductivity: the systematic variation in system size coupled with a finite-size scaling analysis does appear to offer a viable method for taking these effects into account.

The power law behavior of thermal conductivity from experimental data gives an exponent less than unity; this is in contradiction with the Debye model. The origin of this discrepancy is not clear. One possible origin of the disagreement is the effects of point defects or grain boundaries, although grain size in typical reactor fuel may be too large to show significant influence. It is well known that defects can reduce the thermal conductivity and temperature dependence. We will return to this issue in later chapters.

Neither potential can quantitatively match the experimental thermal conductivity without the consideration of the anharmonic effects. Based on the analysis of Govers *et al.*, the two potentials used in the study are of a similar level of materials fidelity as others in the literature.<sup>115</sup> The simple relationship, Equation (4-5), relating the elastic properties, thermal expansion and elastic constants, suggests that a potential with correct elastic properties and thermal expansion, should well reproduce the thermal-transport properties. A truly general purpose potential would also need to well reproduce the point defect properties. Govers *et al.*<sup>115</sup> showed that none of the

twenty-one potentials they examined could satisfactorily reproduce the formation and migration energies. There is thus considerable need for potentials which better describe  $\text{UO}_2$ .

Table 4-1. Parameters of interatomic potentials

		Busker				Yamada		
		O <sup>2-</sup> -O <sup>2-</sup>	U <sup>3+</sup> -O <sup>2-</sup>	U <sup>4+</sup> -O <sup>2-</sup>	U <sup>5+</sup> -O <sup>2-</sup>	U-U	O-O	U-O
$A_{ij}$	(eV)	9547.96	1165.65	1761.775	2386.42	442.208	2346.149	1018.571
$\rho_{ij}$	(Å)	0.2192	0.3786	0.35643	0.3411	0.32	0.32	0.32
$C_{ij}$	(eV·Å <sup>6</sup> )	32			0	0	4.1462	0
$D_{ij}$	(eV)	-		-	-	0	0	0.7810
$\beta_{ij}$	(1/Å)	-		-	-	0	0	1.25
$R^*_{ij}$	(Å)	-		-	-	0	0	2.369
$Z_U$	(e)	+4				+2.4		
$Z_O$	(e)	-2				-1.2		

Table 4-2. Lattice parameter and elastic constants at 300 K.

		GULP		MD		Experiment <sup>3, 23, 120-122</sup>
		Busker	Yamada	Busker	Yamada	
$a$	(Å)	5.481	5.482	5.479	5.481	5.478
$C_{11}$	(GPa)	526	409	547	418	389-396
$C_{12}$	(GPa)	118	55.0			119-121
$C_{44}$	(GPa)	118	53.4			59.7-64.1
$B$	(GPa)	257	174			209-213

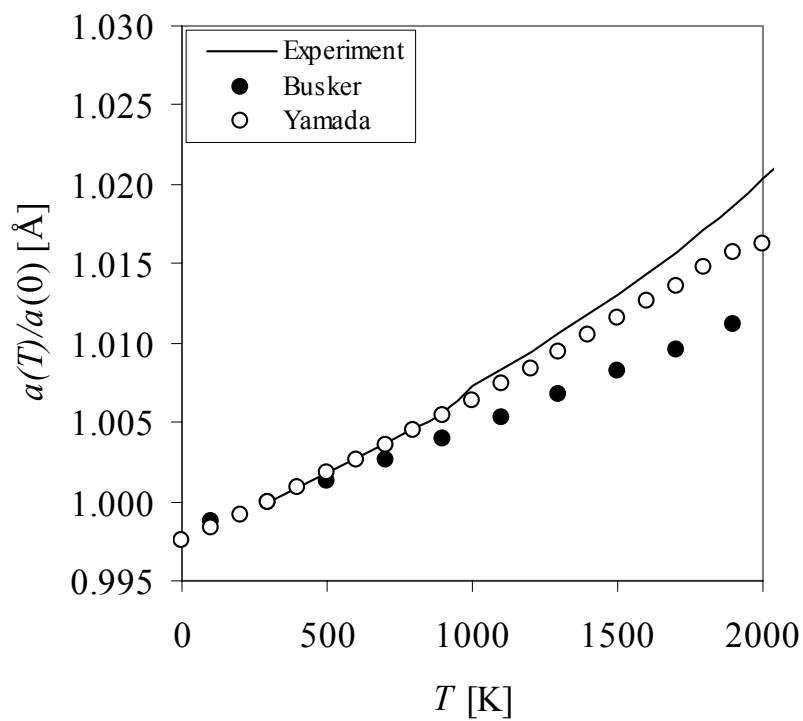


Figure 4-1. Normalized lattice parameter as a function of temperature from experiment <sup>3</sup>, Busker and Yamada potentials.

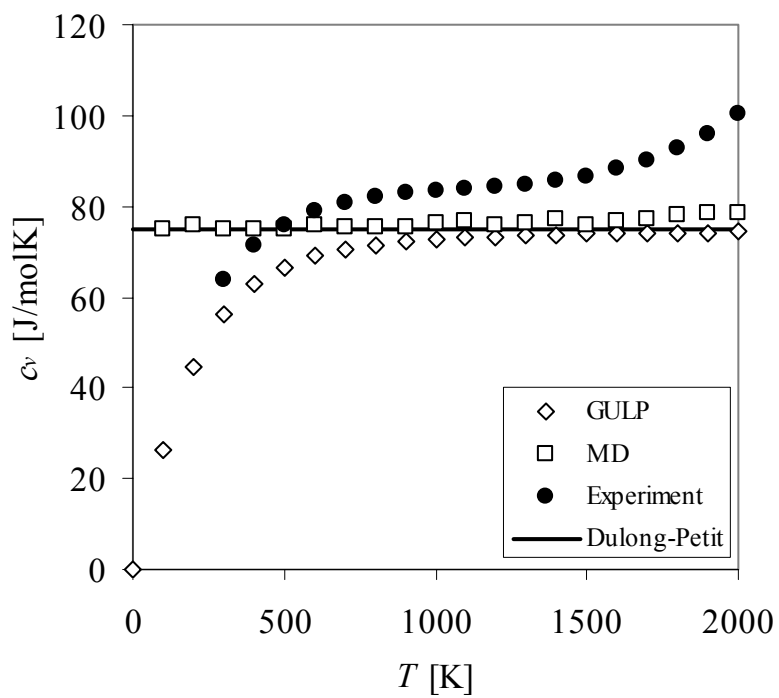


Figure 4-2. Specific heat of  $\text{UO}_2$  from GULP, MD and experiment.<sup>3</sup> The Dulong-Petit value is shown as a reference.

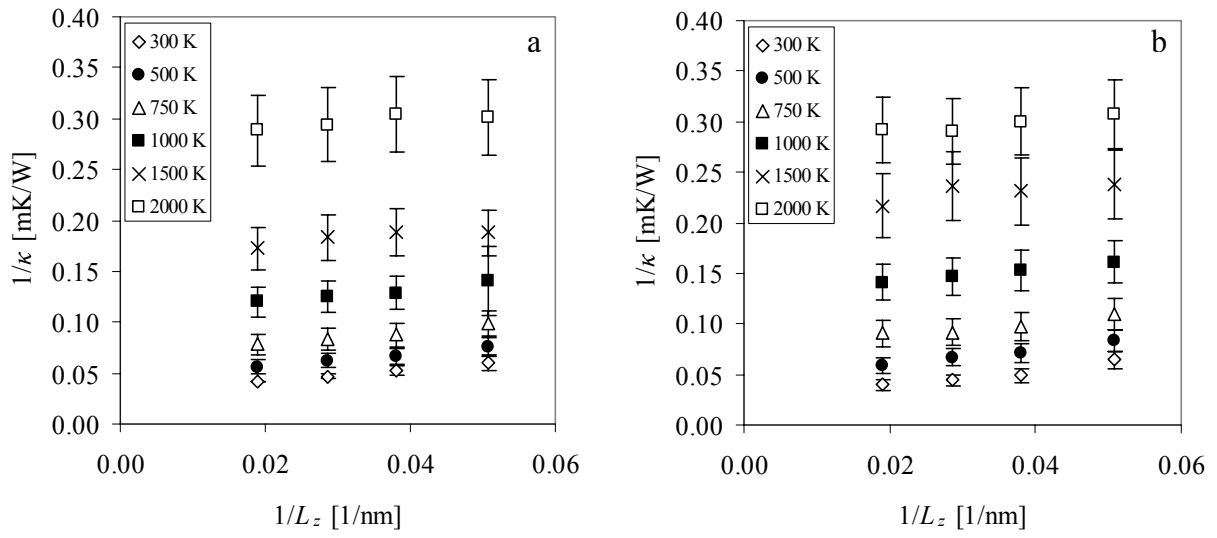


Figure 4-3. Size dependence of thermal conductivity for both the Busker (a) and Yamada (b) potentials.

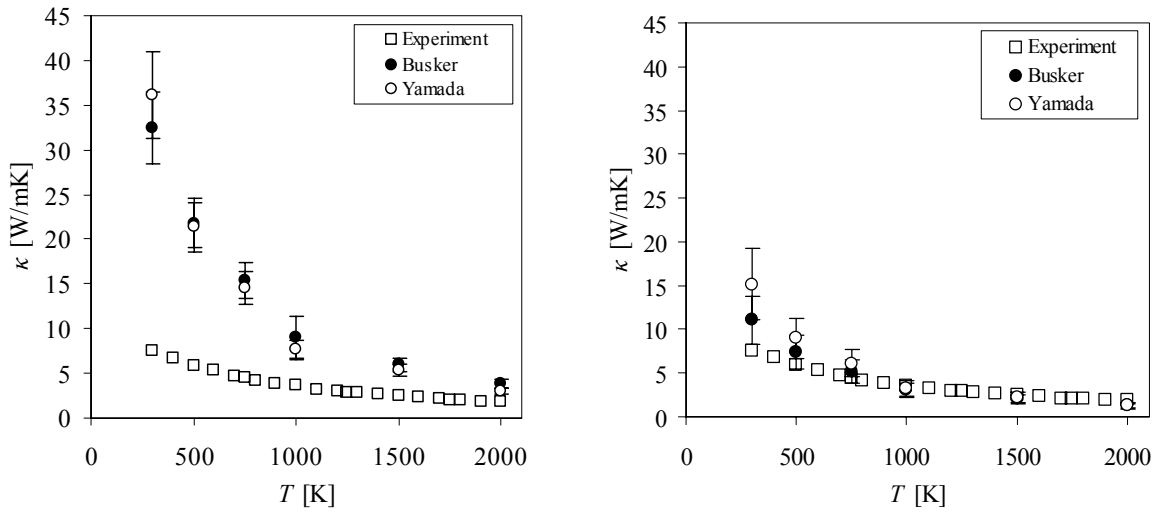


Figure 4-4. Thermal conductivity of  $\text{UO}_2$  from the compilation of experimental data by Fink and simulations using the Busker and Yamada potentials (a) before and (b) after the anharmonic correction

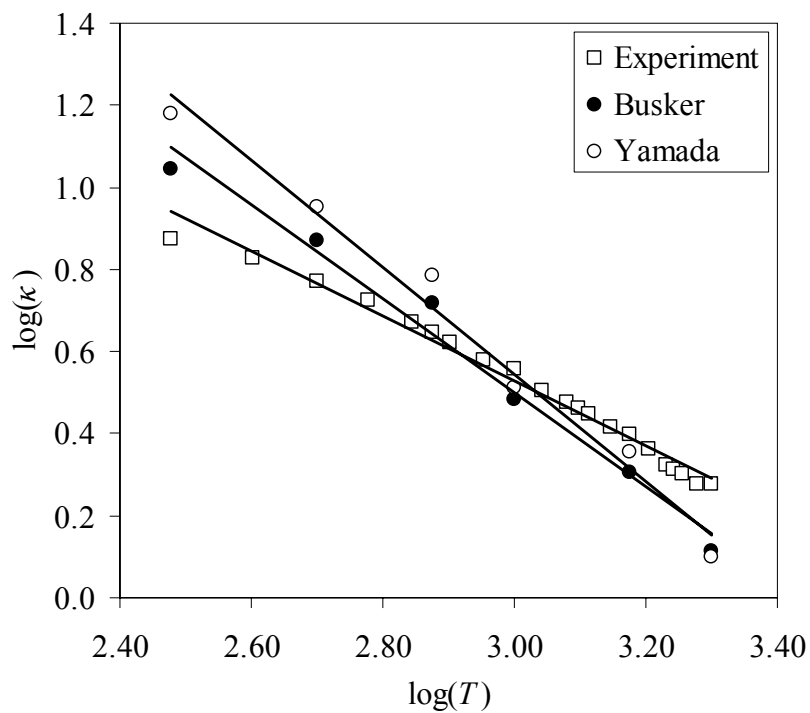


Figure 4-5. The same thermal conductivity data as in Figure. 4-4(b) in log-log scales.

## CHAPTER 5 THERMAL TRANSPORT IN POLYCRYSTALLINE UO<sub>2</sub>

### **Introduction**

Grain boundaries offer a significant obstacle to the transport of heat in phonon conductors as discussed in Chapter 3. Grain boundaries are present in typical fission reactor fuel material. (Chapter 1) Although the average grain size in such materials may be too large (order of 10  $\mu\text{m}$ )<sup>3, 40</sup> to significantly influence thermal transport in UO<sub>2</sub>, finer grains (~150 nm on average) are also present in high burnup structures.<sup>40, 41</sup> However, there has been no systematic study of the grain size dependence of thermal transport properties in UO<sub>2</sub>. In this chapter, the thermal conductivity of a model fine-grained polycrystal of UO<sub>2</sub> is determined. Predictions for the grain-size dependence of its thermal conductivity are also made.

### **Structure of Model Polycrystal**

Experimental grain sizes of the range of tens or hundred of microns are not accessible to MD simulation, since each grain would contain  $\sim 10^{13} - 10^{16}$  ions. In this study considerably smaller systems with grain sizes from 3.8 – 6.5 nm are considered; these small sizes maximize the area of the GB in the system, thereby amplifying the interfacial effects.

The polycrystalline structures used in the simulations consisted of 24 hexagonal columnar grains. When constructing the polycrystalline structure, identical close-packed hexagons are arranged to form a completely periodic structure. Each hexagon is filled with single-crystal UO<sub>2</sub> oriented with [001] along the columnar direction. The in-plane orientations are chosen in such a way that the GBs between the grains are high energy tilt GBs, which ensures that the microstructure is stable against coarsening during the simulation. Because of the way each grain is constructed, initially there are always a small number of atoms in the GBs which are extremely close to each other: See Figure 5-1. To address this issue, if any two ions

are closer than 1.5 Å (66% of the nearest neighbor distance between U<sup>4+</sup> and O<sup>2-</sup>, 2.29 Å), one of the atoms is removed. This removal of atoms is carried out with care to ensure the charge neutrality of the entire system. Once the structure is created, it is quenched at 0 K to equilibrate all of the atom positions and to eliminate any in-plane stress on the system. It is found that no ions have anomalously high energies, indicating that the bonding in the system is physically reasonable. The system is then annealed with a constant-pressure, constant-temperature simulation at 2000 K and slowly relaxed to 0 K to ensure that the structure is equilibrated. Figure 5-2 shows the final relaxed polycrystalline UO<sub>2</sub> structure for a grain size of 3.8 nm.

The columnar microstructure used here allows the simulation cell to be thin along the columnar direction. The cutoff to the potentials is 10.4 Å, which would allow the thickness to be as small as 4 unit cells: in our simulations, 5 unit cells thickness is used so as to minimize any effects of the system size in that direction.

Since all the grains are equiaxial and of equal size, it is easy to calculate the GB area and volume fraction. For a grain size of 3.8 nm, the area of the GB is 439.10 nm<sup>2</sup>. Assuming that the GBs have a thickness of one unit cell, the volume which the GB region occupies is approximately 30 % of the entire volume. The structural disorder at the GBs leads to a total volume expansion of 5.5 % and 5.3 % for Busker and Yamada potentials respectively. The corresponding average GB energies are 2.73 J/m<sup>2</sup> and 1.89 J/m<sup>2</sup>, which are consistent with the GB energies of other ceramic materials.<sup>123, 124</sup>

After the preparation of the equilibrated structure, the thermal expansion of these models of polycrystalline UO<sub>2</sub> were determined at 300 K. The values obtained were 7.57×10<sup>-6</sup> K<sup>-1</sup> with the Busker potential and 8.92×10<sup>-6</sup> K<sup>-1</sup> for the Yamada potential, which are almost

indistinguishable from the corresponding bulk single crystal values of  $7.50 \times 10^{-6} \text{ K}^{-1}$  and  $8.83 \times 10^{-6} \text{ K}^{-1}$ .

### **Thermal Conductivity of Polycrystalline $\text{UO}_2$**

The thermal conductivity of polycrystalline  $\text{UO}_2$  is calculated using the direct method described in Chapter 2. Figure 5-3 shows the temperature dependence of  $\kappa$  for a polycrystal with a grain size of 3.8 nm, as described by both potentials. These calculated thermal conductivities are considerably lower than those of the corresponding the perfect crystals, attesting to the significant resistance of GBs to the flow of heat through the system. Unlike single crystalline  $\text{UO}_2$ , the effects of the finite size of the simulation cell itself are small in polycrystals because the GB scattering dominates over the phonon-phonon scattering; simulations have directly shown that the effect of the size of the simulation cell in polycrystalline MgO is weak<sup>125</sup>. Since  $\text{UO}_2$  has a significantly lower single-crystal thermal conductivity than MgO ( $\text{UO}_2$ : 7 W/mK and MgO 40 W/mK at 300 K)<sup>3, 126</sup> the effect is expected to be even less important in  $\text{UO}_2$ .

The thermal conductivity for the polycrystal is considerably higher for the Busker potential than for the Yamada potential. Since the GB energy is a measure of the structural disorder at the interfaces, we would expect that the higher the energy associated with the GBs, the higher the interfacial thermal resistance would be, and the lower the thermal conductivity of the polycrystal would be. The GB energies obtained using the Busker and Yamada potentials are  $2.73 \text{ J/m}^2$  and  $1.89 \text{ J/m}^2$ , which appears to be inconsistent with this argument. However, the Busker potential is a full charge model, while the Yamada potential is a partial charge model, resulting in cohesive energies of  $-104.482 \text{ eV/UO}_2$  and  $-45.54 \text{ eV/UO}_2$  respectively. Thus, when normalized to the bulk cohesive energies, the GB energies are  $0.0026 \text{ \AA}^{-2}$  and  $0.0016 \text{ \AA}^{-2}$  for Yamada and Busker, respectively. That is, when described by the Busker potential, the GBs

actually offer less of an obstacle to heat transport than for the Yamada potential, which is consistent with the higher thermal conductivity for the Busker potential than for the Yamada potential.

The ensemble-averaged interfacial (Kapitza) resistance of the GBs in the polycrystal can be extracted from the thermal conductivity using simple models. There have several effective medium models proposed, including those of Nan and Birringer<sup>127</sup>, Yang *et al.*<sup>78</sup>, and Amrit.<sup>128</sup>

The model by Nan and Birringer assumes that the grains are identical ellipsoids and embedded in a continuum medium. The orientations of the grains can be random or aligned. The ratio of the single crystal thermal conductivity to that of the polycrystalline solid of identical columnar grains is,

$$\frac{\kappa_0}{\kappa} = 1 + \frac{l_K}{d} . \quad (5-1)$$

$d$  is the grain size and  $l_K$  is called Kapitza length given by the ratio of the single crystal conductivity over the interfacial conductance. The physical interpretation of  $l_K$  is as the thickness of perfect crystal that would offer the same thermal resistance as the interface; thus a long Kapitza length corresponds to a high interfacial resistance.

The model by Yang *et al.* assumes a one dimensional super-lattice type structure. They assume that there is a temperature drop at the interface. The ratio,  $\kappa_0/\kappa$ , is then given by,

$$\frac{\kappa_0}{\kappa} = 1 + \frac{l_K}{d} + \mu , \quad (5-2)$$

where  $\mu$  is a correction term, which accounting for the conditions where the wavelength of the dominant phonon mode approaches the grain size. This can be taken safely to zero for high temperatures.

Amrit's model assumes the polycrystalline structure consists of identical square grains.

This model assumes that the GBs along the direction of heat flow do not contribute to the thermal resistance.  $\kappa_0/\kappa$  in this model is,

$$\frac{\kappa_0}{\kappa} = 1 + \frac{n-1}{n} \frac{l_K}{d}. \quad (5-3)$$

Here  $n$  is the number of grains in the region of interest.

Although these three approaches assume different models for the polycrystalline structures, the resulting expressions for the interfacial conductance are rather similar and none of them is obviously better than the others. We will come back to this point below. Most importantly the qualitative trend of the interfacial conductance will not be affected by the choice of the model. Thus, for this analysis, the model by Yang *et al.*<sup>78</sup> is adopted for its simplicity. In Yang's model (Equation 5-3), the interfacial conductance,  $G_K$ , is then given by:

$$G_K = \frac{1}{d} \frac{\kappa_0 \kappa}{\kappa_0 - \kappa}, \quad (5-4)$$

since  $l_K = \kappa_0 / G_K$ :

The resulting values of  $G_K$  are given in Figure 5-4.. Both potentials show moderate increases of interfacial conductance with temperature. This temperature increase is consistent with the results of simulations of other interfacial systems<sup>129</sup> and, more importantly, with trends in experimental data for various systems.<sup>130</sup> The physical origin of the increase in conductance with temperature can be understood in terms of the properties of the GBs. As the temperature increases, the anharmonicity of the interactions among the atoms is probed more strongly. While in the perfect crystal, the resulting scattering lowers the thermal conductivity, this anharmonic scattering more strongly couples modes across the interfaces, leading to better interfacial thermal transport.

The interfacial conductance can be recast in terms of the Kapitza length. As shown in Figure 5-5, the Kapitza length decreases strongly with increasing temperature; this is a result of the decrease in the thermal conductivity and the increase in the interfacial conductance with temperature.

For both potentials, the Kapitza length is significantly larger than the grain diameter, particularly in the low temperature region. This is an indication that the thermal transport in our model system is dominated by the GBs. It also suggests that the fundamental assumption of separable and grain-size bulk and interfacial thermal properties used for the analysis may be violated at these small grain sizes. There is thus a clear need for a model that treats the GB and grain interiors in an integrated manner.

The effects of grain size on thermal conductivity have been investigated for grain sizes up to 6.5 nm grains. The inset to Figure 5-6 shows the increase in thermal conductivity with increasing grain size determined from the simulations; this increase arises from the decrease in the relative volume of GBs in the system. Our data for polycrystals simulated with the Yamada potential are fit to the model of Yang *et al.*, thereby allowing the thermal conductivity for large grain sizes to be estimated. Taking the bulk single crystal conductivity of 15.2 W/mK at 300 K, the fit gives the Kapitza conductance of 0.15 GW/m<sup>2</sup>K, which is close to the value previously determined for the 3.8 nm polycrystal (see Figure 5-5).

For the sake of comparison, the same fit to the grain size dependence are done using the models by Nan-Birringier and Amrit.  $l_K$  are 8.4 nm for Nan-Birringier model and 12.6 nm for Amrit model, respectively. This compares well to 7.4 nm from the Yang's model.

### **Discussion**

The analysis of the polycrystal to obtain the interfacial conductance is not unambiguous, since the calculated Kapitza lengths are larger than the grain sizes. However, the fact that the

calculated thermal conductivities of polycrystals of different grains sizes, albeit over the narrow range of 3.8 – 6.5 nm, can be fit to the Yang *et al* model, suggest that their use is not unreasonable. Moreover, since the same analysis is used throughout, the trends of interfacial conductance with temperature are reasonable.

Comparison among the three effective medium models showed fairly similar results. Although the Amrit's model predicts a somewhat higher Kapitza length, it is clear that the cause is due to the way his model includes the number of interfaces in between the heat source and sink. More importantly, however, this does not change the qualitative trend of the grain size dependence although the absolute value of the calculated Kapitza length, i.e. the interfacial conductance may be different.

The interfacial conductance obtained from our simulations in fact compares well with those of the other heterogeneous interfaces: see Figure 5-7., indicating the validity of the methodology.

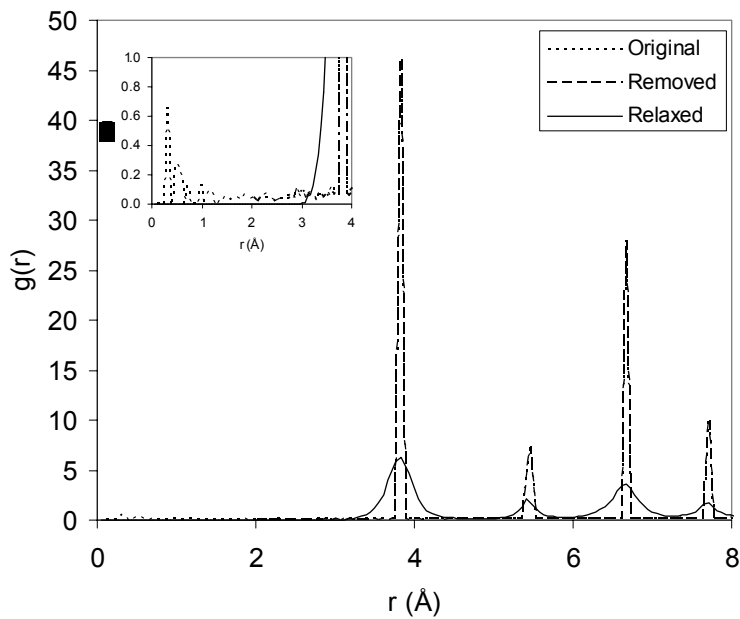


Figure 5-1. Pair distribution function of the polycrystalline structure. The original structure is the unrelaxed reference structure. “Original”: All atoms are in perfect crystal like positions except the ones at the grain boundaries. “Removed”: The original structures has a number of atoms in the grain boundary region, which are so close to each other that they must be removed. “Relaxed” the structure after annealing and thermal equilibration.

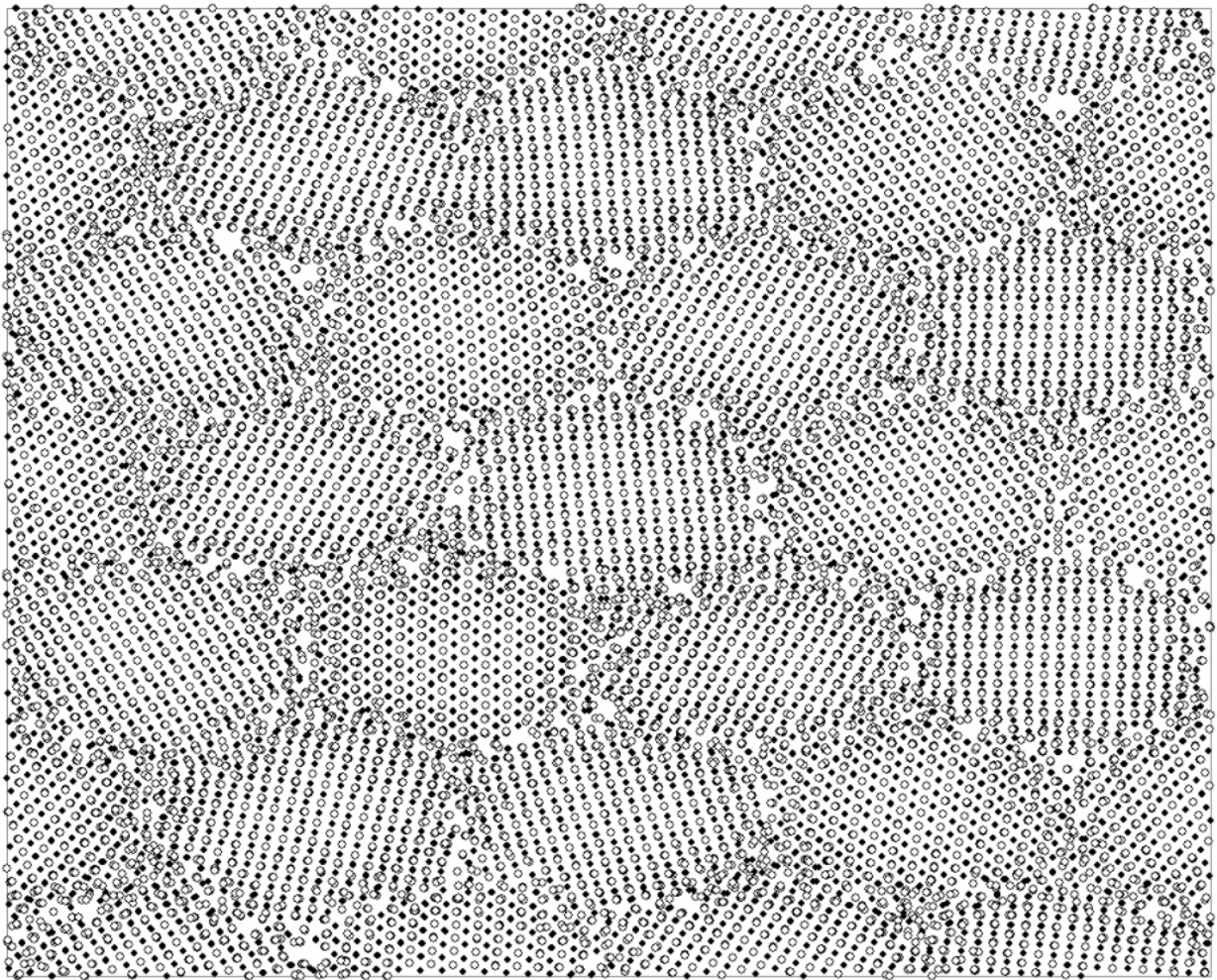


Figure.5-2. The final polycrystalline structure used in the thermal conductivity calculations. Filled and open circles indicate uranium and oxygen ions, respectively. The view is along [001] in the fluorite crystal structure. The PBCs are applied in all three directions.

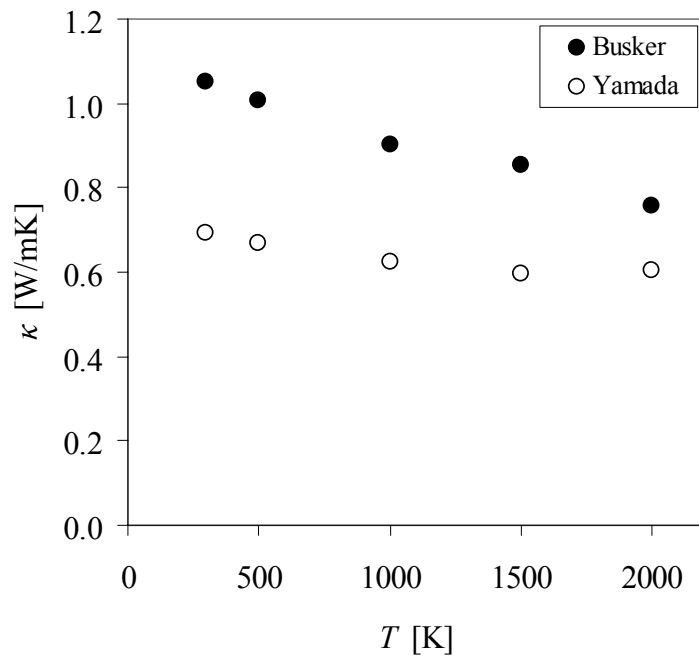


Figure 5-3. Thermal conductivity of 3.8 nm grain polycrystalline  $\text{UO}_2$  from simulation for the two potentials.

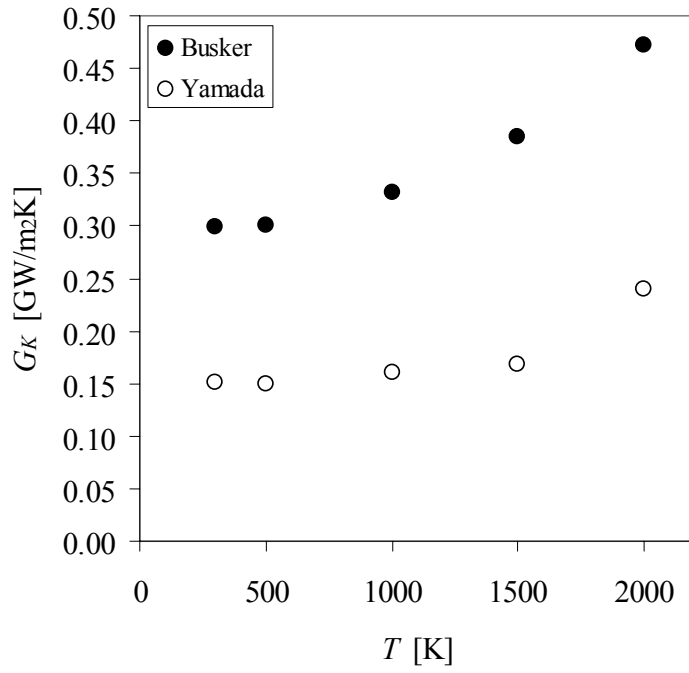


Figure 5-4. Average thermal conductance for the [001] tilt GBs from 3.8 nm grain polycrystalline  $\text{UO}_2$ .

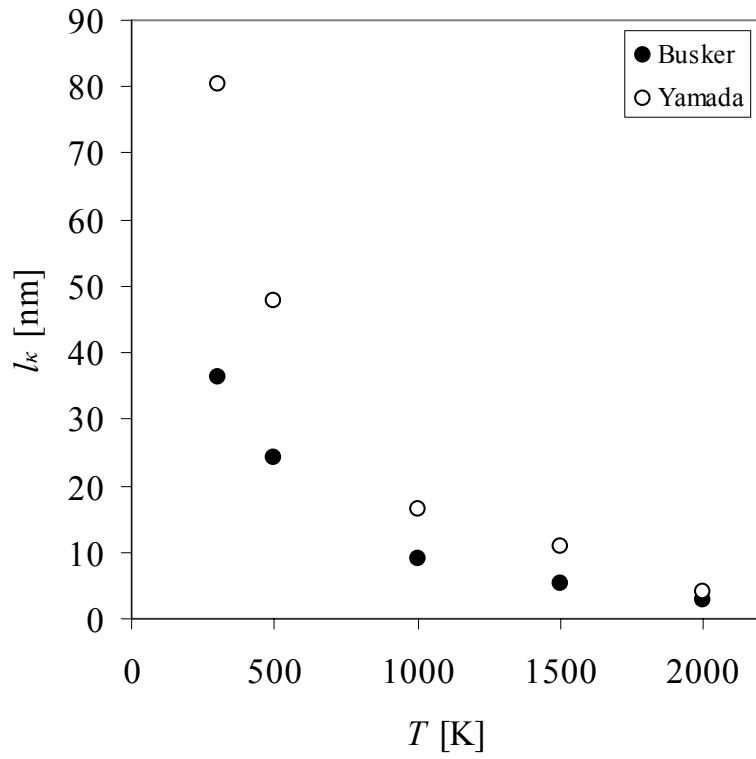


Figure 5-5. Kapitza length from 3.8 nm grain polycrystalline  $\text{UO}_2$  simulations.

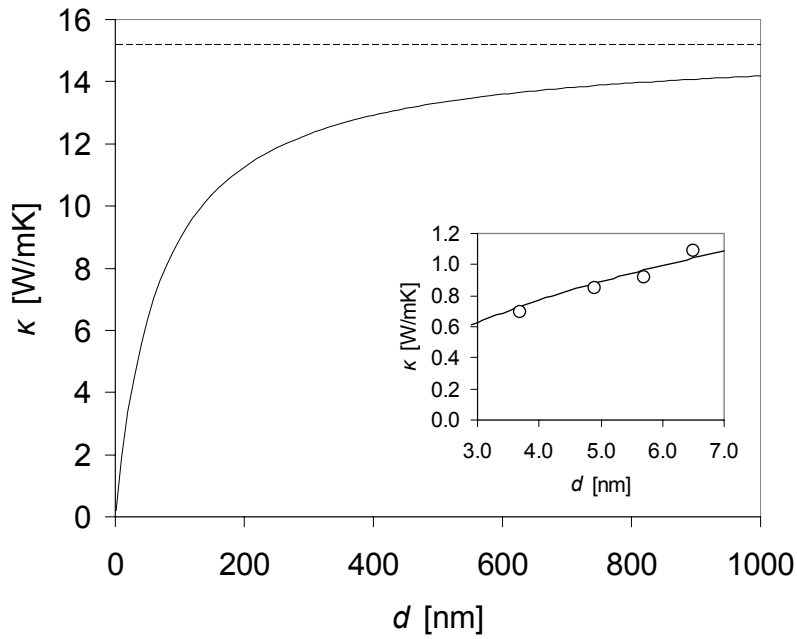


Figure 5-6. Grain size dependence of the thermal conductivity of polycrystalline  $\text{UO}_2$  using Yamada's potential. The solid line is the fit of the model by Yang *et al.*<sup>78</sup>. Inset is the same plot for nano-meter scale indicating the fit with our simulation data.

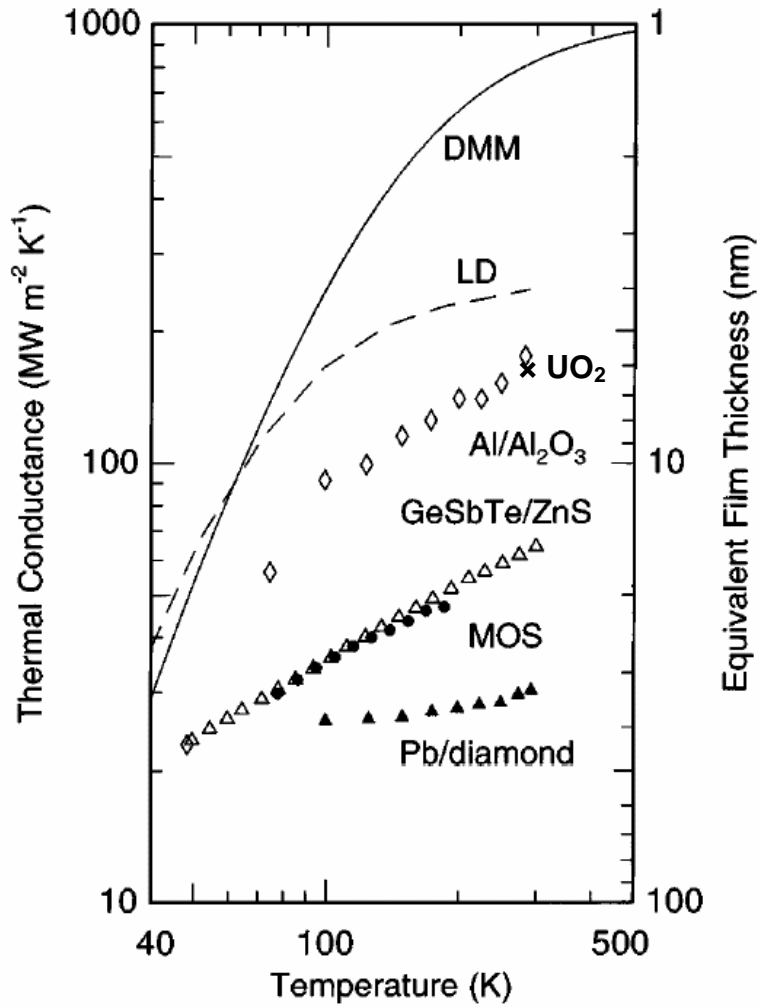


Figure 5-7. Interfacial conductances of selected interfaces as function of temperature.  $\text{UO}_2$  data point is from our MD simulation. DMM and LD are the theoretical predictions for the  $\text{Al}/\text{Al}_2\text{O}_3$  interfaces. The right axis is the equivalent film thickness assuming the bulk conductivity of  $1 \text{ W/mK}$ . [Adapted from reference 130 (Figure 1).]

## CHAPTER 6 THERMAL TRANSPORT IN $\text{UO}_{2\pm X}$

### Introduction

Just as GBs do, point defects also act as scattering centers in crystalline solids and reduce the mean free path of phonons. This results in a reduction of the thermal conductivity of the solid. The thermal conductivity in a single crystal insulator can be very well described by the dynamics of phonons as discussed in detail in Chapters 2 and 4. In the case of highly disordered solids, such as highly doped materials or amorphous solids, the situation is quite different (Chapter 2 for general discussion). In practical applications,  $\text{UO}_2$  often contains a large number of point defects, dislocations, and GBs<sup>11</sup>. Although understanding the mechanisms of how these defects couple to affect thermal transport is currently prohibitively complicated, understanding the effect of individual types of defect is possible. Therefore, in this chapter, the thermal transport properties of non-stoichiometric  $\text{UO}_2$  are characterized by simulation, and the results analyzed in terms of the theory of thermal transport in a disordered solid. While the main focus is on the anion defects, which are the dominant defects in  $\text{UO}_2$ , the effects of other point defects are also discussed. The effects of isotopic defects are also briefly analyzed.

### Point Defects in $\text{UO}_2$

$\text{UO}_2$  contains a wide variety of point defects when it is used for the nuclear fuel application. The extreme conditions of temperature and radiation condition generates intrinsic, extrinsic (fission products), and electronic defects. In pure  $\text{UO}_2$ , the possible intrinsic point defects are  $V_U$ ,  $U_i$ ,  $V_O$ ,  $O_i$ , the Frenkel pair, the anti-Frenkel pair, and the Schottky trio. The defect formation energies for intrinsic defect determined by experiments and density functional theory (DFT) calculations are shown in Table 6-1. Agreement between the experimental and DFT values are reasonable except for the Schottky defect. It can be deduced from this data that

the thermodynamically most relevant intrinsic defects are the anti-Frenkel defects.<sup>3, 34-36</sup>

Although the Schottky trio formation energy is higher than anti-Frenkel pair, it also plays an important role at high temperature<sup>3, 35</sup>. The most recent DFT calculations, by Freyss *et al.*<sup>131</sup> and by Crocombette *et al.*<sup>132</sup>, determined the defect formation energies of individual  $O_I$ ,  $V_O$ ,  $U_I$ , and  $V_U$ , which are very difficult to determine from experiments. They found a negative formation energy for  $O_I$ , which implies that  $UO_2$  readily incorporates oxygen ions under oxidizing condition. So far the DFT and experiments show qualitatively consistent results despite some quantitative discrepancies.

Empirical potentials have been also used to evaluate the defect formation energies of intrinsic defects. Govers *et al.*<sup>115</sup> calculate the Frenkel, anti-Frenkel, Shottkey defect formation energies using 18 existing empirical potentials. Figure 6-1 gives a comparison of the normalized Frenkel and anti-Frenkel pair formation energies from Govers' work. An additional data point for the the rigid-ion Busker potential (used in our simulations of single-crystal and polycrystalline  $UO_2$ ) is included and referred to as Busker1 in the figure. The error bars for the reference point indicates the scatter in the available DFT and experimental data. Most potentials do a fairly good job in reproducing the oxygen anti-Frenkel pair formation energies, except for a few outliers. However, all the empirical models overestimate the uranium Frenkel pair formation energies.

Intrinsic defects in  $UO_2$  often have rather complex structures.  $UO_2$  has a broad hyperstoichiometric phase at high temperature (See Figure 1-7.) because of the low defect formation energy of  $O_I$ . Willis<sup>24, 25, 133-135</sup> and later Hutchings<sup>22</sup> characterized the defect structures in  $UO_{2+x}$ , by neutron diffraction. Willis' neutron diffraction data on  $UO_{2.13}$  showed that the excess anions were not at the body center interstitial site: rather, the unit cell structures

were distorted and formed a complex of defects including oxygen vacancies<sup>25, 133</sup>. He argued that the dominant structural defect is the anion Frenkel defect. A similar observation was made in fluorite (CaF<sub>2</sub>) by Cheetham *et al.*<sup>136</sup>, and the result was interpreted as an 2:2:2 interstitial cluster (Figure 6-2.). The 2:2:2 notation indicates that the cluster consists of 2 vacancies, 2 atoms shifted in along <110>, and 2 shifted along <111>. This defect cluster structure is often referred to as the Willis cluster in the literature. Hubbard *et al.*<sup>137</sup> performed optical absorption spectroscopy experiments and explained the change in the charge state of cation sublattice as due to the formation of the defect clusters. Allen *et al.*<sup>138, 139</sup> also observed the defect clusters in their diffraction data and proposed ordered defect substructures for UO<sub>2+x</sub> phases. There are several types of defect clusters in UO<sub>2+x</sub> reported such as 2:1:2 and 4:3:2, which can combine to form larger defect clusters.<sup>137, 138</sup>

A UO<sub>2-x</sub> phase also can occur at high temperature and low oxygen partial pressure.<sup>36</sup> However, this UO<sub>2-x</sub> phase occurs more commonly by the formation of oxygen vacancies through extrinsic defects.<sup>34, 140</sup>

Catlow undertook the first general theoretical survey of defects properties in UO<sub>2</sub>.<sup>34</sup> He used an empirical model derived from experimental data of UO<sub>2</sub> bulk properties and Hartree-Fock calculations. The defects considered were  $V_o^{**}$ ,  $O_i''$ ,  $V_u'''$ ,  $U_i$ ,  $V_o^*$ ,  $O_i'$ , Frenkel and anti-Frenkel pairs, and the Schottky trio. His work on formation energies of these defects established that the anti-Frenkel pair of a doubly charged interstitial and a vacancy is the dominant intrinsic atomic disorder in UO<sub>2</sub>. This result is in agreement with the neutron diffraction studies by Willis<sup>24, 25, 134, 135</sup> although the charge state of the defects is not known in the experiment. Catlow also found that the lattice is distorted in the hyperstoichiometric structure and that the interstitial is slightly shifted in <110> at the lowest energy state. Interstitials shifted along <100> and

$\langle 111 \rangle$  are also lower in energy compared to the perfectly symmetric body centered position, but none of these shifts are significant enough to account for the 2:2:2 defect cluster structure by Willis. In addition to the atomic defects, the electronic defects were also considered and turned out to be much more favorable than such atomic disorder.<sup>34, 141, 142</sup>

When used as a fuel in a LWR,  $\text{UO}_2$  also contains a certain level of isotopes of uranium.  $^{235}\text{U}$  is the fissile element in  $\text{UO}_2$  and produces the neutrons necessary for the chain reactions. The dominant isotope is  $^{238}\text{U}$ ; however it is not fissile. The concentration of  $^{235}\text{U}$  is controlled and in a typical fuel is about 3-4 wt.%. This isotope acts as a mass defect in  $\text{UO}_2$  and can scatter phonons in the crystal. The isotope effect is important in the thermal transport properties of materials such as diamond<sup>51</sup> and Si<sup>143, 144</sup>. However, isotopic effects in the  $\text{UO}_2$  fuel thermal transport properties have not been investigated.

In addition to the intrinsic defects, the effect of extrinsic defects such as fission products is critical.<sup>11</sup> As discussed in Chapter 1, fission products consist of a wide variety of elements having different masses and sizes.<sup>37</sup> Some of them are even radioactive.<sup>11</sup> They can reside in the  $\text{UO}_2$  matrix as gases<sup>42</sup>, solid solutions<sup>36, 145</sup>, or different phases<sup>36, 146</sup>. Although they can have significant effects on the  $\text{UO}_2$  properties including thermal transport<sup>40</sup>, the study of the effects of fission products is beyond the focus of this work.

### **Thermal Transport in $\text{UO}_2$ with Point Defects**

One of the earliest studies on the effect of stoichiometry on thermal transport of  $\text{UO}_{2+x}$  was undertaken by Hobson *et al.*<sup>147</sup>. They measured the thermal diffusivities from 550 to 2500 K by laser flash on samples with between 93 and 96 % of the theoretical density. The degree of off-stoichiometry studied was  $x=0.006$ , 0.030, and 0.060. The thermal conductivity was determined from the measured thermal diffusivity and mass density of the sample, with the heat capacity data taken from the work by Affortit and Macron.<sup>148</sup> In general, the thermal conductivities of all

the samples showed monotonic decreases with increasing temperature, but there was a sudden change in the slope around 700 K for high concentration of oxygen interstitials at  $x=0.060$ . This change was later ascribed to the formation of  $U_4O_9$  phases in the sample.

Lucuta *et al.*<sup>149</sup> determined the effect of thermal conductivity of  $UO_{2+x}$  between 298 and 1773 K. Thermal conductivities were determined by measurements of thermal diffusivities, heat capacity and mass density. All the samples used were 98 % of the theoretical density, but the conductivity values for 100 % dense material were also estimated from the data. The thermal conductivity of  $UO_{2+x}$  was found to decrease with increasing degree of off-stoichiometry, with reductions for  $x=0.007$ , 0.035, and 0.084 of 13, 37, and 56 % at 827 K, and 11, 23, and 33 % at 1773 K. Just as Hobson did, Lucuta *et al.* also observed a change in the behavior of the thermal conductivity for  $x=0.035$  and 0.084. By X-ray diffraction observation, they determined that this effect is due to the precipitation of  $U_4O_9$  phase. Even with careful preparation, the formation of the secondary phase in their samples could not be avoided.

Lewis and his collaborators undertook both experimental and numerical studies on the oxidation behavior of  $UO_2$  in a defective fuel rod, and on the effect of oxidation on the thermal conductivity of the fuel.<sup>150</sup> They employed a phenomenological model for thermal conductivity as a function of degree of off-stoichiometry. They showed that  $\kappa$  depends significantly on the value of  $x$  within the range of  $0 \leq x \leq 0.2$  below 2000 K. The contributions from the radiation (Chapter 7) and polarons (Chapter 1) hardly made any difference in this temperature range and were not affected by the oxygen interstitials introduced in the material.

There is also a recent MD simulation study performed by Yamasaki *et al.*<sup>151</sup> on the thermal conductivity of  $UO_{2+x}$ . They developed a rigid-ion type interatomic potential based on the thermal expansion due to the incorporation of  $O_I$  using the experimental values of Grønvold

<sup>152</sup>. They employed the Green-Kubo (GK) method to calculate the thermal conductivity by an equilibrium MD simulation. Their value of the thermal conductivity was in good agreement with experimentally observed conductivity data. In particular, their data shows a decrease of conductivity with increasing concentration of defects, the same trend as observed in the experiments <sup>149, 153</sup>. However, the direct integration of the GK formula is known to result in ambiguous results<sup>87, 154-156</sup>. In the case of single crystal Si, Shelling *et al.*<sup>87</sup> showed that the simulation must be run for longer than 1 ns, and the time integral must be performed for at least 200 ps. Although  $\text{UO}_{2+x}$  has lower thermal conductivity than Si (experimental value of the isotopically enriched Si is  $\sim 200 \text{ W/mK}^{143}$ ), it is not clear how long the necessary simulation time and integration interval must be for  $\text{UO}_{2+x}$ . Furthermore, Yamasaki *et al.* constructed the structures based on the 2:2:2 clusters, such defect structures are not consistent with the assumption of homogeneity in the GK method.

### **Molecular Dynamics Simulations**

The theoretical stand point of view, there has been no reliable simulation work on the effect of stoichiometry on the thermal conductivity of  $\text{UO}_2$ . In the following, the approach taken to perform thermal conductivity calculations of  $\text{UO}_{2\pm x}$  using MD simulations is described. The range of off-stoichiometry investigated was between  $x=-0.02$  and  $0.25$ . This range was chosen based on the phase diagram of  $\text{UO}_{2\pm x}$  between 800 and 1600 K (See Figure 1-7). Although this range of  $x$  is beyond the range of off-stoichiometry studied in any of the previous experimental and simulation works, this broad range enhances the effect of the defects to thermal transport and clearly indicates the concentration dependence of the thermal conductivity. Implications of the outcome of the simulations are discussed in terms of the thermal conductivity of a disordered solid.

## Preparation of the Structures

In order to perform MD simulations with oxygen defects, interatomic potentials must be modified to retain the charge neutrality. Standard MD simulations do not allow the charges of the atoms to vary during the simulation. Therefore, in order to include  $O^{2-}$  and  $V_o^{**}$ , interatomic interaction for  $U^{3+}$  and  $U^{5+}$  must be added. The potential parameters are given in Table 4-1. These parameters were provided from Prof. Grimes in Imperial College London. Note that there is no short-range interaction between the cations.

The  $UO_{2+x}$  structures are prepared in the following fashion. First a defect free  $UO_2$  structure is prepared in the desired size. Then a number of excess oxygen atoms corresponding to the desired concentration are inserted in randomly selected octahedral (4b) sites. In addition, randomly selected  $U^{4+}$  atoms are replaced with  $U^{5+}$  atoms such that overall charge neutrality is maintained. Once the structure is created, the simulation cell is heated to 3000 K for 10 ps. This allows the oxygen atoms to diffuse and minimizes the possibility of any sort of artificial configuration. After the high temperature equilibration is complete, the system is slowly cooled to 0 K in a step wise fashion at an average cooling rate of 30 K/ps. Finally the structure is quenched by steepest decent algorithm to ensure the minimum energy configuration.

A similar procedure is performed to create  $UO_{2-x}$  structures. From the single crystal  $UO_2$ , an appropriate number of the randomly selected oxygen atoms are removed to create a desired concentration of oxygen vacancies. At the same time, randomly selected  $U^{4+}$  atoms are replaced with  $U^{3+}$  atoms for charge neutrality. After the structure is created, the same annealing and relaxation procedure is performed to achieve the minimum energy configuration.

Characterization of the oxygen excess and deficient structures is performed by the pair distribution function analysis. Figure 6-3 shows the pair distribution functions (PDF) of

$\text{UO}_{2+x}$ . between uranium and oxygen ions<sup>-</sup>. The PDF of the defected structure before annealing is shown as a reference for the ideal single crystal separation of uranium and oxygen ions. The PDF before annealing shows secondary peaks by the primary peaks. The primary peaks are the  $\text{O}^{2-}$  ions at 8c positions in the fluorite structure. These secondary peaks are the locations of oxygen interstitials at the octahedral (4b) sites. We also note that before the structure is relaxed, all  $\text{O}^{2-}$  ions are at 8c sites such that there is no difference between the PDF between  $\text{U}^{4+}-\text{O}^{2-}$  and  $\text{U}^{5+}-\text{O}^{2-}$ . After annealing and relaxing at 0 K, the peaks are broadened and their heights decreased. The differences in PDF between  $\text{U}^{4+}-\text{O}^{2-}$  and  $\text{U}^{5+}-\text{O}^{2-}$  appear. The secondary peaks corresponding to  $\text{U}^{5+}-\text{O}^{2-}$  are merged with the primary peaks. Furthermore, the first peak of the PDF of  $\text{U}^{5+}-\text{O}^{2-}$  is shifted inward compared to the same peak of  $\text{U}^{4+}-\text{O}^{2-}$  by  $\sim 0.2 \text{ \AA}$ . This shift is expected from the stronger electrostatic attraction between  $\text{U}^{5+}-\text{O}^{2-}$  than  $\text{U}^{4+}-\text{O}^{2-}$ . The higher order peaks are also shifted, but the differences are so small that they cannot be seen in the figure.

In the  $\text{UO}_{2-x}$ , similar observations can be made. After relaxation, the peaks are also broadened and the heights are reduced. Although the  $\text{U}^{4+}-\text{O}^{2-}$  peak does not move, the  $\text{U}^{3+}-\text{O}^{2-}$  peak is shifted to larger distances. Just as in the case of  $\text{UO}_{2+x}$ , this is expected by the reduction of the electrostatic attraction between  $\text{U}^{3+}-\text{O}^{2-}$ .

### **Chemical Expansion of $\text{UO}_{2\pm x}$**

Using the method described in the previous section,  $\text{UO}_{2\pm x}$  structures are prepared, and are relaxed at 0 K. The range of off-stoichiometry for this study is from  $\text{UO}_{1.98}$  to  $\text{UO}_{2.25}$ . This range is chosen based on the phase diagram of U-O system (Figure 1-7.). Although, in the actual reactor fuel, such a wide range of stoichiometry does not occur, this broad range of defect concentrations will enhance the influence on the thermophysical properties in our simulation.

These structures show a change in lattice parameter due to the excess or deficiency of oxygen ions in the system. This effect is known as the chemical expansion or contraction.

Figure 6-5 shows that the normalized lattice parameter of  $\text{UO}_{2+x}$  at 0 K decreases with increasing concentration of oxygen interstitials. The lattice parameter at the highest defect concentration ( $x=0.250$ ) is  $\sim 0.5\%$  smaller than the lattice parameter of stoichiometric  $\text{UO}_2$ . This is the result of the increased electrostatic attractions by the competition between the contraction due the replacement of some of the  $\text{U}^{4+}$  ions by  $\text{U}^{5+}$ , and the expansion from the addition of extra  $\text{O}^{2-}$  in the octahedral sites. This indicates that the expansion of the lattice due to the strain of the oxygen interstitials at 8c sites is overwhelmed by the strong electrostatic attraction.

Grønvold<sup>152</sup> performed X-ray studies to determine the thermal expansion of  $\text{UO}_{2+x}$ . His data indicates no significant difference in the lattice parameter from that of stoichiometric  $\text{UO}_2$  over the range of  $x=0.0\sim 0.2$ , i.e, no chemical expansion. However, the phase diagram of  $\text{UO}_{2+x}$  is rather complex and is still an active area of research.<sup>157</sup> Furthermore, there has been no systematic study on the chemical expansion of  $\text{UO}_{2+x}$  after Grønvold, and more recent work is needed to draw a conclusion as to the presence or absence of a chemical effect.

The  $\text{UO}_{2-x}$  phase is analyzed in the same fashion. Figure 6-6 gives the normalized lattice parameter of  $\text{UO}_{2-x}$  at 0 K after relaxation determined from simulation. In contrast to  $\text{UO}_{2+x}$ , the lattice parameter increases with increasing concentration of defects. The change in lattice parameter is linear because of the narrow range of defect concentrations. There is no experimental data on the chemical expansion of  $\text{UO}_{2-x}$  available due to experimental difficulties and due to the limited relevance to the applications.

### **Thermal Expansions of $\text{UO}_{2\pm x}$**

Figure 6-7 gives the thermal expansion of  $\text{UO}_{2+x}$  obtained from the MD simulations. For each composition, the data is normalized by the 0 K lattice parameter, such that the effect of chemical expansion does not play a role. The temperature dependence of the lattice parameter is almost linear for all the concentrations of defects studied. The thermal expansion,  $\alpha$ , indicated

by the slope of the curves, decreases from  $6.8 \times 10^{-6} \text{ K}^{-1}$  to  $5.4 \times 10^{-6} \text{ K}^{-1}$  as the defect concentration increases. Figure 6-8 is the plot of  $\alpha$  vs.  $x$  extracted from the data in Figure 6-7. in  $\text{UO}_{2+x}$ . It shows the gradual linear decrease of  $\alpha$  with increasing  $x$ . Again, there is no systematic study on the effect of defect concentration on  $\alpha$  except for the Grønvold's work, which showed no effect of composition.

The thermal expansion of  $\text{UO}_{2-x}$  is shown in Figure 6-9. The data indicates that the defect concentration has a very minor effect on the thermal expansion of the lattice. This is the case because the low concentration of the defect introduced.

### **Thermal Conductivity of $\text{UO}_{2+x}$**

Using the technique described in the beginning of this section,  $\text{UO}_{2+x}$  structures of  $21.9 \times 21.9 \text{ \AA}^2$  ( $4 \times 4$  unit cells) cross sections are prepared. This is the same cross section size as the ones used in Chapter 4 for the single crystal  $\text{UO}_2$  study. The effect of the simulation cell length is still important and must to be investigated to obtain the infinite size bulk thermal conductivity. Therefore, the simulation cell lengths of 262.5, 350.0, 437.4, and 524.9  $\text{\AA}$  were used.

The simulations were run at 800 and 1600 K, which correspond approximately to the surface and centerline temperatures of a fuel pellet during the operation of a typical PWR. The rest of the simulation conditions were the same as in the single crystal  $\text{UO}_2$  (Chapter 3). The results are shown in Figure 6-10 and 6-11 as  $1/\kappa$  vs.  $1/L_z$ . The data points of the each defect concentration were fit to the straight lines expected from the kinetic theory of phonon gas (Equation 3-10). At 800 K, the data points fit well with the straight line for the defect concentrations. In particular, the quality of the fit is better at the low concentrations ( $x \leq 0.75$ ) with the correlation of fit being better than 0.95. For  $x > 0.75$ , the correlation varies between 0.60 and 0.78. This is reasonable since Equation 3-10 assumes independent phonon scattering which

is most likely true at low concentrations of defects. However, at higher concentrations of defects ( $x \geq 0.0125$ ) at the same temperature, the data points do not follow a linear fit as well as that of lower concentrations. For  $x \geq 0.175$ , the conductivity values are statistically identical and error bars overlaps. At 1600 K (See Figure 6-11), the quality of fit is somewhat poorer ( $r^2 \geq 0.92$  for  $x \leq 0.75$  and  $0.62 < r^2 \leq 0.73$  for  $x > 0.75$ ) than at 800 K, and the errors are slightly larger. At this temperature, the inverse conductivities are statistically indistinguishable from each other for  $x \geq 0.125$ . Slopes of the linear regressions for 800 K and 1600 K are rather similar, indicating that the size dependence is not strongly dependent on the temperatures between 800 K and 1600 K.

From the linear fit to the data in Figs. 6-10 and 6-11, the thermal conductivities of infinitely large system at 800 and 1600 K are obtained by extrapolation. The results are shown in the top of Figure 6-12. The data for both 800 and 1600 K show monotonic decreases of the conductivity with increasing concentration of oxygen interstitials. Interestingly, the two curves converges to the same value of the conductivity of  $\sim 3.6$  W/mK above  $x = 0.125$ .

Besides the trend of the thermal conductivity on  $O_I$  concentration, there is an apparent discrepancy in the values of thermal conductivity relative to the experimental data by Lucuta<sup>149</sup>. The thermal conductivity from the MD simulation is much higher than that of experiment by a factor of roughly 2-3. This difference is most likely due to the quality of the interatomic potential (Chapter 3 for the discussion in single crystal  $UO_2$ ). Using the same scaling factor, 0.34, from the ratio of the square of the thermal expansion and bulk modulus between the experimental and simulation, we obtain the thermal conductivity curves shown in Figure 6-13. The resulting rescaled conductivities agree well with experimental. This suggests that this treatment is appropriate for the simulation of the effects of point defects on the thermal conductivity.

## Thermal Conductivity of $\text{UO}_{2-x}$

The thermal conductivity of  $\text{UO}_{2-x}$  was calculated using exactly the same methods as for  $\text{UO}_{2+x}$ . Figures 6-14 and 6-15 are the inverse thermal conductivity at 800 and 1600 K as a function of simulation cell length for the oxygen vacancy concentrations of  $0.00 \leq x \leq 0.02$ . Just as in the case of  $\text{UO}_{2+x}$ , the simulation size effect is investigated. The quality of the fits is fair at both temperatures ( $r^2 > 0.91$  at 800 K, and  $r^2 > 0.82$  for 1600 K), and there is no significant difference between the two data sets.

The predicted bulk thermal conductivity obtained from the linear fits is shown in Figure 6-16. The thermal conductivity values at both 800 and 1600 K decrease almost linearly with concentration. This is reasonable considering the low concentration of defects. The linear fits give the slope of -122 W /mK at 800 K and -53 W /mK at 1600 K. (Note that the unit of concentration is hidden for simplicity.) The smaller slope for 1600 K is an indication of the weaker concentration dependence because of the significant phonon-phonon scattering. Unfortunately there is no reliable thermal conductivity data from experiments to compare the data from the MD simulations.

Finally the thermal conductivity at low defect concentrations in both  $\text{UO}_{2+x}$  and  $\text{UO}_{2-x}$  are characterized. Figure 6-17 shows the thermal conductivity for  $\text{UO}_{1.98}$ - $\text{UO}_{2.02}$  at 800 K and 1600 K. Although  $\text{UO}_{2+x}$  data is linear,  $\text{UO}_{2-x}$  data show some curvature. For analysis the data set from  $\text{UO}_{2+x}$  is fit to tangent line at  $x=0.000$ . The slopes of the tangent for 800 K and 1600 K data are -141 W/mK and -64 W/mK, respectively, similar to the slopes of  $\text{UO}_{2-x}$ .

## Isotopic Effect

The effect of uranium isotopes in  $\text{UO}_2$  was also studied. As described in Chapter 1 and the beginning of this chapter,  $\text{UO}_2$  in a typical LWR is isotopically enriched to increase the fissile  $^{235}\text{U}$ . The concentration of  $^{235}\text{U}$  may vary depending on the specification of the reactor, but it is

typically in the range of 3-4 wt. %.<sup>11</sup> In the MD simulation, <sup>235</sup>U was introduced as a simple mass defect and the concentration is set to 5 at. %, which is comparable to the concentration of the isotopes in the actual fuel.

$\kappa$  obtained from the simulation at 300 K was 5.8 W/mK, which is within the error bar of the value of the defect free UO<sub>2</sub>, 6.0 W/mK. Thus, there is no obvious influence of the mass defects to the thermal conductivity.

### **Lattice Dynamics Calculations**

Although the thermal conductivities of UO<sub>2±x</sub> have been quantitatively determined by the non-equilibrium MD simulations, further understanding in the mechanism of heat transfer in this material can be gained by lattice dynamics (LD) calculations. LD is a method which allows analysis of vibrational modes in solid. The formalism of LD is described in Appendix I. As discussed in Chapter 2, we followed the approach of Allen *et al.*<sup>85</sup> and performed LD calculations on 6×6×6 unit cells of UO<sub>2±x</sub> for this analysis. The calculations are performed only at the zone center ( $k=0$ ) because of the large repeat unit. In principle, using a larger structure is better since the resolution of frequency is proportional to the number of atoms in the repeat unit,  $N$ . However, increasing the number of atoms increases the size of the dynamical matrix which is proportional to  $N^2$ , and diagonalization of a large matrix is very demanding. Thus the computational load rapidly increases with the number of atoms in the system. For example, using a 2.2 GHz 64-bit AMD Opteron processor with 4 GB of RAM, a single LD calculation on the 6x6x6 unit-cell system takes approximately 48 hours to complete.

As the first step in characterizing the the structures, phonon densities of states (DOS),  $g(\omega)$ , of UO<sub>1.98</sub>-UO<sub>2.25</sub> were calculated. Figures 6-15 (a)-(f) are the phonon DOS as a function of concentration. In the defect free structure, UO<sub>2.00</sub>, the vibrational frequencies are well defined resulting in very sharp peaks over the entire frequency range. The Debye model like behavior

$(g(\omega) \sim \omega^2)$  continues up to  $\sim 4$  THz. As the defect concentration is increased, either in the hyper- or hypo-stoichiometric directions, the DOS smear out and the minor peaks disappear. There is no significant change in the DOS for  $-0.020 \leq x \leq 0.020$  indicating that the concentrations of defects are indeed low enough that they do not influence the dynamics of the vibrational modes in  $\text{UO}_2$ .

As discussed in Chapter 2, materials containing defects can have vibrational modes that are spatially localized. These modes are called locons and they cannot carry thermal energy through the system;<sup>85</sup> therefore they can act as a source of thermal resistance. The degree of localization of each mode can be quantified by the participation ratio,  $p_\lambda$ , as given in Equation I-5.

$$p_\lambda^{-1} = N \sum_i \left( \sum_\alpha e_{\lambda,i\alpha}^* e_{\lambda,i\alpha} \right)^2,$$

In an ideal crystalline structure,  $p_\lambda$  is of order of unity for some atoms and small for others, indicating that specific atoms are associated with any given mode; this is equivalent to the mode having a well-defined wave vector.<sup>158</sup> If the localization occurs,  $p_\lambda$  approaches  $\sim 1/N$ .

Figure 6-19 is the participation of  $6 \times 6 \times 6$  single crystal  $\text{UO}_{2\pm x}$ . The participation ratio of the defect free  $\text{UO}_2$  is shown in Figure 6-19 (c).  $p_\lambda$  is widely scattered around 0.5, which is a characteristic of a crystalline solid. Once the defects are introduced,  $p_\lambda$  displays much narrower range of distribution. This means that the nearby vibrations in frequency space in the  $\text{UO}_{2\pm x}$  are coupled to each other, and should thus contribute approximately equally to the thermal transport. Even for the lowest concentrations ( $|x|=0.010$ ) of defects, this is still true.

The propogon and diffuson modes can be distinguished by using the polarization of vibrational modes in  $\text{UO}_{2\pm x}$ . (Chapter 2) Figure 6-20 is a comparison of the polarization vectors at 1.5 THz in  $\text{UO}_{2\pm x}$ . Since the polarization vectors lies on the sphere of unit radius, two projection methods, *i.e.* direct and equal-area projection, are used for comparison. The direct

projection is the simple projection of the vector components in the Cartesian coordinates. The equal-area projection is achieved by scaling the two coordinates according to their polar angle. For instance, if the equal-area projection is about the z-axis, x and y components of the vectors are scaled by  $2\sin(\theta/2)$ , where  $\theta$  is the angle between z-axis and the vector. The frequency of 1.5 THz was chosen since it is at the low end of the frequency range which is expected to be dominated by the propagon modes. The polarization vectors in the defect free  $\text{UO}_2$  are well defined and take the value of  $\pm 1$ . For the low concentrations of defects ( $-0.020 \leq x \leq 0.020$ ), there are areas which data points are concentrated on both projection methods. This indicating that there are still a fair number of modes with well defined polarization vectors. At  $x=0.125$ , the distribution of the data points is uniform and there is no well defined polarization vector.

The story is different at 10 THz (Figure 6-21). The polarization vectors are homogeneous and isotropic at all the concentrations of defects in both projections. There is no obvious feature to distinguish the materials from the polarization plots. Thus, there is no well defined polarization vector, which is the feature of diffuson modes.

### **Discussion**

Our analysis showed that the  $\text{UO}_{2+x}$  displays a chemical contraction compared to pure  $\text{UO}_2$ . Further analysis showed that this contraction is due to the electrostatic attraction by the  $\text{O}_I$  and  $\text{U}^{5+}$ . A similar, but opposite, effect takes place in  $\text{UO}_{2-x}$ . The thermal expansion of the  $\text{UO}_{2+x}$  decreased with increasing concentration of defects, while over the small range of stoichiometry considered,  $\text{UO}_{2-x}$  structures showed no such change. The reason for this difference is due to the range of concentrations considered. The small concentration of oxygen vacancies in  $\text{UO}_{2-x}$  also resulted in negligible change in the thermal expansion. If only the range of  $x \leq 0.025$  is considered,  $\text{UO}_{2+x}$  also show no discernible change in the thermal expansion.

The concentration dependence of the thermal conductivities of  $\text{UO}_{2\pm x}$  was determined by the MD simulations using the direct method. At low concentrations, both  $\text{UO}_{2+x}$  and  $\text{UO}_{2-x}$  show approximate linear dependence. These results are consistent with the Klemens-Callaway (KC) theory of phonon-defect scattering which suggests that the scattering rate to be proportional to the defect concentration.<sup>74, 159</sup> The concentration dependence in the low concentration limit is rather similar in  $\text{UO}_{2+x}$  and  $\text{UO}_{2-x}$  despite the different defects in the structures. The ratios of the slopes of the concentration dependence are -2.3 and -2.2 when the absolute temperature is doubled from 800 K to 1600 K. This suggests that at these low concentrations, the defect free bulk thermal conductivity temperature dependence of  $1/T$  is still valid; phonon-phonon scattering still dominates over the phonon-defect scattering. At higher concentrations ( $x > 0.025$ ), however, there is no useful model available and a more sophisticated theory is needed.

Further analysis was performed using the LD calculations. The resulting picture was consistent with the Allen-Feldman theory of amorphous materials, and work on YSZ by Schelling *et al.*<sup>160</sup>. From the participation ratio analysis, most of the vibrational modes are found to be delocalized. The only case where there was some localization was observed was  $x=0.125$  at around 27-28 THz. However, the fraction of modes localized is still a small portion of the entire vibrational modes. Polarization analysis did not show a clear transition frequency between propagon and diffuson modes, but it is determined to be in between 1.5 and 10 THz.

This study showed that the  $\text{UO}_2$  with anion vacancies and interstitials do not hinder the heat transfer by the localization of vibrational modes. Although the thermal conductivity is reduced by ~60 % for high concentration of oxygen interstitials, the reduction comes from the low diffusivity of the diffuson modes. At low concentrations of  $|x| < 0.020$ ,  $\kappa$  decreases with

increasing temperature just like a single crystalline bulk  $\text{UO}_2$ ; therefore, the phonon description appears to remain valid.

As a final remark, it is worthwhile noting the effect of extrinsic point defects. There are several forms of fission products present in nuclear fuel material: solid solutions, dispersions and fission gases. Fission products forming solid solutions lower the thermal conductivity of  $\text{UO}_2$  by becoming mass defects or straining the host crystal, thereby acting as scattering centers for phonons.<sup>36, 145</sup> The effect of formation of a second phase consisting of fission products is known to either increase or decrease the thermal conductivity depending on the type of the phase.<sup>36, 146</sup> Fission products are often metallic precipitates and their behavior depends on the effect of burn up.<sup>40</sup> Near the center line region, the relatively high temperature allows formation of 0.05 – 1  $\mu\text{m}$  metallic particles, and their electrical conductivity improves the heat transfer in  $\text{UO}_2$ .<sup>146, 149</sup> In a high burnup structure, the precipitates are often quite tiny (order of nanometers) and they contribute to phonon scattering and lower the thermal conductivity of the fuel. The effect of porosity has also been studied quite extensively. Again, there are different effects depending on the size of the pore. Micro-bubbles often found in the crystal lattice act as obstacles to the phonons. Larger porosities are commonly found at GBs and impede heat transfer. A very nice review on the topic of the effect of fission products on thermal transport is included in the work by Lucuta *et al.*<sup>36</sup>.

Table 6-1. Experimental and DFT values of the formation energies.

	$E_{\text{Exp}}$ (eV)	$E_{\text{DFT}}$ (eV)
O <sub>I</sub>	–	-2.9--2.5 <sup>131, 132</sup>
V <sub>O</sub>	–	6.1-6.7 <sup>131, 132</sup>
U <sub>I</sub>	–	7.0-7.3 <sup>131, 132</sup>
V <sub>U</sub>	–	3.3-4.8 <sup>131, 132</sup>
O Frenkel	3.1-5.4 <sup>22, 140, 161-165</sup>	3.6-3.9 <sup>131, 132, 166, 167</sup>
U Frenkel	8.5-9.6 <sup>140</sup>	9.5-12.6 <sup>131, 132</sup>
Schottky	6-7 <sup>140</sup>	4.9-6 <sup>131, 132</sup>

Table 6-2. Potential parameters for the short-range interactions in  $\text{UO}_{2\pm x}$ .

		$\text{O}^{2-}\text{-O}^{2-}$	$\text{U}^{4+}\text{-O}^{2-}$	$\text{U}^{5+}\text{-O}^{2-}$	$\text{U}^{3+}\text{-O}^{2-}$
$A_{ij}$	(eV)	9547.96	1761.775	2386.42	1165.65
$\rho_{ij}$	(Å)	0.2192	0.35643	0.3411	0.3786
$C_{ij}$	(eV·Å <sup>6</sup> )	32	0	0	0

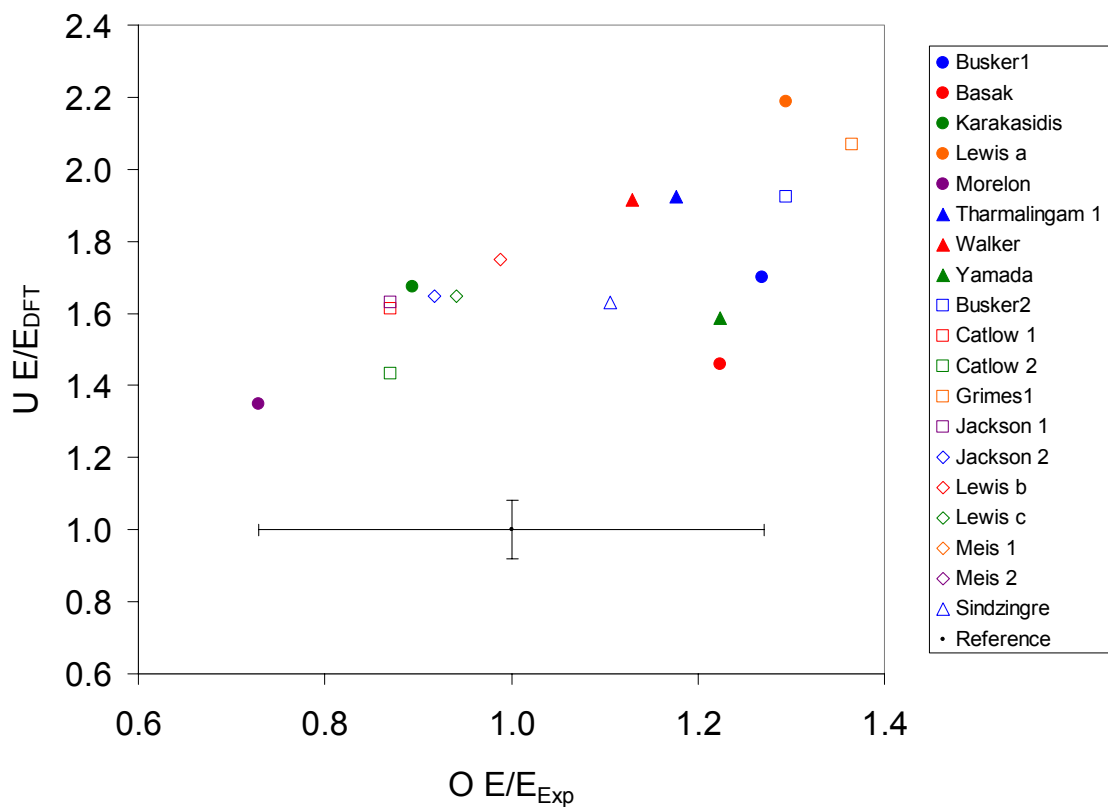


Figure 6-1. Normalized Frenkel and anti-Frenkel pair formation energies by empirical potentials. Filled symbols are the rigid ion models and open symbols are for the shell models. Uranium FP and oxygen anti-FP formation energies are normalized by the DFT and experimental values, respectively. All data except Busker1 are taken from the work of Govers',<sup>115</sup>

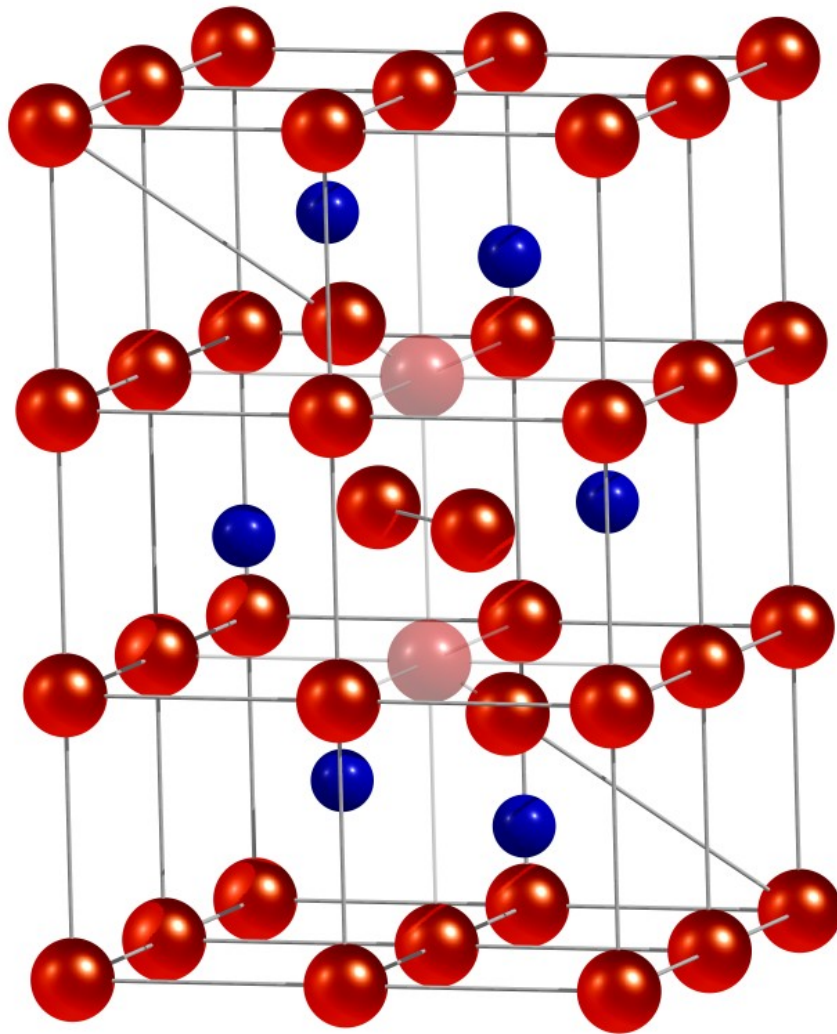


Figure 6-2. The 2:2:2 defect cluster in  $\text{UO}_2$ . Blue and red are uranium and oxygen ions; only the interstitial oxygens are shown. Faded red is used to indicate the oxygen vacancies. The lines are used to clarify the relative positions of the atoms.

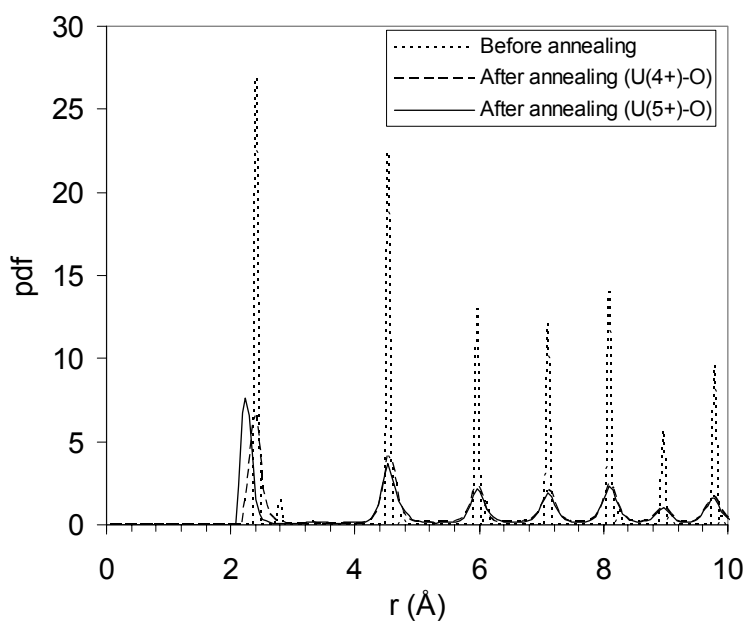


Figure 6-3. Pair distribution function between U-O in  $\text{UO}_{2.25}$ . Blue curve is the U-O PDF for both  $\text{U}^{4+}\text{-O}^{2-}$  and  $\text{U}^{5+}\text{-O}^{2-}$ . There is no difference before relaxation. The PDF for  $\text{U}^{4+}\text{-O}^{2-}$  and  $\text{U}^{5+}\text{-O}^{2-}$  after annealing are shown by red and green curves, respectively.

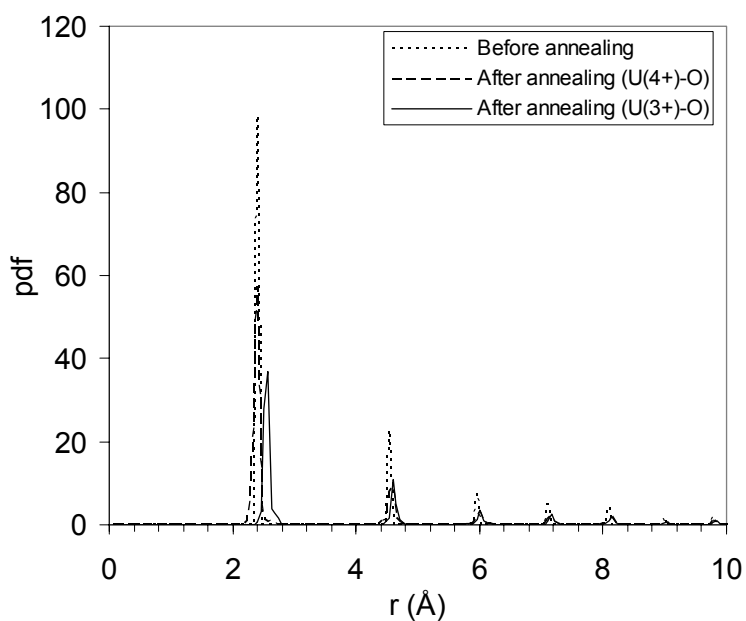


Figure 6-4. Pair distribution function between U-O in  $\text{UO}_{1.80}$ . Blue curve is the U-O PDF for both  $\text{U}^{4+}\text{-O}^{2-}$  and  $\text{U}^{3+}\text{-O}^{2-}$ . There is no difference before relaxation. The PDF for  $\text{U}^{4+}\text{-O}^{2-}$  and  $\text{U}^{3+}\text{-O}^{2-}$  after annealing are shown by red and green curves, respectively.

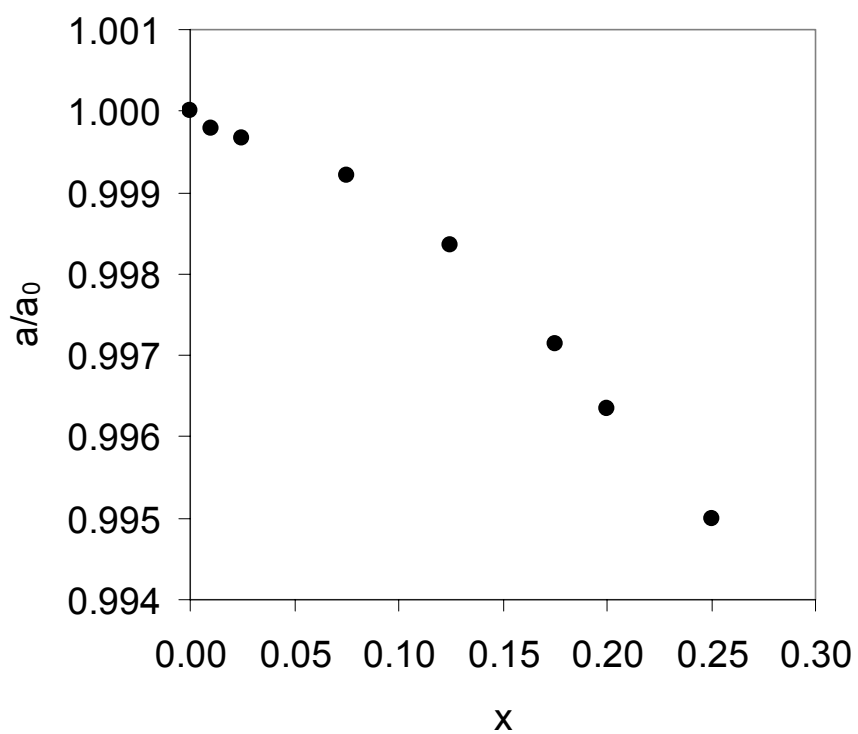


Figure 6-5. Normalized lattice parameter of  $\text{UO}_{2+x}$  as a function of defect concentration. The lattice parameters are given at 0 K after the high temperature annealing.  $a_0$  is the lattice parameter of  $\text{UO}_{2.000}$ .

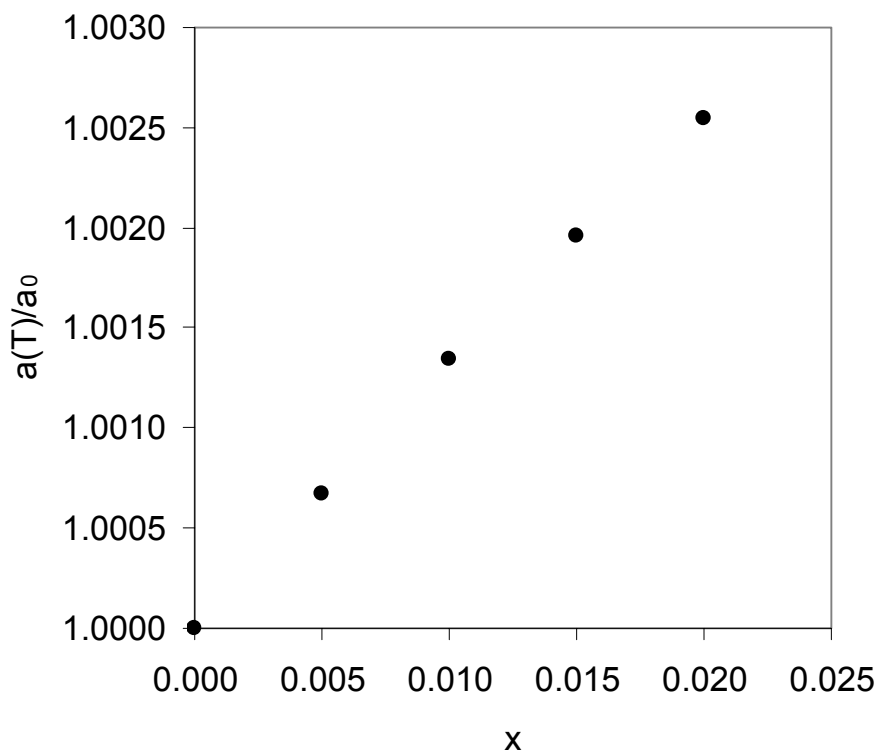


Figure 6-6. Normalized lattice parameter of  $\text{UO}_{2-x}$  as a function of defect concentration. The lattice parameters are given at 0 K after the high temperature annealing.  $a_0$  is the lattice parameter of  $\text{UO}_{2.000}$ .

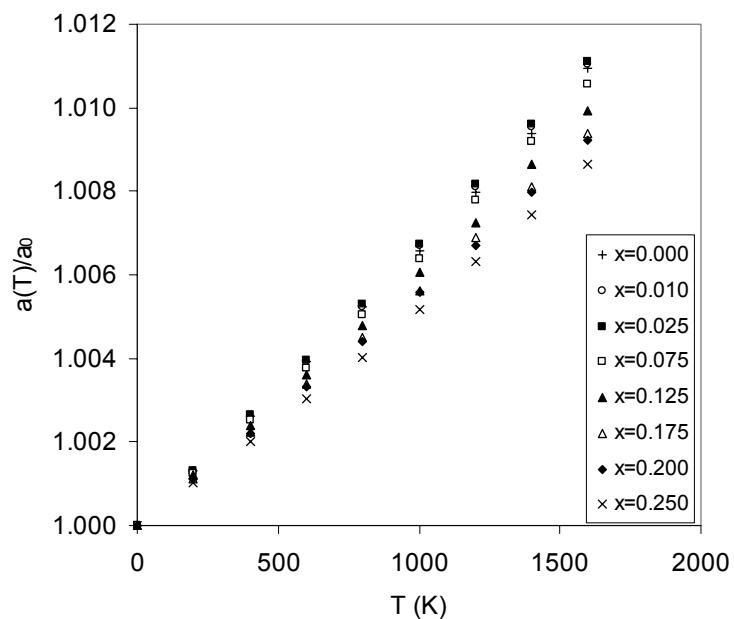


Figure 6-7. Thermal expansion of  $\text{UO}_{2+x}$ . Lattice parameters are normalized by the 0 K lattice parameter obtained from the chemical expansion.

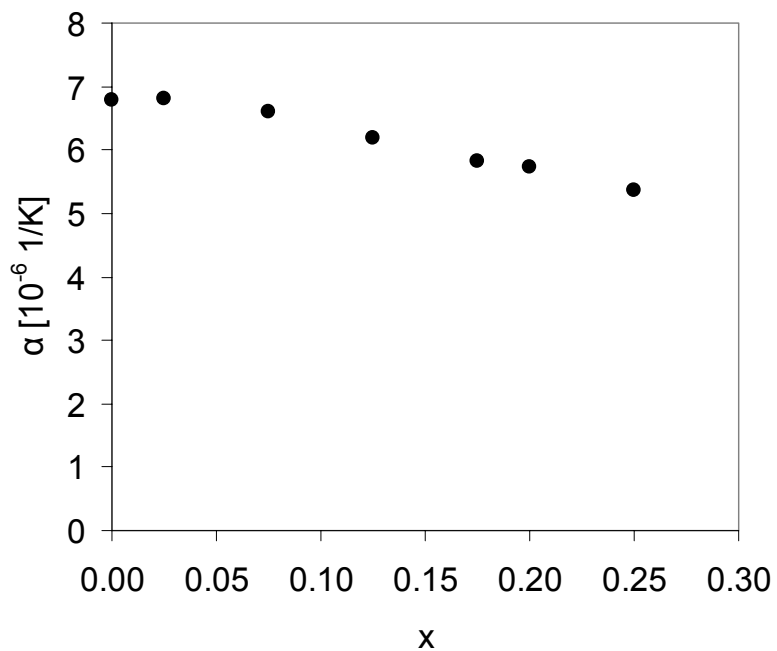


Figure 6-8. Thermal expansion coefficient of  $\text{UO}_{2+x}$  as a function of  $x$ .  $\alpha$  is obtained by a linear fit to the data in Figure 6-7.

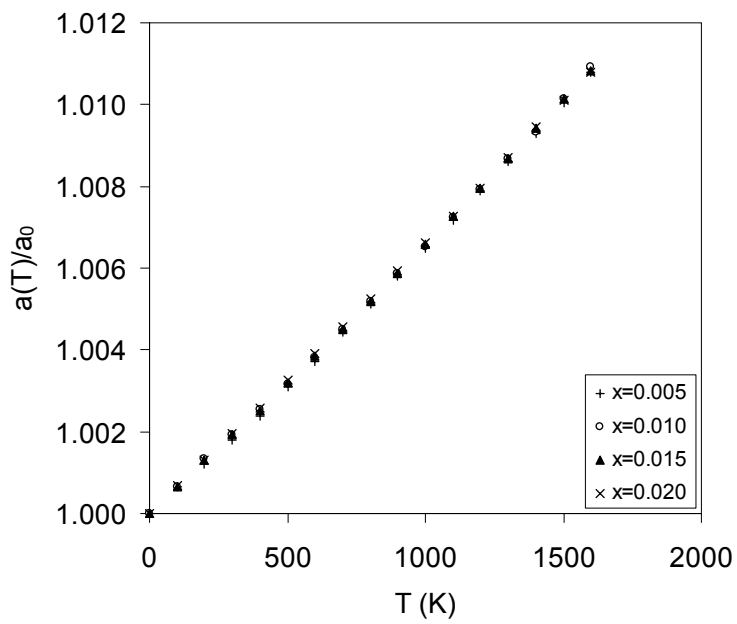


Figure 6-9. Thermal expansion of  $\text{UO}_{2-x}$ . Lattice parameters are normalized by the 0 K lattice parameter obtained from the chemical expansion.

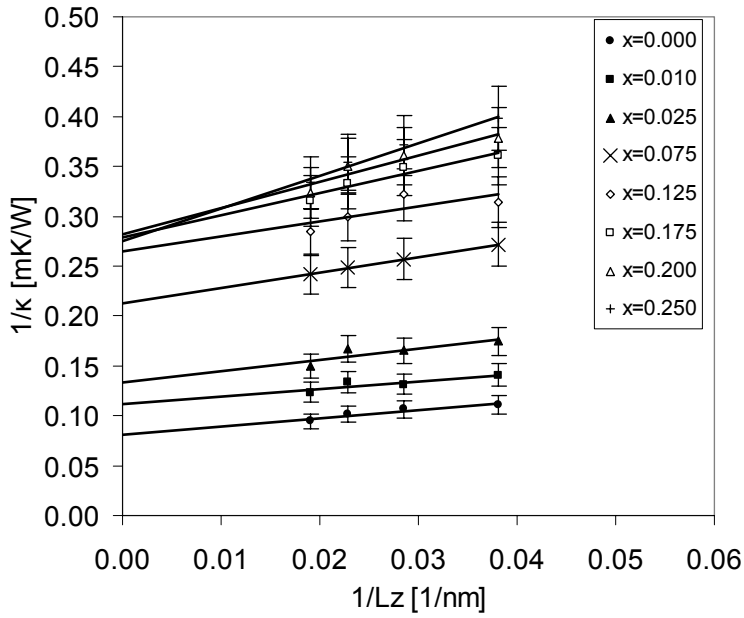


Figure 6-10. Inverse thermal conductivity of  $\text{UO}_{2+x}$  with various concentrations of oxygen interstitials as a function of simulation cell length at 800 K.

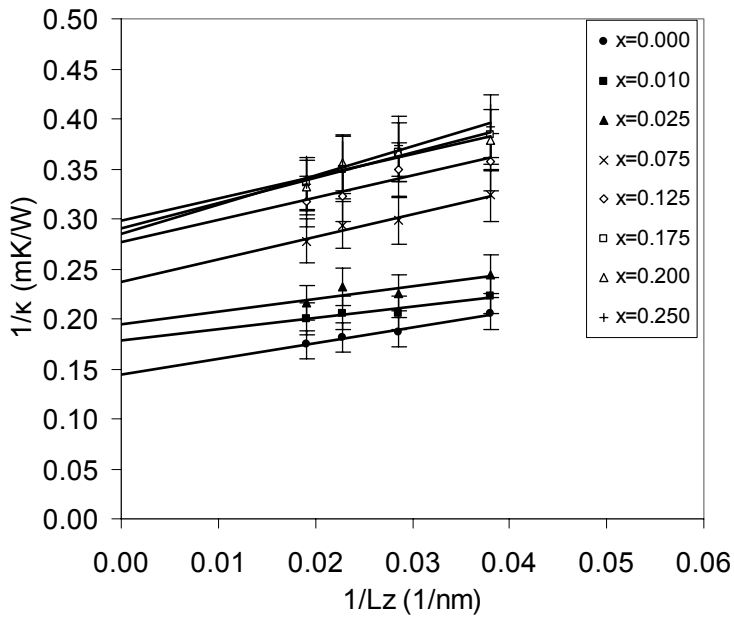


Figure 6-11. Inverse thermal conductivity of  $\text{UO}_{2+x}$  with various concentrations of oxygen interstitials as a function of simulation cell length at 1600 K.

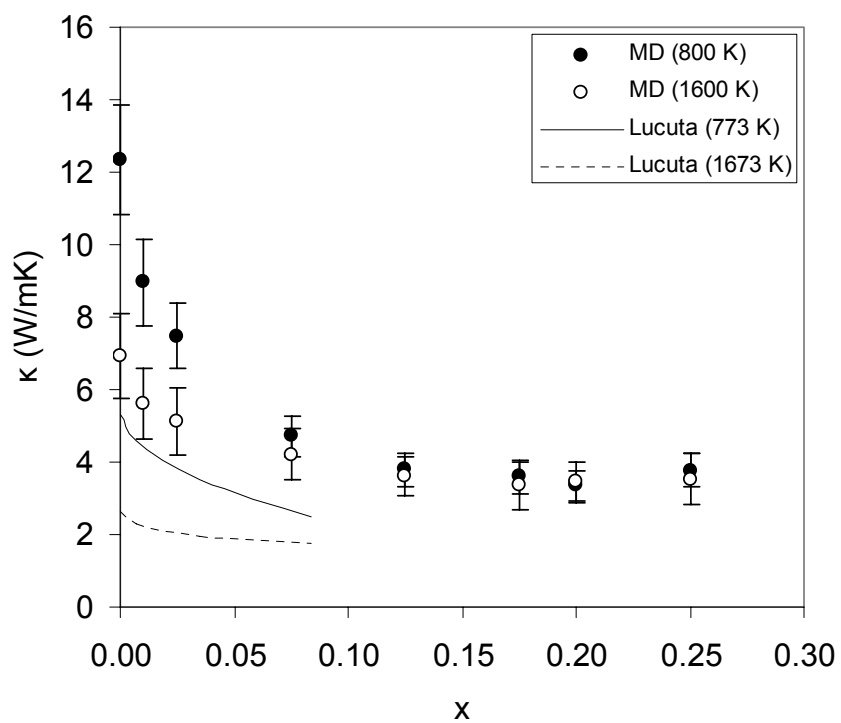


Figure 6-12. Bulk thermal conductivity of  $\text{UO}_{2+x}$  as a function of degree of off-stoichiometry without the anharmonic correction at 800 and 1600 K. The experimental data are obtained from Lucuta *et al.*<sup>149</sup>.

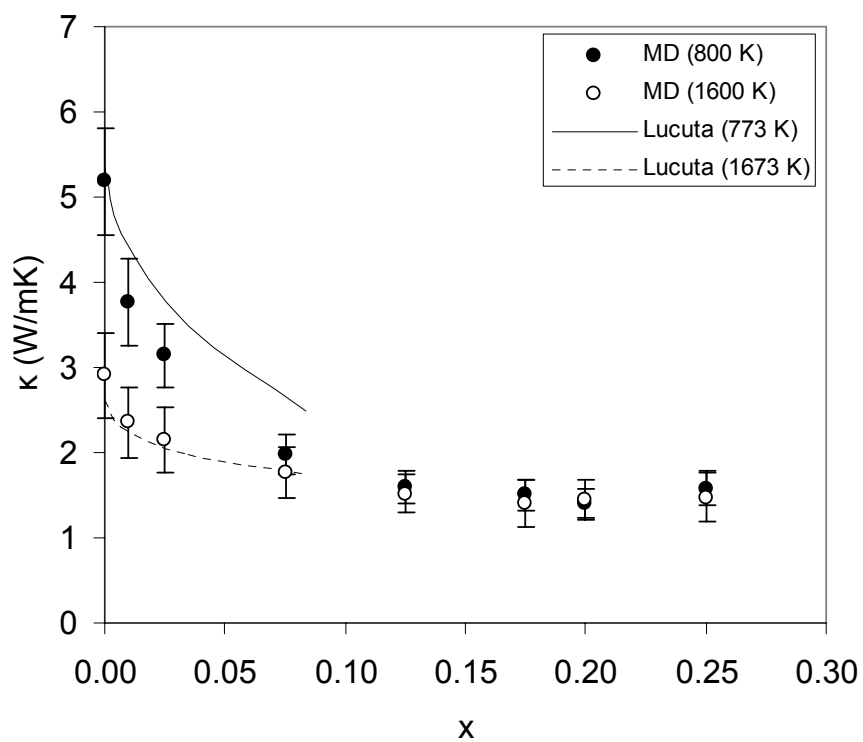


Figure 6-13. Bulk thermal conductivity of  $\text{UO}_{2+x}$  as a function of degree of off-stoichiometry with anharmonic correction at 800 and 1600 K. The thermal conductivity from MD simulations were rescaled by the anharmonicity correction.

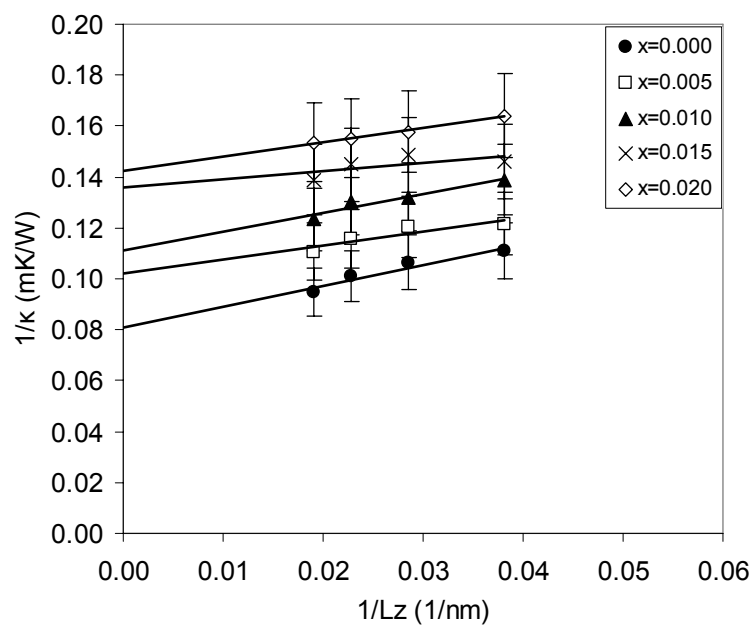


Figure 6-14. Inverse thermal conductivity of  $\text{UO}_{2-x}$  with various concentrations of oxygen vacancies as a function of simulation cell length at 800 K.

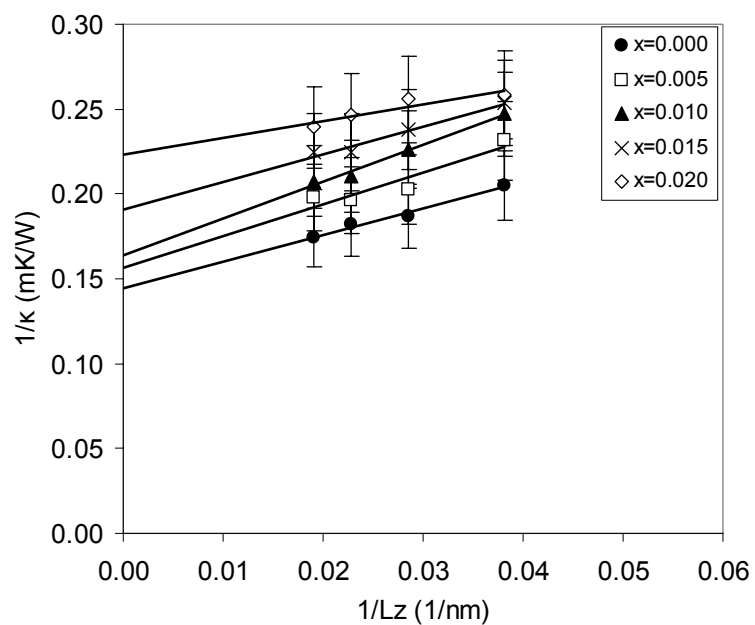


Figure 6-15. Inverse thermal conductivity of  $\text{UO}_{2-x}$  with various concentrations of oxygen vacancies as a function of simulation cell length at 1600 K.

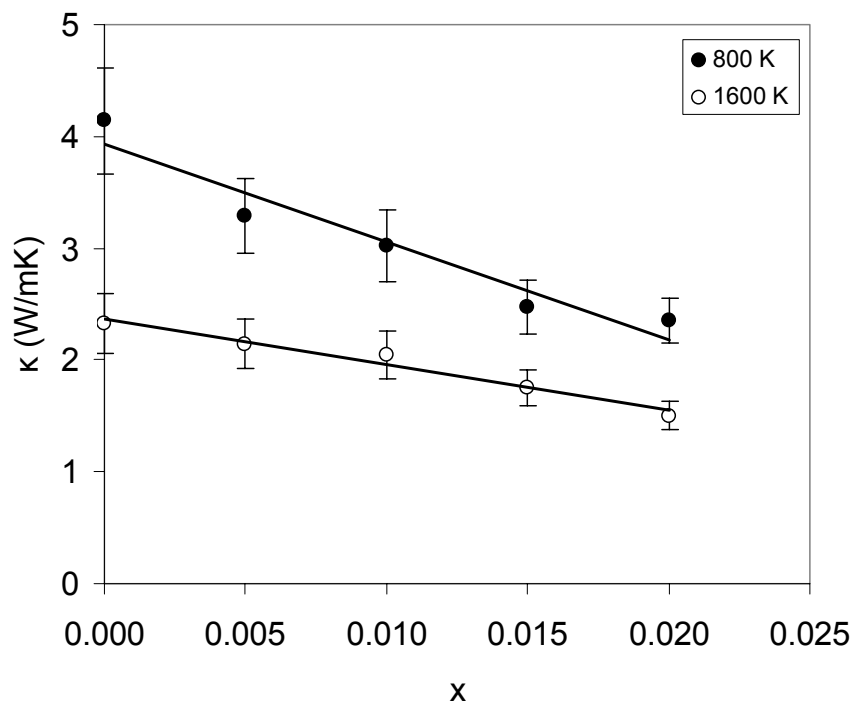


Figure 6-16. Bulk thermal conductivity of  $\text{UO}_{2-x}$  as a function of degree of off-stoichiometry at 800 K and 1600 K.

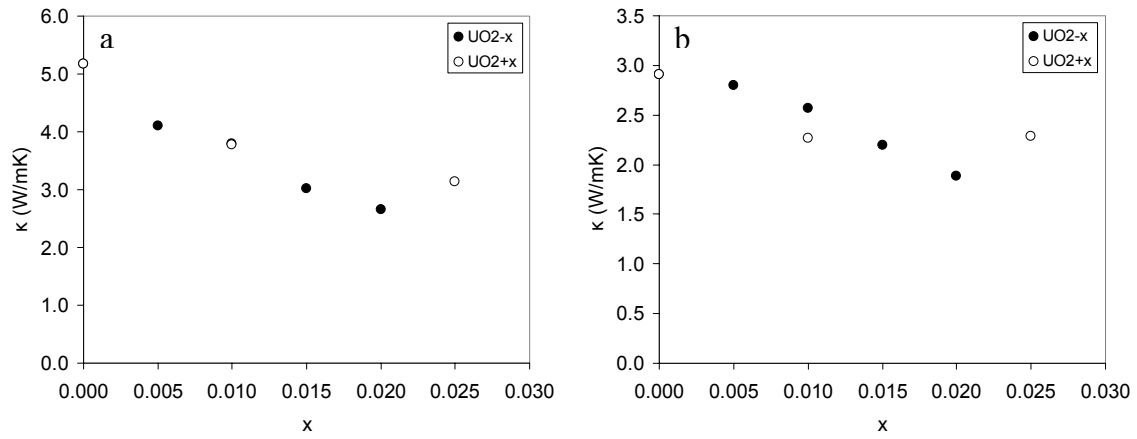


Figure 6-17. Thermal conductivity of  $\text{UO}_{2\pm x}$  as a function of degree of off-stoichiometry at 800 K (a) and 1600 K (b) for  $x \leq 0.025$ .

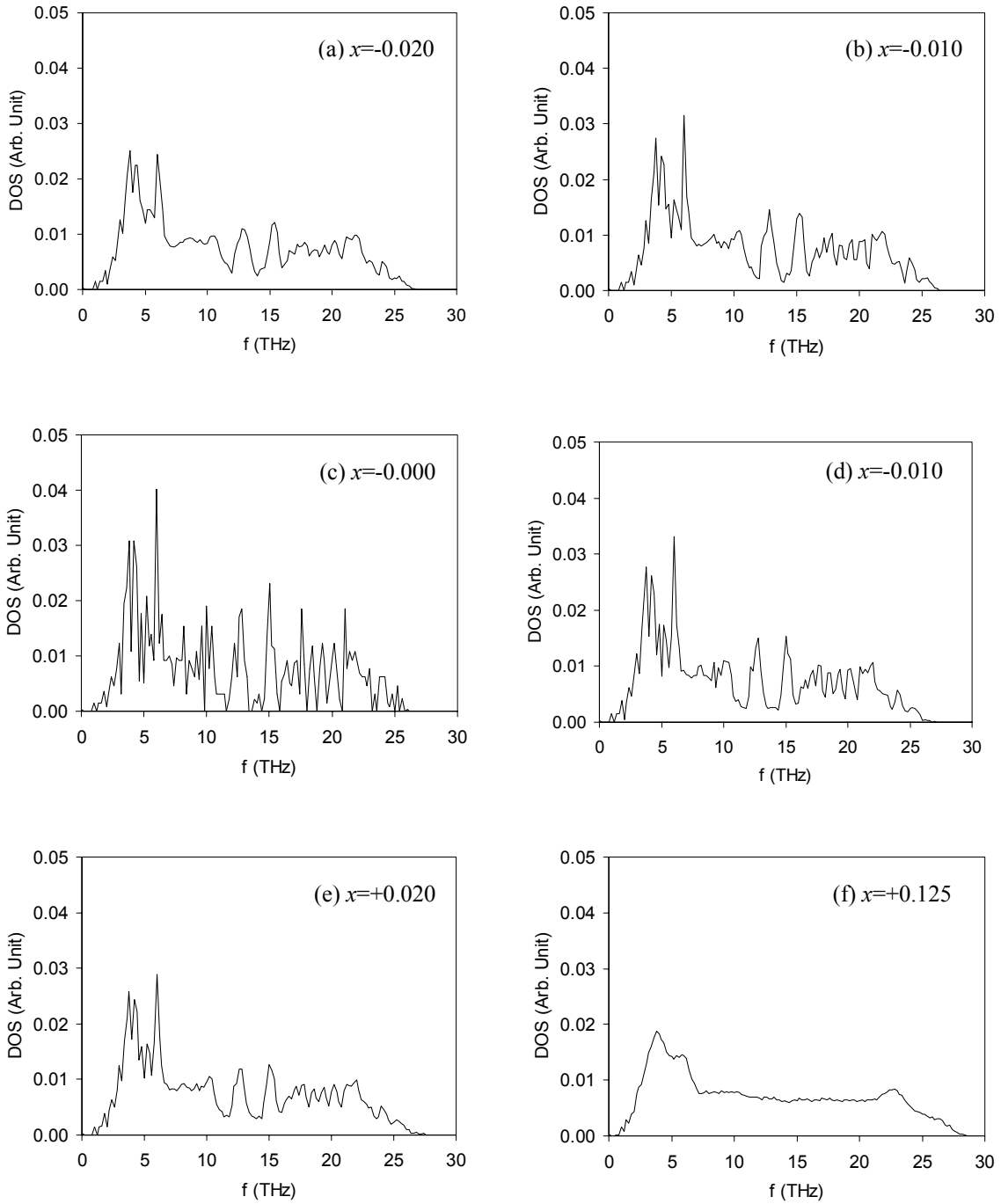


Figure 6-18. Phonon density of states of  $\text{UO}_{2+x}$  for  $-0.020 \leq x \leq 0.125$ . System size is  $6 \times 6 \times 6$  unit cells. The frequency bin size is 0.2 THz.

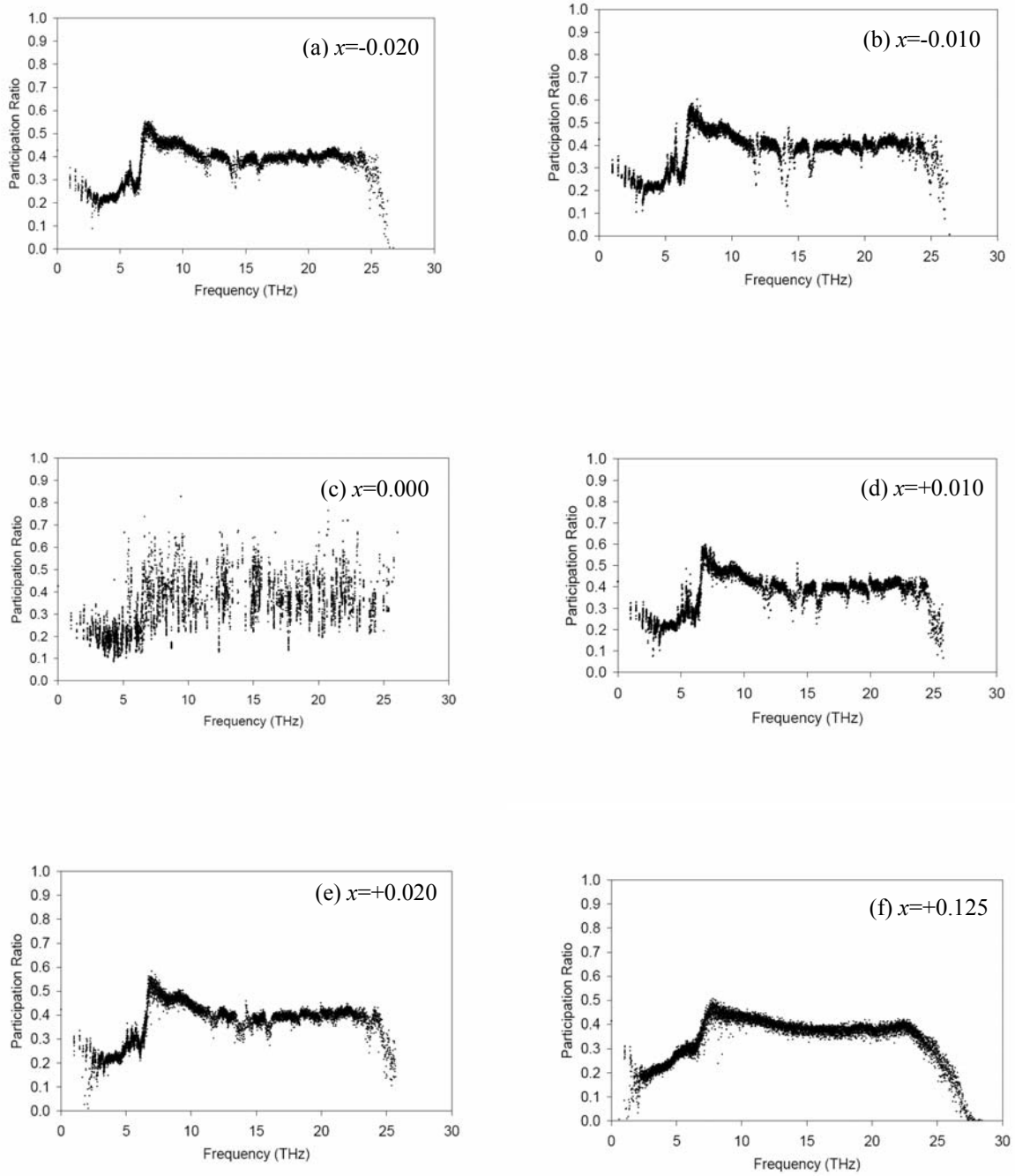


Figure 6-19. Participation ratios of  $\text{UO}_{2\pm x}$  for  $-0.020 \leq x \leq 0.125$ . System size is  $6 \times 6 \times 6$  unit cells. The frequency bin size is 0.2 THz.

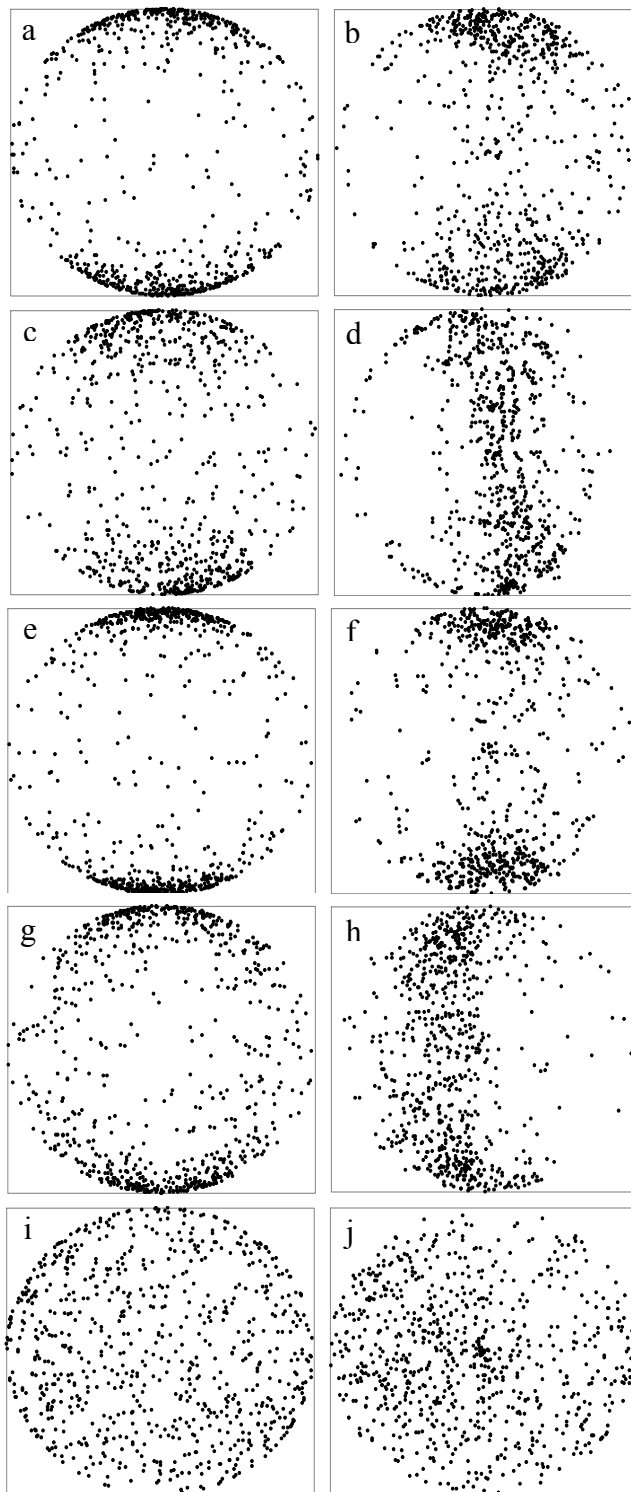


Figure 6-20. Projections of the polarization vectors of vibrational modes in  $\text{UO}_{2\pm x}$  at 1.5 THz. Figures correspond to the defect concentrations of  $x=-0.020$  (a,b),  $-0.010$  (c,d),  $0.010$  (e,f),  $0.020$  (g,h), and  $0.125$ (i,j). Left figures are direct projection, and the right figures are the equal-area projections.

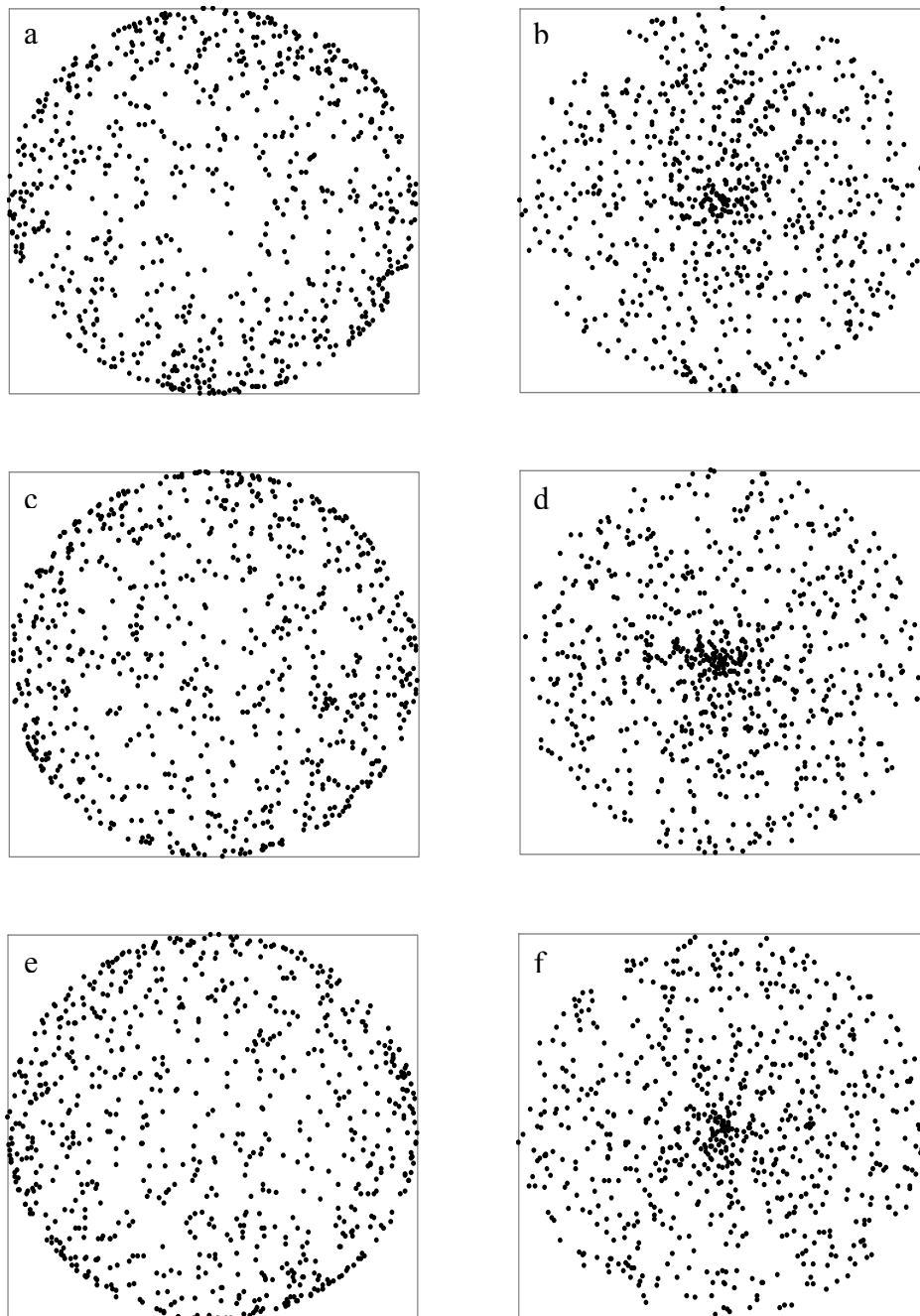


Figure 6-21. Projections of the polarization vectors of vibrational modes in  $\text{UO}_{2+x}$  at 10 THz. Figures correspond to the concentrations of  $x = -0.020$  (a,b),  $0.020$  (c,d), and  $0.125$  (e,f). Left figures are direct projection, and the right figures are the equal-area projections.

## CHAPTER 7 METHODOLOGY FOR THE SIMULATION OF RADIATION DAMAGE IN UO<sub>2</sub>

### **Introduction**

In nuclear fuel materials such as UO<sub>2</sub>, it is extremely important to consider the effects of radiation when assessing the performance in both operating and storage conditions. However, the complexity of the processes occurring under irradiation makes it very difficult to decouple each phenomenon and to understand the mechanisms of certain processes. For instance, high energy radiation causes the atoms to be knocked off their lattice sites. Because of the high energy deposited by the radiation into the solid, extreme local temperature and pressure gradients can be created, with atoms diffusing accordingly. The local thermal transport properties will also be altered. At the same time, radiations can also cause electronic excitations and can initiate chemical reactions. All these processes are entangled and the complexity is overwhelming. For this reason, simulations are a valuable tool to characterize the details of such processes, albeit with certain limitations depending on the methodology. MD simulation is one of the tools which allow investigation of highly non-equilibrium phenomenon such as radiation damage. However, the conventional MD algorithm does not work in such extreme conditions and some modifications are required. This chapter, therefore, establishes a methodology for the simulation of the radiation damage studies in UO<sub>2</sub> and presents the implementation and validation of a radiation damage simulation code. At least one of these methods, the form of the variable time step algorithm is completely new. While the other methods have been used previously, their applicability and their limitations have not been systematically established.

## Background

### Type of Radiation

Naturally occurring radioactive materials such as uranium, radium, and radon, are everywhere on the earth. Radiation also comes from space and constantly penetrates or is absorbed by the atmosphere. The natural background radiation is roughly 100 times greater than any of the human caused background radiations.<sup>61</sup> Man-made radiation sources are used for a number of applications including electrical power generation, medical imaging, radiation therapy, food processing, and weapons.<sup>61</sup> All the materials used in these applications must be designed to take account of the effects of radiation. In order to understand the effects of radiation, one must understand the different types of radiations that exist in nature. There are four types of radiations typically considered in nuclear applications: neutrons, alpha, beta, and gamma radiations.

Neutron radiation consists of a ray of energetic neutrons. The neutron is one of the two nucleons, the other being the proton, which are the building blocks of the nuclei of atoms. It has no electric charge, and has mass a mass of  $938.27 \text{ MeV}/c^2$  ( $1.6726 \times 10^{-27} \text{ kg}$ ).<sup>168</sup> Because of the absence of electric charge, neutrons often travel significant distance depending on the energy without interacting with other atoms.

Alpha radiation consists of the nucleus of a helium atom, i.e., two neutrons and two protons. It has charge of +2 and a mass of  $3.7274 \text{ GeV}/c^2$  ( $6.6447 \times 10^{-27} \text{ kg}$ ).<sup>61</sup> It is produced by radioactive decay processes and changes the atomic number of the atoms involved. Alpha radiation does not propagate a long distance because of the relatively large charge and mass.

Beta radiation is electrons or positrons released during certain types of radioactive decays, called beta decays. The decay processes involve ionization of the decay products because of the loss or gain of electrons.

Gamma ray is the radiation of high energy electromagnetic waves (photons) produced during radioactive decay. In contrast to the other types of radiation, this radiation involves transition of the energy levels of atoms. Quite often atoms produced through alpha or beta decays are in excited states. When the excited atoms transition from their energy levels to lower energy states, the excess energy is released in the form of energetic photons. A simple example is  $^{60}\text{Co}$  decaying to  $^{60}\text{Ni}$  through beta decay with the half life of 5.27 years.<sup>169</sup> The gamma radiation from this decay process is commonly used in medical and industrial applications.

All these different types of radiation occur in nuclear materials and can change the materials properties.

### **Fission and Radiation**

Nuclear power reactors for electrical power generation today involve fission reactions. Fission reactions are created by neutron radiation to fissile elements. When a neutron collides with the nucleus of a fissile element, the nucleus can split into nuclei of lighter elements and produces more neutrons. A good example is the fission of  $^{235}\text{U}$ .  $^{235}\text{U}$  is the only naturally occurring stable fissile element on earth. This is the reason that the uranium is used for nuclear fuel. A representative fission reaction of  $^{235}\text{U}$  is,



In this reaction, with one incident neutron, 2 neutrons are produced. There are a number of fission reactions which result in producing more than one neutron from a single incident neutron. Consequently, the number of neutrons can increase like an avalanche or chain reaction to sustain the reactions. The energy released during the fission reactions dissipates as heat and can be used to produce electrical power. Many of the fission products (FP) are unstable and spontaneously

decay into lighter elements including radioactive ones. Subsequent decays of these FPs produce  $n$ ,  $\alpha$ ,  $\beta$ , and  $\gamma$  radiations.

### **Fission Products and the Type of Stopping**

Before going into the specifics of the radiation effects in  $UO_2$ , the general concept of energy loss process of energetic particles in solid must be introduced. Energetic particles in a solid can lose their energies by either collision with nuclei or electrons. A projectile ion (often referred to as primary knock-on atom, or PKA) in a solid can collide with the ions in the solid. The energy transfer between the ions depends on the mass, charge, and momentum of both PKA and the target ion. While the PKA passes through the solid, the matrix atoms recoil and absorb energy, and the PKA is deflected. This process is described by the nuclear-nuclear collisions and the collision is elastic. In addition to colliding with the nuclei, the atoms can collide with electrons. The nature of electronic energy loss is rather complex and the following factors must be considered:

- Direct energy transfer by electron-electron collisions
- Excitation or ionization of target atoms (promotion of localized electrons)
- Excitation of transition in the band structure (promotion of weakly localized or free electrons)
- Excitation, ionization, and electron capture of the projectile ion itself

There are several well-known electronic energy loss models with different assumptions on the charge distribution,<sup>170-172</sup> however, the details of these models are beyond the scope of this work.

## Previous Experimental Studies on Radiation Damage in UO<sub>2</sub>

The effect of the radiation is determined by its type.  $\beta$  radiation causes ionization of the surrounding matrix and is responsible for chemical reactions, bond rupture, valence changes, formation of oxygen bubbles, etc. Their effect is mainly chemical in nature and produces very little structural damage. Regarding damage to the structure,  $\alpha$ -decays are most detrimental in the fissile fuel matrix. A typical  $\alpha$ -decay process produces a high energy  $\alpha$  particle of  $\sim 5$  MeV, with the daughter atom receiving a recoil energy of  $\sim 0.1$  MeV<sup>173, 174</sup>. An  $\alpha$ -particle loses its energy mostly by electronic stopping, thus causing ionization; it loses only a small portion of the energy for atomic displacement. By contrast, heavy recoil atoms from  $\alpha$ -decays lose almost all of their energy by nuclear stopping and generate roughly 90 % of the lattice damage in the fuel matrix<sup>173, 174</sup>. Because of the differences in the energies and masses,  $\alpha$ -particles and the recoil atoms have different ranges of propagation.  $\alpha$ -particles often travel from 20 to 30  $\mu\text{m}$ , but the recoil atoms travel only about 25 nm.<sup>173, 174</sup> This implies that the damage from the recoil atoms is spatially localized, but the damage from  $\alpha$ -particles is dispersed. The effects of such structural damage on nuclear reactor fuel significantly affect its physical and chemical properties. However, the details of such effects have never been characterized in detail. Furthermore, there is no satisfactory model for the defect production and annihilation mechanisms.

Neutrons also occasionally collide with the lattice atoms, but they are not as effective as charged particles especially at the energy range typical in typical fission reactors. Therefore the direct collision of neutrons to non-fissile elements is rare and hardly damages the structure. The only way neutrons can contribute to structural change is through the fission reactions<sup>173</sup>. In fact, the energy dissipated by the slowing down of the fission products is the major source of thermal energy for the electrical power generation in the nuclear fission reactors.<sup>11</sup>

In  $\text{UO}_2$ , the high energy fission products lose most of their energy by electronic stopping. Therefore, a significant thermal effect is expected because  $\text{UO}_2$  is an electrical insulator; the energy deposited by the electronic stopping cannot dissipate like that of free electrons in metals. Roughly 30 % of the energy is lost in instantaneous X-ray radiation and elastic waves, and the rest is transformed into heat which is referred to as the thermal spike.<sup>173, 174</sup> The thermal spike has several effects, including generating a significant local temperature and pressure gradient, causing surrounding atoms to diffuse. This extreme temperature and pressure gradient is known to cause the formation of the  $\text{U}_4\text{O}_9$  phase in  $\text{UO}_2$ .<sup>173, 174</sup> The thermal spike also allows the recovery of defects formed by the impact of highly energetic atoms. The recovery process is more significant in  $\text{UO}_2$  than in UN or UC, both of which are electrically conductive materials. Figure 7-1 is an Arrhenius plot of the cation diffusion coefficient in  $(\text{U,Pu})\text{O}_2$ ,  $(\text{U,Pu})\text{N}$ , and  $(\text{U,Pu})\text{C}$ . In all three materials, the curve is strongly temperature dependent for temperatures above  $\sim 1100$  °C indicating that the diffusion process is thermally activated.<sup>173</sup> However, below 1100 °C, the self-diffusion coefficients are independent of temperature and much higher than that of thermal diffusion. Detail of how the diffusion of cations takes place in this regime remains unclear. It has been postulated that because of the extremely high temperature and pressure of the fission spike uranium atoms diffuse through the core of the displacement cascade.<sup>173</sup> It should be noted that the order of diffusion coefficients is  $D(\text{UO}_2) > D(\text{UN}) > D(\text{UC})$ , which is opposite to the order of their thermal conductivities.

Some experimental studies have been performed on simulated fuel and ion implantations rather than the actual fuel samples.<sup>175-178</sup> These studies show a consistent picture of the effect of radiation damage on the stability of the crystal structure, and in producing significant changes in the lattice parameter. Recently Ronchi *et al.*<sup>178</sup> reported the effect of fission fragment on  $\text{UO}_2$

single crystal film. Despite the extremely high energy ( $\sim 80$  MeV) of the fission products, no significant structural change was observed; however, the  $U_4O_9$  phase was present in the sample after the irradiation. Ronchi *et al.*<sup>178</sup> attributed the very small structural damage to the shock wave produced in  $UO_2$ , which is unloaded on the free surfaces.

The above experimental studies show the unresolved issues in the radiation damage of  $UO_2$ . It is not clear how the athermal diffusion of U atoms occur in the radiation environment. How does the recovery process take place to heal the crystal at such high energy irradiation? What is the role of oxygen ions in such processes? Are these processes affected by the presence of defects such as point defects, dislocations, and GBs?

### **Previous Simulation Studies on Radiation Damage in $UO_2$**

A number of simulations have been performed to investigate radiation damage in solids, especially metals and oxide materials. Simulations of radiation damage were pioneered by Gibson *et al.*<sup>179</sup> They studied the effects of PKA energy and direction on single crystal copper. Later extensive development on the simulation method was done by Harrison and his collaborators<sup>180-183</sup> for the application of sputtering studies on Si and metal surfaces. During the time of Gibson and Harrison, the availability of the computational power was limited and their studies were restricted to small systems ( $<1000$  atoms) with simple interatomic potentials. Consequently, the energy of PKA had to be low ( $\sim$  a few 10s of eV). As more computational power became available, the area flourished. Today atomistic simulations of radiation damage are routinely performed on metals, oxides and semiconductors using the state-of-art interatomic potentials.<sup>184-189</sup>

The first MD simulation of radiation damage in  $UO_2$  was done by Van Brutzel *et al.*<sup>190</sup> They developed their own  $UO_2$  potential based on the defect formation energies of U and O defects.<sup>191</sup> The potential was a Buckingham type rigid-ion potential consisting of three radial

sections. They performed the radiation damage simulation in single crystalline  $\text{UO}_2$  from a few keV<sup>190</sup> up to 80 keV<sup>192</sup>. They investigated the defect structure and the number of displaced atoms. There was no correlation between the number of defects produced and the directions of PKA. The number of Frenkel pairs produced as a function of PKA energy showed that the exponent is  $\sim 0.9$  rather than the Norgett-Robinson-Torrens linear dependence.<sup>193</sup> They have also performed simulations to investigate the effect of cascade overlap. They found that the number of Frenkel pairs formed saturated after 7<sup>th</sup> PKA irradiation. The PKA dose rate of 0.79 keV/ps perhaps is unrealistically high since the defects recombination may take place on a much longer time scale. Furthermore their defect identification method is different in different publications,<sup>190, 192</sup> and a number of technical issues associated with the thermostat and variable time step algorithm are not addressed.

### **Implementation of the Molecular Dynamics Simulation Code**

As discussed in the previous section, there a number of issues to be resolved in the effects of radiation damage on  $\text{UO}_2$ . Although it is impossible to capture all the physical and chemical properties well by any simulations, simulation approaches have the advantage of having complete control over the material. In particular, MD simulations allow us to follow the highly nonlinear dynamic process of the defect production and annihilation by the radiation damage which occurs in very short time (order of pico-seconds) with atomic resolution. Since standard MD simulation codes are not capable of simulating extreme radiation condition, some significant modifications are needed. The algorithm and implementation of such modifications are described in the following.

### **Universal Ziegler-Biersak-Littmark Potential**

During high energy collisions of atoms which occur in a radiation environment, two atoms can get extremely close (typically  $\sim 1$  Å or less) compared to the normal distance given by

the thermodynamic equilibrium. Standard interatomic potentials are not designed to adequately describe the interatomic interactions at such short distances. For example, the commonly used Buckingham type potential has the functional form given in Equation 3-8:

$$V(r_{ij}) = A_{ij} \exp(-r_{ij} / \rho_{ij}) - \frac{C_{ij}}{r_{ij}^6}.$$

The second term, which represents the van der Waals interaction, goes to negative infinity when  $r$  goes to zero although the first exponential term remains finite. This means that the atoms collapse to a singularity if they are brought very close to each other. This is illustrated in Figure 7-2, which shows the plot of the Buckingham potential for O-O interaction with the Yamada model. It can be seen in Figure 7-2 that without the ZBL potential, the height of the potential energy barrier of the Buckingham potential is only about 260 eV or so, and a rather low energy PKA can overcome this barrier. This low barrier is an artifact of the functional form of the interatomic potential since we know that the repulsion of the electron clouds should prevent this. Another example is the electrostatic interaction: the attractive electrostatic interaction between two oppositely charged atoms also goes to negative infinity as  $r$  approaches 0. In typical MD simulations, however, these singularities does not cause an problems due to small atomic displacements; however, once the force on an atom becomes very large, the atom will jump unrealistically large distance in a single step. (An exception is when the time step size is allowed to vary according to the force on the atom. If the time step is adjusted according to the force, the two atoms will keep approaching to the singularity indefinitely. The method of variable time step is discussed below.) Even if such catastrophic failure does not happen, it is possible for the potential to fail in a rather subtle manner by giving unrealistic potential energies. Empirical potentials in general are fit to the bulk properties of the materials to reproduce the static and dynamic behavior of the materials near equilibrium. These potentials are therefore not meant to

reproduce the realistic potential energy surface in extreme conditions such as high energy collisions. A more realistic model of the very short-ranged interaction was given by Ziegler, Biersak and Littmark (ZBL).<sup>194</sup> They found from two body collision experiments of a large number of elements that the interatomic interaction can be simplified in a universal form, which may be applied to any element in the periodic table. This potential, referred to as the Universal ZBL potential, is based on the models of Thomas-Fermi and Linhard.<sup>195</sup> The ZBL potential is in fact a screened electrostatic potential of the nucleon-nucleon interaction:

$$V(r) = \frac{Z_1 Z_2 e}{r} \Phi(r). \quad (7-1)$$

$Z_1$  and  $Z_2$  are the atomic numbers of the atoms in collision,  $e$  is the electron charge, and  $r$  is the interatomic distance.  $\Phi(r)$  is the screening function,

$$\Phi(r) = \sum_{i=1,4} A_i \exp(-b_i r / a_u). \quad (7-2)$$

$A_i$  and  $b_i$  are predefined parameters, whose values are given in Table 7-2.  $a_u$  is the length scale given by,

$$a_u = \frac{0.8854}{Z_1^{0.23} + Z_2^{0.23}} a_{Bohr}. \quad (7-3)$$

And  $a_{Bohr}$  is the Bohr radius, 0.539177 Å. Details of the derivation of this potential is given in the literature.<sup>194</sup>

Since the ZBL potential is intended to operate only at very short distances and the Buckingham potential works well for near-equilibrium separations, it is important to know how to connect these two potentials. Unfortunately, there is no unique way to define where the transition between the two potentials should occur, although in reality there is a single potential energy surface for a pair of atoms. The standard approach is to connect the Buckingham and ZBL potentials by a spline of the exponential of a polynomial of the form,

$$V(r) = \exp(f_0 + f_1 r + f_2 r^2 + f_3 r^3 + f_4 r^4 + f_5 r^5). \quad (7-4)$$

The  $f_i$  are constants determined by matching the  $V(r)$ ,  $dV(r)/dr$ , and  $d^2V(r)/dr^2$  at the connection points to the ZBL and Buckingham potential. However, the choice of the spline region is arbitrary and depends very much on the atoms to be modeled. In principle, there is no need to use all the 6 parameters since the continuity of the 2<sup>nd</sup> derivatives are not required. However, in ionic solids, the gap between the ZBL and Buckingham can be quite large, unlike metals, and having the extra parameters can be helpful. (See the work by Fikar *et al.*<sup>196</sup> for the spline with 4 parameters for metals.) The values of the spline parameters and connection points that we have chosen for are given in Table 7-1.

How all the potentials are combined to form the MD potential is illustrated in Figure 7-2 for the case of O-O interaction. In order to show how the ZBL potential works, a simple simulation of an O-O collision is performed. In this demonstration, an oxygen atom is fixed at center of the simulation cell. Another O is simply placed 0.1 Å away from the center where the ZBL potential is active. Figure 7-3 shows the comparison of the trajectory of the O atom. With the ZBL potential, the atom simply is simply repelled by the potential of the O atom at the origin and rolls down the potential energy surface. By contrast, without the ZBL potential, the O atom is trapped in the potential well and violently rattles. In this simulation, the time step was fixed at 0.005 fs, but the interaction is so violent and the trajectory cannot be accurately calculated and eventually the atom escapes from the well. If the time step is small enough, the O atom will approach the origin and will fall into the singularity. Thus, the ZBL potential must be implemented in the radiation damage simulation.

## Variable Time Step Algorithm

Even when the ZBL potential is used, the interatomic forces can still be extremely large when two atoms are very close to each other. This still poses a major problem if a normal MD time step ( $\sim 1$  fs) is used. Such a large force on an atom can cause the atom to move a very large distance in a single step, resulting in very inaccurate trajectory. One solution to this problem is to use an extremely short time step size. However, for such a case, the simulation will take an unreasonably long time to complete. A better approach is to allow the time step to change during the course of the simulation. When an atom is highly energetic, the time step is automatically reduced. Once the energy is dissipated, the time step size is allowed to increase. This will allow accurate atom trajectories to be determined, while maximizing the time simulated. The common algorithm to do this in radiation damage simulation is to set a restriction on the maximum distance any atom can travel in a single MD time step from which the necessary time step size can be calculated<sup>197</sup>. The typical limit on the maximum distance for an atom to travel in a single step is  $<1$  Å. Although this algorithm has been extensively used,<sup>190, 192, 195, 198-200</sup> the accuracy of the atomic trajectories has not been clearly established.

We have therefore developed a new variable time step algorithm specifically designed to ensure that the trajectory of the energetic atoms is accurate. The original idea is taken from the orbit calculation of an satellite under a gravitational field described in the astrophysics literature<sup>201</sup>. Orbit calculations are known to require rather high accuracy; otherwise, the energy conservation deteriorates rapidly and the trajectory will be incorrect. This is because the differential equation to be solved is of a type called “stiff problem” in mathematics whose solution indicates rapid change in certain regions of the parameter space. The high energy collision of atoms also falls into this stiff problem category. The original algorithm of the adaptive time step method was applied to a purely two body interaction and the Runge-Kutta

method was applied to integrate the equation of motion.<sup>201</sup> In our in-house MD code, the scheme is modified to work with the 5<sup>th</sup> order Gear predictor-corrector integrator which is already incorporated for solving the equation of motion.

The idea is to calculate the trajectory of the most energetic atom in the system in two ways: one consisting of a single time step, the other consisting of two half time steps; see Figure 7-4 for the illustration of this process. The two half-step trajectory is in principle more accurate than the one large step. The two trajectories therefore should agree within the accuracy of the integration method used. If the discrepancy in the trajectory is smaller than the intrinsic accuracy of the integration method or of a user defined accuracy, then the time step used is adequate. However, if the discrepancy in the trajectory is too large, then the next trial time step size is determined based on the size of the discrepancy between the two trajectories. The whole process repeats until an acceptable time step size is determined. By performing this analysis for the most energetic (i.e., fastest moving) atom in the system, accurate trajectories for all other atoms are guaranteed. Moreover, since only the trajectory of the PKA is used in the analysis, the method is both fast and naturally parallelizable.

The implementation of this algorithm naturally follows the process of the Gear predictor-corrector integration scheme. First the most energetic atom in the system is identified by the predictor step, which is nothing but a calculation of the trajectory using the Taylor expansion:

$$\bar{x}(t + dt) = \bar{x}(t) + \bar{v}(t)dt + \frac{1}{2}\bar{a}(t)dt^2 + \dots \quad (7-5)$$

where  $x(t)$ ,  $v(t)$ ,  $a(t)$  are the position, velocity, acceleration of the atom at time  $t$ . This step is very fast, and the most energetic atom will give the largest displacement. Then the force calculation is performed using the predicted positions of the atoms as in standard predictor-corrector step, but the calculation is done only on the most energetic atom. Then the trajectory

of the energetic atom is corrected by the corrector step. Once the new position of the atom is determined using time step,  $dt$ , the code proceeds to calculate the same trajectory by two half steps. The entire process of the determination of the time step is shown in Figure 7-5 as a flow chart. The most expensive part of this scheme is the first half of the two small steps since this step requires the force calculation on all the atoms. In order to reduce the calculation, this step is done only on the near neighbor atoms. When the computation is done using multiple processors, this part of the calculation can be done on a single processor.

Another key step is the estimation of the new time step size. First the estimate of the time step is given by

$$dt_{est} = dt_{current} \times \left( \frac{\delta x_0}{\delta x} \right)^{1/6}, \quad (7-6)$$

where  $\delta x_0$  and  $\delta x$  are the user defined error of the trajectory and the calculated difference in the trajectories from the large and half steps calculations.  $\delta x_0/\delta x$  defines the error ratio of the trajectory.  $dt_{est}$  and  $dt_{current}$  are the new estimate and current time step size. The power 1/6 comes from the local truncation error being proportional to  $dt^6$  for the 5<sup>th</sup> order Gear predictor-corrector algorithm. The  $dt_{est}$  is merely an estimate and it is possible that this value becomes either extremely large or small. In order to avoid drastic change in a single iteration, a safety net is also applied:

$$dt_{new} = \begin{cases} S_2 dt_{current} & \text{if } S_1 dt_{est} > S_2 dt_{current} \\ dt_{current} / S_2 & \text{if } S_1 dt_{est} > dt_{current} / S_2 \\ S_1 dt_{est} & \text{otherwise} \end{cases} \quad (7-7)$$

$S_1$  and  $S_2$  are the safety factors set to 0.9 and 4.0, but the exact value is not critical. The important point is that  $S_1$  should be slightly less than 1.0 and  $S_2$  should be somewhat larger than

1.0. The more these numbers deviate from 1.0, the more aggressive the estimate of the new time step is.

In order to establish the validity of the variable time step scheme, the results of short test runs are compared with a fixed time step simulation with a small time step size. Figure 7-6 shows the trajectory of the PKA in a  $10 \times 10 \times 10$  unit cells single crystal  $\text{UO}_2$ . The PKA is 1 keV U in [100]; the statistical ensemble used was microcanonical, i.e., constant energy and constant volume. Each color in the plot corresponds to a specific error ratio as indicated in the legend. The trajectory from the fixed time step of  $dt=0.10$  fs simulation is indicated by the solid line. In order to obtain the base case scenario with the fixed time step simulation, a number of fixed time step runs were performed with different time step size. The time step size of 0.10 fs was determined to be sufficiently small for the generation of accurate trajectories in this case. Figure 7-6 clearly indicates that the variable time step can faithfully reproduce the base case trajectory if the error ratio is sufficiently small ( $\leq 10^{-4}$ ). In this simulation, the PKA traveled along the [100] direction and hit the adjacent U atom, transferring most of its momentum while small amount of the energy was dissipated to the rest of the system. This process continued during the entire 2 fs simulation. This process is apparent when the variable time step algorithm is used since the time step size is not uniform. When the collision occurred, the time step size decreased and thereby the density of the data points increased.

To explore the power of this variable time step algorithm, simulations with 80 keV U PKA were performed using the same simple model system. 80 keV is roughly the upper limit that we can handle in a more realistic simulation setup, because of the current limitations on the computational resources. Figure 7-7 shows the trajectories of the PKA obtained from the runs with three different error ratios and one fixed time step. Again, a number of fixed time

simulations were run prior to this comparison so as to determine the maximum time step size needed for the accurate calculation of the PKA trajectory. The result was that for 80 keV U PKA, the time step has to be at most  $1 \times 10^{-4}$  fs. The variable time step algorithm was able to successfully follow the fixed time step trajectory when the error ratio was  $1 \times 10^{-5}$ .

To analyze the efficiency of the variable time step scheme, the time evolutions of the time step size in the same 80 keV simulations were monitored. (See Figure 7-8.) With the variable time step, the time step size decreases when collisions occur. The decrease in the time step depends on the error ratio used in the simulation: the smaller the error ratio, the smaller the time step size at the collisions. The time step size reaches down to  $1 \times 10^{-4}$  fs, only when the error ratio is  $1 \times 10^{-5}$ . In between the collision events, the time step size can go up 3 orders of magnitude from  $10^{-4}$  fs to  $10^{-1}$  fs. This difference gives the gain in the efficiency of the variable time step scheme. In terms of the overall efficiency, the fixed time step simulation took approximately 208 min to complete 2 fs of the run, but the variable time step took only about 10 min: more than a magnitude of improvement in efficiency, with no loss in the fidelity of the trajectory.

### **Thermostat**

The last piece of modification needed in the MD code is in the control of the temperature of the system via the thermostat. During radiation damage, a large amount of energy is converted from the ballistic energy of the PKA to the thermal vibrations of the atoms in the entire system. In reality, when the PKA collides with the ions in the material, the ballistic energy is distributed over  $\sim 10^{24}$  atoms, and the energy dissipates at the rate determined by the material's thermal conductivity and the temperature gradient. However, MD simulations are limited by the number of atoms (typically less than a few millions of atoms for ionic materials). For such a small simulation cell this thermal energy can be overwhelming if the heat generated is not appropriately treated, even leading to melting of the system. Therefore to mimic the thermally

absorbing effects of a very large system, a thermostat is applied around the region of the simulation cell where all the interesting dynamics takes place (the called active region). Figure 7-9 shows the configuration of the MD simulation cell. Since the simulation cell configuration is a hybrid of NVE and NVT, this ensemble was dubbed the pseudo-NVE (or pNVE) by Corrales *et al.*<sup>200</sup>, and we will follow the same nomenclature.

The default thermostat in our in-house MD code is the velocity rescaling thermostat. However, this thermostat is rather primitive and is known to have some problems,<sup>98, 202</sup> the most prominent of which is that the statistical nature of the system is not canonical. In this thermostat, since the velocities of the atoms in the thermostat region are changed simply by rescaling the ratio of the target and current temperature,  $\sqrt{T_0/T}$ , the equation of motion is modified. Thus no energy and momentum conservation laws are obeyed. It also means that the Liouville theorem no longer holds and the phase space distribution function of the system is broken.<sup>203, 204</sup> Moreover, the ergodic theorem will not hold and physical observables cannot be calculated from the ensemble average.<sup>203, 204</sup> In short, it means that the dynamics of atoms in the thermostat region are not realistic. There are also other subtle problems as well. In particular, since the dynamics of the thermostat region is not correct, the atoms adjacent to the thermostat will not behave in a realistic manner; it is not clear how far this effect extends. Another problem is that since the velocity rescaling will take place every time step during the simulation, the rate of change in the temperature may depend on the time step size. Because of these problems, one should be very cautious when performing simulations using velocity rescaling thermostat.

There are other thermostat schemes which are known to work better.<sup>96, 98</sup> Among the available thermostats, the Berendsen thermostat was chosen for this study.<sup>205</sup> The Berendsen thermostat is also a type of velocity rescaling, but is both physically more reasonable and is

better founded in statistical mechanics. The Berendsen thermostat is derived from the same formalism as the Langevin thermostat<sup>205, 206</sup>. The idea of the Langevin thermostat is to couple the system with an imaginary heat bath in appropriate manner such that the system remains in the canonical ensemble.<sup>206</sup> The details of the derivation are given in Berendsen's original paper.<sup>205</sup> The Berendsen thermostat can be viewed as a first order approximation to the full Langevin approach. The way Berendsen thermostat adjusts the velocity is through a scaling factor,

$$\lambda = \sqrt{1 + \frac{dt}{\tau} \left( \frac{T_0}{T} - 1 \right)}, \quad (7-6)$$

where  $dt$  is the current time step size, and  $\tau$  is the user-defined time constant for thermal equilibration.  $T_0$  and  $T$  are the target and current temperature. From its form, it is clear that the Berendsen rescaling can be much gentler than the simple velocity rescaling. To illustrate the range of the strength of Berendsen thermostat, consider the two extreme cases. When  $\tau$  is infinity,  $\lambda=1$  and no rescaling is done; this corresponds to the microcanonical ensemble. When  $\tau=dt$ , then it is identical to the simple velocity rescaling. The beauty of the Berendsen thermostat is that since it is a simplification to the Langevin approach, it is approximately canonical and its strength can be controlled to minimize the disturbance to the system unlike the simple velocity rescaling scheme. Thus the dynamics of the system can be kept close to the realistic phase space distribution.

The Berendsen thermostat was implemented in the MD simulation code and several test runs were performed. Figure 7-10 shows the time evolution of the  $10 \times 10 \times 10$  unit cells single crystal  $\text{UO}_2$  using the Berendsen thermostat. The entire simulation cell was set to be in the thermostat region.  $\tau=400$  fs was used, based on the recommendation to use  $\tau=100$ -400 fs in the original work by Berendsen on simulations of liquid water.<sup>205</sup> We see that the thermal

equilibrium is clearly reached by 5 ps with very small fluctuation at the end. This indicates that the thermostat is correctly implemented.

In order to identify the appropriate value of  $\tau$  for the solid  $\text{UO}_2$ , NPT simulations with a wide range of  $\tau$  were performed on the thermally equilibrated single crystal structure at 300 K. The total energy of the system was monitored as a function of time (See Figure 7-18). The two extreme case of NVE and velocity rescaling simulations with  $dt=0.1$  fs are also included for the purpose of comparison. It is apparent that the velocity rescaling significantly interrupts the system and the the total energy violently fluctuates. With a small value of  $\tau$ , the Berendsen thermostat closely follows this behavior. As  $\tau$  increases, the behavior approaches that of NVE simulation. Since the system is thermally equilibrated to start with, the total energy should be constant. The variation in the total energy is quantified by the standard deviation and it is plotted as a function of  $\tau$  in Figure 7-12. Note that the abscissa is in log scale. The solid lines are used to indicate the trend and are extended to the limiting values of the NVE ensemble. The standard deviation in the kinetic energy increases with increasing  $\tau$ , and that of the potential energy decreases as  $\tau$  increases. The fluctuations in the kinetic and potential energy are actually correlated and out of phase. Thus these fluctuations cancel each other, and the the net fluctuation in the total energy is the difference of the fluctuations in the kinetic and potential energies. The variation in the total energy smoothly decreases with increasing  $\tau$ , and the drop is minimal after  $\sim 1000$  fs. This trend is very similar to that given in the Berendsen's original work on liquid water. Thus  $100 \leq \tau \leq 500$  fs is also applicable for the solid  $\text{UO}_2$ .

### **Defect Identification Method**

Before going into the analysis of the radiation damage simulations, the method of defect identifications must be described. The code used was developed by our collaborator Dr. Srinivasan G. Srivilliputhur in MST-8 at Los Alamos National Laboratory. Some minor

modifications were made to work for  $\text{UO}_2$  and to seamlessly integrate with our in-house MD code output files.

The identification method is to find defects in a structure by comparing the atom positions relative to the defect free structure. Figure 7-13 shows an illustration of this method. In this section, the defect free structure is structure A, and the structure with defects is structure B. To identify an interstitial, the analysis code looks through structure B and tries to find the corresponding atoms in structure A. Two atoms in the different structures are considered to be matched when they are within radius  $r_0$  of each other. If some atoms in structure B do not have any corresponding atom in structure A, then the atom in structure B is an interstitial. To find vacancies, the exact opposite is done; the code goes through structure A and look for neighbors of each atom in structure B. If there is no neighbor for some atoms, they are considered vacancies. Anti-site defects can be found in a similar manner.

The neighbor radius  $r_0$  is the critical parameter in this method. The results of analysis depend on the value of  $r_0$ , and this cannot be avoided if this algorithm is used. The dependence of the number of defects on  $r_0$  is characterized and discussed later.

### **Radiation Damage Simulations**

The ZBL potential, variable time step algorithm, and Berendsen thermostat have been successfully implemented and tested individually. Now all the methods are combined and applied to radiation damage simulations.

#### **Time Step Size**

The first step is to characterize the base case scenario using a fixed time step. The result from this simulation will be the foundation to validate the successful implementation of all the modifications together.

The radiation damage simulations with 1 keV U PKA were performed with varying fixed time step sizes. A single crystal  $10 \times 10 \times 10$  unit cells  $\text{UO}_2$  was used, and the simulation was done with NVE ensemble: no thermostat was applied. This small simple setup will provide an extreme case where the maximum time step determined here will be sufficient for 1 keV PKA in larger systems with thermostat. Figure 7-14 shows the vacancies of uranium and oxygen atoms produced during the simulation. The number of both U and O vacancies rapidly increased until 200 fs and then they heat plateau for  $\sim 300$  fs. The maximum numbers of U and O vacancies are roughly 20 and 80, respectively. Around 500 fs, the number of both vacancies decreased at varying rates. The numbers of U and O vacancies are exactly identical at each time step for  $dt \leq 0.1$  fs. Thus, 0.1 fs is sufficient for simulations with 1 keV U PKA.

The result from a variable time step simulation with the same system is also shown in Figure 7-14. The error ratio used is  $10^{-4}$  as determined from the preliminary runs (see Figure 7-6). The data is taken at the time interval of 10 fs. The result is identical to those of  $dt < 0.1$  fs, and this proves that the variable time step algorithm works.

After the maximum time step size was determined by the NVE simulations, pNVE runs were performed to show that the same time step can be used in pNVE. The system used was a single crystal  $22 \times 22 \times 22$  unit cells  $\text{UO}_2$  with 1 keV U PKA. The system size was chosen following van Brutzel's work<sup>190</sup>. A 1 unit cell thick Berendsen thermostat with  $\tau = 400$  fs was applied around the simulation cell. The initial location of the PKA was chosen to be  $(x,y,z) = (-6,0,0)$ , based on some trial and error to ensure that the defect cascade does not interact with the thermostat and boundary of the simulation cell.

As mentioned above, the number of defects counted in the analysis depends on the value of  $r_0$ . Figure 7-15 is the number of defects produced in the simulation with  $dt = 0.1$  fs as a function

of  $r_0$ .  $V_U$ ,  $U_I$ ,  $V_O$ , and  $O_I$  all decrease with increasing the size of radius  $r_0$  since the larger  $r_0$ , the higher the likelihood of finding neighbor in the corresponding structure. In addition, we see that the number of the vacancies and interstitials of the same species do not agree when  $r_0$  is greater than roughly 1.2 Å. The value of  $r_0$  is typically chosen to be slightly smaller than the half of the nearest neighbor distance in the perfect crystalline structure.<sup>186, 190</sup> In  $UO_2$ , the nearest neighbor distance is the distance between U and O atoms in 4a and 8c sites, which is  $\sim 2.37$  Å. The value of 1 Å seems to be appropriate. Thus, from hereon,  $r_0=1$  Å is used throughout.

Figure 7-16 shows the result of 4 different runs with  $dt=0.100$ , 0.050, 0.001, and 0.0001 fs. It turns out that the number of defects produced was not identical even with  $dt<0.1$  fs although they closely follow each other. This is because the time step size affects the way the thermostat draw energy out of the system. At least it suggests that the  $dt=0.1$  is sufficient of producing the same number of defects as the smaller time step size.

### **Berendsen Time Constant**

Now the time step size of 0.1 fs is used to characterize the effect of the thermostat. The same single crystal  $22\times 22\times 22$  unit cells  $UO_2$  with 1 keV U PKA was used to perform several radiation damage simulations in pNVE ensemble. The value of the time constant was changed from 1 fs to  $10^{-4}$  fs. The results from an NVE simulation are also included for comparison.

Figure 7-17 is the plot of how the temperature in the active region evolves with varying  $\tau$ . Initially the temperature starts out at approximately 380 K which corresponds to the energy of the 1 keV PKA in the thermally equilibrated system at 300 K. Then the temperature drops rapidly to  $\sim 330$  K in 370 fs. After that point, the behavior depends on the value of  $\tau$ . In the NVE ensemble, the temperature remain fairly constant around 330 K. As  $\tau$  decreases, the rate of cooling becomes faster. For  $\tau$  smaller than 100 fs, the temperature evolutions are almost identical and approach the target temperature of 300 K.

The change in the total energy is shown in Figure 7-18. Curves in this plot indicate how fast the energy is removed by the thermostat as a function of  $\tau$ . In the case of NVE, the energy remains constant, as it should. In real  $\text{UO}_2$ , the cooling rate is dictated by the thermal conductivity of the material, and the heat dissipates to the  $10^{24}$  atoms which are in thermal equilibrium at infinity. The cooling rate cannot go beyond the materials natural ability to transfer heat while keeping the thermostat at 300 K. Figure 7-18 clearly shows that the cooling rate is very similar for  $\tau \leq 100$  fs. On taking a closer look, fluctuations in the total energy is clear for  $\tau \leq 10$  fs. Thus  $\tau = 100$  fs is a good choice in terms of the fast cooling rate and minimal disturbance to the dynamics of the system.

Finally we compare the number of defects in the same set of the simulations. Figure 7-19 is the result. Reassuringly, the number of defects produced as a function of time is very similar in all the cases regardless of what value of  $\tau$  is used. This means that even if the thermostat is not applied, the number of the defects is not affected despite the higher final temperature. The final temperature ranges from 300 K to 330 K. This 30 K difference makes hardly any difference in the defect production and annihilation.

### **Statistics**

Since the defect production and annihilation process is a highly nonlinear stochastic process, simulations with slightly different conditions can result in somewhat different result. The difference in the initial condition can be minute differences in the atom positions and velocities. A good analog of this may be the billiard balls: a tiny difference in the relative positions and the amount of push you give can give quite different results. A solid crystalline well equilibrated structure is much more ordered than billiard balls and the variation in the results will not be completely chaotic. Nevertheless, it is necessary to characterize how much variation is expected when equivalent simulations were performed.

In order to characterize the variation, a single crystal  $22 \times 22 \times 22$  unit cells  $\text{UO}_2$  was used to perform 6 independent simulations. The PKA was 1 keV U atom but in each simulation, different U atoms were chosen. Their locations were  $(\pm 6, 0, 0)$ ,  $(0, \pm 6, 0)$ ,  $(0, 0, \pm 6)$  and in all cases the PKAs were pointing toward the center of the simulation cell. Figure 7-20 is the plot of the number of U and O vacancies produced during the 6 simulations. The error bars are used to indicate the standard deviation from all 6 simulations. The number of  $V_U$  with the standard deviation is approximately  $7 \pm 3$ . The same number for  $V_O$  is  $70 \pm 20$ . Therefore, there is a significant variation in the data even though the PKA directions are crystallographically equivalent. We speculate that this is the effect of small differences in the atomic positions and velocities. Although, the system is thermally equilibrated, every PKA and its surrounding atoms in the 6 simulations have different relative positions and velocities. This can cause some difference in the number of defects formed.

### **Active Volume Effect**

The size of the active region of the simulation cell can affect the defects produced even if the defects do not directly interact with the thermostat region. This is because the energy density of the system is controlled by the amount of the PKA energy and volume of the active region.

The effect of the active system size was investigated by comparison of two system sizes:  $20 \times 20 \times 20$  and  $30 \times 30 \times 30$  unit cells active region volume. The volume of the thermostat was kept almost the same,  $\sim 2650$  atoms since this volume determines the amount of the energy to be removed. The entire systems, therefore, are  $22 \times 22 \times 22$  and  $31 \times 31 \times 31$  unit cells. Figure 7-21 is the results of these two simulations in terms of the number of U and O vacancies produced as a function of time. The difference between the two runs are reasonably similar and well within the variation expected from the statistical uncertainty determined previously. This implies that the

20×20×20 unit cells for the active region volume is already sufficiently large to perform the radiation damage simulations with 1 keV U PKA.

### **Discussion**

Necessary modifications to perform radiation damage simulations in UO<sub>2</sub> have been implemented in our in-house MD code. These include the ZBL potential, a new and powerful variable time step algorithm, and the Berendsen thermostat. Each modifications made is tested individually and also in the combined situation of the actual radiation damage simulation setup. Some of the basic parameters needed to perform the radiation damage simulation with 1 keV U PKA were characterized.

There are other parameters yet to be explored. In the actual simulation of the radiation damage in UO<sub>2</sub>, the effects of the PKA energy and incident direction need to be understood. The estimated PKA energy in a typical reactor condition is a few hundreds of MeV<sup>173, 174</sup> which is unattainable in the current MD simulation capability because of the computational requirement for extraordinarily large system sizes. However, in repository condition, the required energy is much lower and is about 80 keV.<sup>173, 174</sup> As mentioned before, van Brutzel group has already performed the simulation at this energy although there were some inconsistencies with their own study with the low energy PKA.

The direction of the PKA may also manifest some difference in the number and structure of the defects produced. However, in reality, the PKA travels in arbitrary directions; therefore, the statistics of the variation in the results is needed to be understood.

Another important parameter to explore is the temperature of the system. Under reactor condition, the temperature of the fuel pellet can rise up from 800 K to 1600 K. At these high temperatures, the thermal diffusion of the defects is important and the number and structure of the radiation-induced defects formed will most likely be affected.

The effect of the thermostat thickness was not studied, but it is expected not to affect the result least for 1 keV U PKA case. This is because essentially the same effect was studied when characterizing the Berendsen time constant.

Simulations in single crystal structure are useful, but in a real fuel pellet there are a number of defects such as point defects, dislocations, GBs, and surfaces. The effects of these defects are particularly interesting since they may indicate the possibility of controlling the radiation properties of UO<sub>2</sub>.

Finally the characterization of the number and structure of the defects and their clusters is interesting but challenging. Experimentally UO<sub>2</sub> is known to be very radiation tolerant.<sup>207</sup> Our simulations in fact showed that a significant number of the defects were annihilated within a very short time (<2 fs) and the number remain steady from thereon. Thus the crystalline structure was still retained. However, this may depend on how high the PKA energy is. van Brutzel *et al.* saw no amorphization observed in their simulation,<sup>192</sup> but their defect identification method used is questionable. Our interatomic potential is different from van Brutzel *et al.* and the result will depend on the interaction model.

Complex defect structures, defect clusters such as 2:2:2 cluster discussed in Chapter 6 cannot be formed in our MD simulation because of the values of the fixed charges of the U and O. Although it is possible to fit a potential to allow the production of a particular defect cluster, it will not be universal. It is very likely that not all the defect clusters can be allowed using a fixed charge model. Nevertheless, further investigation of the radiation damage in MD simulations will be able to address several issues, such as the interaction of defect cascade and point defects and GBs, also influence of the defect cascade on the thermal transport.

Table 7-1. Spline parameters and connection points for U-U, O-O, and U-O interactions.

	$r_1$ (Å)	$r_2$ (Å)	$f_0$ (-)	$f_1$ (Å)	$f_2$ (Å <sup>2</sup> )	$f_3$ (Å <sup>3</sup> )	$f_4$ (Å <sup>4</sup> )	$f_5$ (Å <sup>5</sup> )
U-U	2.0009	1.2003	452.3712	-1502.56	1995.418	-1301.83	415.5172	-51.9609
O-O	1.0005	0.1999	9.8149	-15.5372	13.5114	12.2027	-25.8868	10.4897
U-O	1.2003	0.6002	31.64577	-143.702	341.1256	-408.432	236.589	-52.9624

$r_1$  and  $r_2$  are the connection between Buckingham-spline and ZBL-spline, respectively.

Table 7-2. The ZBL screening function parameters.

$i$	$A_i$	$b_i$
1	0.1818	3.2000
2	0.5099	0.9423
3	0.2802	0.4028
4	0.02817	0.2016

All the values are unitless.

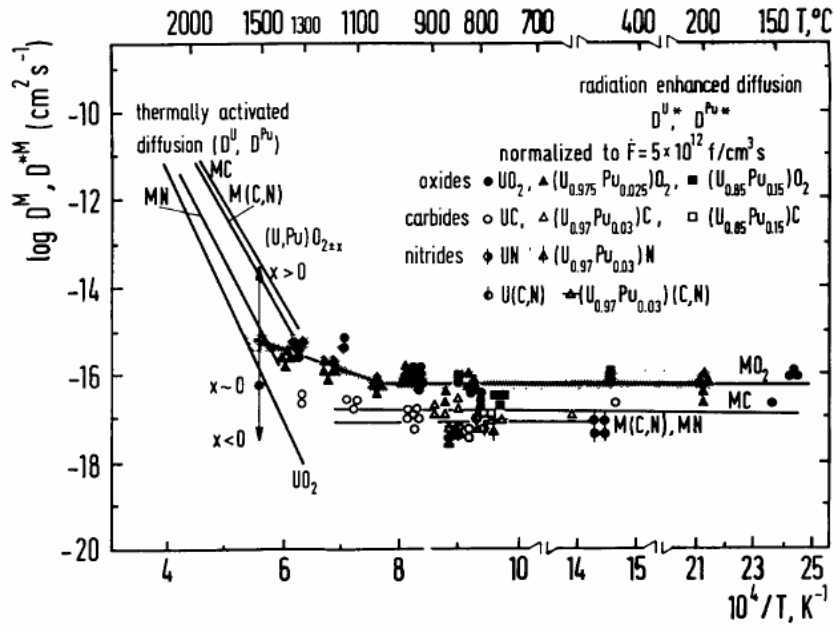


Figure 7-1. Potential, kinetic, and total energy per atom from radiation damage simulations with various fixed time step size.<sup>173</sup>

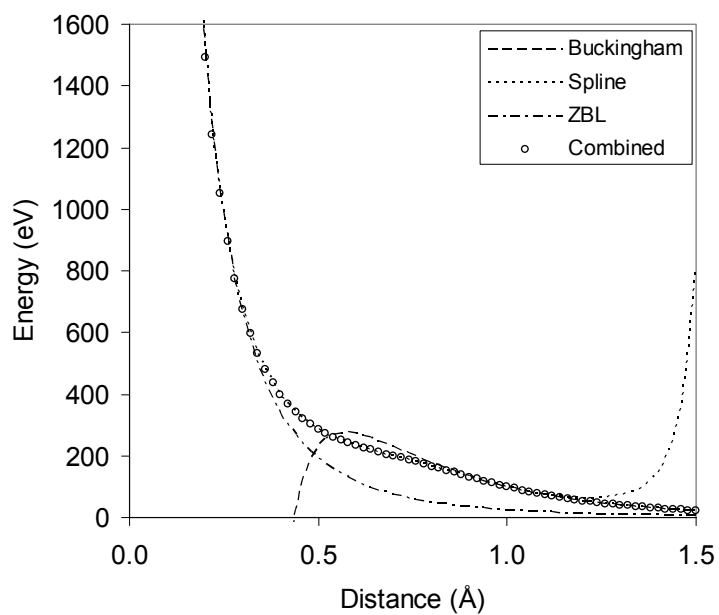


Figure 7-2. Potential energy of O-O interactions as a function of the interatomic distance. The connections between ZBL-Spline and Spline-Buckingham are made at 0.2 Å and 1.0 Å, respectively. The combined potential is used in MD simulations for radiation damage.

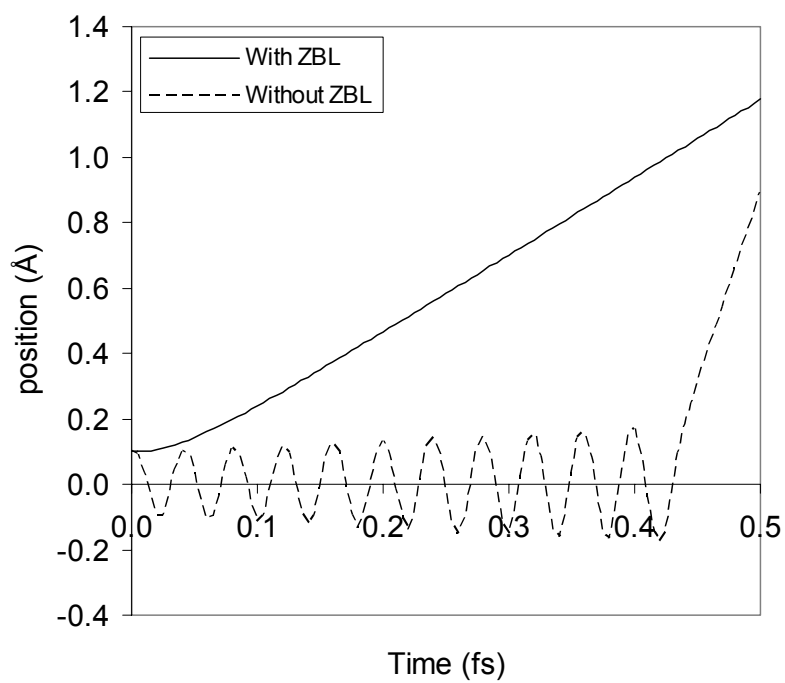


Figure 7-3. Trajectory of the O atom placed at 0.1 Å away from another O atom at the origin.

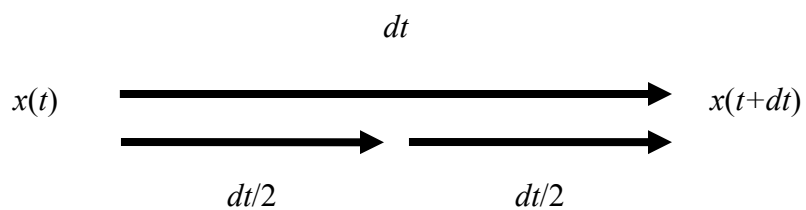


Figure 7-4. The calculation of the PKA trajectory in two ways: one large step and two half steps. The final positions from the two-way calculations are compared to obtain the error in the calculation and used to estimate the next time step.

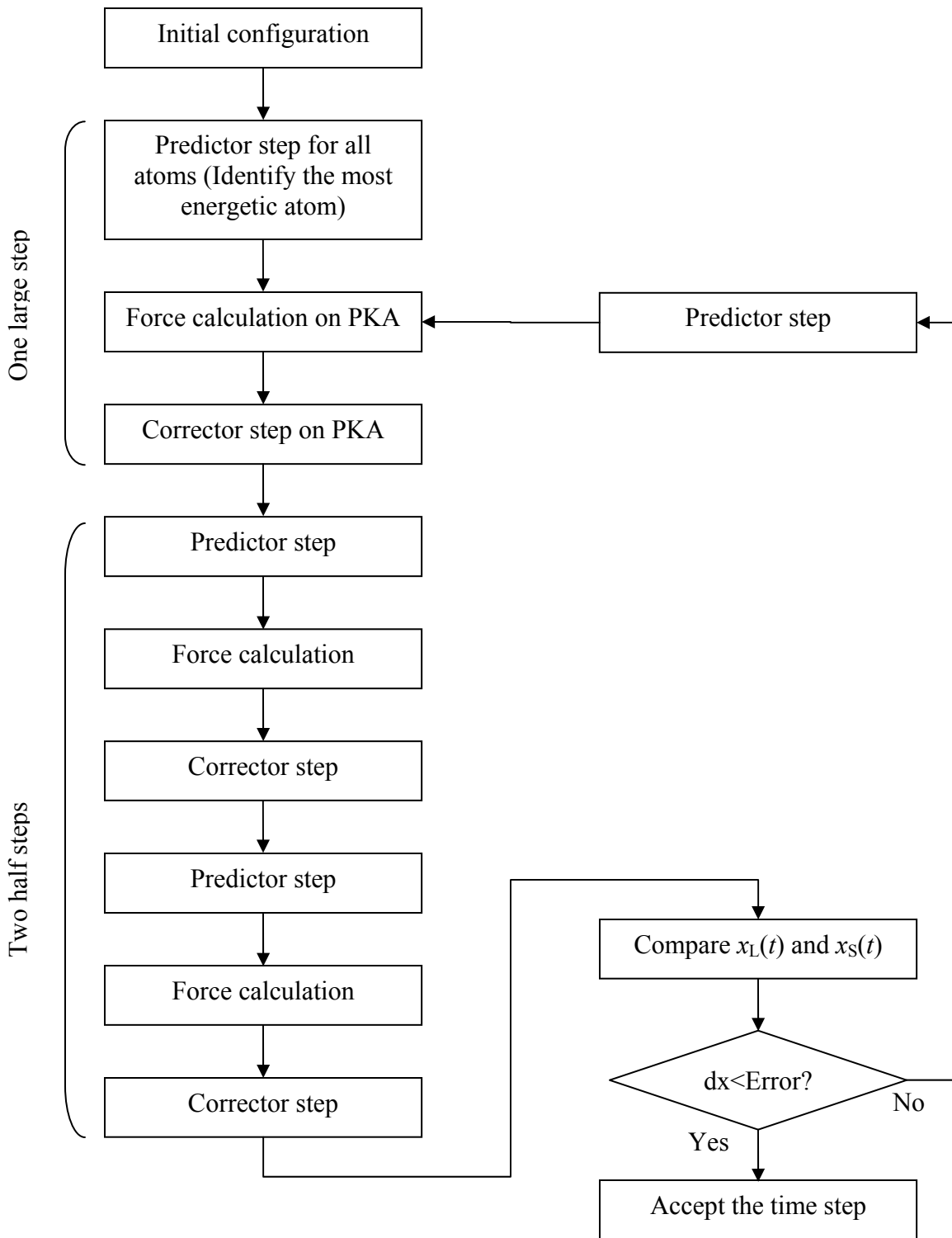


Figure 7-5. Flow chart of the determination of the variable time step algorithm.

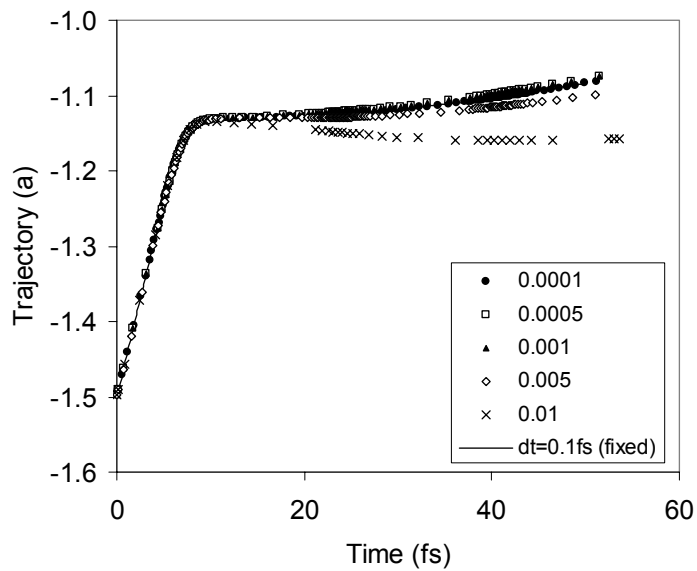


Figure 7-6. Trajectory of 1 keV U PKA atom along [100] direction in  $10 \times 10 \times 10$  single crystal  $\text{UO}_2$ . The results from the variable time step and fixed time step simulations are compared. The values in the legend are the values of the error ratio. The data from the fixed time step run with  $dt=0.1$  fs are indicated by the solid line.

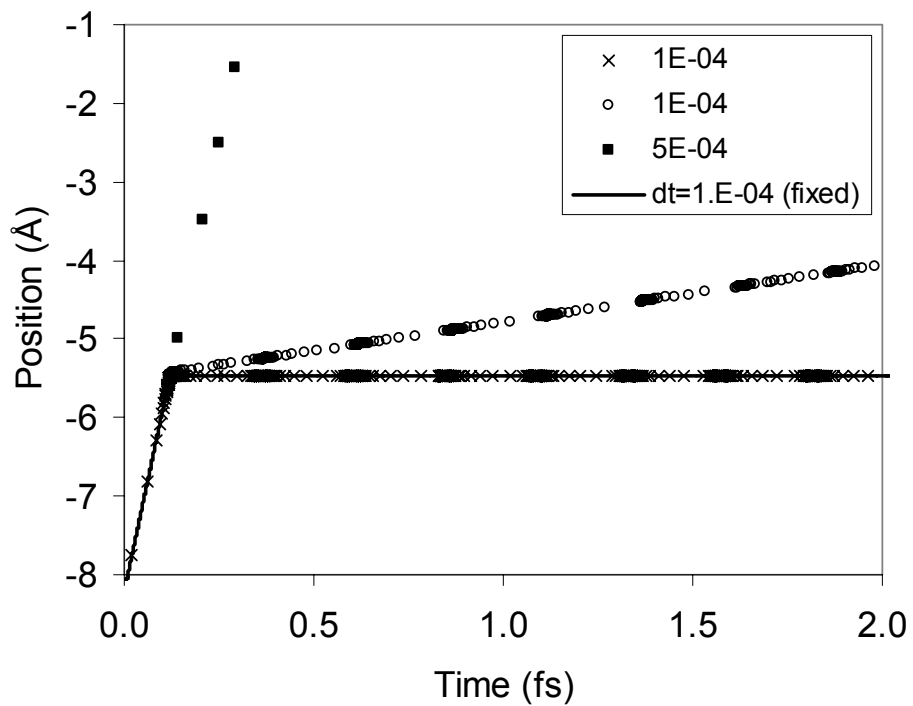


Figure 7-7. Trajectory of 80 keV U PKA along [100] direction in  $10 \times 10 \times 10$  single crystal  $\text{UO}_2$ . The legend indicates the values of the error ratio, and the data from the fixed time step run with  $dt=1 \times 10^{-4}$  fs.

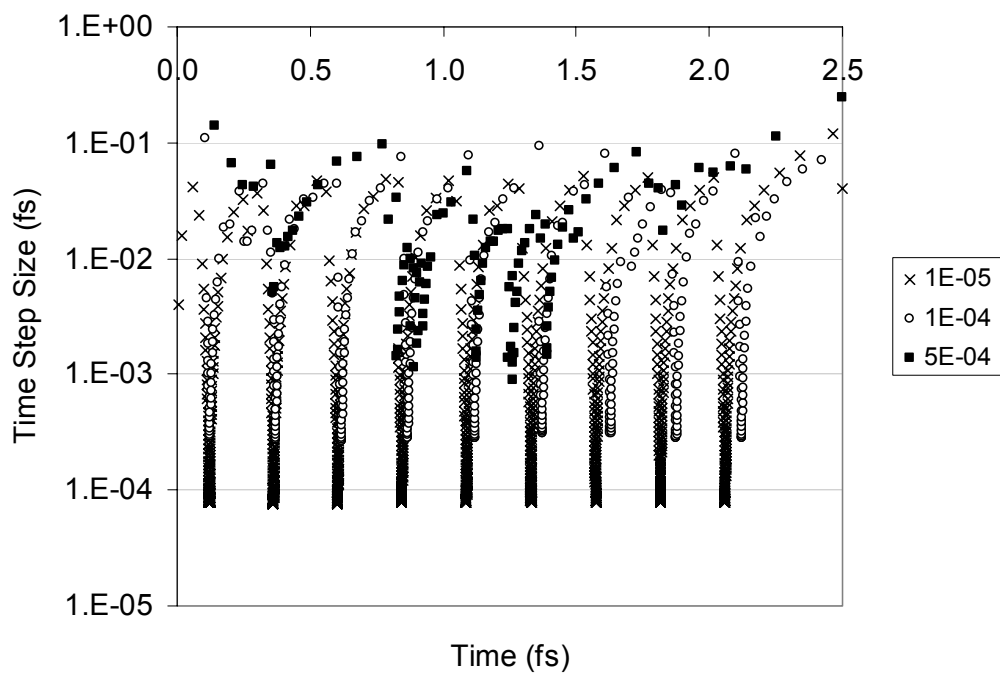


Figure 7-8. Evolution of the time step size in the 80 keV U PKA simulation. The vertical axis is in log scale.

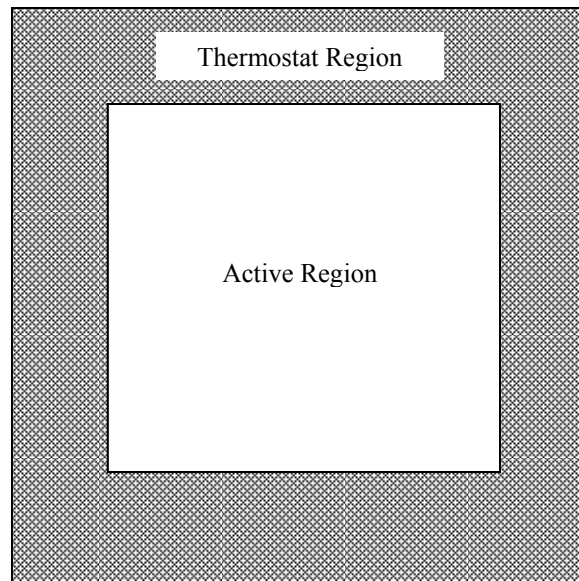


Figure 7-9. The configuration of the MD simulation cell used in our radiation damage simulations. The central region is called active region where all the interesting dynamic processes take place. The surrounding shaded area is the thermostat region to control the temperature of the system.

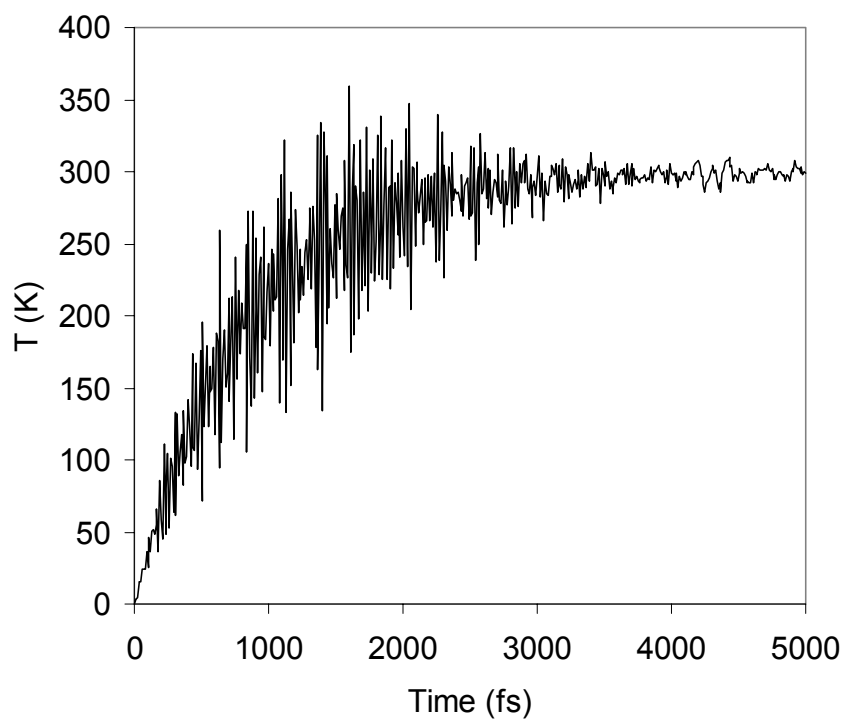


Figure 7-10. Temperature evolution of  $10 \times 10 \times 10$  unit cells single crystal  $\text{UO}_2$  during equilibration with the Berendsen thermostat with  $\tau=400$  fs.

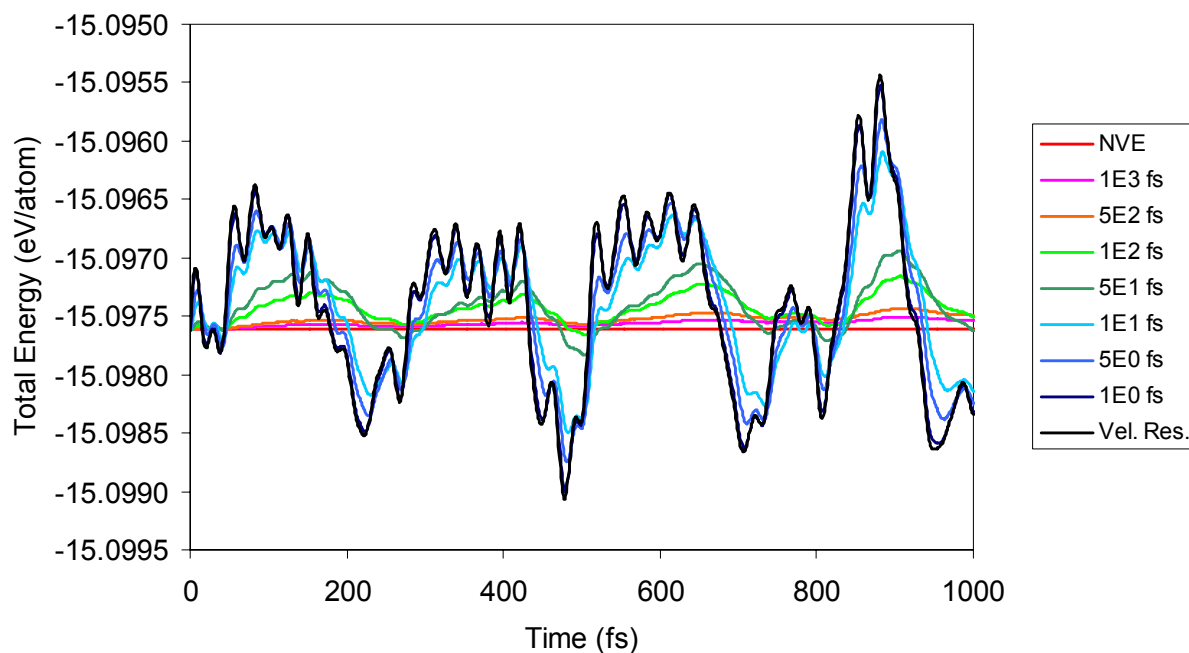


Figure 7-11. Total energy per atom of the equilibrated single crystalline  $\text{UO}_2$  at 300 K. The warmer color indicate the larger Berendsen time constant [what does this mean?]. Data from the NVE and velocity rescaling simulations are also included for comparison.

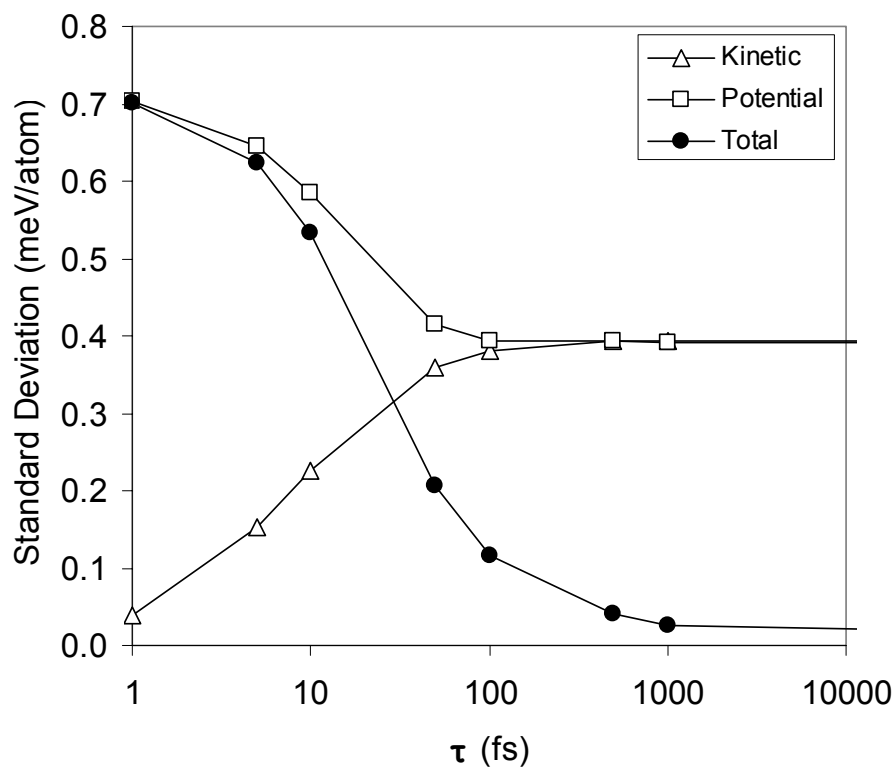


Figure 7-12. Standard deviation of the kinetic, potential and total energies per atom as a function of time constant,  $\tau$ , from the equilibrated single crystalline  $\text{UO}_2$  at 300 K.

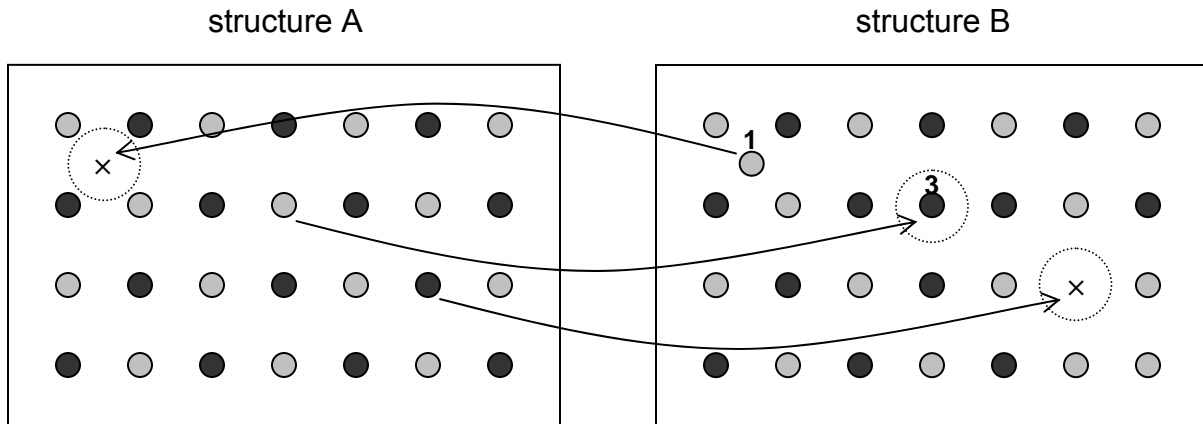


Figure 7-13. Defect identification method in crystalline structures. Structure A is the defect free perfect crystal, and structure B is the structure with defects. Black and grey are used to indicate two different types of atoms. The defects in structure B are numbered as (1) interstitial, (2) vacancy, and (3) anti-site. The arrows are used to indicate the same coordinates in both A and B. The dot lined circles indicates the sphere for finding the neighbors.

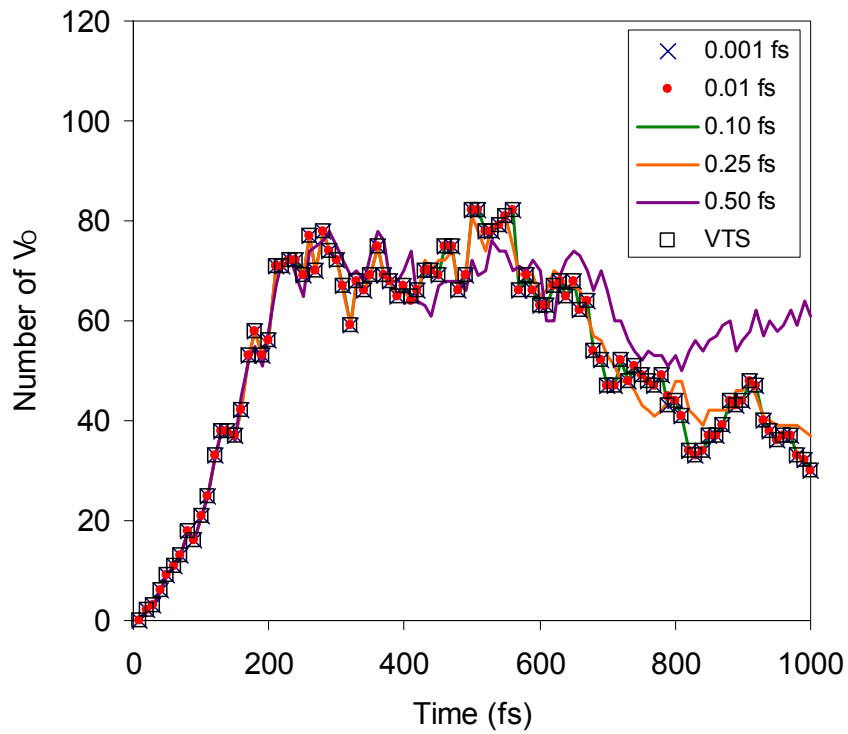
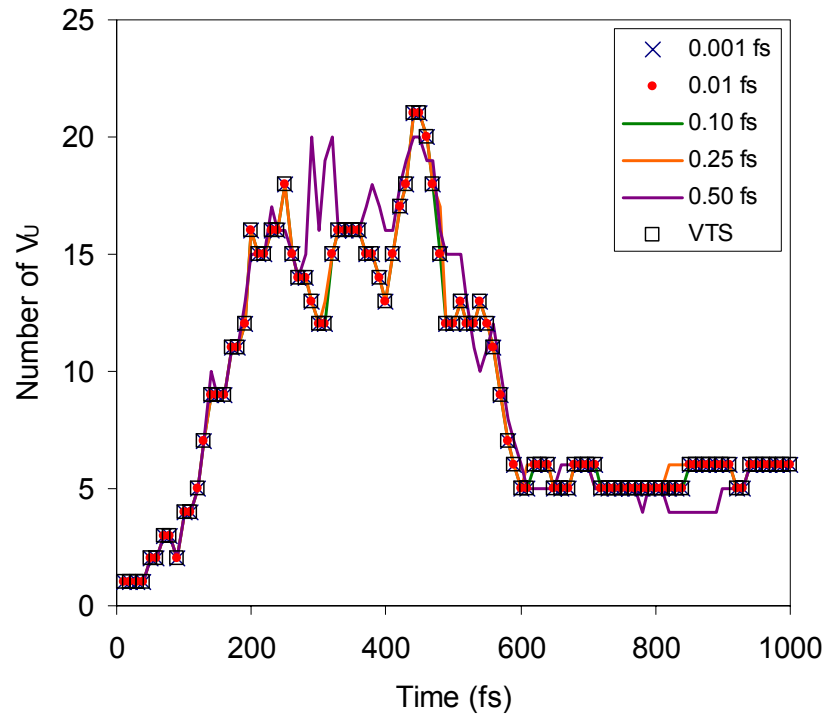


Figure 7-14. Effect of the time step size on radiation damage simulation in NVE ensemble. The system is  $10 \times 10 \times 10$  single crystal  $\text{UO}_2$  with 1 keV U PKA in [100]. The variable time step (VTS) was done with the error ratio of  $10^{-4}$ .

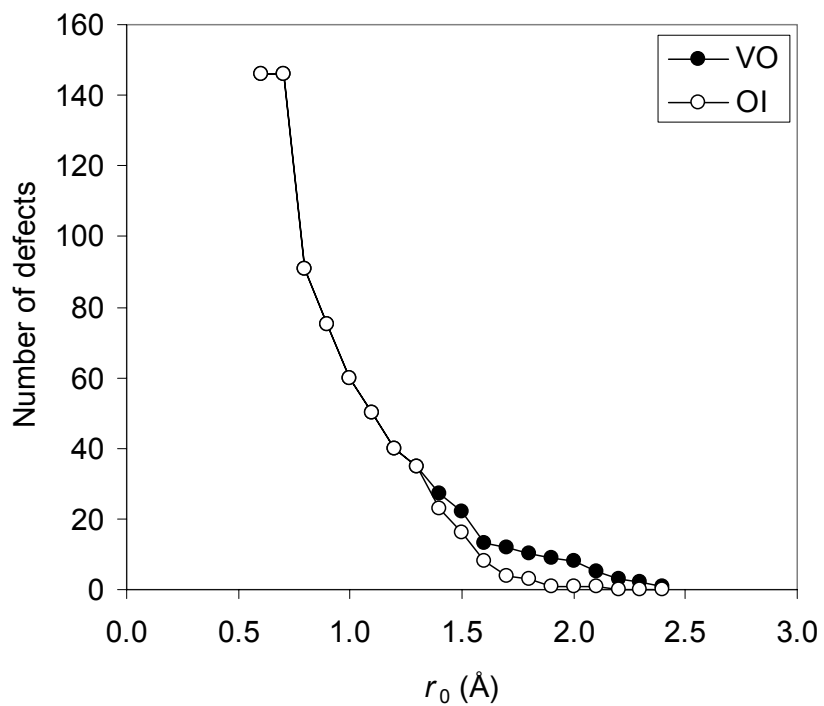
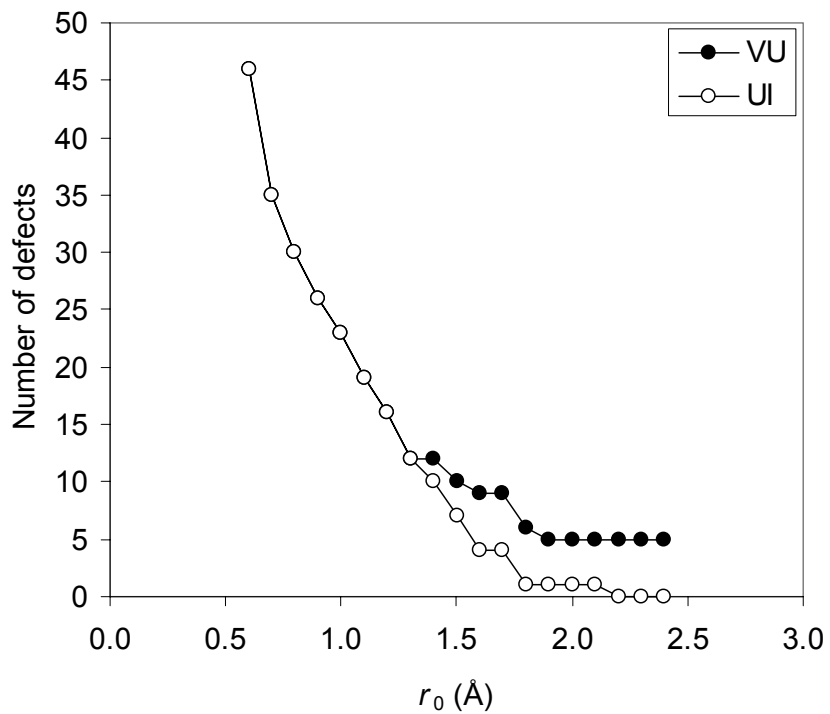


Figure 7-15. Number of  $V_U$ ,  $U_I$ ,  $V_O$ , and  $O_I$  produced after the 1 keV U PKA radiation damage in a single crystal  $UO_2$ . The simulation was run for 10 ps.

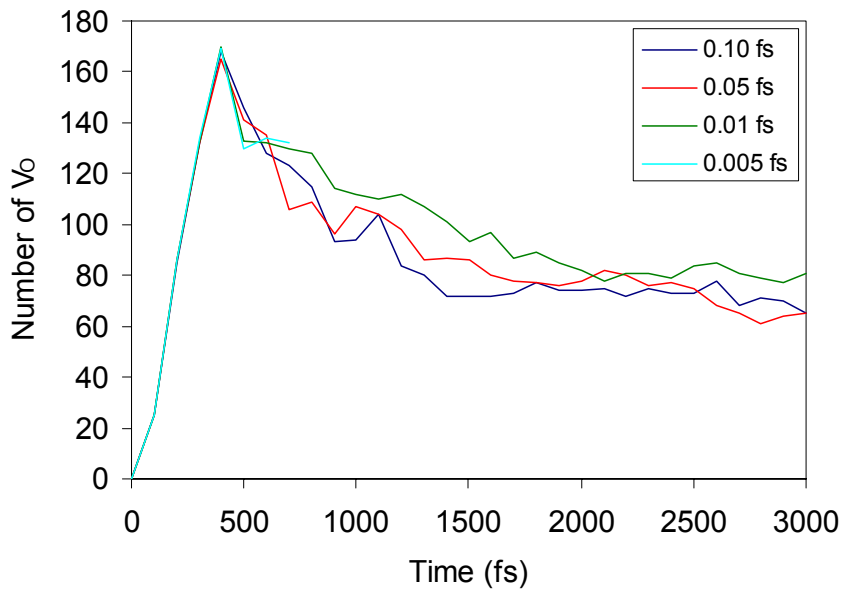
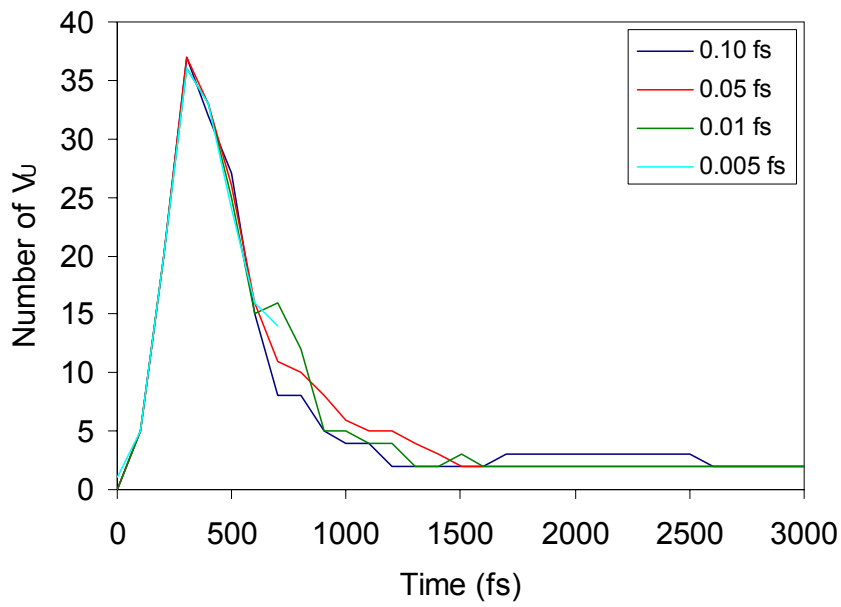


Figure 7-16. Effect of time step size in radiation damage simulation in pNVE. The system is  $22 \times 22 \times 22$  single crystal  $\text{UO}_2$  with 1 keV U PKA in [100].

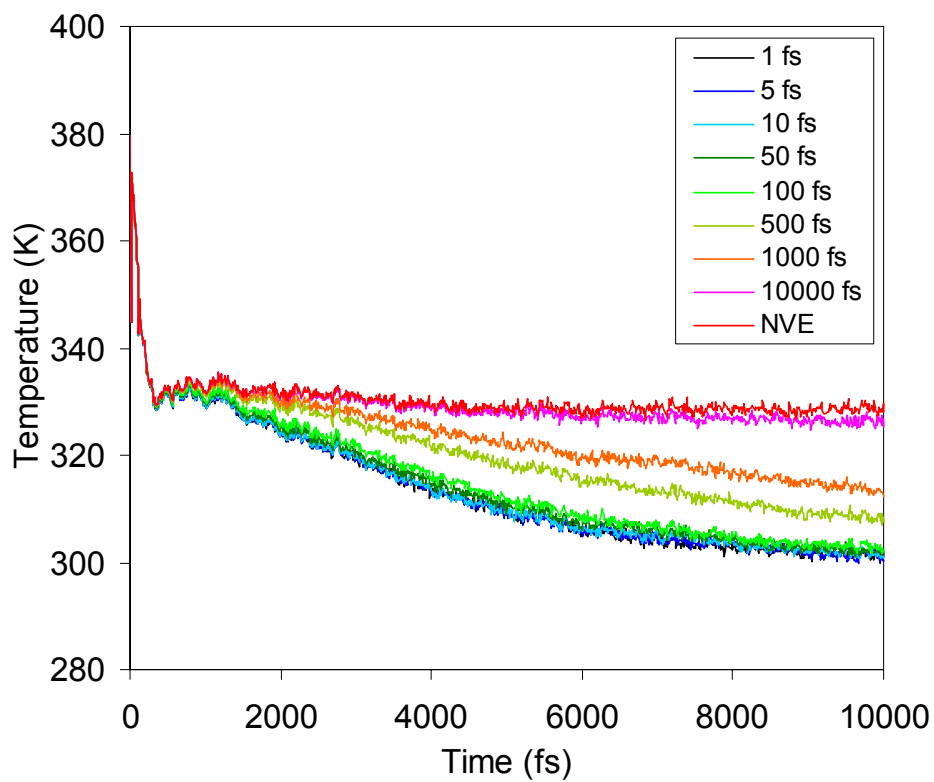


Figure 7-17. Temperature of the active region during the radiation damage simulations with different Berendsen time constants.

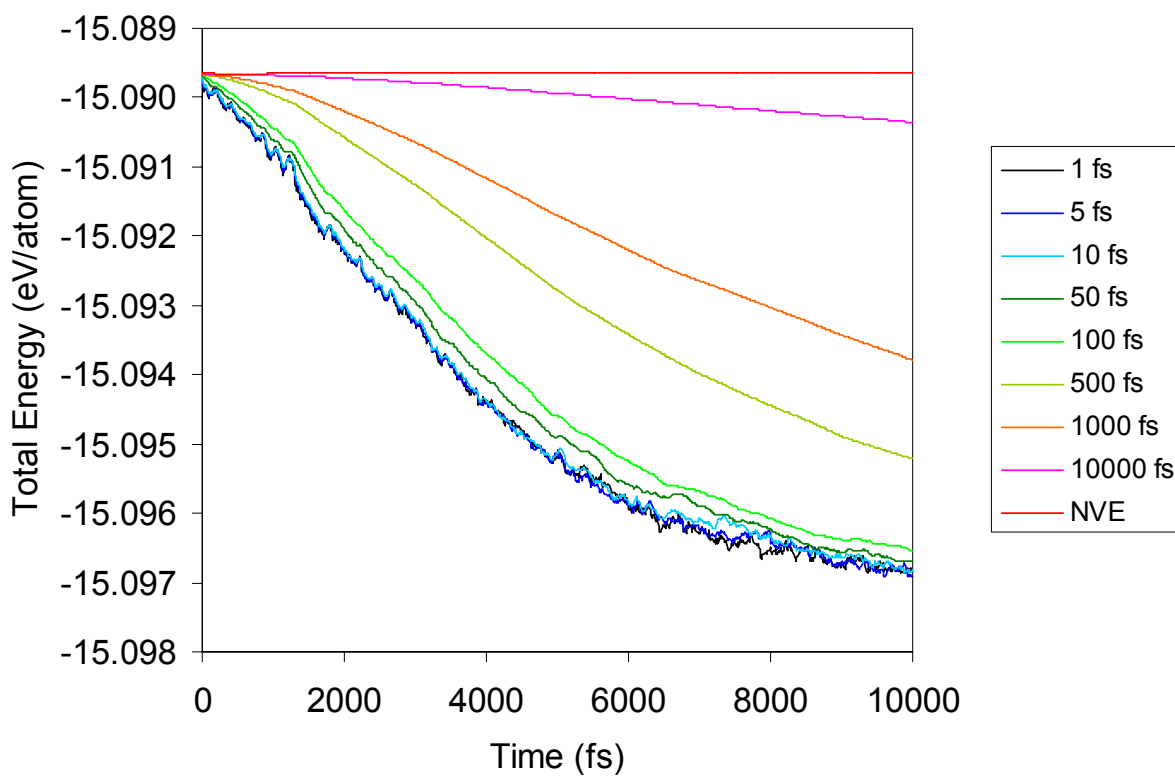


Figure 7-18. Total energy per atom during the radiation damage simulations with different Berendsen time constant. The larger the time constant, the warmer the color.

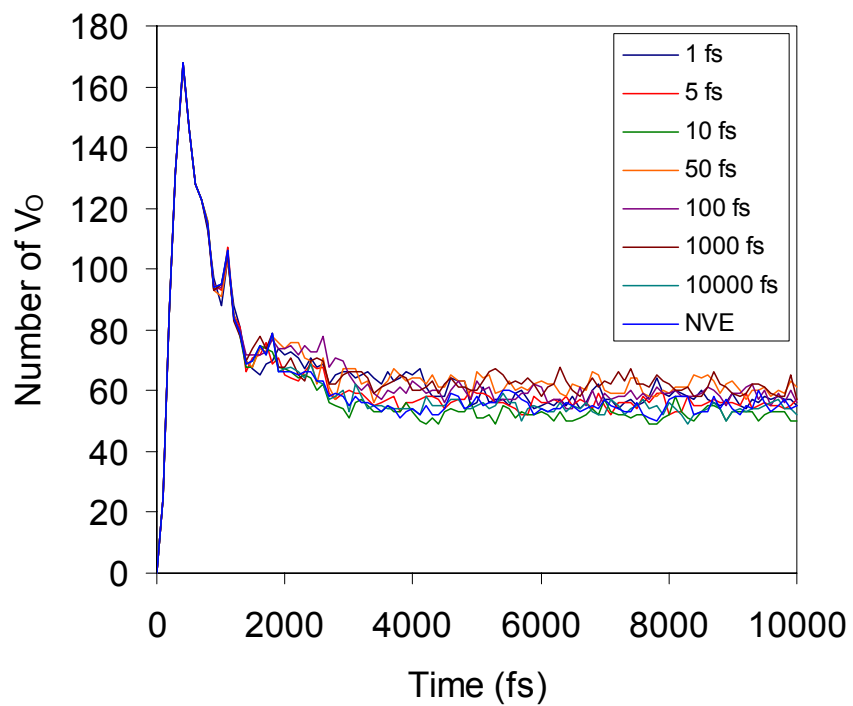
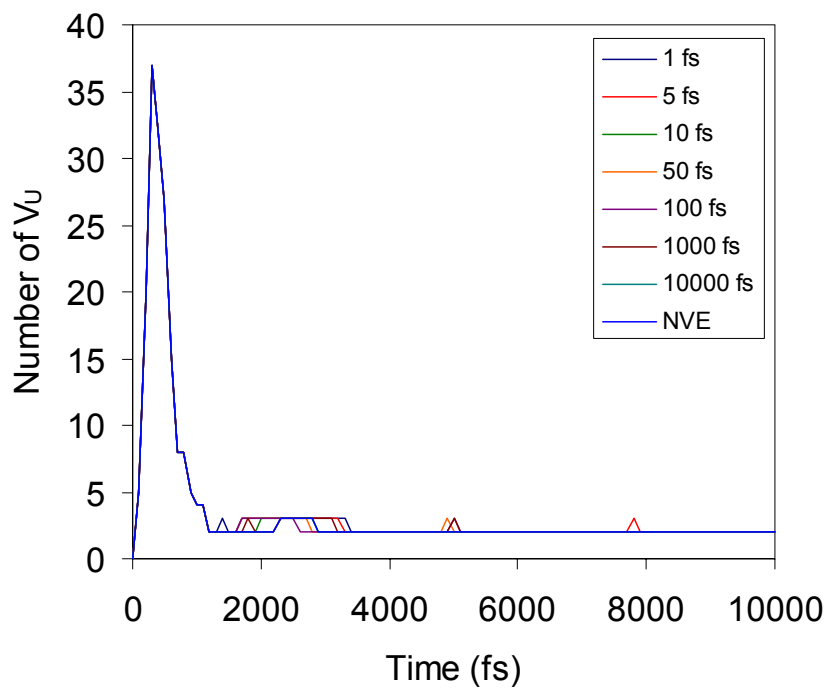


Figure 7-19. Number of uranium (top) and oxygen (bottom) vacancies produced in radiation damage simulations as a function of the Berendsen time constant

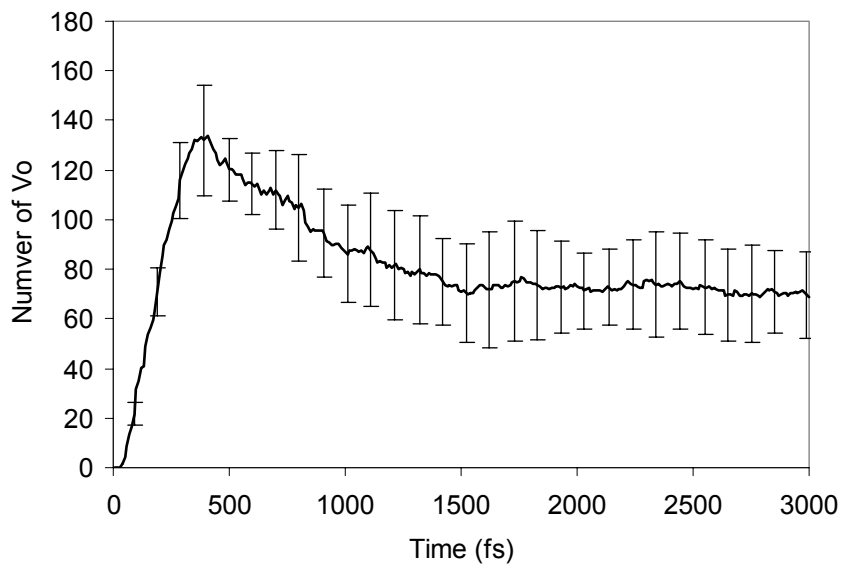
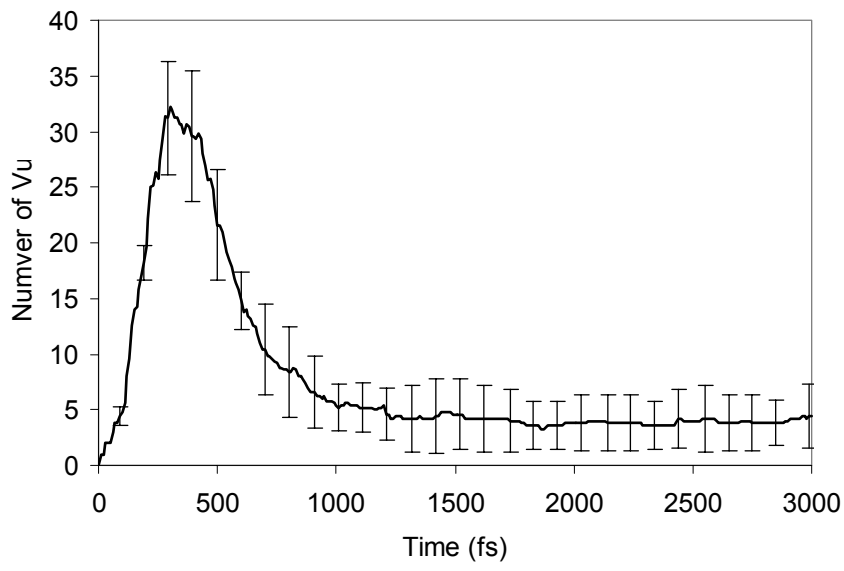


Figure 7-20. Number of uranium (top) and oxygen (bottom) vacancies produced in radiation damage simulations with equivalent PKA directions.

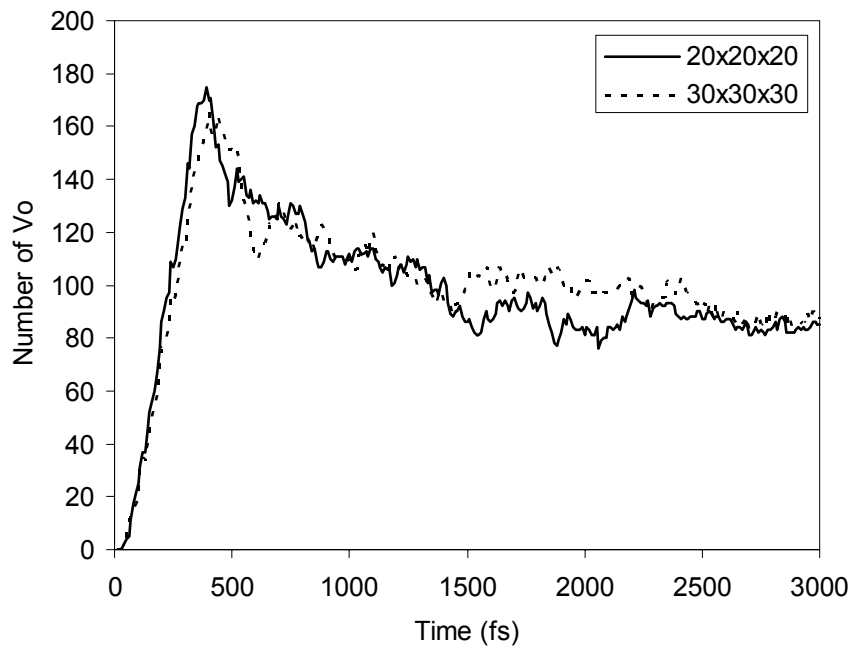
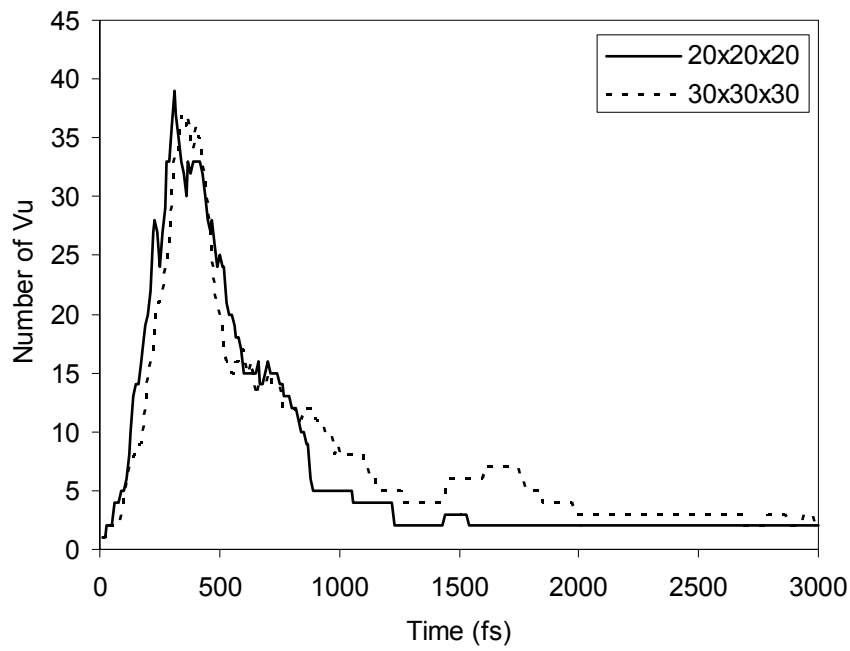


Figure 7-21. The number of U and O vacancies produced by the radiation damage simulations in 20×20×20 and 30×30×30 unit cells active volume.

## CHAPTER 8 INTERFACIAL THERMAL TRANSPORT IN DIAMOND

### Introduction

Diamond is an ideal laboratory in which to characterize crystallographic effects on interfacial conductance since it has the largest thermal conductivity of any material; thus the detrimental effects of the GBs can be expected to be particularly evident. In addition, diamond is of considerable technological interest.<sup>7, 208-210</sup>

In this chapter, the interfacial conductance of diamond GBs is determined as a function of temperature and twist angle. Furthermore, the relation between GB energies and interfacial conductance is elucidated. From our simulations, we find that the interfacial conductance is extremely high; however, when appropriately normalized, it is less than that of the corresponding GBs in silicon, a result that we can understand in terms of the bonding at the interfaces. Moreover, we find that the interfacial resistance is an approximately linear function of the GB energy. As a consequence, we find that it is possible to construct a Read-Shockley type model for the thermal conductance of these boundaries.

### Single Crystal Diamond

In order to test the fidelity of the Tersoff potential for thermal-transport applications, bulk single crystal properties have been studied. First, energy minimization of the diamond structure at 0 K yields a lattice parameter of 3.567 Å, and the cohesive energy of -7.36819 eV. These values agree well with experimental values of 3.567 Å<sup>1, 6, 211, 212</sup> and -7.36 eV<sup>6, 209</sup>. Second, the thermal expansion of single crystal diamond is determined using the Andersen NPT ensemble (refer to Chapter 3). A 4×4×4 unit-cell system of 512 atoms is equilibrated for 1.25 psec at 300, 500, 750, 1000, 1250, and 1500 K. The temperature dependence of the lattice parameter is found to be linear ( $r^2=0.999$ ) and the thermal expansion is determined to be  $6.00 \times 10^{-6}$  1/K, independent

of temperature between 0 and 1500 K (see, Figure 8-1). Slack and Bartram<sup>212</sup> have compiled thermal expansion data of a wide variety of ceramics and metals including diamond. Their value of the linear thermal expansion is, of course, temperature dependent ranging from nearly 0 below 100 K to  $5.87 \times 10^{-6}$  1/K at 1600 K. The lattice parameter calculated from their thermal expansion data is also shown in Figure 8-1. The discrepancy between simulation and experimental lattice parameter is at most 0.006 Å (0.16 %) over this temperature range. This agreement can be considered as excellent.

We can use thus use this potential with some confidence to characterize the thermal conductivity of single crystalline diamond using the direct method (Chapter 3). Figure 8-2 shows the temperature profile obtained from  $4 \times 4 \times 400$  unit cells single crystal diamond after 400 psec. The z-axis is along [001], and the temperature profile was obtained from the mean kinetic temperature of all of the atoms in each atomic plane averaged over 250 fsec of time. In the first 1 psec, the system is equilibrated at 1000 K, and then the heat source and sink are turned on to create steady state temperature gradient. Figure 8-3 shows the evolution of temperature at  $z=0$  and  $L_z/2$ . The plane-by-plane temperature is calculated from the mean kinetic energy of atoms in each plane averaged over 250 fsec intervals. This data shows that after  $\sim 100$  psec the temperature fluctuate within approximately 5 K of the nominal temperature of the system of 1000 K. The temperature profile shown in Figure 8-2 is determined from an average of the kinetic energy of atoms in each plane over the last 200 psec.

Once the temperature profile is obtained, the linear temperature gradient is extracted to calculate the thermal conductivity, according to Fourier's Law (Equation 2-2). In order to minimize the error from the noise, it is best to take the linear temperature gradient over as long a distance as possible. However, the longer the section taken, the more likely it is to include

regions with a nonlinear temperature gradient, where Fourier's law is not valid. To determine, the region over which the temperature gradient is determined, two criteria are applied: (i) keep the center of the linear temperature gradient regime half way between the heat source and heat sink; (ii) take as wide a region as possible without deviating from the linear behavior, as measured by a correlation of fit in excess of 0.95. The fit to the temperature gradient is shown in Figure 8-4. This careful selection of the linear region reduces the error from the noise, but not the error from the discrepancy of the temperature gradient between two regions to the left and the right of the heat source. The difference of the slopes in Figure 8-4 is approximately 15 % of the average of the slopes. This is perhaps due to the long wavelength phonons having extremely long relaxation time, which cannot be easily controlled in the simulation. Therefore, the thermal conductivity calculated from this method typically has a statistical error of the order of 10 – 15 %.

As discussed in the context of  $\text{UO}_2$ , the imposition of a heat current on the system leads to large temperature gradients. It is therefore important to establish the effects of the size of the heat current and to compare with results from a method in which no heat current is imposed. Shelling et al. performed simulations to determine the thermal conductivity of Si using both equilibrium and nonequilibrium methods. They found that the conductivities obtained from both methods agree when sufficiently large system is used. They also determined that the effect of heat current density and found that the energy density of  $\sim 2 \times 10^{-4}$  eV/nm<sup>2</sup> per 0.55 fs gives least error in the final result. Since this value may depend on the material of interest, we performed seven test runs with heat current densities ranging from  $1 \times 10^{-4}$  to  $8 \times 10^{-4}$  eV/nm<sup>2</sup> per 0.2 fsec. As apparent from Figure 8-8, the noise level increases as the current density decreases. The result from  $1 \times 10^{-4}$  eV/nm<sup>2</sup> is shown but excluded from since the maximum difference in the conductivity value

was 15 % of the average value and there was no systematic trend. A similar weak dependence in the heat flux was observed in previous work on Si GBs.<sup>213</sup> Moreover, the previous study in Si for perfect crystals showed quantitative agreement for the predicted thermal conductivity between the imposed heat current method and a Green-Kubo approach, in which there is no heat current at all.<sup>213</sup> The heat current density for subsequent simulations was kept constant at  $2.5 \times 10^{-3}$  eV/nm<sup>2</sup>·fsec. The resulting temperature profile in Figure 8-11 clearly shows the symmetry of the simulation setup.

As discussed in Chapters 3 and 4, the size of the simulation cell can have a large effect on the calculated value for the bulk thermal conductivity. This is particularly true for materials with high thermal conductivities, such as diamond. A series of simulations were performed with different system lengths and temperatures to investigate the size effect (Figure 8-5). The thermal conductivity extrapolated to  $1/L_z=0$  is shown in Figure 8-6 as a function of temperature. Three experimental data<sup>2, 51, 214</sup> are also included in the plot for comparison. The values from Olson and Onn are from isotopically pure (<sup>13</sup>C<0.07 %) diamond and from Touloukian are for type IIa natural diamond (<sup>13</sup>C<1.01 %) (Chapter 1). Our simulation results agree very well with the experimental data. The same data on log-log plot shows that the slope of experimental and simulation data to be approximately -1.35 and -1.16, respectively. Although the isotopically pure and natural diamonds give somewhat different values of the thermal conductivity, our results seem to lie right in between the experimental data.

### **Interfacial Conductance of (001) Twist GBs**

The diamond crystal structure is characterized by four covalent bonds pointing along <111> directions. A GB on an arbitrary plane will thus have two covalent bonds projecting back into the grain itself and two bonds across the GB (Figure 8-7).<sup>124</sup> The two bonds across the interface can be expected to be significantly different from the bonds in the bulk, due to the

structural disorder at the GB. If we examine the principal planes in the diamond lattice, GBs on the (111) plane have three bonds back into the crystal and one across the interface; GBs on the (011) plane have one bond pointing back into the crystal, two parallel to the interface and one pointing across the interface. Neither of these is similar to the typical GB described above.

However, GBs on the (001) plane have two bonds pointing back into the crystal and two pointing across the interface. A high-angle twist boundary on the (001) plane may thus be considered as being, to a considerable extent, representative of the GBs in polycrystalline and nanocrystalline diamond.<sup>124</sup> Therefore, to elucidate the structure-property relationship for a generic GB in diamond, we determine how the thermal conductance of (001) GBs varies with twist angle.

The diamond lattice has a two-fold symmetry axis in the  $\langle 001 \rangle$  direction. Thus on forming symmetric twist boundaries on this plane, a rotation of one semi-crystal with respect to the other by  $180^\circ$  will result in a single crystal. Therefore, to probe the full range of GBs, we need only consider twist angles from  $0^\circ$  to  $90^\circ$ . We have simulated the thermal transport properties of 12 such GBs, with twist angles ranging from  $8.80^\circ$  to  $90.0^\circ$ . These GBs were formed by cutting a single crystal along an (001) plane and rotating one half of the crystal with respect to the other. The unit cells for the GBs considered range in areal dimensions from being equal to that of the perfect crystal ( $\theta=90^\circ$ ,  $\Sigma=1$ ) to being 101 times larger ( $\theta=11.42^\circ$ ,  $\Sigma=101$ ). Lower angle GBs are excluded from this study because of their too large system sizes

The  $90^\circ$  GB is a special case and is actually a symmetric twin GB. In the  $\langle 001 \rangle$  direction, the stacking of the perfect crystal can be written as ...AaBbAaBbAb..., where the Aa and Bb layers come from the fcc Bravais lattice with a basis of two atoms at (0,0,0) and (0.25,0.25,0.25). The  $90^\circ$  twist GB then corresponds to a stacking sequence of ...AaBbAbBaAb..., in which we can see that the stacking sequence is symmetric about one of the A planes. Full crystallographic

details of all of the GBs considered and a summary of the simulation results are given in Table 8-1.

To prepare the GBs for the thermal conductivity simulations, the unrelaxed GB structures were heated to 2000 K for 10 psec to minimize the stress, then slowly cooled to near 0 K in a stepwise fashion; equilibrium  $T=0$  K structures were then determined by steepest descents quenches to minimize the energies and to reduce the forces and stresses to negligible values. This process was determined to be appropriate in earlier work on Si GBs.<sup>124</sup> The coordination of atoms within the typical high-angle high-energy GB,  $\Sigma 29(001)$  agree very well with the previous results (Table 6-1).<sup>124</sup> To minimize the computer time, the relaxation process was performed on simulation cells that were only 16 unit cells long. After the relaxed structures were obtained, perfect crystal regions were inserted to form structures long enough in the  $z$ -direction for the thermal conductivity simulations.

von Alftan *et al.*<sup>215</sup> investigated the zero-temperature structures of Si GB structures by removing atoms from the GB region and found GB structures with energies lower than those previously reported. We have explored this effect by performing the same procedure on a  $\Sigma 29(001)$  GB in diamond, but we did not find any structures with energies lower than those formed by the process described above. Figure 8-9 shows the GB energies as a function of atoms removed. Initially a certain number of atoms are removed from unrelaxed  $\Sigma 29(001)$  GB, and then the structures are relaxed by simulated annealing. The annealing and cooling processes are exactly the same as the process described above. Atoms are systematically removed from (001) plane and relaxed to obtain the GB energies. Since the diamond unit cell contains 4 distinct atomic planes in the [001] direction and a 4-fold symmetry along [001], removal of two (004) planes is sufficient to investigate all of the possibilities. Once a complete (004) plane is

removed, the grain is shifted by 1/4 of the unit cell in [001] direction to keep the density similar to the original  $\Sigma 29(001)$  GB. This operation does not make any difference in the final GB energies, as von Althaus *et al.*'s group also confirms. When the atoms are removed the structure was relaxed by the same procedure described above to relax the GBs. Our data shows that the GB energies do not differ significantly from the relaxed  $\Sigma 29(001)$  GB with the GB energy generally remaining below  $8 \text{ J/m}^2$ . We have also observed a few cases where the GB energies are significantly higher reaching close to  $12 \text{ J/m}^2$ . The  $\Sigma 29(001)$  GB has one of the highest energies and is thus one of the most likely to undergo reconstruction, since the potential energy saving is the largest. Because, our simulations on this GB show no reconstruction, it is unlikely that the other, lower energy, GBs will further lower their energies by reconstruction.

Before discussing the dependence of the thermal-transport properties on the twist angle, we examine the representative case of the  $\Sigma 29(001) \theta=43.60^\circ$  GB. Because, the simulation is set up as a 3-D periodic system with crystallographically identical GBs at the center of the unit cell and at the edge, the heat source and heat sink are placed equidistant between the two GBs. The resulting temperature profile in Figure 8-11 clearly shows the symmetry of the simulation setup.

In our simulation, temperature in each  $0.89 \text{ \AA}$  thick slice (i.e., a single (004) plane) through in the simulation cell is defined by the average kinetic energy of per atomic plane averaged over the last 560 psec. The temperature drop across a GB is quantified in the following manner: (i) the temperature profiles in the bulk regions surrounding the interface are fit linearly, with the range of  $z$  values fit determined by the minimizing the difference between the absolute values of the slopes. The linear fits are made over the region of between 12 nm and 25 nm, depending on the length of the simulation cell. The regions are considered bulk like when  $r^2$  of the linear fit is above 0.95. Because of the symmetry of the structure, all the slopes are found to

be the same within small error bars. (ii) The temperature jumps are determined from the equations to the linear fits. Analysis from the linear fits yield the values of 21.1 K and 23.8 K for the temperature drops at the two crystallographically identical GBs (see, Figure 8-11). The average temperature drop from these two GBs is thus 22.5 K; the corresponding thermal conductance is  $8.8 \pm 0.6 \text{ GW/m}^2 \cdot \text{K}$ , with the estimated uncertainty in the conductance coming from the difference in the two temperature drops.

As described above, the size of the simulation cell has a considerable effect on the calculated thermal conductivity of perfect crystals.<sup>213, 216</sup> The origin of this effect is the restriction on the maximum phonon mean free path set by the length of the periodic simulation cell.

To explore the possibility of an analogous size effect for the interface conductance, we have determined the temperature drop at the interface and the corresponding interfacial conductance for the  $\Sigma 29$  GB for simulation cells ranging 14.3 nm to 287 nm in length. As Figure 8-12 shows, there is strong system size dependence; however, it appears that  $\Delta T$  reaches an asymptotic value at large system sizes. To confirm this, we have fit these data by a shifted exponential:

$$\Delta T = \Delta T_{\infty} + A \exp(-Lz/L_0). \quad (8-2)$$

Figure 8-12 shows that this functional form fits the data well. The values of parameters  $A$  and  $L_0$  obtained from the fit are 60.9 K and 70.7 nm, respectively. The formal description of the Kapitza conductance is given by Stoner *et al.*<sup>81</sup> as an integration over the wave vector summed over all the branches. Due to the complexity of phonon density of states and dependence of transmission coefficients as a function of dispersion relation, extracting an analytical expression of the size dependence is not straightforward. At present, we do not have a theoretical argument

for this functional form, but simply justify its use *a posteriori* by the quality of the fit shown in Figure 8-12. The infinite limit temperature drop,  $\Delta T_\infty$ , is 17.6K. The calculated interfacial conductances show a corresponding increase with an asymptotic value of 12.3 GW/m<sup>2</sup>K. Interestingly, no such effect was observed in previous (albeit less extensive) simulations of this effect for Si GBs;<sup>77</sup> however, the thermal conductivity of single crystal Si is much lower than that of single-crystal diamond and the bonding of atoms at the interfaces are quite different, as is described below.

Because the simulations for the longer systems are extremely computer-time intensive, for our systematic studies of the effects of crystallography, we have used a unit cell of 142.4 nm (400 unit cells) in length. The values of the interfacial conductances discussed below are thus ~30 % lower than the asymptotic values we would predict for a simulation cell of infinite length.

In addition to the effects of the length of the simulation cell, we have considered the effect of its cross section. In the previous study on Si single crystal, the dependence on the width of simulation cell was found to be very weak beyond 3×3 unit cells for the cross section<sup>213</sup>. The periodic planar unit cell is  $\Sigma$  times larger for GBs than for the single crystal. As a result the smallest cross sectional area is ~3.5×3.5 units (for the  $\Sigma 29$  GB), with most of the simulation cells have larger cross sectional areas.

For the case of the  $\Sigma 29$  GB, we have also determined the temperature dependence of the interfacial conductance. As 8-13 shows, the interfacial conductance increases almost linearly with the temperature up to 1250 K, above which it decreases. This increase is in strong contrast to the bulk thermal conductivity which decreases strongly with temperature (Figure 8-6). This behavior is actually similar to that in UO<sub>2</sub> (see Figure 5-4). We can understand this in a qualitative manner as arising from the significant obstacle that the GB offers to heat transport. As

such, there is poor coupling of the phonon modes on opposite sides of the interface. As the temperature increases, the anharmonicity of the system increases, which increases the coupling of previously weakly coupled phonon modes across the interfaces, thereby enhancing the thermal transport. This increase with temperature is consistent with experiments and simulation on a wide range of heterointerfaces.<sup>129, 130, 217</sup>

Detailed analysis shows that the drop in the conductance at 1500 K is due to the structural change at the interface, rather than a change in the thermal-transport mechanism itself.

### **Interfacial Thermal Conductance: Diamond vs. Silicon**

To determine the effect of crystallography on the interfacial conductance, Figure 8-14 shows the calculated thermal conductance at 1000 K of the twelve diamond GBs as a function of the twist angle for a simulation cell length of 142.4 nm. The interfacial conductance decreases from about 17 GW/m<sup>2</sup>K for low twist angles to 9 GW/m<sup>2</sup>K for  $\theta = 43.6^\circ$ , before increasing again to 12 W/m<sup>2</sup>K for the 90°  $\Sigma 1$  GB. The uncertainty in the calculated values is represented by the error bars, which are typically  $\pm 1.3$  GW/m<sup>2</sup>K.

This significant structural dependence, which we analyze in detail below, is quite reasonable since the degree of structural disorder at the GB, for which the energy is a measure, is lowest at small and high twist angles, for which dislocation models of GBs are appropriate<sup>19</sup> and highest at intermediate twist angles.

In an earlier paper on structure and mechanical behavior<sup>124</sup>, a comparison of the structure and properties of diamond and silicon GBs was found to be quite instructive. In particular, diamond readily forms sp<sup>2</sup> graphitic bonding at GBs, while Si strongly favors the retention of sp<sup>3</sup> bonding at the interface, even at the expense of the generation of a significant amount of structural disorder. Therefore, in addition to results for diamond, Figure 8-14 also includes the

previously determined<sup>77</sup> values for the interfacial conductance of two (001) twist GBs in Si. These values are close to an order of magnitude lower than for the corresponding diamond GBs, which should not be too surprising since the room-temperature thermal conductivity of bulk Si is also much less than that of diamond (150 vs. 2000 W/mK). This difference in bulk properties can be taken into account through the Kapitza length,  $l_K = \kappa / G_K$ , which is the thickness of perfect crystal offering the same thermal resistance as the GB. Figure 8-15 shows the Kapitza length, given in terms of the lattice parameter of the respective materials, as a function of twist angle. We see that due to its lower single-crystal thermal conductivity and its larger lattice parameter, the Si GBs actually have somewhat lower Kapitza lengths, indicating that Si GBs actually allow more efficient heat flow than the corresponding diamond GBs.

To understand the origin in these differences in interfacial conductances, it is necessary to consider the structure of the GBs in more detail. Figure 8-16 shows edge-on views of the  $\Sigma 29$  GB in both Si and C. It is evident from the figure, and quantified in Table II, that there is considerably less bonding across the interface in diamond than in silicon. In particular, in diamond only 14 % of atoms at the GB have two bonds across the interface, while in Si 82% of atoms have two bonds across the interface.<sup>124</sup> Thus structurally, the Si GB is much better connected. This extra bonding across the Si interface naturally makes it easier for vibrational excitations, i.e. heat, to cross the interface also.

### **Extended Read-Shockley Model For Interfacial Thermal Conductance**

The Read-Shockley (RS) model describes the energies of low-angle GBs in terms of dislocation cores and an associated strain field<sup>19</sup>. Wolf has made an empirical extension to the RS model – the extended Read-Shockley (ERS) model<sup>18</sup> – which fits the energies of GBs over

the full range of twist angle. For the case of two-fold rotational symmetry, as on the (001) plane of diamond, the ERS model is given by:

$$E_{gb} = \begin{cases} \sin 2\theta \cdot (E_c^< - E_s^< \ln(\sin 2\theta)) / b & \text{for } 0^\circ \leq \theta < 45^\circ \\ E^{STGB} + \sin(180^\circ - 2\theta) \cdot (E_c^> - E_s^> \ln(\sin(180^\circ - 2\theta))) / b & \text{for } 45^\circ \leq \theta < 90^\circ \end{cases} \quad (8-4)$$

$E_c$  and  $E_s$  are the energies associated with dislocation core and strain field.  $E^<$  and  $E^>$  are used to indicate the parameters for angle lower than or greater than  $45^\circ$  twist angle.  $E^{STGB}$  is the energy of the symmetric twin GB ( $\theta=90^\circ$ ).  $b$  and  $\theta$  are the Burger's vector and twist angle, respectively. This functional form guarantees continuity in the energy and its first derivative at  $\theta=45^\circ$ .

Figure 8-17 shows the calculated GB energy for a large number of (001) diamond twist GBs. (There are many more data points in this plot than in the plot for the Kapitza conductance because the GB energy calculations are not computationally very demanding.) The solid line in Figure 8-17 is the ERS fit to the data, which quite well reproduces the trend in the energies.

Also shown in Figure 8-17, are the contributions to the energy from the dislocation core (dashed line) and the strain field (dash-dot line), as determined from the extended Read-Shockley equation. At most twist angles, the structural contribution, which at low angles is due to dislocation cores, dominates the energy. In particular, at  $45^\circ$  and  $90^\circ$ , there is no strain field contribution. The only boundary condition that restricts the value of these coefficients is the continuity of the two functions at  $45^\circ$ , which yields the constraint,  $E_c^</b = E_c^>/b - E^{STGB}$ .  $E_{GB}$  at  $0^\circ$  and  $dE_{GB}/d\theta$  at  $45^\circ$  are zero by default. The parameters of the ERS model obtained from the fit are

$$\begin{aligned}
E_c^</b>/b &= 5.94 \text{ J/m}^2 \\
E_s^</b>/b &= 5.24 \text{ J/m}^2 \\
E_c^>/b &= 4.19 \text{ J/m}^2 \\
E_s^>/b &= 5.42 \text{ J/m}^2 \\
E^{STGB} &= 1.75 \text{ J/m}^2
\end{aligned} \tag{8-5}$$

Interestingly, the general trend in the Kapitza length shown in Figure 8-15 is similar to that of the GB energy shown in Figure 8-17. To show this correlation more clearly, Figure 8-18 shows that the Kapitza length depends approximately linearly on the GB energy; the slope of the linear fit is  $85.3 \text{ m}^3/\text{J}$ .

This approximate linear relation indicates that the Kapitza length should also be describable by an ERS model:

$$l_K = \begin{cases} \sin 2\theta \cdot (l_c^< - l_s^< \ln(\sin 2\theta)) & \text{for } 0^\circ \leq \theta < 45^\circ \\ l^{STGB} + \sin(180^\circ - 2\theta) \cdot (l_c^> - l_s^> \ln(\sin(180^\circ - 2\theta))) & \text{for } 45^\circ \leq \theta < 90^\circ \end{cases} \tag{8-6}$$

The solid line in 8-15 is an ERS fit to the Kapitza length. In analogy with the energy of the dislocation core and the strain field energy, it is natural to identify the coefficients of this ERS model as the Kapitza length associated with the structural disorder in the GBs and with the strain field.

From the fit obtained from the  $E_{GB}$ , we determine the coefficients of  $l_K$  to be the following:

$$l_c^< = 134.3a_0, \quad l_s^< = 105.3a_0, \quad l_c^> = 13.4a_0, \quad l_s^> = 71.1a_0, \quad l^{STGB} = 121.0a_0 \tag{8-7}$$

As in the case of the energy, the ERS form forces the condition  $l^{STGB} + l_c^> = l_c^<$  by continuity. The strain contributions to the Kapitza length differ by  $\sim 30\%$  in contrast to the corresponding values for the energy that differ by only 5%.

## Discussion

The work presented here has shown that the interfacial (Kapitza) resistance of (001) twist GBs in diamond depends systematically on the twist angle. Importantly, the Kapitza length is proportional to the energy of the GB, allowing us to fit it with an extended Read-Shockley model.

These results suggest that the energy of a GB, which is easily calculated, might be used as a surrogate quantity for the interfacial conductance, which is more difficult and computationally very expensive to determine. Further work on different GBs in diamond, and on different materials systems, is required to establish if this is a general behavior or if it is particular to this system.

Regardless of the specific details however, this work does suggest that it should be possible to determine an empirical relationship for the interfacial conductance as a function of the crystallography of the material. Such a relationship will be of considerable value as input to mesoscale simulations of thermal transport.<sup>218</sup>

Table 8-1. Summary of the diamond (001) GBs properties.

$\Sigma$	$\theta$ (degree)	$E_{GB}$ (J/m <sup>2</sup> )	$\delta V$ ( $a_0$ )	$G_K$ (GW/m <sup>2</sup> K)	$l_K$ ( $a_0$ )	$\langle C \rangle$ (-)	$C_2$ (%)	$C_3$ (%)	$C_4$ (%)
85	8.80	3.66	0.28	17.6	75.9	3.24	0.00	76.5	23.46
101	11.42	4.34	0.30	13.3	100.3	3.19	0.48	80.2	19.33
41	12.68	4.18	0.30	13.3	100.3	3.17	0.57	82.4	17.05
25	16.26	4.87	0.31	13.9	96.0	3.15	0.97	83.5	15.53
13	22.62	5.10	0.32	11.2	119.7	3.12	2.33	83.7	13.95
17	28.07	5.36	0.35	10.1	132.8	3.13	0.00	87.1	12.86
5	36.87	5.84	0.38	11.7	113.7	3.12	0.00	87.8	12.2
29	43.60	6.19	0.37	8.8	151.2	3.11	3.31	82.6	14.05
5	53.13	5.98	0.36	8.4	157.8	3.18	1.25	80.0	18.75
17	61.93	6.38	0.38	7.6	174.2	3.18	1.47	85.3	13.24
25	73.74	5.21	0.31	9.9	135.0	3.21	0.00	78.9	21.09
1	90.00	2.60	0.24	10.9	122.4	3.17	1.56	79.7	18.75

$\Sigma$  indicates the size of the coincident site lattice (CSL) planar unit cell of the GB.  $\theta$  is the twist angle in degree,  $E_{GB}$  is the GB energy, and  $\delta V$  is the volume expansion in units of lattice parameter  $a_0$ .  $G_K$  is the calculated thermal conductance,  $l_K$  is the Kapitza length defined by  $l_K = \kappa / G_K$  where  $\kappa$  is the thermal conductivity of the perfect crystal diamond.  $\langle C \rangle$  is the average coordination number of the atoms within the GBs, and  $C_n$  is the fraction of n coordinated atoms within the GBs.

Table 8-2. Comparison of the GB energies and coordination of the atoms of  $\Sigma 29(001)$   $\theta=43.6^\circ$  GB in diamond and Si. <sup>124</sup>

	Diamond	Si
$E_{GB}$ (J/m <sup>2</sup> )	6.19	1.62
$\langle C \rangle$	3.11	4.02
$C_2$ (%)	3	0
$C_3$ (%)	83	8
$C_4$ (%)	14	82
$C_5$ (%)	0	10

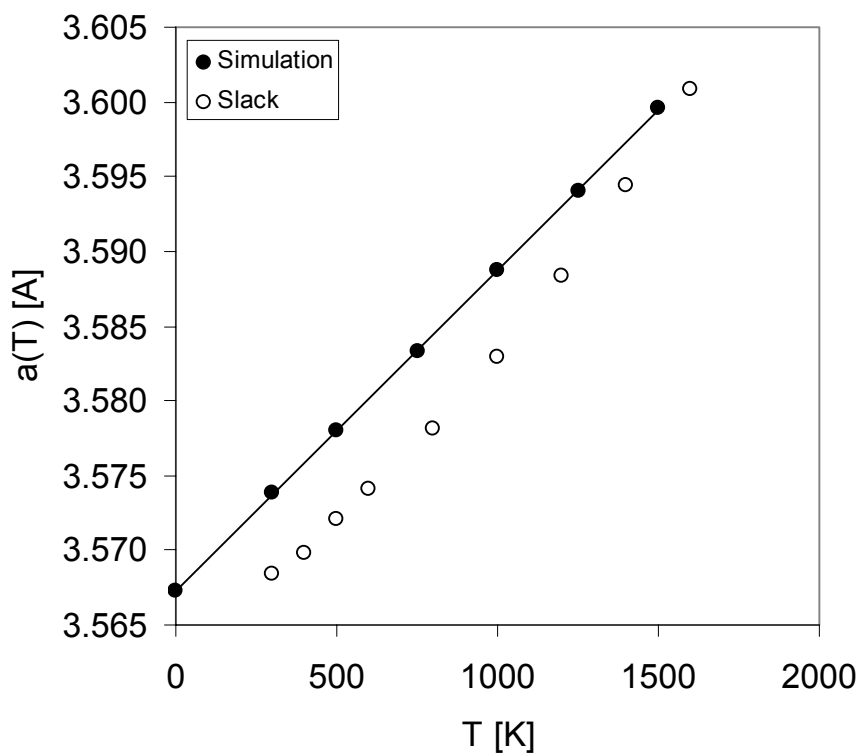


Figure 8-1. Lattice parameter of a single crystal diamond as a function of temperature. Experimental data is taken from the compilation of experimental data by Slack and Bartram.<sup>212</sup>

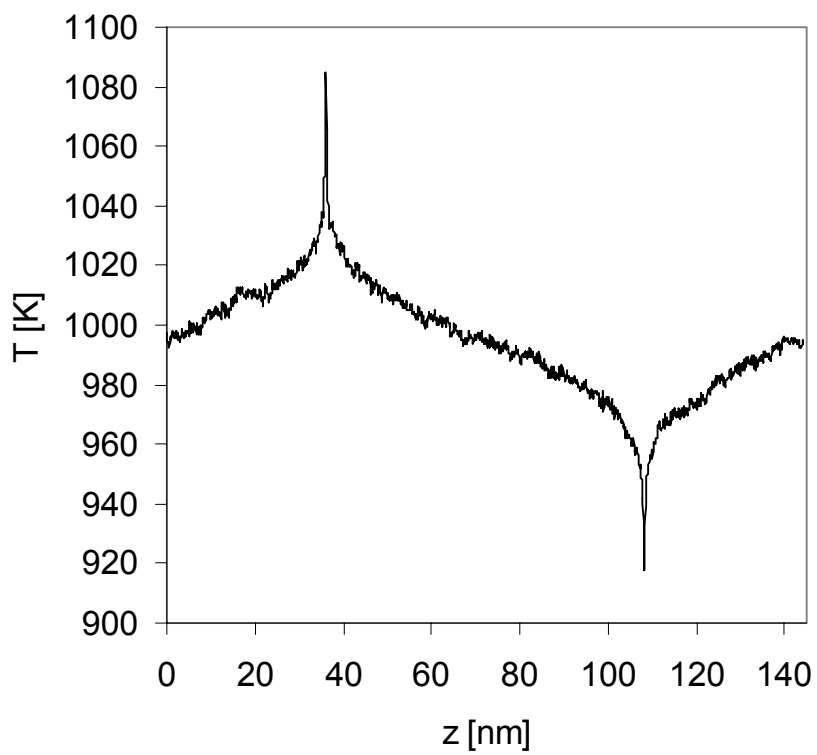


Figure 8-2. Temperature profile of  $4 \times 4 \times 400$  unit cells single crystal diamond after 4 ps.

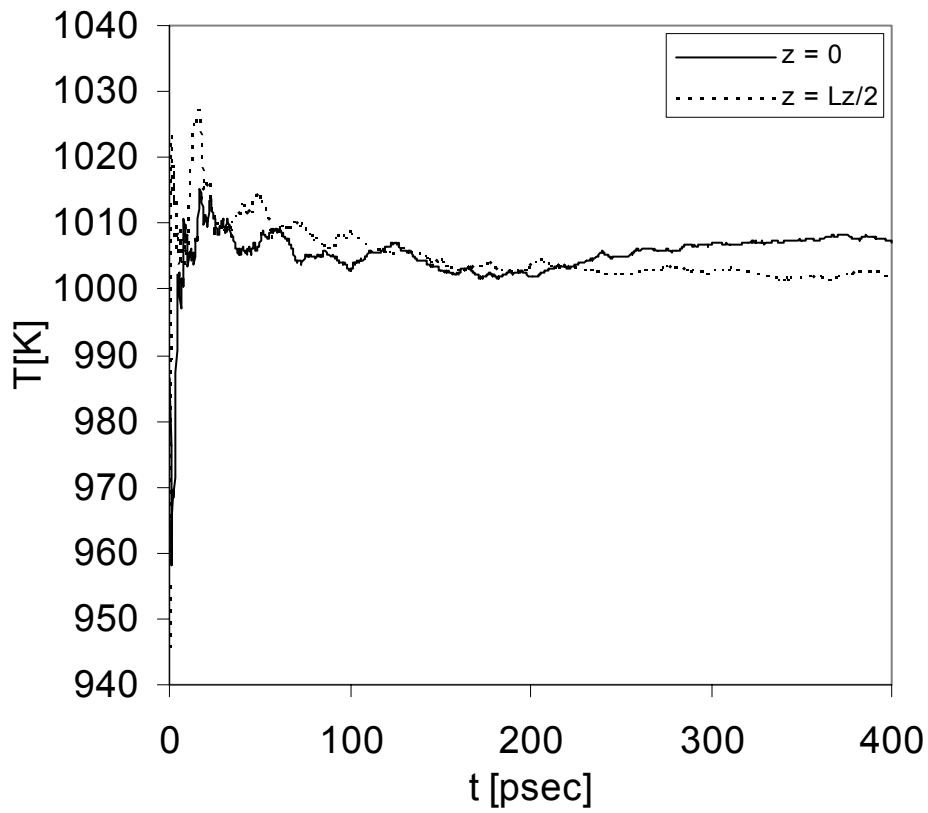


Figure 8-3. Time evolution of the temperature at the edge ( $L_z=0$ ) and center ( $z=L_z/2$ ) of the simulation cell.

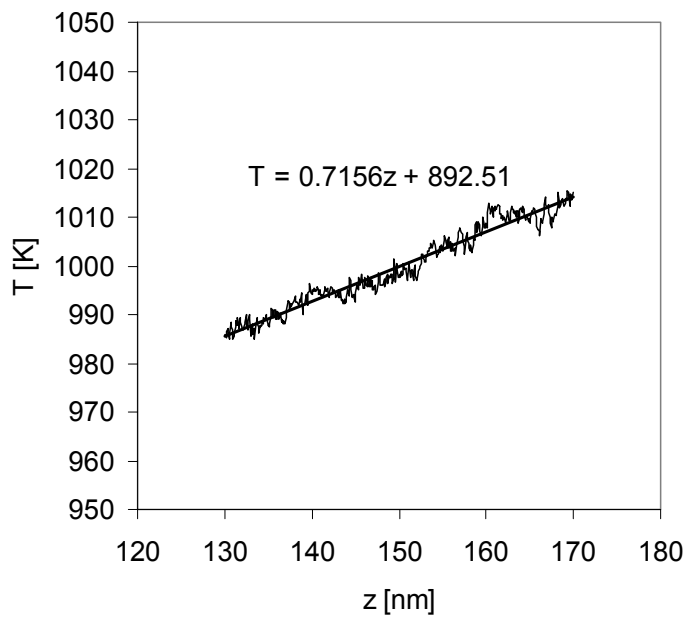
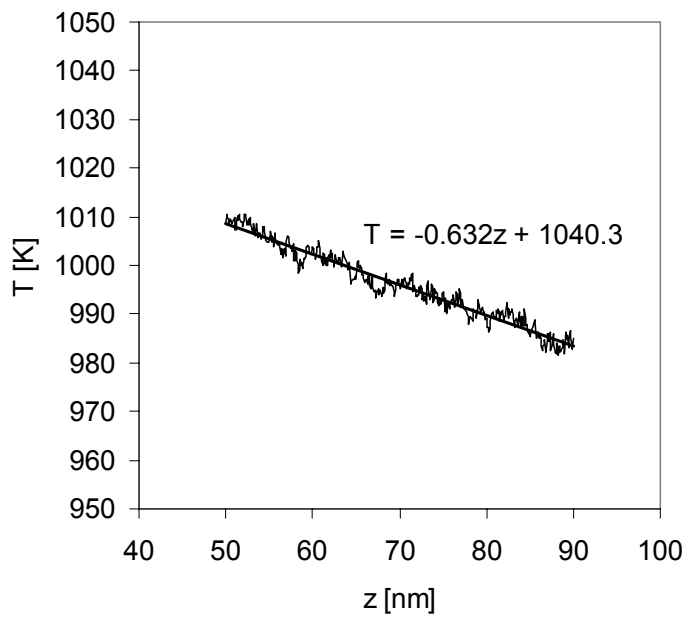


Figure 8-4. Slopes of the linear region of the temperature profile shown in Figure 8-2.

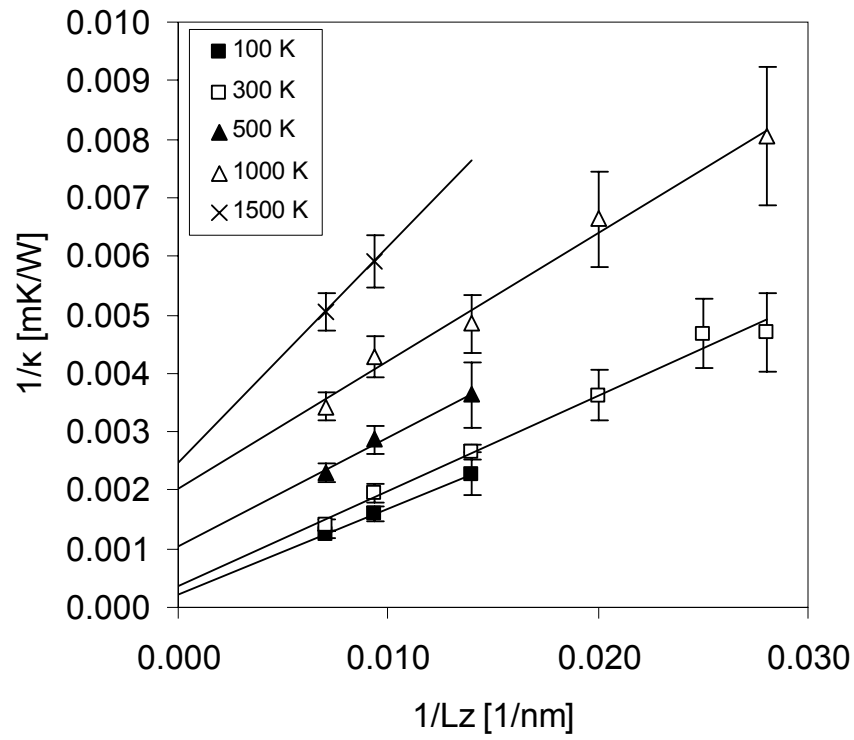


Figure 8-5. Slopes of the linear region of the temperature profile shown in Figure 8-4.

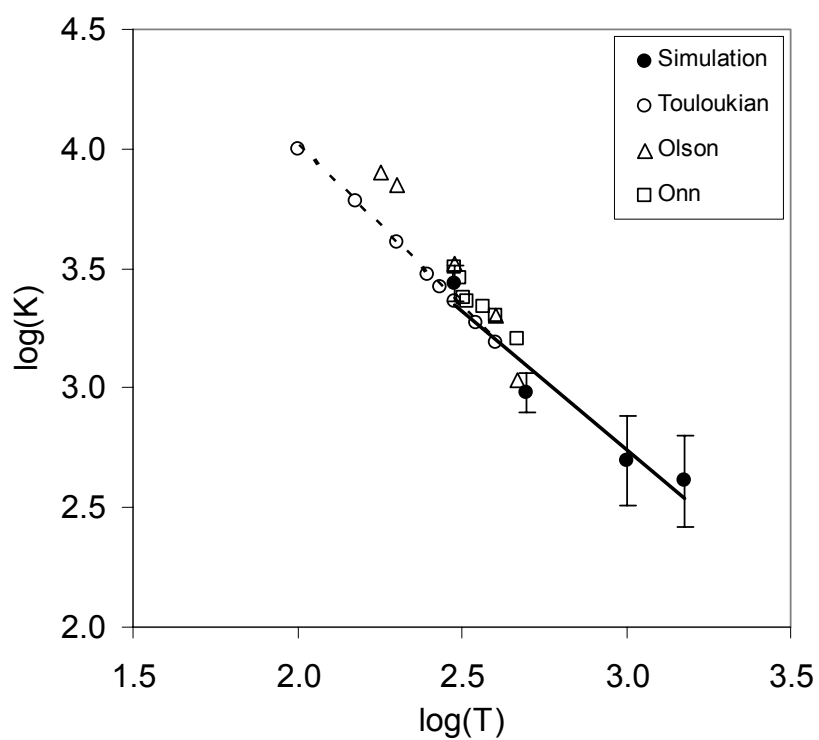
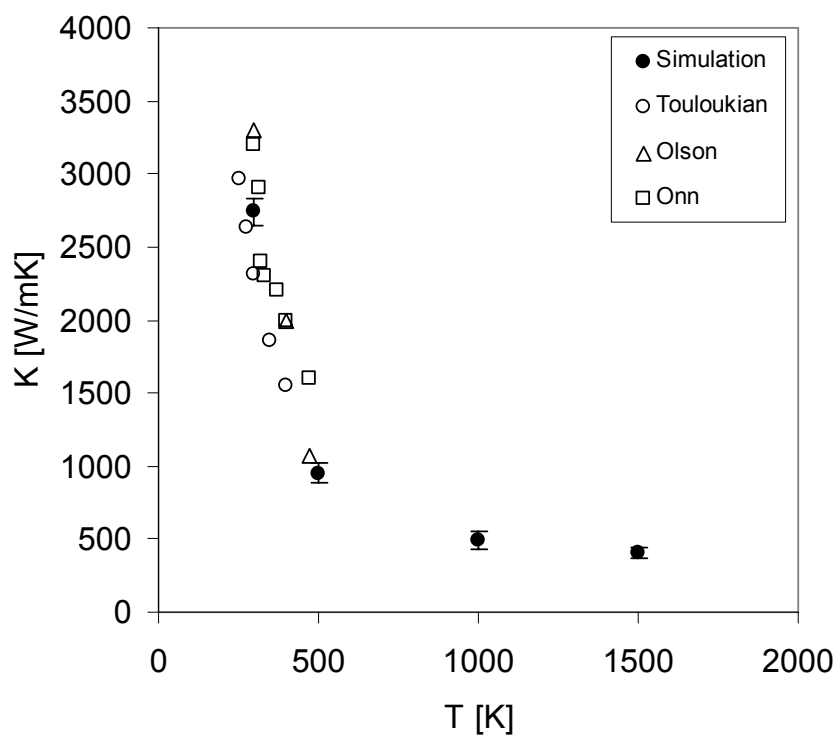


Figure 8-6. Thermal conductivity versus temperature in both linear and log-log plots from our simulation (filled) and the experimentals<sup>2</sup> (open).

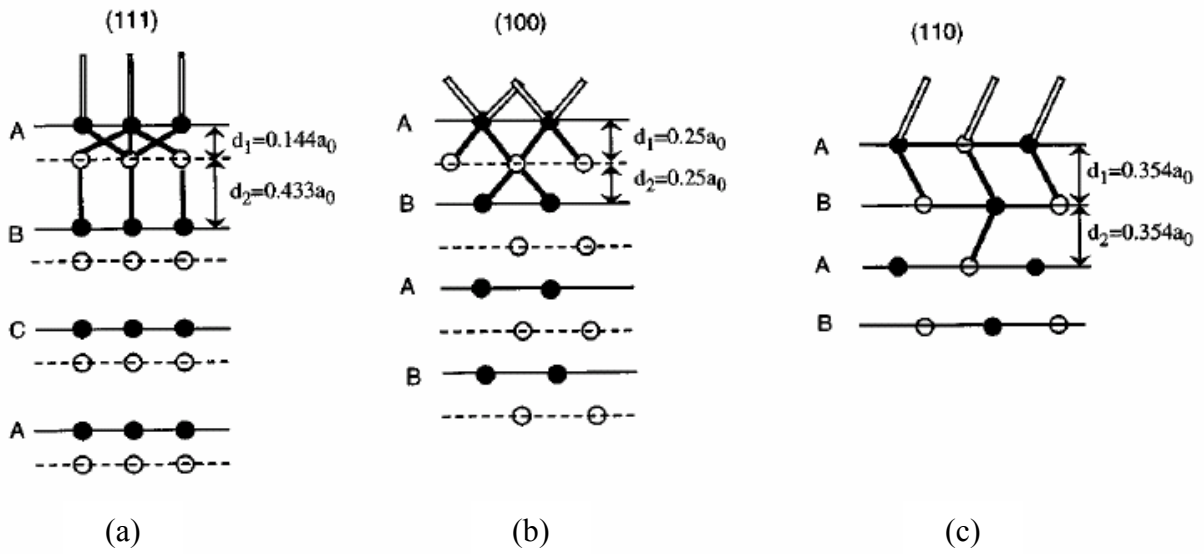


Figure 8-7. Bonding of atoms in diamond structure along (a) [111], (b) [100] and (c) [110] directions.<sup>124</sup> All points are carbon atoms. Filled and empty points are used to distinguish the carbon atoms at FCC sites and tetrahedral interstitial sites for clarity. Interplanar distances are given by  $d_1$  and  $d_2$  in the unit of lattice parameter. [Adapted from reference 124 (Figure 6).]

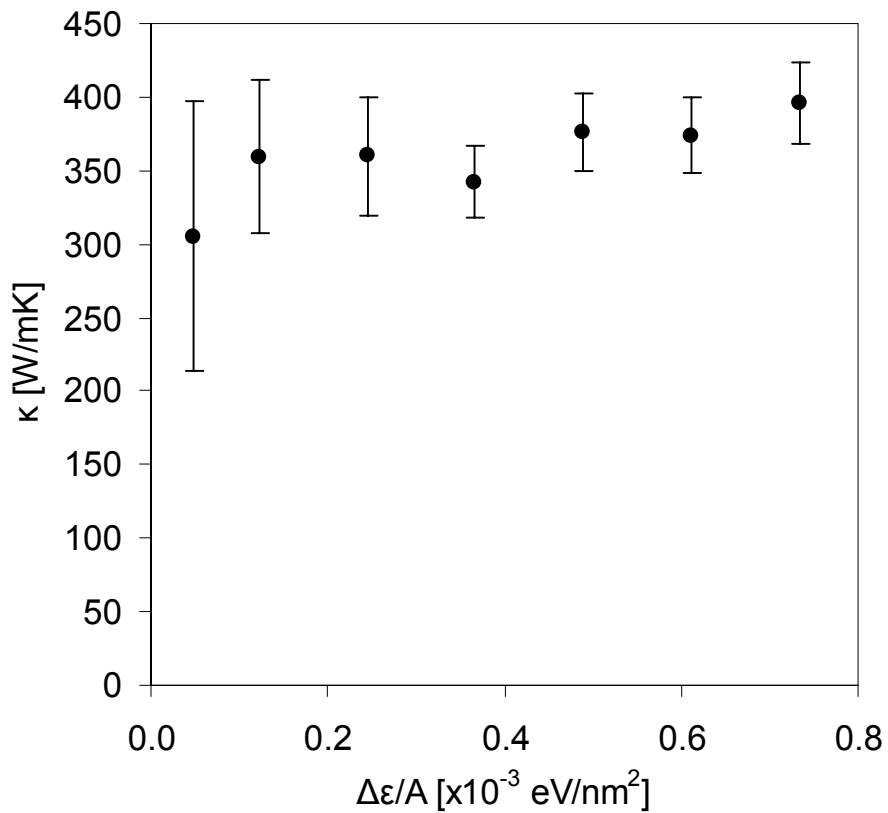


Figure 8-8. Thermal conductivity as a function of heat current density.

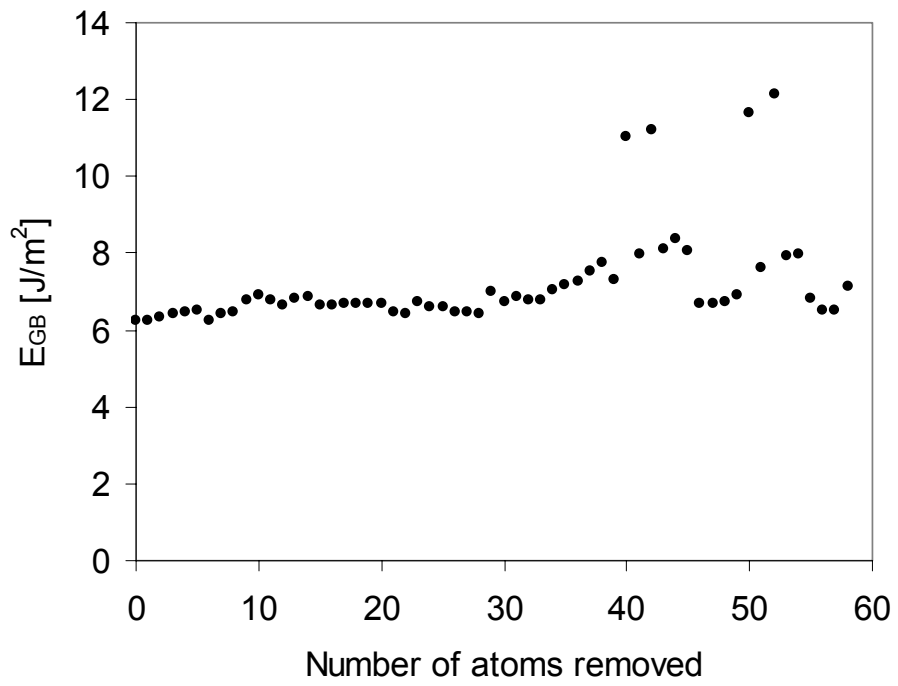


Figure 8-9. GB energy as a function of the number of atoms removed.

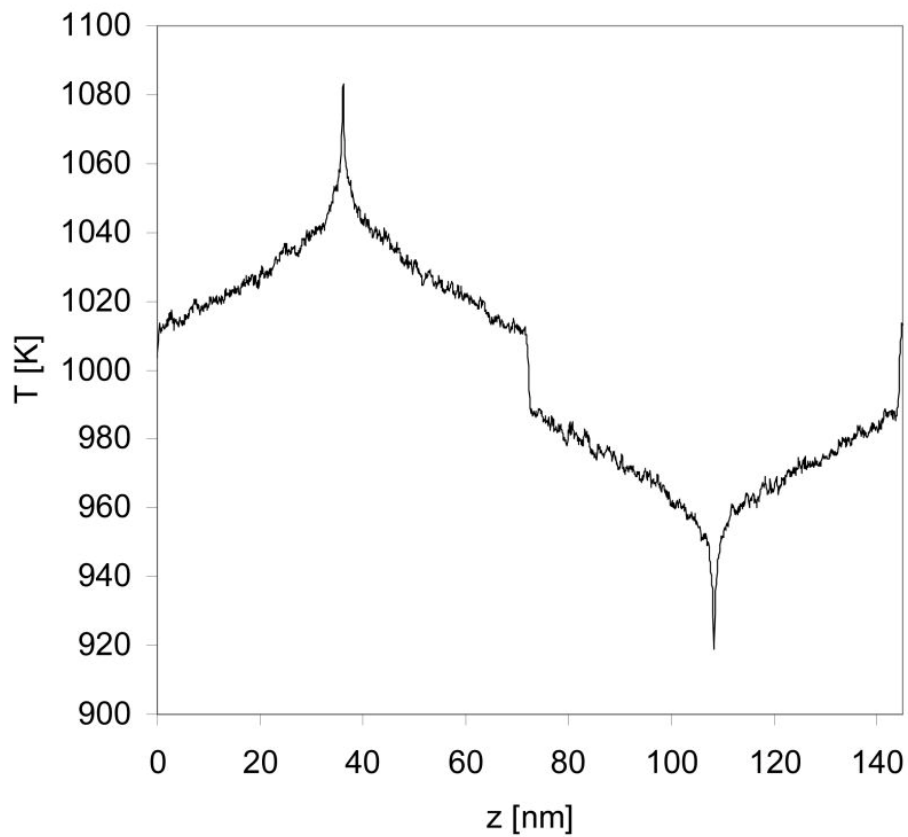


Figure 8-10. A typical temperature profile of a system with GBs, in this case (001)  $\theta=43.60^\circ$   $\Sigma 29$  symmetric twist boundaries. The GBs are located at the center and the edge of the simulation cell. The average temperature drop across the GBs is 22.5 K.

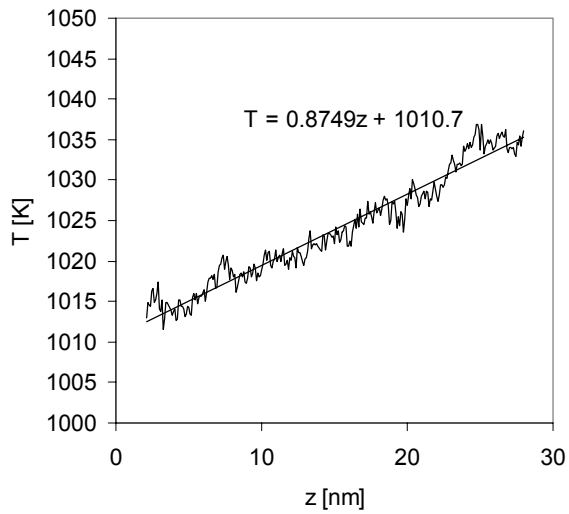
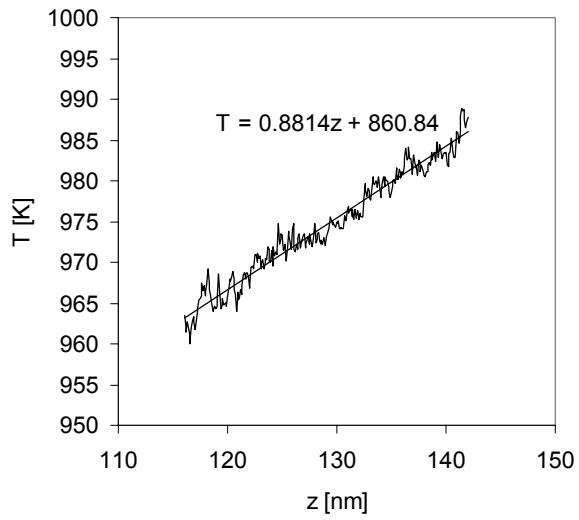
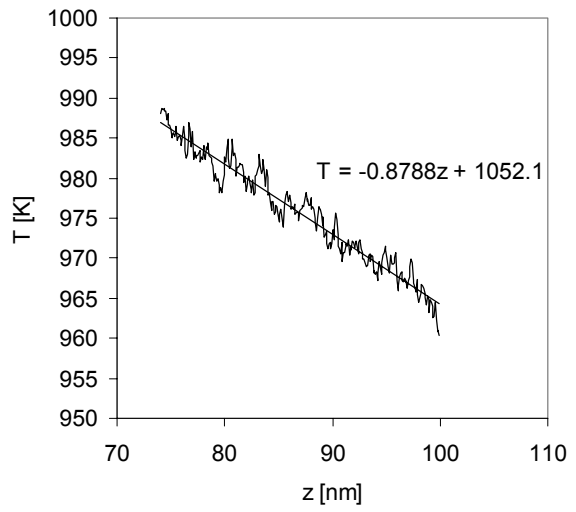
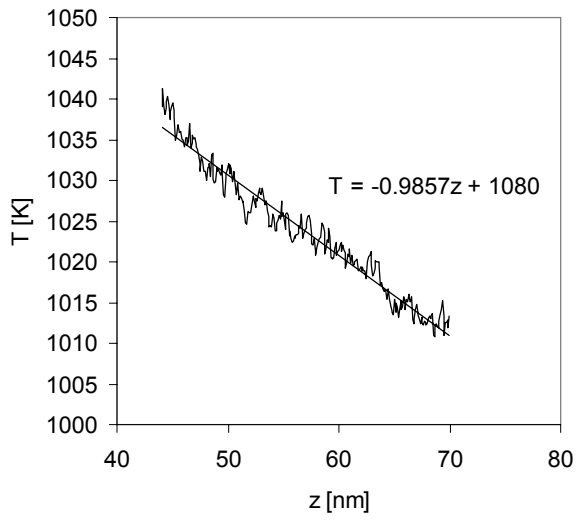


Figure 8-11. Linear temperature gradient from the temperature profile of the  $\Sigma 29$  (001)  $\theta=43.60^\circ$  GB.

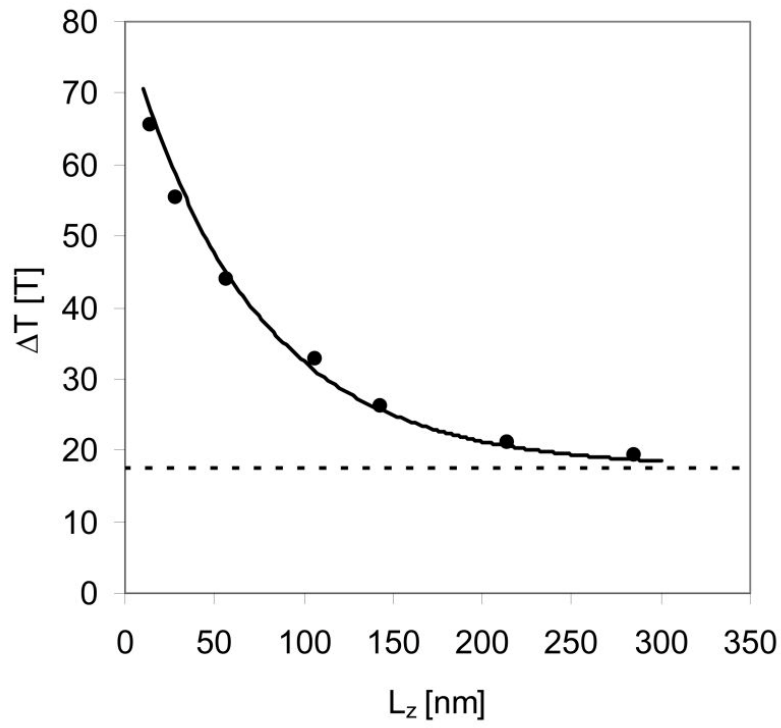


Figure 8-12. Size dependence of the thermal conductance of the  $\Sigma 29 \theta=43.60^\circ$  GB fitted to a shifted exponential.  $\Delta T_\infty$  is the asymptotic temperature drop in the infinite size limit indicated by the dotted line.

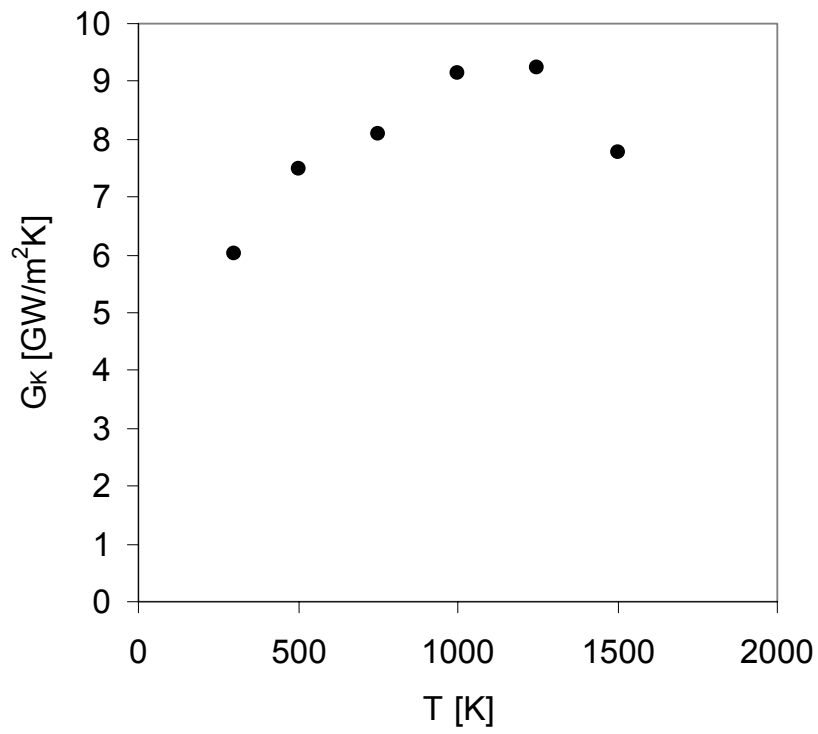


Figure 8-13. Temperature dependence of the thermal conductance of the (001)  $\Sigma 29$   $\theta=43.60^\circ$  GB. The conductance increases almost linearly with the temperature up to about 1250 K. The drop at 1500 K is due to a change in structure.

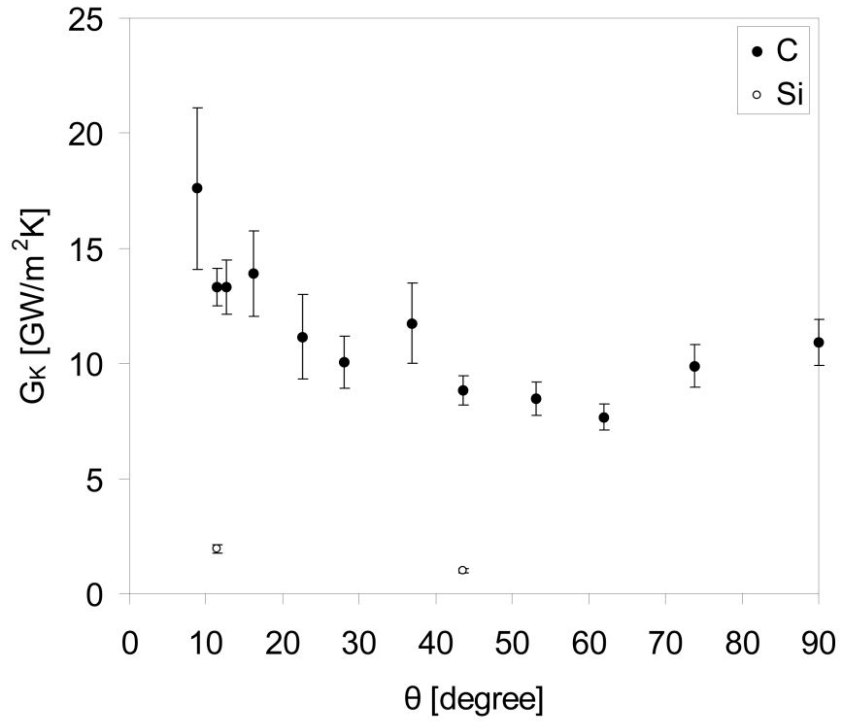


Figure 8-14. Thermal conductance as a function of twist angle for diamond (001) symmetric twist GBs from our simulations (filled circles), and corresponding Si GBs (open circles)<sup>77</sup>.

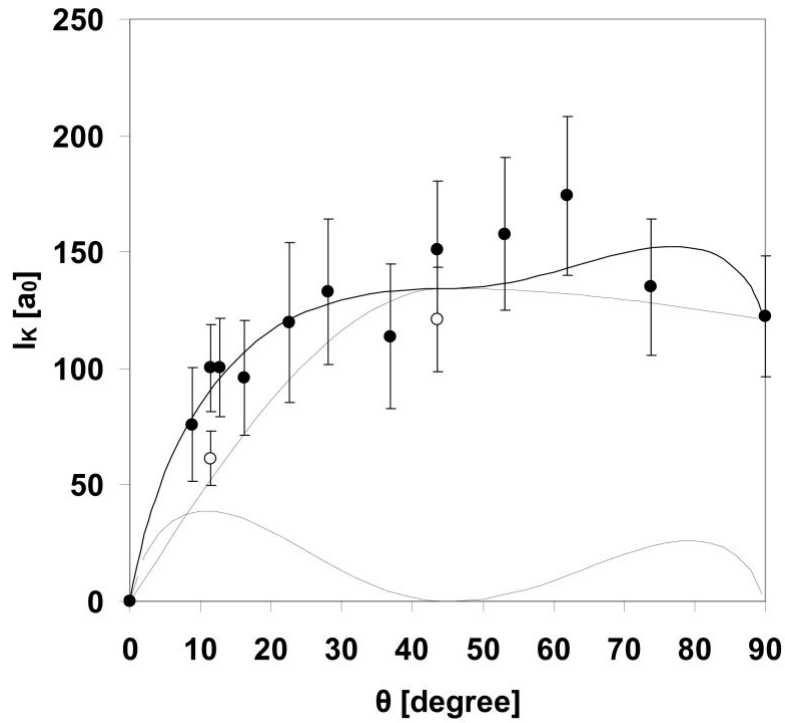


Figure 8-15. Kapitza length in units of their respective lattice parameters as a function of twist angle for both diamond and Si at 1000 K. Filled circles (●) are for diamond, and the open circles (○) are for Si. The solid line is the extended Read-Shockley fit to the diamond data. The dashed line is the dislocation core contribution, while the dash-dot line is the strain field contribution. Both points for Si are about  $30 a_0$  lower than for diamond.

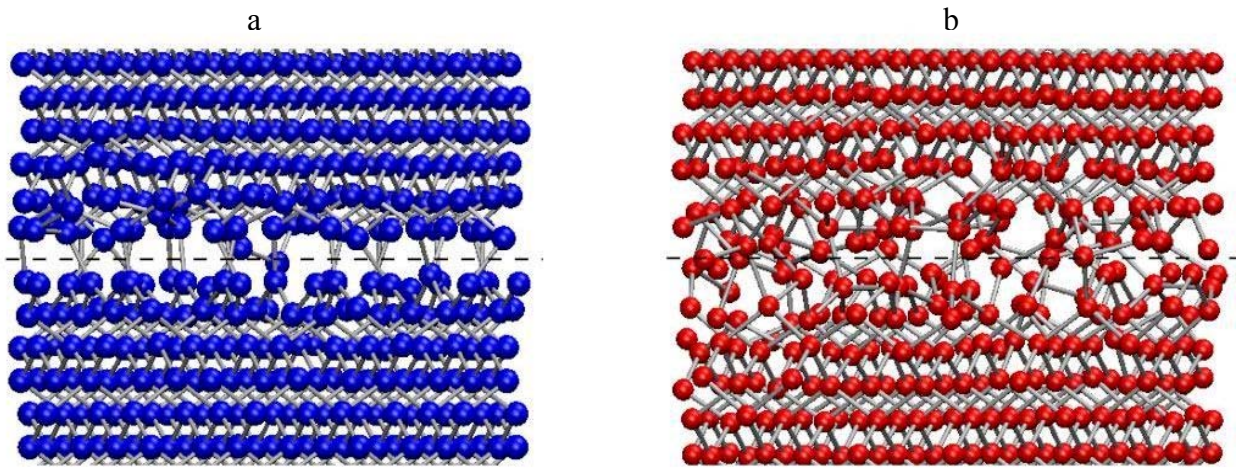


Figure 8-16. Cross section of  $\Sigma 29(001)$  GB in diamond (a) and Si (b). The freedom for C atoms to choose  $sp^2$  and  $sp^3$  hybridization results in the rather open structure within the GB. The dashed lines indicate the location of the GBs.

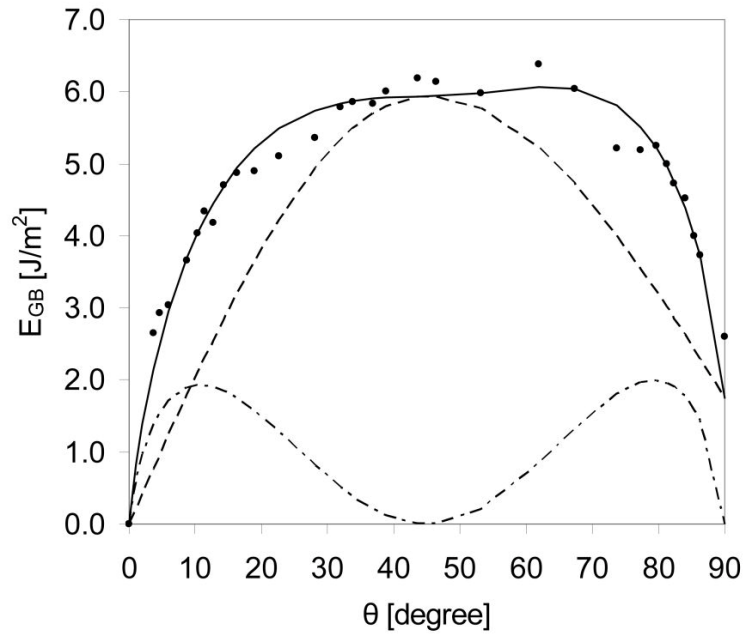


Figure 8-17. GB energy (symbols) and the fit to the extended Read-Shockley model (solid line). The dashed line is the dislocation core contribution to the GB energy. The dash-dot line is the strain field contribution.

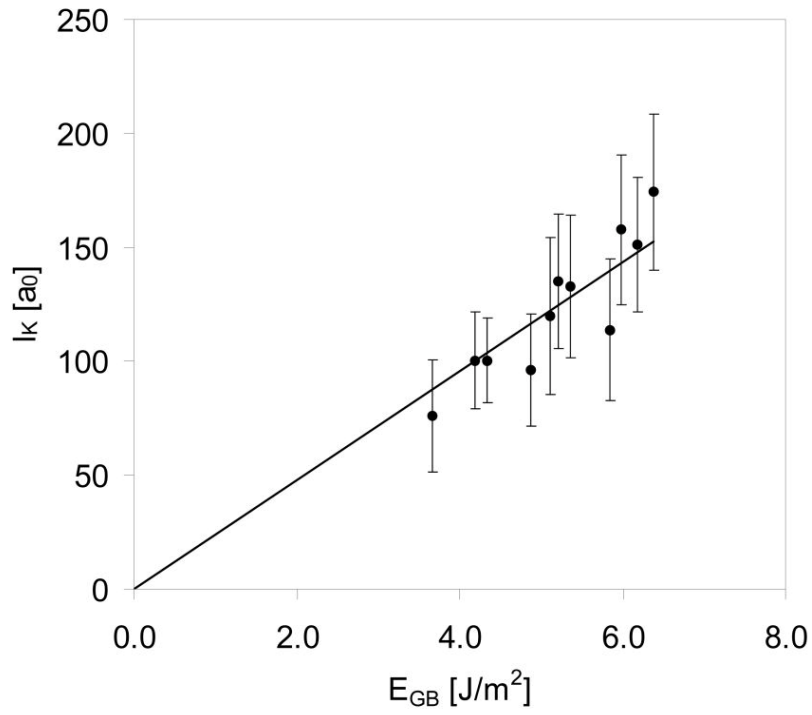


Figure 8-18. The Kapitza length is a reasonably linear function of the GB energy.

## CHAPTER 9 SIMULATIONS OF THERMAL TRANSPORT IN NANOCRYSTALLINE DIAMOND AND COMPARISON WITH EXPERIMENTAL RESULTS<sup>1</sup>

### Introduction

As mentioned in Chapter 1, diamond has the highest thermal conductivity of any known materials (the thermal conductivity of bulk single-crystal type IIa diamond is about 2200 W/m·K). It also exhibits exceptional optical, thermal, tribological and electrochemical properties<sup>220</sup>. Unfortunately, the use of single-crystal diamond is not feasible for many applications because of the cost. Ultrananocrystalline diamond (UNCD)<sup>54</sup> however, is an attractive alternative because it can be produced in thin film form at low processing temperatures with very little surface roughness.

UNCD coatings consist of diamond grains 3-5 nm in size with atomically abrupt high energy GBs.<sup>221</sup> UNCD exhibits many exceptional materials properties, including high hardness and Young's modulus<sup>209</sup>, low friction and low surface energies (as deposited)<sup>222</sup>, tunable electrical conduction via doping with nitrogen<sup>223</sup>, hermeticity, bio-inertness, and resistance to biofouling<sup>224</sup>. Given the extremely small grain size of UNCD, the thermal conductivity should not be nearly as high as natural polycrystalline diamond with large grain sizes. In fact, if the interfacial resistance at UNCD GBs were similar to heterophase interfaces (~150 MW/m<sup>2</sup>·K), one would expect the room temperature thermal conductivity to be similar to, or less than, that of thermal-barrier coating materials (*i.e.*, < 2 W/m·K). It is thus an open question as to whether UNCD thin films can be a useful thermal-management material for nano-applications.

---

<sup>1</sup> In this chapter, I describe a collaboration on thermal transport in ultrananocrystalline diamond, including experiments done by the group at Argonne National Laboratory, and simulation work by Watanabe and Phillpot at UF and Bodapati and Keblinski group at RPI. This work was published in Ref.

<sup>219</sup>M. A. Angadi, T. Watanabe, A. Bodapati, X. C. Xiao, O. Auciello, J. A. Carlisle, J. A. Eastman, P. Keblinski, P. K. Schelling, S. R. Phillpot, *Thermal transport and grain boundary conductance in ultrananocrystalline diamond thin films*, Journal of Applied Physics **99** (2006).

There have been numerous experimental studies of the thermal conductivity of diamond films prepared by chemical vapor deposition. This data is collected in Figure 9-1. While there is a clear trend for the thermal conductivity to decrease with decreasing grain size, there is considerable scatter. The dash-dot line is a fit to these experimental data using a simple thermal resistors model by Yang *et al.*<sup>78</sup>, which is the same effective medium model used in Chapter 5 for polycrystalline UO<sub>2</sub>. This model gives the experimentally measured thermal conductivity,  $\kappa$ , in terms of the bulk, conductivity,  $\kappa_0$ , the grain size,  $d$ , and the interfacial conductance,  $G_K$  as:

$$\kappa = \frac{\kappa_0}{1 + \frac{\kappa_0}{G_K \cdot d}} \quad (9-1)$$

The best fit to these experimental data yields a value of  $G_K=325 \text{ MW/m}^2\text{K}$ , a value that is only a little larger than typical values determined for heterophase interfaces<sup>225</sup>.

Essentially any structural imperfection will decrease the thermal conductivity of a sample. Thus, the significant scatter in these data for a single nominal grain size may be attributed to the microstructural variations arising from different film thickness, growth conditions, and system geometry. Moreover, the high fraction of GBs, typically containing disordered sp<sup>2</sup> bonded carbon, dangling bonds and other defects, can be expected to lower thermal conductivity for nanocrystalline diamond. (As described in the previous chapter, roughly 83 % of C atoms are 3 coordinated in MD simulation.) Interestingly, there are some data that give significantly higher values of the thermal conductivity than the trend in the rest of the data. Given that any structural defects lower the thermal conductivity, it is natural to interpret these values as being a better measure of the intrinsic thermal conductivity of polycrystalline diamond itself.

The consistent picture emerging from these studies is that the interfacial conductance of GBs in UNCD is extremely high, in excess of  $3000 \text{ MW/m}^2\cdot\text{K}$  at room temperature, more than ten times that of any material interface previously characterized.

### **Experimental Approach**

A series of UNCD films with thickness ranging from  $0.8 - 7.5 \mu\text{m}$  were synthesized by the Argonne group using microwave plasma chemical vapor deposition using argon-rich Ar/CH<sub>4</sub> plasma chemistries.<sup>226</sup> The films were deposited at  $800^\circ\text{C}$  on silicon wafers ( $500 \mu\text{m}$  thick) using a microwave plasma CVD system at  $1275 \text{ W}$  power and  $200 \text{ mbar}$  chamber pressure. To improve the seeding process and minimize porosity at the UNCD-substrate interface, for some samples,  $10 \text{ nm}$  thickness W layers were deposited by magnetron sputter-deposition, resulting in much denser UNCD microstructure and much smoother surfaces. While, initially, hydrogen ( $2-10\%$ ) was added to the chamber to stabilize the plasma, after reaching a chamber pressure of  $200 \text{ mbar}$  the gas composition was maintained at  $1.6\% \text{ CH}_4$  and  $98.4\% \text{ argon}$ . The growth rate was approximately  $0.5 \mu\text{m/h}$ . For each seeding technique (*i.e.*, growth on W/Si or on Si), visible ( $\lambda=632 \text{ nm}$ ) Raman spectroscopy indicated that samples of different thicknesses had similar film qualities. The films exhibit nanostructures characterized by  $3-5 \text{ nm}$  diameter diamond grains separated by GBs that contain a mixture of  $\text{sp}^3$  and  $\text{sp}^2$  bonding.<sup>226</sup> The hardness, Young's modulus, refractive index, and friction properties are all essentially equivalent to natural diamond<sup>54</sup>; indeed several materials properties of UNCD have been shown to be superior those of natural diamond.<sup>227</sup>

The thermal conductivity was measured using the  $3\Omega$  method<sup>228</sup> and analyzed using the offset model.<sup>229</sup> According to this model, the film is treated as a thermal resistor, which results

in an experimental  $\Delta T$  vs. frequency curve that has the same shape as the curve calculated for uncoated silicon but is offset by an amount  $\Delta T_f$  given by

$$\Delta T_f = \frac{P \cdot t}{l \cdot \kappa \cdot 2b}, \quad (9-2)$$

where  $t$  is the film thickness,  $\kappa$  is the thermal conductivity of the film,  $l$  is the length of the metal line,  $b$  is the width of metal line, and  $P$  is the amplitude of the ac power generated in the metal line.  $\Delta T_f$  represents the difference between the thermal signal for the UNCD coated substrate and the bare silicon substrate. The UNCD film thickness was determined by cross-section SEM. An important assumption in the analysis employed here is that the thermal transport is one-dimensional (*i.e.*, the rate of heat transfer in the direction normal to the film, into the substrate, is much larger than in the plane of the film). Since we observe that the thermal conductivity of the UNCD is small compared to that of silicon, this condition is met.

### **Experimental Results**

Because the  $3\Omega$  experimental technique measures the conductivity through the film, in addition to the effects of the UNCD GBs, it includes the effects of the interface between the substrate and the UNCD film. To specifically determine the effects of the heterophase interface, the Argonne group grew films both on a Si substrate directly, and on a thin (10 nm) tungsten layer grown on the Si substrate.

Thermal conductivities obtained by the Argonne group for a series of UNCD thin films grown on silicon substrates are shown as circles in Figure 9-2. We first note that for all film thicknesses, the measured thermal conductivity ranged from as little as 1.2 W/mK to as high as 12 W/m·K. Interestingly, as shown in Figure 9-1, this lower value, obtained for thinner films of UNCD grown directly on Si is quite consistent with the extrapolation of the best fit to the previous experimental results. An SEM analysis of the thin film microstructure of these films

(inset a to Figure 9-2) shows that there are large voids at the interface. It thus seems that for these thin films the intrinsic thermal properties of the diamond GBs are not being measured. By contrast, inset B shows that for UNCD grown on an intermediate W layer, there is no porosity at the interfaces, a consequence of the greatly enhanced initial nucleation density at the UNCD/W interface, thereby inhibiting the formation of voids seen at the UNCD/Si interface.<sup>230</sup> For these films  $\kappa \sim 9\text{-}10$  W/m·K is obtained; this higher value can be attributed to the absence of porosity. Moreover, the considerable increase in the thermal conductivity of the UNCD/Si films over the thickness 3.5 – 5 mm can then be understood as the result of a change in the interface structure from porous to non-porous. These films yield thermal conductivities as high as 12 W/m·K, which can be taken as an estimate of the lower bound to the true intrinsic thermal conductivity of UNCD. This best estimate is also shown in Figure 9-1, and is a considerable outlier compared with most of the previous experiments.

Recall that Yang's model (Equation 5-4) gives the interfacial conductance by,

$$G_K = \frac{1}{d} \frac{\kappa_0 \kappa}{\kappa_0 - \kappa}.$$

For an average grain diameter of 4 nm, a bulk conductivity of 2200 W/m·K, and a measured thermal conductivity of 12 W/m·K,  $G_K$  is calculated to be 3000 MW/m<sup>2</sup>·K at the measurement temperature of 310 K. This value is more than an order-of-magnitude larger than any previously reported room-temperature GB or heterophase interface conductance<sup>78, 225</sup>.

It should be noted that  $G_K$  was calculated from the measured thermal conductivity values under the assumption that Equation 5-4 is valid. An assumption implicit in Equation 5-4 is that the UNCD grain interiors have the conductivity of single crystal diamond. This assumption is supported by previous HREM observations that have indicated that UNCD grain interiors are indistinguishable in structure from crystalline.<sup>3,4</sup>

It can be concluded from these experimental studies that UNCD allows an estimate of the intrinsic thermal properties of diamond GBs. However, the value obtained for  $G_K=3000 \text{ W/m}^2\text{K}$  is startlingly high compared with other materials systems.

### **Simulation Results**

To provide additional credibility for this unusually high experimental value for Kapitza conductance obtained in the Argonne groups experiments, atomic-level simulations of the thermal conductivity of both model diamond nanostructures of a similar grain size to the experimentally investigated systems, and of an individual grain boundary, representative of those in nanocrystalline diamond have been performed. The value of the simulations is that we can investigate systems without pores or impurities, thereby examining the intrinsic thermal-transport properties of diamond.

We have constructed two model diamond nanocrystals with grain sizes of 2 nm and 3 nm respectively; recall that the grain size in UNCD is  $\sim 3.5 - 5 \text{ nm}$ . They are constructed in the same method as  $\text{UO}_2$  polycrystals (Chapter 5): 3 dimensional columnar grains rotated in the plane of the texture. The only difference from the  $\text{UO}_2$  polycrystals is that there is no restriction of charge neutrality of the system. In all of our simulations on both nanocrystals and individual GBs, diamond is described by the Tersoff many-body potential as described in Chapter 1. The basic bulk single crystal properties of diamond were established and described in the Chapter 7. The polycrystalline diamond structures were constructed by Watanabe, while the thermal transport simulations were performed by Bodapati at RPI.

To determine the thermal conductivity of our model nanostructures, the direct method was used (Chapter 3). The resulting temperature profile for the 2 nm system is shown in Figure 9-3.

The thermal conductivity determined from this system, using Fourier's Law  $J = -\kappa \frac{dT}{dx}$ , is  $\kappa=9.2$

W/m·K; for the 3 nm grain size, we obtain 13.8 W/m·K. This 50% increase in thermal conductivity on increasing the grain size by 50% is consistent with Equation 9-2 with the bulk conductivity being very high and the interface conductivity being independent of grain size. These calculated values for the thermal conductivity are remarkably consistent with the experimental results for UNCD (at a grain size of 3-5 nm) of 12 W/m·K, described in the last section. Using Equation 5-4, these simulation data yield an average interfacial conductance of  $G_K = 4600 \text{ MW/m}^2\cdot\text{K}$  for the tilt boundaries in our model nanocrystal. We have used this estimate of the intrinsic interfacial conductance obtained from simulation to give the solid line in Figure 9-1. This gives a slightly higher predicted value of the thermal conductivity of UNCD than we found experimentally, and a higher value than almost all of the experimental values at any grain size.

Because the simulation estimate of the interfacial conductance is based on the same rather simple analysis of the model nanocrystal as the experimental data (*i.e.*, Equation 5-4), it is highly desirable to have a direct measure of the interfacial resistance itself. While this is not possible experimentally, simulation can again help us (Chapter 8). Figure 9-4 shows the temperature profile through the GB at room temperature. The heat source and sink are at the left and right respectively. The temperature drop at the interface,  $\Delta T$ , is 25.4K. The smooth temperature decrease in the diamond perfect crystal is characteristic of the bulk thermal conductivity. The imposed heat current was  $217 \text{ GW/m}^2$ , allowing us to determine the Kapitza conductance to be  $8500 \text{ MW/m}^2\cdot\text{K}$ . Conductance only varies by approximately a factor of two over a wide range of twist angles (Chapter 7), indicating that the specific choice of the grain-boundary twist angle is not important for this discussion.

This calculated value of the Kapitza conductance of an isolated GB is somewhat larger than that deduced from the simulations of the model nanocrystals. This is attributable to (a) the bicrystal contains a single (001) twist boundary, whereas there are a number of different (001) tilt boundaries in the nanocrystal, and (b) the more complicated microstructure in the model nanocrystals.

### Discussion

The results from experiment and simulation provide a reassuringly consistent picture of interfacial thermal transport in diamond, indicating that the interfacial conductance is at least 3000 MW/m<sup>2</sup>·K, more than ten-times that previously seen: specifically, in reviewing the literature, Cahill *et al.*<sup>225</sup> noted that the interfacial conductance for a number of heterophase interfaces spanned the range of 20-200 MW/m<sup>2</sup>·K. In the only previous study of a homophase system, Yang *et al.* found that the interfacial resistance of yttria-stabilized zirconia lies at the high end of this range<sup>78</sup>.

When we put the diamond interfacial conductance into the appropriate context, however, the interfacial conductance, though larger than any previous value, is not in fact anomalously large. As discussed in Chapter 7, materials-independent measure of the interfacial conductance is provided by the Kapitza length  $l_K = \kappa_0 / G_K$ , which measures the thickness of perfect crystal offering the same resistance to heat transport as the interface. Taking  $\kappa_0 = 2200 \text{ W/m}\cdot\text{K}$  and  $G_K = 3000 \text{ MW/m}^2\cdot\text{K}$  for UNCD, yields  $l_K = 730 \text{ nm}$ . This is surprisingly similar to the Kapitza length for the aluminum-alumina interface<sup>225</sup>:  $G_K = 170 \text{ MW/m}^2\cdot\text{K}$  and  $\kappa = \frac{1}{2}(\kappa_0^{\text{Al}} + \kappa_0^{\text{alumina}}) = \frac{1}{2}(237 + 36) = 150 \text{ W/m}\cdot\text{K}$ , gives a Kapitza length of  $l_K = 800 \text{ nm}$ .

The determination of the Kapitza length in diamond to be of the order of 1  $\mu\text{m}$  is consistent with thermal transport measurements of conventional diamond polycrystalline films which have

demonstrated that to reach bulk-like conductivities grain size has to be larger than several microns. In this large grain size limit, thermal resistance due to GBs becomes small by comparison with the intrinsic bulk resistance<sup>53</sup>.

It is interesting to note that a UNCD conductivity of 12 W/m·K is similar to the high-end conductivity of what Morath *et al.* referred to as amorphous diamond<sup>231</sup>, an sp<sup>3</sup>-bonded glass structure. Both materials have much higher thermal conductivities than either diamond-like carbon (a sp<sup>3</sup>-bonded glass structure but with a large fraction of bonds terminated by hydrogen), or amorphous carbons containing significant sp<sup>2</sup> bonding component<sup>232</sup>. This comparison indicates that while crystalline grain interiors in UNCD enhance thermal conductivity with respect to amorphous carbon structures, the significant sp<sup>2</sup>-bonding component in UNCD GBs offer higher thermal resistance than the corresponding layer of an amorphous diamond sp<sup>3</sup>-bonded structure.

We have determined values of 12 W/m·K, 3000 MW/m<sup>2</sup>·K, and 750 nm for the room temperature thermal conductivity, interfacial conductance, and Kapitza length, respectively of ultrananocrystalline diamond. The interfacial conductance is an order of magnitude higher than any previously reported, but the relative interface conductance compared is not anomalously high, as indicated by a characteristic Kapitza length similar to, or larger than, that of other materials.

Although the thermal transport coefficient of UNCD is not as high as that of polycrystalline diamond with larger grains, the combination with a much smoother surface morphology makes these films very attractive for many applications. These include thermal spreaders for applications such as cooling of microchips in the next generation of high density CMOS devices, control of temperature in the heads of magnetic storage media, and MEMS and

NEMS structures with combined optimum mechanical and thermal stability properties. Diamond structural layers with different grain sizes could be integrated together into a microsystem to effectively pipe heat to specific locations.

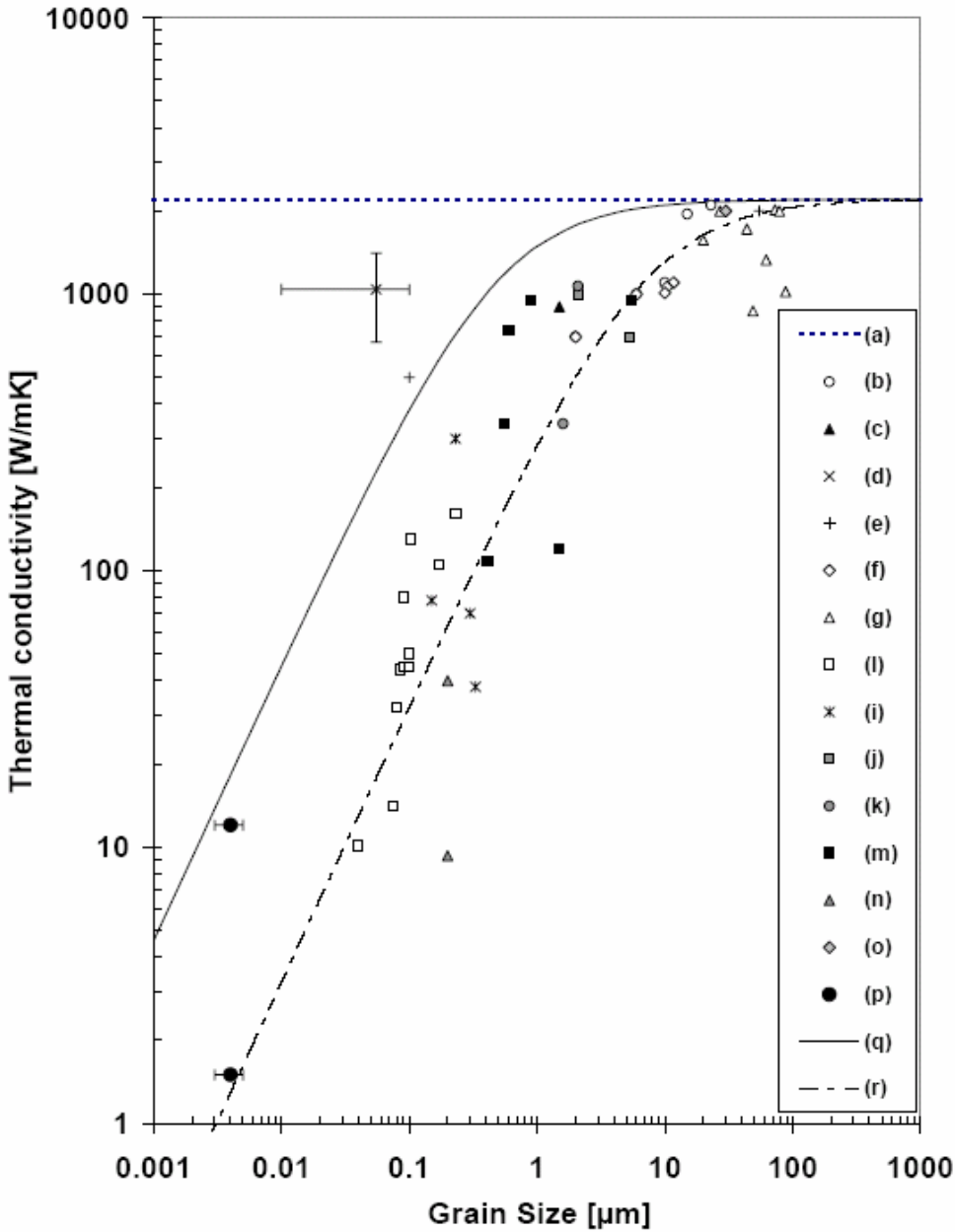


Figure 9-1. Compilation of diamond thermal conductivity versus grain size  $d$ . (a) typical single crystal, (b) Ref: 233 (c) Ref: 234 (12) (d) Ref: 235 (e) Ref: 236 (f) Ref: 237, (g) Ref: 238, (h) Ref: 239, (i) Ref: 240, (j) Ref: 52, (k) Ref: 241, (l) Ref: 242, (m) Ref: 239, (n) Ref: 243, (o) Ref: 244, (p) data from this study, (q) Equation (9-1) for  $G_K=4600$  MW/m<sup>2</sup>·K obtained from simulation of UNCD, (r) Fit of Equation 9-2 to data (a) – (o) yields  $G_K=325$  MW/m<sup>2</sup>·K. Compilation and analysis by Watanabe.<sup>219</sup>

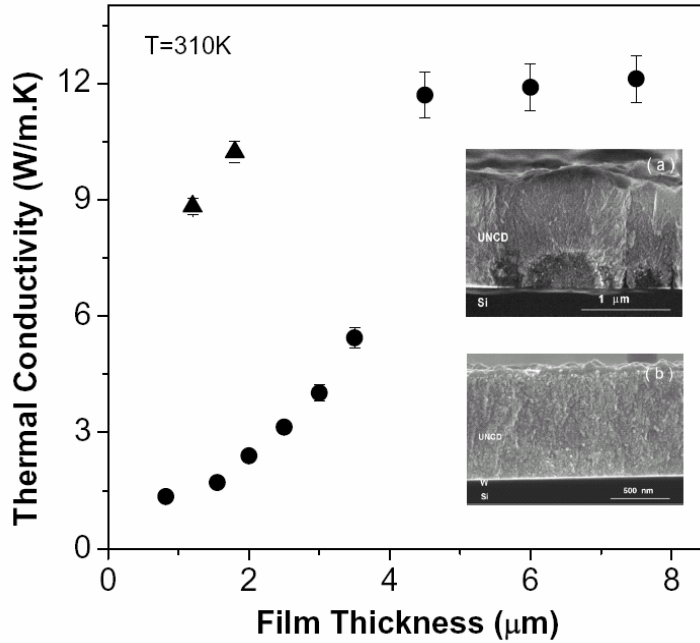


Figure 9-2. UNCD thermal conductivity as a function of film thickness. ▲ UNCD films grown on W/Si; ● UNCD films on Si. Insets show SEM cross-sections the film structure: (a) UNCD/Si with voids and, (b) UNCD/W/Si with a dense interface. Each data point corresponds to a single sample of the indicated average grain size. Each error bar indicates the standard deviation from multiple measurements of that particular sample. This work is done by the Argonne group.<sup>219</sup>

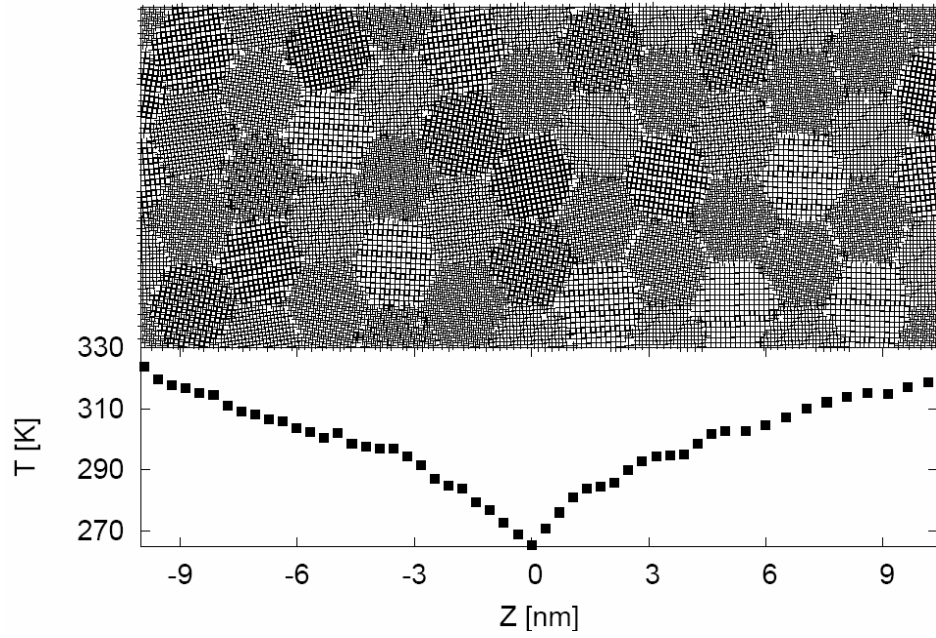


Figure 9-3. Microstructure (top) and temperature profile (bottom) of polycrystalline diamond. Model structure was created by Watanabe, the thermal conductivity simulation was performed by Bodapati at RPI.<sup>219</sup>

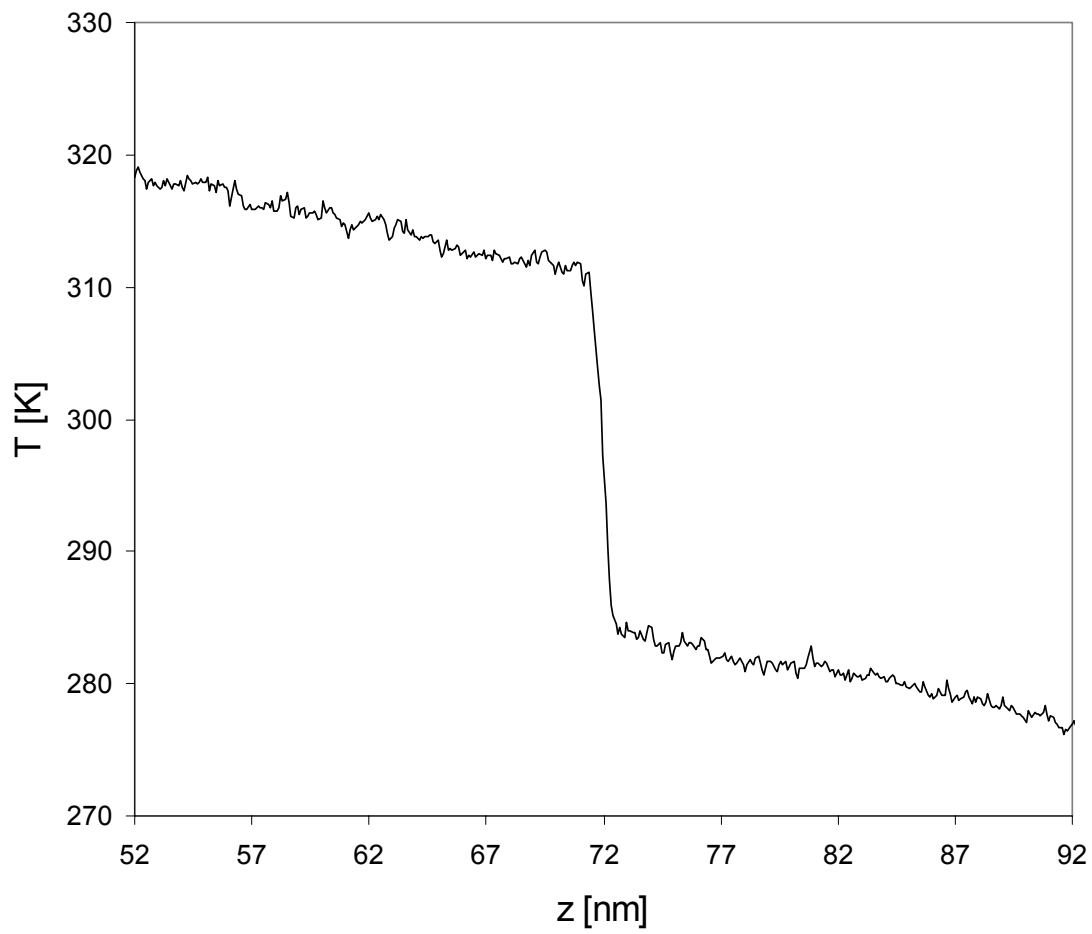


Figure 9-4. Temperature profile through a diamond  $\Sigma 29$  (001)  $\theta=43.60^\circ$  twist GB determined by simulation.

## CHAPTER 10 CONCLUSIONS

A systematic investigation of the thermal transport properties in  $\text{UO}_2$  and diamond has been done using atomic level simulation technique. The main focus was to establish the basic physical properties of bulk single crystal materials, and to elucidate the effect of defects such as point defects and GBs on the thermal transport of  $\text{UO}_2$  and diamond. A number of contributions to our understanding of heat transfer in defected crystalline solids have been made.

The thermal transport properties of  $\text{UO}_2$  single crystal was established using MD simulation technique. The theory of phonon mediated heat transfer was used to relate anharmonicity and thermal conductivity of dielectric solid. Results were compared with available experimental data and good agreement was obtained.

The temperature and grain size dependence of the thermal conductivity of polycrystalline  $\text{UO}_2$  was investigated and characterized. An effective medium model for polycrystalline solids was used to calculate the interfacial conductance. Analysis of the Kapitza length showed that the interfacial resistance significantly dominates the bulk thermal conductivity of very fine grain polycrystalline  $\text{UO}_2$ .

The dependence of the thermal conductivity of on off-stoichiometry in  $\text{UO}_{2\pm x}$  was obtained at 800 K and 1600 K. The thermal conductivity of  $\text{UO}_{2+x}$  was found to decrease with increasing concentration of the oxygen interstitials and eventually reach a plateau when  $x > 0.125$ . At low concentrations, the effect of oxygen vacancies and interstitials to thermal transport were found to be similar. Analysis using the theory of disordered solid supports this similarity: there were no significant difference in the vibrational modes at low concentrations of oxygen defects. A small fraction of localized modes was found only at very high concentration of interstitials. In

addition, it was found that the effect of different U isotopes on the thermal transport of  $\text{UO}_2$  was almost negligible.

A molecular dynamics simulation code for the radiation damage simulations was developed. The in-house MD code was modified to include ZBL potential, variable time step, and Berendsen thermostat. Each modification was independently verified.

A systematic study of the interfacial conductance of the diamond GB was performed. The thermal conductance of the twist grain boundary was obtained as a function of twist angle. The grain boundary energy was found to follow the extended Read-Schockley (ERS) model. An ERS type model for the interfacial conductance was developed. The relation between the grain boundary structure and interfacial conductance was characterized through the comparison of GBs in Si and diamond.

Consistent values of the interfacial conductance were obtained from both experiment and two simulations with distinct microstructures. The coordination number analysis also showed agreement between the experiment and simulation.

Thermal transport in both  $\text{UO}_2$  and diamond are mediated by phonons as described in Chapter 1 and 2. Phonon mediated heat transfer is significantly affected by the presence of point defects and grain boundaries regardless of what the material was. The anharmonic analysis shown to work on  $\text{UO}_2$  should apply to any electrical insulators because the theory is based on the phonon mediated thermal transport theory in bulk single crystalline solid.

Both diamond and  $\text{UO}_2$  grain boundaries significantly reduced the thermal conductivity of the solid. Comparing the ratios of the thermal conductivities of polycrystal of similar grain sized to the single-crystal values, we find that the ratio is about  $\sim 12/500 = 1/80$  for diamond and  $\sim 2/35 = 1/12.5$  for  $\text{UO}_2$ . Thus diamond grain boundaries of more significant obstacles to heat

flow than do GBs in  $\text{UO}_2$ . The reason for this difference is most likely the difference in mean free path in these two materials. Since diamond naturally had larger mean free path, the reduction in thermal conductivity is more pronounced.

A comparison of the effects of point defects and grain boundaries is instructive;  $\text{UO}_{2.125}$  gives a minimum thermal conductivity of  $\sim 1.5$  W/mK at 300 K. By contrast polycrystalline  $\text{UO}_2$  shows a thermal conductivity of  $\sim 0.7$  W/mK at 300 K. This is interesting since the effect of the oxygen interstitial has been saturated and it seems that the thermal conductivity cannot be lowered with further increases in off-stoichiometry. However, the 3.8 nm grain size polycrystalline  $\text{UO}_2$  has a thermal conductivity of almost half this value. This suggests that GBs are inherently stronger scatterers of phonons than oxygen interstitials.

This work also suggests a number of directions for future work. One of the most important improvements one can make on the  $\text{UO}_2$  model is the interatomic potential. If the thermal expansion and bulk modulus are improved, the thermal conductivity of  $\text{UO}_2$  should be able to give values much closer to the experimental data.

Since the effects point defects and GBs have been identified separately, it would be interesting to see what the effect of the combination of the two. How does the interaction of the defects affect the thermal transport? What is the effect of defects in GBs on the thermal conductivity?

The same question applies to the radiation damage. Since real  $\text{UO}_2$  has point defects and GBs, the effects of the presence of point defects and/or grain boundaries in radiation damage are of significant importance. Will these defects reduce or enhance the radiation resistance?

In connection to both to the thermal transport and radiation damage, the effect of defect clusters will be interesting to look at. Radiation damage in  $\text{UO}_2$  will create significant number of

defects with a variety of sizes and distributions of defect clusters. Can we categorize and make meaningful analysis of the effects of defect cluster on the thermal transport?

Finally, these studies show the power of atomic-level simulations for elucidating the thermal transport properties of electronic insulators. Also they offer the promise for helping the development of better thermal management methods in solids.

## APPENDIX LATTICE DYNAMICS

Lattice dynamics (LD) is the theory of lattice vibrations in a solid. It allows detailed inspection of frequency of vibrational modes, and the identification of the atoms associated with each mode. The following survey of the pertinent aspects of lattice dynamics are based on discussions by Allen *et al.*<sup>85</sup>. The basis of LD lies in solving the equation of motion in the form of eigenvalue problem. Imagine a solid consisting of  $M$  atoms. If the structure is crystalline, the solid can be thought of as made of smaller set of  $N$  atoms. Thus  $N$  can be the number of basis atoms, or number of atoms in a unit cell. For example, a typical equation of motion of point particles in a lattice can be cast into the form of,

$$\omega_{\lambda}^2(\vec{k})e_{\lambda,ai}(\vec{k}) = D_{\alpha\beta}(\vec{k})e_{\lambda,fi}(\vec{k}), \quad (\text{I-1})$$

where  $\omega_{\lambda}^2(\vec{k})$  and  $e_{\lambda,ai}(\vec{k})$  are the eigenvalue and eigenvector.  $D_{\alpha\beta}(\vec{k})$  is a tensor of 2<sup>nd</sup> rank and known as the dynamical matrix, and given by,

$$D_{\alpha\beta}(jj', \vec{k}) = \frac{1}{\sqrt{m_j m_{j'}}} \sum_l \Phi_{\alpha\beta} \begin{pmatrix} j & j' \\ l & l' \end{pmatrix} \exp[-i\vec{k} \cdot (\vec{r}_{jl} - \vec{r}_{j'l'})]. \quad (\text{I-2})$$

Here  $j$  and  $j'$  refer to the atoms within a repeat unit, and  $l$  and  $l'$  are for the index of the repeat unit.  $m_j$  is the mass of atom  $j$ ,  $r_{jl}$  is the coordinate of atom  $j$  in cell  $l$ .  $\alpha$  and  $\beta$  indicate the direction in Cartesian coordinates. Thus, the size of the dynamical matrix is  $3N \times 3N$ .  $\Phi_{\alpha\beta}$  is called the force constant matrix and is given by,

$$\Phi_{\alpha\beta} \begin{pmatrix} j & j' \\ l & l' \end{pmatrix} = \frac{\partial^2 V}{\partial u_{\alpha}(jl) \partial u_{\beta}(j'l')}, \quad (\text{I-3})$$

under the harmonic approximation.  $V$  is the total potential energy, and  $u_{\alpha}(jl)$  is the displacement of atom  $j$  in cell  $l$  in  $\alpha$  direction. The size of force constant matrix is  $3M \times 3M$ .

Note that when  $\vec{k} = 0$ , the dynamical matrix is the force constant matrix divided by the mass.

The solution of the eigenvalue equation, solution of equation of motion (I-1) is in the form of plane waves:

$$u_{\lambda,\alpha}(jl) = e_{\lambda,\alpha} \exp[-i(\vec{k} \cdot \vec{r}_{jl} - \omega_{\lambda} t)], \quad (\text{I-4})$$

Here  $e_{\lambda,\alpha}(\vec{k})$  is the polarization vector which describes the direction in which atoms move. In (I-4),  $\lambda$  is used explicitly to indicate the vibrational mode.

The analysis on the localization of vibrational modes can be quantified using the eigenvectors since the eigenvector of the vibrational mode contains all the spatial information.

The participation ratio,  $p_{\lambda}$ , can be calculated using the following relation:

$$p_{\lambda}^{-1} = N \sum_i \left( \sum_{\alpha} e_{\lambda,i\alpha}^* e_{\lambda,i\alpha} \right)^2, \quad (\text{I-5})$$

$p_{\lambda}$  takes values between  $1/N$  and 1 depending on the degree of localization of the vibrational mode. If the vibration is localized  $p_{\lambda}$  is small ( $\sim 1/N$ ), and if not,  $p_{\lambda}$  will be of order 1. To further analyze the contribution of each element, it is helpful to decompose the contribution as following:

$$p_{\lambda}^A = p_{\lambda} \sum_{i \in A} \left( \sum_{\alpha} e_{\lambda,i\alpha}^* e_{\lambda,i\alpha} \right), \quad (\text{I-6})$$

where  $A$  is the label for the species.

To compare the polarization of particular modes,  $e_{\lambda,i\alpha}$  should be appropriately normalized. The normalized polarization can be given by

$$\hat{e}_{\lambda,i\alpha} = \frac{e_{\lambda,i\alpha}}{\sum_{\beta} e_{\lambda,i\beta}^* e_{\lambda,i\beta}}, \quad (\text{I-7})$$

This allows us to distinguish the nature of vibrational modes. As discussed in Chapter 2, in the case of highly disordered solid, propagon modes are the only ones that have well defined

polarization vector. Thus,  $\hat{e}_{\lambda,i\alpha}$  can be used to distinguish propagon and rest of the vibrational modes can be distinguished.

## LIST OF REFERENCES

- <sup>1</sup>D. R. Lide, *Handbook of Chemistry and Physics* (CRC Press, Cleaveland, OH., 2007).
- <sup>2</sup>Y. S. Touloukian, *Thermophysical Properties of Matter* (IFI/Plenum, New York, 1970-1979).
- <sup>3</sup>J. K. Fink, *Thermophysical Properties of Uranium Dioxide*, *Journal of Nuclear Materials* **279**, 1 (2000).
- <sup>4</sup>C. Haertling, R. J. Hanrahan, *Literature Review of Thermal and Radiation Performance Parameters for High-temperature, Uranium Dioxide Fueled Cermet Materials*, *Journal of Nuclear Materials* **366**, 317 (2007).
- <sup>5</sup>J. H. Yang, K. W. Song, K. S. Kim, Y. H. Jung, *A Fabrication Technique for a UO<sub>2</sub> Pellet Consisting of UO<sub>2</sub> Grains and a Continuous W Channel on the Grain Boundary*, *Journal of Nuclear Materials* **353**, 202 (2007).
- <sup>6</sup>R. Berman, *The Properties of Diamond* (Academic Press, London, 1979).
- <sup>7</sup>R. F. Davis, *Diamond Films and Coatings* (William Andrew Publishing/Noyes, 1993).
- <sup>8</sup>Y. Baer, J. Schoenes, *Electronic-Structure and Coulomb Correlation-Energy in UO<sub>2</sub> Single-Crystal*, *Solid State Communications* **33**, 885 (1980).
- <sup>9</sup>Y. Yun, H. Kim, H. Lim, K. Park, *Electronic Structure of UO<sub>2</sub> from the Density Functional Theory with on-site Coulomb Repulsion*, *Journal of The Korean Physical Society* **50**, 1285 (2007).
- <sup>10</sup>C. D. Clark, P. J. Dean, P. V. Harris, *Intrinsic Edge Absorption In Diamond*, *Proceedings of The Royal Society of London Series A-Mathematical and Physical Sciences* **277**, 312 (1964).
- <sup>11</sup>C. K. Gupta, *Materials in Nuclear Energy Applications* (CRC Press, Boca Raton, 1989).
- <sup>12</sup>K. Kapoor, S. V. R. Rao, Sheela, T. Sanyal, A. Singh, *Study on Solid Solubility of Gd in UO<sub>2</sub> using X-ray Diffraction*, *Journal of Nuclear Materials* **321**, 331 (2003).

- <sup>13</sup>Z. A. Munir, *The Electrical Conductivity of Doped and Undoped Uranium Oxide*, International Journal of Thermophysics **2**, 177 (1981).
- <sup>14</sup>J. H. Yang, K. S. Kim, K. W. Kang, K. W. Song, Y. H. Jung, *Electrical Conductivity and Non-stoichiometry in the (U,Gd)O<sub>2±x</sub> System*, Journal of Nuclear Materials **340**, 171 (2005).
- <sup>15</sup>M. Amaya, M. Hirai, T. Kubo, Y. Korei, *Thermal Conductivity Measurements on 10 wt% Gd<sub>2</sub>O<sub>3</sub> Doped UO<sub>2±x</sub>*, Journal of Nuclear Materials **231**, 29 (1996).
- <sup>16</sup>M. Hirai, S. Ishimoto, *Thermal Diffusivities And Thermal-Conductivities of UO<sub>2</sub>-Gd<sub>2</sub>O<sub>3</sub>*, Journal of Nuclear Science and Technology **28**, 995 (1991).
- <sup>17</sup>J. M. Howe, *Interfaces in Materials* (John Wiley & Sons, Inc, New York, 1997).
- <sup>18</sup>D. Wolf, S. Yip, *Materials Interfaces: Atomic-level Structure and Properties* (Springer, 1992).
- <sup>19</sup>W. Shockley, W. T. Read, *Quantitative Predictions From Dislocation Models Of Crystal Grain Boundaries*, Physical Review **75**, 692 (1949).
- <sup>20</sup>W. I. Finch, *Uranium - Fuel for Nuclear Energy*, U.S. Geological Survey, (2002), 1
- <sup>21</sup>D. Strahan, *Uranium in Glass, Glazes and Enamels: History, Identification and Handling*, Studies in Conservation **46**, 181 (2001).
- <sup>22</sup>M. T. Hutchings, *High-Temperature Studies of UO<sub>2</sub> and ThO<sub>2</sub> Using Neutron-Scattering Techniques*, Journal of the Chemical Society-Faraday Transactions II **83**, 1083 (1987).
- <sup>23</sup>D. G. Martin, *The Thermal-Expansion of Solid UO<sub>2</sub> and (U, Pu) Mixed Oxides - a Review and Recommendations*, Journal of Nuclear Materials **152**, 94 (1988).
- <sup>24</sup>B. T. M. Willis, *Neutron Diffraction Studies of Actinide Oxides. I. Uranium Dioxide and Thorium Dioxide at Room Temperature*, Proceedings of the Royal Society of London Series a-Mathematical and Physical Sciences **274**, 122 (1963).

- <sup>25</sup>B. T. M. Willis, *Neutron Diffraction Studies of Actinide Oxides.2. Thermal Motions of Atoms in Uranium Dioxide and Thorium Dioxide between Room Temperature and 1100 Degrees C*, Proceedings of the Royal Society of London Series a-Mathematical and Physical Sciences **274**, 134 (1963).
- <sup>26</sup>R. D. Shannon, *Revised Effective Ionic-Radii and Systematic Studies of Interatomic Distances in Halides and Chalcogenides*, Acta Crystallographica Section A **32**, 751 (1976).
- <sup>27</sup>L. Pauling, *The Principles Determining the Structure of Complex Ionic Crystals*, Journal of the American Chemical Society **51**, 1010 (1929).
- <sup>28</sup>L. Pauling, *General Chemistry* (Dover Publications, San Francisco, 1988).
- <sup>29</sup>B. J. Lewis, W. T. Thompson, F. Akbari, D. M. Thompson, C. Thurgood, J. Higgs, *Thermodynamic and Kinetic Modelling of Fuel Oxidation Behaviour in Operating Defective Fuel*, Journal of Nuclear Materials **328**, 180 (2004).
- <sup>30</sup>P. Y. Chevalier, E. Fischer, B. Cheynet, *Progress in the thermodynamic modelling of the O-U binary system*, Journal of Nuclear Materials **303**, 1 (2002).
- <sup>31</sup>C. Gueneau, M. Baichi, D. Labroche, C. Chatillon, B. Sundman, *Thermodynamic Assessment of the Uranium-Oxygen system*, Journal of Nuclear Materials **304**, 161 (2002).
- <sup>32</sup>J. Schoenes, *Electronic-Transitions, Crystal-Field Effects and Phonons in UO<sub>2</sub>*, Physics Reports-Review Section of Physics Letters **63**, 301 (1980).
- <sup>33</sup>N. C. Pyper, I. P. Grant, *Studies In Multiconfiguration Dirac-Fock Theory.3. Interpretation Of The Electronic-Structure Of Neutral And Ionized States Of Uranium*, Journal of The Chemical Society-Faraday Transactions II **74**, 1885 (1978).

- <sup>34</sup>C. R. A. Catlow, *Point-Defect and Electronic Properties of Uranium-Dioxide*, Proceedings of the Royal Society of London Series a-Mathematical Physical and Engineering Sciences **353**, 533 (1977).
- <sup>35</sup>C. Ronchi, G. J. Hyland, *Analysis of Recent Measurements of the Heat-Capacity of Uranium-Dioxide*, Journal Of Alloys And Compounds **213**, 159 (1994).
- <sup>36</sup>P. G. Lucuta, H. Matzke, I. J. Hastings, *A Pragmatic Approach to Modelling Thermal Conductivity of Irradiated UO<sub>2</sub> Fuel: Review and Recommendations*, Journal of Nuclear Materials **232**, 166 (1996).
- <sup>37</sup>R. W. Grimes, C. R. A. Catlow, *The Stability of Fission-Products in Uranium-Dioxide*, Philosophical Transactions of the Royal Society of London Series A-Mathematical Physical and Engineering Sciences **335**, 609 (1991).
- <sup>38</sup>C. Kittel, *Introduction to Solid State Physics* (John Wiley & Sons, Inc., 1996).
- <sup>39</sup>C. Ronchi, M. Sheindlin, M. Musella, G. J. Hyland, *Thermal Conductivity of Uranium Dioxide up to 2900 K from Simultaneous Measurement of the Heat Capacity and Thermal Diffusivity*, Journal of Applied Physics **85**, 776 (1999).
- <sup>40</sup>C. T. Walker, D. Staicu, M. Sheindlin, D. Papaioannou, W. Goll, F. Sontheimer, *On the Thermal Conductivity of UO<sub>2</sub> Nuclear Fuel at a High Burn-up of around 100 MWd/kgHM*, Journal of Nuclear Materials **350**, 19 (2006).
- <sup>41</sup>J. Spino, K. Vennix, M. Coquerelle, *Detailed Characterisation of the Rim Microstructure in PWR Fuels in the Burn-up Range 40-67 CWd/tM.*, Journal of Nuclear Materials **231**, 179 (1996).
- <sup>42</sup>P. Losonen, *On the Behaviour of Intragranular Fission Gas in UO<sub>2</sub> Fuel*, Journal of Nuclear Materials **280**, 56 (2000).

- <sup>43</sup>H. Matzke, H. Blank, M. Coquerelle, K. Lassmann, I. L. F. Ray, C. Ronchi, C. T. Walker, *Oxide Fuel Transients*, Journal Of Nuclear Materials **166**, 165 (1989).
- <sup>44</sup>M. T. Aybers, A. A. Aksit, S. Akbal, S. Ekinici, A. Yayli, L. Colak, A. Van, B. Kopuz, N. Ates, in *Euro Ceramics Viii, Pts 1-3* (Trans Tech Publications Ltd, Zurich-Uetikon, 2004), Vol. 264-268, p. 985.
- <sup>45</sup>K. C. Radford, J. M. Pope, *UO<sub>2</sub> Fuel Pellet Microstructure Modification Through Impurity Additions*, Journal Of Nuclear Materials **116**, 305 (1983).
- <sup>46</sup>K. Une, M. Hirai, K. Nogita, T. Hosokawa, Y. Suzawa, S. Shimizu, Y. Etoh, *Rim Structure Formation and High Burnup Fuel Behavior of Large-grained UO<sub>2</sub> Fuels*, Journal of Nuclear Materials **278**, 54 (2000).
- <sup>47</sup>K. Kurosaki, Y. Saito, H. Muta, M. Uno, S. Yamanaka, *Nanoindentation Studies of UO<sub>2</sub> and (U,Ce)O<sub>2</sub>*, Journal of Alloys and Compounds **381**, 240 (2004).
- <sup>48</sup>F. Dherbey, F. Louchet, A. Mocellin, S. Leclercq, *Elevated Temperature Creep of Polycrystalline Uranium Dioxide: From Microscopic Mechanisms to Macroscopic Behaviour*, Acta Materialia **50**, 1495 (2002).
- <sup>49</sup>V. Blank, M. Popov, G. Pivovarov, N. Lvova, K. Gogolinsky, V. Reshetov, *Ultrahard and Superhard Phases of Fullerite C-60: Comparison with Diamond on Hardness and Wear*, Diamond and Related Materials **7**, 427 (1998).
- <sup>50</sup>W. Kaiser, W. L. Bond, *Nitrogen, a Major Impurity in Common Type-I Diamond*, Physical Review **1**, 857 (1959).
- <sup>51</sup>J. R. Olson, R. O. Pohl, J. W. Vandersande, A. Zoltan, T. R. Anthony, W. F. Banholzer, *Thermal-Conductivity of Diamond between 170 and 1200-K and the Isotope Effect*, Physical Review B **47**, 14850 (1993).

- <sup>52</sup>K. E. Goodson, O. W. Kading, R. Zachai, in *Proceedings of the American Society of Mechanical Engineers Conference, Heat Transfer Division*, edited by R. A. W. e. al., 1994), Vol. 292, p. 83.
- <sup>53</sup>K. M. Leung, A. C. Cheung, B. C. Liu, H. K. Woo, C. Sun, X. Q. Shi, S. T. Lee, *Measuring thermal conductivity of CVD diamond and diamond-like films on silicon substrates by holographic interferometry*, *Diamond and Related Materials* **8**, 1607 (1999).
- <sup>54</sup>D. M. Gruen, *Nanocrystalline diamond films*, *Annual Review of Materials Science* **29**, 211 (1999).
- <sup>55</sup>*International Technology Roadmap for Semiconductors*, (2005)
- <sup>56</sup>*International Technology Roadmap for Semiconductors: Update*, (2006)
- <sup>57</sup>E. Pop, S. Sinha, K. E. Goodson, *Heat Generation and Transport in Nanometer-scale Transistors*, *Proceedings of The IEEE* **94**, 1587 (2006).
- <sup>58</sup>K. Oshima, S. Cristoloveanu, B. Guillaumot, H. Iwai, S. Deleonibus, *Advanced SOI MOSFETs with Buried Alumina and Ground Plane: Self-heating and Short-channel Effects*, *Solid-State Electronics* **48**, 907 (2004).
- <sup>59</sup>L. T. Su, J. E. Chung, D. A. Antoniadis, K. E. Goodson, M. I. Flik, *Measurement And Modeling of Self-Heating in SOI NMOSFETs*, *IEEE Transactions On Electron Devices* **41**, 69 (1994).
- <sup>60</sup>N. W. Ashcroft, D. N. Mermin, *Solid State Physics* (Saunders College Publishing, 1976).
- <sup>61</sup>A. Beiser, *The Concepts of Modern Physics* (McGraw-Hill, Inc., New York, 1995).
- <sup>62</sup>J. D. Jackson, *Classical Electrodynamics* (Wiley, New York, 1998).
- <sup>63</sup>F. Kreith, M. S. Bohn, *Principles of Heat Transfer* (West Publishing, St. Paul, 1993).
- <sup>64</sup>D. R. Clarke, C. G. Levi, *Materials Design for the Next Generation Thermal Barrier Coatings*, *Annual Review of Materials Research* **33**, 383 (2003).

- <sup>65</sup>R. Siegel, C. M. Spuckler, *Analysis of Thermal Radiation Effects on Temperatures in Turbine Engine Thermal Barrier Coatings*, Materials Science and Engineering A - Structural Materials Properties Microstructure and Processing **245**, 150 (1998).
- <sup>66</sup>X. Huang, D. M. Wang, P. Patnaik, J. Singh, *Design and Computational Analysis of Highly Reflective Multiple Layered Thermal Barrier Coating Structure*, Materials Science and Engineering A - Structural Materials Properties Microstructure and Processing **460**, 101 (2007).
- <sup>67</sup>G. J. Hyland, *Thermal-Conductivity of Solid  $UO_2$  - Critique and Recommendation*, Journal of Nuclear Materials **113**, 125 (1983).
- <sup>68</sup>K. Bakker, H. Kwast, E. H. P. Cordfunke, *The Contribution of Thermal-Radiation To The Thermal-Conductivity of Porous  $UO_2$* , Journal of Nuclear Materials **223**, 135 (1995).
- <sup>69</sup>S. L. Hayes, K. L. Peddicord, *Radiative Heat-Transfer In Porous Uranium-Dioxide*, Journal of Nuclear Materials **202**, 87 (1993).
- <sup>70</sup>J. M. Ziman, *Electrons and Phonons* (Oxford University Press, London, UK, 1960).
- <sup>71</sup>R. E. Peierls, *Quantum Theory of Solids* (Oxford University Press, Oxford, 1955).
- <sup>72</sup>C. Herring, *Role of Low-Energy Phonons in Thermal Conduction*, Physical Review **95**, 954 (1954).
- <sup>73</sup>H. B. G. Casimir, *Note on the conduction of heat in crystals*, Physica **5**, 495 (1938).
- <sup>74</sup>P. G. Klemens, *The Scattering of Low-Frequency Lattice Waves by Static Imperfections*, Proceedings of the Physical Society of London Section A **68**, 1113 (1955).
- <sup>75</sup>E. Merzbacher, *Quantum Mechanics* (Wiley, New York, 1997).
- <sup>76</sup>P. G. Klemens, *Thermal Conductivity and Lattice Vibrational Modes*, Solid State Physics-Advances in Research and Applications **7**, 1 (1958).

- <sup>77</sup>P. K. Schelling, S. R. Phillpot, P. Keblinski, *Kapitza Conductance and Phonon Scattering at Grain Boundaries by Simulation*, Journal of Applied Physics **95**, 6082 (2004).
- <sup>78</sup>H. S. Yang, G. R. Bai, L. J. Thompson, J. A. Eastman, *Interfacial thermal resistance in nanocrystalline yttria-stabilized zirconia*, Acta Materialia **50**, 2309 (2002).
- <sup>79</sup>E. T. Swartz, R. O. Pohl, *Thermal-Boundary Resistance*, Reviews of Modern Physics **61**, 605 (1989).
- <sup>80</sup>R. M. Costescu, M. A. Wall, D. G. Cahill, *Thermal Conductance of Epitaxial Interfaces*, Physical Review B **67** (2003).
- <sup>81</sup>R. J. Stoner, H. J. Maris, *Kapitza Conductance and Heat-Flow between Solids at Temperatures from 50 to 300 K*, Physical Review B **48**, 16373 (1993).
- <sup>82</sup>C. Kittel, *Interpretation of the Thermal Conductivity of Glasses*, Physical Review **75**, 972 (1949).
- <sup>83</sup>G. A. Slack, *Solid State Physics* (Academic Press, New York, 1979).
- <sup>84</sup>D. G. Cahill, R. O. Pohl, *Heat-Flow and Lattice Vibrations in Glasses*, Solid State Communications **70**, 927 (1989).
- <sup>85</sup>P. B. Allen, J. L. Feldman, J. Fabian, F. Wooten, *Diffusons, Locons and Propagons: Character of Atomic Vibrations in Amorphous Si*, Philosophical Magazine B-Physics of Condensed Matter Statistical Mechanics Electronic Optical and Magnetic Properties **79**, 1715 (1999).
- <sup>86</sup>J. L. Feldman, M. D. Kluge, P. B. Allen, F. Wooten, *Thermal-Conductivity and Localization in Glasses - Numerical Study of a Model of Amorphous-Silicon*, Physical Review B **48**, 12589 (1993).

- <sup>87</sup>P. K. Schelling, S. R. Phillpot, *Mechanism of Thermal Transport in Zirconia and Yttria-stabilized Zirconia by Molecular-Dynamics Simulation*, Journal of The American Ceramic Society **84**, 2997 (2001).
- <sup>88</sup>C. J. Glassbrenner, G. A. Slack, *Thermal Conductivity of Silicon + Germanium from 3 Degrees K to Melting Point*, Physical Review A - General Physics **134**, 1058 (1964).
- <sup>89</sup>J. A. Carruthers, T. H. Geballe, H. M. Rosenberg, J. M. Ziman, *The Thermal Conductivity of Germanium and Silicon between 2-Degrees-K and 300-Degrees-K*, Proceedings of the Royal Society of London Series a-Mathematical and Physical Sciences **238**, 502 (1957).
- <sup>90</sup>O. L. Anderson, I. Suzuki, *Anharmonicity of 3 Minerals at High-Temperature - Forsterite, Fayalite, and Periclase*, Journal of Geophysical Research **88**, 3549 (1983).
- <sup>91</sup>M. Lucht, M. Lerche, H. C. Wille, Y. V. Shvyd'ko, H. D. Ruter, E. Gerdau, P. Becker, *Precise measurement of the lattice parameters of alpha-Al<sub>2</sub>O<sub>3</sub> in the temperature range 4.5-250 K using the Mossbauer wavelength standard*, Journal of Applied Crystallography **36**, 1075 (2003).
- <sup>92</sup>S. R. Phillpot, A. J. H. McGaughey, *Introduction to the Thermal Transport*, Materials Today, (2005), 18
- <sup>93</sup>R. M. Martin, *Electronic Structure - Basic Theory and Practical Methods* (Cambridge University Press, Cambridge, 2004).
- <sup>94</sup>R. D. Cook, D. S. Malkus, M. E. Plesha, R. J. Witt, *Concepts and Applications of Finite Element Analysis* (Wiley, New York, 2001).
- <sup>95</sup>L. Q. Chen, *Phase Field Models for Microstructure Evolution*, Annual Review of Materials Research **32**, 113 (2002).
- <sup>96</sup>M. P. Allen, D. J. Tildesley, *Computer Simulation of Liquids* (Oxford University Press, 1987).

- <sup>97</sup>W. H. Press, B. P. Flannery, S. A. Teukolsky, W. T. Vetterling, *Numerical Recipes in Fortran* 77 (Cambridge University Press, Cambridge, 1992).
- <sup>98</sup>D. Frenkel, B. Smit, *Molecular Dynamics Simulation* (Academic Press, 2002).
- <sup>99</sup>D. Wolf, P. Keblinski, S. R. Phillpot, J. Eggebrecht, *Exact Method for the Simulation of Coulombic Systems by Spherically Truncated, Pairwise  $r^{-1}$  Summation*, Journal of Chemical Physics **110**, 8254 (1999).
- <sup>100</sup>R. A. Buckingham, *The Classical Equation of State of Gaseous Helium, Neon and Argon*, Proceedings of the Royal Society of London Series a-Mathematical and Physical Sciences **168**, 264 (1938).
- <sup>101</sup>J. Tersoff, *Empirical Interatomic Potential for Carbon, with Applications to Amorphous-Carbon*, Physical Review Letters **61**, 2879 (1988).
- <sup>102</sup>J. Tersoff, *New Empirical-Model for the Structural-Properties of Silicon*, Physical Review Letters **56**, 632 (1986).
- <sup>103</sup>G. V. Lewis, C. R. A. Catlow, *Potential Models For Ionic Oxides*, Journal of Physics C-Solid State Physics **18**, 1149 (1985).
- <sup>104</sup>C. R. A. Catlow, K. M. Diller, M. J. Norgett, *Interionic Potentials For Alkali-Halides*, Journal of Physics C-Solid State Physics **10**, 1395 (1977).
- <sup>105</sup>H. C. Andersen, *Molecular-Dynamics Simulations at Constant Pressure and-or Temperature*, Journal of Chemical Physics **72**, 2384 (1980).
- <sup>106</sup>M. Parrinello, A. Rahman, *Polymorphic Transitions in Single-Crystals - a New Molecular-Dynamics Method*, Journal of Applied Physics **52**, 7182 (1981).
- <sup>107</sup>P. Jund, R. Jullien, *Molecular Dynamics Calculation of the Thermal Conductivity of Vitreous Silica*, Physical Review B **59**, 13707 (1999).

- <sup>108</sup>P. K. Schelling, S. R. Phillpot, P. Keblinski, *Comparison of atomic-level simulation methods for computing thermal conductivity*, Physical Review B **65** (2002).
- <sup>109</sup>K. Yamada, K. Kurosaki, M. Uno, S. Yamanaka, *Evaluation of thermal properties of uranium dioxide by molecular dynamics*, Journal Of Alloys And Compounds **307**, 10 (2000).
- <sup>110</sup>M. Abramowski, R. W. Grimes, S. Owens, *Morphology of UO<sub>2</sub>*, Journal of Nuclear Materials **275**, 12 (1999).
- <sup>111</sup>G. Busker, in *Department of Materials* (Imperial College of Science, Technology, and Medicine, London, UK, 2002), Vol. Ph.D.
- <sup>112</sup>Y. Ida, *Interionic Repulsive Force And Compressibility Of Ions*, Physics Of The Earth And Planetary Interiors **13**, 97 (1976).
- <sup>113</sup>J. D. Gale, *GULP: A computer program for the symmetry-adapted simulation of solids*, Journal of the Chemical Society-Faraday Transactions **93**, 629 (1997).
- <sup>114</sup>J. D. Gale, A. L. Rohl, *The General Utility Lattice Program (GULP)*, Molecular Simulation **29**, 291 (2003).
- <sup>115</sup>K. Govers, S. Lemehov, M. Verwerft, *Comparison of Interatomic Potentials for UO<sub>2</sub>. Part I: Static Calculations*, Journal of Nuclear Materials **266**, 161 (2007).
- <sup>116</sup>E. Wigner, *On the Quantum Correction for Thermodynamic Equilibrium*, Physical Review **40**, 0749 (1932).
- <sup>117</sup>G. Leibfried, E. Schloemann, *Nachr. Akad. Wiss. Gottingen, Math. Physik.* **K1 IIa**, 71 (1954).
- <sup>118</sup>P. G. Klemens, *Thermal Conductivity and Lattice Vibrational Modes*, 1954).
- <sup>119</sup>G. H. Geiger, D. R. Poirier, *Transport Phenomena in Metallurgy* (Addison-Wesley, 1973).
- <sup>120</sup>J. B. Wachtman, M. L. Wheat, H. J. Anderson, J. L. Bates, *Elastic Constants of Single Crystal UO<sub>2</sub> at 25 Degrees C*, Journal of Nuclear Materials **16**, 39 (1965).

- <sup>121</sup>I. J. Fritz, *Elastic Properties of UO<sub>2</sub> at High-Pressure*, Journal of Applied Physics **47**, 4353 (1976).
- <sup>122</sup>G. Dolling, R. A. Cowley, A. D. B. Woods, *Crystal Dynamics of Uranium Dioxide*, Canadian Journal of Physics **43**, 1397 (1965).
- <sup>123</sup>H. Yoshida, K. Yokoyama, N. Shibata, Y. Ikuhara, T. Sakuma, *High-temperature grain boundary and grain boundary energy in cubic sliding behavior zirconia bicrystals*, Acta Materialia **52**, 2349 (2004).
- <sup>124</sup>P. Koblinski, D. Wolf, S. R. Phillpot, H. Gleiter, *Role of bonding and coordination in the atomic structure and energy of diamond and silicon grain boundaries*, Journal of Materials Research **13**, 2077 (1998).
- <sup>125</sup>P. Shukla, T. Watanabe, S. R. Phillpot, *Thermal Transport Properties of MgO and Nd<sub>2</sub>Zr<sub>2</sub>O<sub>7</sub> Pyrochlore by Molecular Dynamics Simulation*, unpublished (2007).
- <sup>126</sup>G. A. Slack, *Thermal Conductivity of MgO, Al<sub>2</sub>O<sub>3</sub>, MgAl<sub>2</sub>O<sub>4</sub>, and Fe<sub>3</sub>O<sub>4</sub> Crystals from 3 Degrees to 300 Degrees K*, Physical Review **126**, 427 (1962).
- <sup>127</sup>C. W. Nan, R. Birringer, *Determining the Kapitza resistance and the thermal conductivity of polycrystals: A simple model*, Physical Review B **57**, 8264 (1998).
- <sup>128</sup>J. Amrit, *Grain boundary Kapitza resistance and grain-arrangement induced anisotropy in the thermal conductivity of polycrystalline niobium at low temperatures*, Journal of Physics D- Applied Physics **39**, 4472 (2006).
- <sup>129</sup>R. J. Stevens, L. V. Zhigilei, P. M. Norris, *Effects of temperature and disorder on thermal boundary conductance at solid–solid interfaces: Nonequilibrium molecular dynamics simulations*, International Journal of Heat and Mass Transfer **50**, 3977 (2007).

- <sup>130</sup>D. G. Cahill, W. K. Ford, K. E. Goodson, G. D. Mahan, A. Majumdar, H. J. Maris, R. Merlin, S. R. Phillpot, *Nanoscale thermal transport*, Journal of Applied Physics **93**, 793 (2003).
- <sup>131</sup>M. Freyss, T. Petit, J. P. Crocombette, *Point Defects in Uranium Dioxide: ab initio Pseudopotential Approach in the Generalized Gradient Approximation*, Journal of Nuclear Materials **347**, 44 (2005).
- <sup>132</sup>J. P. Crocombette, F. Jollet, L. N. Nga, T. Petit, *Plane-wave Pseudopotential Study of Point Defects in Uranium Dioxide*, Physical Review B **6410** (2001).
- <sup>133</sup>B. T. M. Willis, *Crystallographic Studies of Anion-Excess Uranium-Oxides*, Journal of the Chemical Society-Faraday Transactions II **83**, 1073 (1987).
- <sup>134</sup>B. T. M. Willis, *Structures of  $UO_2$ ,  $UO_{2+x}$  and  $U_4O_9$  by Neutron Diffraction*, Solid State Communications **2**, 23 (1964).
- <sup>135</sup>B. T. M. Willis, *Structures of  $UO_2$ ,  $UO_{2+x}$  and  $U_4O_9$  by Neutron Diffraction*, Journal de Physique **25**, 431 (1964).
- <sup>136</sup>A. K. Cheetham, B. E. F. Fender, M. J. Cooper, *Defect Structure of Calcium Fluoride Containing Excess Anions. I. Bragg Scattering*, Journal of Physics C - Solid State Physics **4**, 3107 (1971).
- <sup>137</sup>H. V. S. Hubbard, T. R. Griffiths, *An Investigation of Defect Structures in Single-Crystal  $UO_{2+x}$  by Optical-Absorption Spectroscopy*, Journal of the Chemical Society-Faraday Transactions II **83**, 1215 (1987).
- <sup>138</sup>G. C. Allen, P. A. Tempest, *Ordered Defects in the Oxides of Uranium*, Proceedings of the Royal Society of London Series a-Mathematical Physical and Engineering Sciences **406**, 325 (1986).

- <sup>139</sup>G. C. Allen, P. A. Tempest, J. W. Tyler, *Coordination Model For The Defect Structure Of Hyperstoichiometric  $UO_{2+x}$  And  $U_4O_9$* , *Nature* **295**, 48 (1982).
- <sup>140</sup>H. Matzke, *Atomic Transport-Properties in  $UO_2$  and Mixed Oxides (U, Pu) $O_2$* , *Journal of the Chemical Society-Faraday Transactions II* **83**, 1121 (1987).
- <sup>141</sup>P. Ruello, K. D. Becker, K. Ullrich, L. Desgranges, C. Petot, G. Petot-Ervas, *Thermal Variation of the Optical Absorption of  $UO_2$ : Determination of the Small Polaron Self-energy*, *Journal of Nuclear Materials* **328**, 46 (2004).
- <sup>142</sup>F. Jollet, T. Petit, S. Gota, N. Thromat, M. Gautier-Soyer, A. Pasturel, *The Electronic Structure of Uranium Dioxide: an Oxygen K-edge X-ray Absorption Study*, *Journal of Physics-Condensed Matter* **9**, 9393 (1997).
- <sup>143</sup>W. S. Capinski, H. J. Maris, E. Bauser, I. Silier, M. AsenPalmer, T. Ruf, M. Cardona, E. Gmelin, *Thermal Conductivity of Isotopically Enriched Si*, *Applied Physics Letters* **71**, 2109 (1997).
- <sup>144</sup>D. G. Cahill, F. Watanabe, A. Rockett, C. B. Vining, *Thermal Conductivity of Epitaxial Layers of Dilute SiGe Alloys*, *Physical Review B* **71** (2005).
- <sup>145</sup>J. Janeczek, R. C. Ewing, V. M. Oversby, L. O. Werme, *Uraninite and  $UO_2$  in Spent Nuclear Fuel: a Comparison*, *Journal of Nuclear Materials* **238**, 121 (1996).
- <sup>146</sup>P. G. Lucuta, H. Matzke, R. A. Verrall, *Modeling of  $UO_2$ -Based Simfuel Thermal-Conductivity - the Effect of the Burnup*, *Journal of Nuclear Materials* **217**, 279 (1994).
- <sup>147</sup>I. C. Hobson, R. Taylor, Ainscoug, Jb, *Effect of Porosity and Stoichiometry on Thermal-Conductivity of Uranium-Dioxide*, *Journal of Physics D-Applied Physics* **7**, 1003 (1974).
- <sup>148</sup>C. Affortit, J. P. Marcon, *High Temperatures-High Pressures* **7**, 236 (1970).

- <sup>149</sup>P. G. Lucuta, H. Matzke, R. A. Verrall, *Thermal-Conductivity of Hyperstoichiometric Simfuel*, Journal of Nuclear Materials **223**, 51 (1995).
- <sup>150</sup>B. J. Lewis, B. Szpunar, F. C. Iglesias, *Fuel Oxidation and Thermal Conductivity Model for Operating Defective Fuel Rods*, Journal of Nuclear Materials **306**, 30 (2002).
- <sup>151</sup>S. Yamasaki, T. Arima, K. Idemitsu, Y. Inagaki, *Evaluation of thermal conductivity of hyperstoichiometric  $UO_{2+x}$  by molecular dynamics simulation*, International Journal of Thermophysics **28**, 661 (2007).
- <sup>152</sup>F. Gronvold, *High-Temperature X-Ray Study of Uranium Oxides in the  $UO_2$ - $U_3O_8$  Region*, Journal of Inorganic & Nuclear Chemistry **1**, 357 (1955).
- <sup>153</sup>M. Amaya, T. Kubo, Y. Korei, *Thermal Conductivity Measurements on  $UO_{2+x}$  from 300 to 1,400 K*, Journal of Nuclear Science and Technology **33**, 636 (1996).
- <sup>154</sup>J. W. Che, T. Cagin, W. Q. Deng, W. A. Goddard, *Thermal Conductivity of Diamond and Related Materials from Molecular Dynamics Simulations*, Journal of Chemical Physics **113**, 6888 (2000).
- <sup>155</sup>J. Li, L. Porter, S. Yip, *Atomistic Modeling of Finite Temperature Properties of Crystalline Beta-SiC - II. Thermal Conductivity and Effects of Point Defects*, Journal of Nuclear Materials **255**, 139 (1998).
- <sup>156</sup>S. G. Volz, G. Chen, *Molecular Dynamics Simulation of Thermal Conductivity of Silicon Crystals*, Physical Review B **61**, 2651 (2000).
- <sup>157</sup>J. D. Higgs, W. T. Thompson, B. J. Lewis, S. C. Vogel, *Kinetics of Precipitation of  $U_4O_9$  from Hyperstoichiometric  $UO_{2+x}$* , Journal of Nuclear Materials **366**, 297 (2007).
- <sup>158</sup>R. J. Bell, P. Dean, Hibbins, D.C., *Localization of Normal Modes in Vitreous Silica, Germania and Beryllium Fluoride*, Journal of Physics Part C Solid State Physics **3**, 2111 (1970).

- <sup>159</sup>J. Callaway, *Model for Lattice Thermal Conductivity at Low Temperatures*, Physical Review **113**, 1046 (1959).
- <sup>160</sup>P. K. Schelling, S. R. Phillpot, D. Wolf, *Mechanism of the Cubic-to-Tetragonal Phase Transition in Zirconia and Yttria-stabilized Zirconia by Molecular Dynamics Simulation*, Journal of the American Ceramic Society **84**, 1609 (2001).
- <sup>161</sup>K. Clausen, W. Hayes, M. T. Hutchings, J. E. Macdonald, R. Osborn, P. Schnabel, *Investigation of Oxygen Disorder, Thermal Parameters, Lattice-Vibrations and Elastic-Constants of UO<sub>2</sub> and ThO<sub>2</sub> at Temperatures up to 2930-K*, Revue de Physique Appliquee **19**, 719 (1984).
- <sup>162</sup>K. Clausen, W. Hayes, J. E. Macdonald, R. Osborn, M. T. Hutchings, *Observation of Oxygen Frenkel Disorder in Uranium-Dioxide above 2000-K by Use of Neutron-Scattering Techniques*, Physical Review Letters **52**, 1238 (1984).
- <sup>163</sup>K. N. Clausen, M. A. Hackett, W. Hayes, S. Hull, M. T. Hutchings, J. E. Macdonald, K. A. McEwen, R. Osborn, U. Steigenberger, *Coherent Diffuse Neutron-Scattering from UO<sub>2</sub> and ThO<sub>2</sub> at Temperatures above 2000 K*, Physica B **156**, 103 (1989).
- <sup>164</sup>K. C. Kim, D. R. Olander, *Oxygen Diffusion in UO<sub>2-x</sub>*, Transactions of the American Nuclear Society **39**, 382 (1981).
- <sup>165</sup>R. Szwarc, *Defect Contribution to Excess Enthalpy of Uranium Dioxide-Calculation of Frenkel Energy*, Journal of Physics and Chemistry of Solids **30**, 705 (1969).
- <sup>166</sup>T. Petit, C. Lemaignan, F. Jollet, B. Bigot, A. Pasturel, *Point Defects in Uranium Dioxide*, Philosophical Magazine B-Physics of Condensed Matter Statistical Mechanics Electronic Optical and Magnetic Properties **77**, 779 (1998).

<sup>167</sup>M. Freyss, N. Vergnet, T. Petit, *ab initio Modeling of the Behavior of Helium and Xenon in Actinide Dioxide Nuclear Fuels*, Journal of Nuclear Materials **352**, 144 (2006).

<sup>168</sup>W. M. Yao, C. Amsler, D. Asner, R. M. Barnett, J. Beringer, P. R. Burchat, C. D. Carone, C. Caso, O. Dahl, G. D'Ambrosio, A. De Gouvea, M. Doser, S. Eidelman, J. L. Feng, T. Gherghetta, M. Goodman, C. Grab, D. E. Groom, A. Gurtu, K. Hagiwara, K. G. Hayes, J. J. Hernandez-Rey, K. Hikasa, H. Jawahery, C. Kolda, Y. Kwon, M. L. Mangano, A. V. Manohar, A. Masoni, R. Miquel, K. Monig, H. Murayama, K. Nakamura, S. Navas, K. A. Olive, L. Pape, C. Patrignani, A. Piepke, G. Punzi, G. Raffelt, J. G. Smith, M. Tanabashi, J. Terning, N. A. Tornqvist, T. G. Trippe, P. Vogel, T. Watari, C. G. Wohl, R. L. Workman, P. A. Zyla, B. Armstrong, G. Harper, V. S. Lugovsky, P. S. Schaffner, M. Artuso, K. S. Babu, H. R. Band, E. Barberio, M. Battaglia, H. Bichel, O. Biebel, P. Bloch, E. Blucher, R. N. Cahn, D. Casper, A. Cattai, A. Ceccucci, D. Chakraborty, R. S. Chivukula, G. Cowan, T. Damour, T. De Grand, K. Desler, M. A. Dobbs, M. Drees, A. Edwards, D. A. Edwards, V. D. Elvira, J. Erler, W. Fetscher, B. D. Fields, B. Foster, D. Froidevaux, T. K. Gaiser, L. Garren, H. J. Gerber, G. Gerbier, L. Gibbons, F. J. Gilman, G. F. Giudice, A. V. Gritsan, M. Grunewald, H. E. Haber, C. Hagmann, I. Hinchliffe, A. Hocker, P. Igo-Kemenes, J. D. Jackson, K. F. Johnson, D. Karlen, B. Kayser, D. Kirkby, S. R. Klein, K. Kleinknecht, J. G. Knowles, R. V. Kowalewski, P. Kreitz, B. Krusche, Y. V. Kuyanov, O. Lahav, P. Langacker, A. Liddle, Z. Ligeti, T. M. Liss, L. Littenberg, J. C. Liu, K. S. Lugovsky, S. B. Lugovsky, T. Mannel, W. J. Marciano, A. D. Martin, D. Milstead, M. Narain, P. Nason, Y. Nir, J. A. Peacock, S. A. Prell, A. Quadt, S. Raby, B. N. Ratcliff, E. A. Razuvaev, B. Renk, P. R. Richardson, S. Roesler, G. Rolandi, M. T. Roman, L. J. Rosenberg, C. T. Sachrajda, Y. Sakai, S. Sarkar, M. Schmitt, O. Schneider, D. Scott, T. Sjostrand, G. F. Smoot, P. Sokolsky, S. Spanier, H. Spieler, A. Stahl, T. Staney, R. E. Streitmatter, T. Sumiyoshi, N. P. Tkachenko, G. H. Trilling, G. Valencia, K. van

- Bibber, M. G. Vincker, D. R. Ward, B. R. Webber, J. D. Wells, M. Whalley, L. Wolfenstein, J. Womersley, C. L. Woody, A. Yamamoto, O. V. Zenin, J. Zhang, R. Y. Zhu, *Review of particle physics*, Journal of Physics G-Nuclear and Particle Physics **33**, 1 (2006).
- <sup>169</sup>G. F. Knoll, *Radiation Detection and Measurement* (Wiley, New York, 1989).
- <sup>170</sup>O. B. Firsov, *A Qualitative Interpretation of the Mean Electron Excitation Energy in Atomic Collisions*, Soviet Physics JETP-USSR **9**, 1076 (1959).
- <sup>171</sup>J. Lindhard, M. Scharff, *Energy Dissipation by Ions in Kev Region*, Physical Review **1**, 128 (1961).
- <sup>172</sup>O. S. Oen, M. T. Robinson, *Computer Studies of Reflection of Light-Ions from Solids*, Nuclear Instruments & Methods **132**, 647 (1976).
- <sup>173</sup>H. Matzke, *Radiation-Damage Effects in Nuclear-Materials*, Nuclear Instruments & Methods in Physics Research Section B-Beam Interactions with Materials and Atoms **32**, 455 (1988).
- <sup>174</sup>H. Matzke, *Radiation-Damage in Crystalline Insulators, Oxides and Ceramic Nuclear-Fuels*, Radiation Effects and Defects in Solids **64**, 3 (1982).
- <sup>175</sup>K. Hayashi, H. Kikuchi, K. Fukuda, *Radiation-Damage of UO<sub>2</sub> Implanted with 100-Mev Iodine Ions*, Journal of Alloys and Compounds **213**, 351 (1994).
- <sup>176</sup>H. J. Matzke, *Radiation Effects in Fuel Materials for Fission Reactors*, Institute of Physics Conference Series, 423 (1983).
- <sup>177</sup>K. Minato, T. Shiratori, H. Serizawa, K. Hayashi, K. Une, K. Nogita, M. Hirai, M. Amaya, *Thermal Conductivities of Irradiated UO<sub>2</sub> and (U,Gd)O<sub>2</sub>*, Journal of Nuclear Materials **288**, 57 (2001).
- <sup>178</sup>C. Ronchi, T. Wiss, *Fission Fragment Spikes in Uranium Dioxide*, Journal of Applied Physics **92**, 5837 (2002).

- <sup>179</sup>J. B. Gibson, A. N. Goland, M. Milgram, G. H. Vineyard, *Dynamics of Radiation Damage*, Physical Review **120**, 1229 (1960).
- <sup>180</sup>D. E. Harrison, *Application Of Molecular-Dynamics Simulations To The Study Of Ion-Bombarded Metal-Surfaces*, Crc Critical Reviews In Solid State And Materials Sciences **14**, S1 (1988).
- <sup>181</sup>B. J. Garrison, N. Winograd, D. M. Deaven, C. T. Reimann, D. Y. Lo, T. A. Tombrello, D. E. Harrison, M. H. Shapiro, *Many-Body Embedded-Atom Potential for Describing the Energy and Angular-Distributions of Rh Atoms Desorbed from Ion-Bombarded Rh(111)*, Physical Review B **37**, 7197 (1988).
- <sup>182</sup>D. Y. Lo, T. A. Tombrello, M. H. Shapiro, B. J. Garrison, N. Winograd, D. E. Harrison, *Theoretical-Studies of Ion-Bombardment - Many-Body Interactions*, Journal of Vacuum Science & Technology a-Vacuum Surfaces and Films **6**, 708 (1988).
- <sup>183</sup>M. H. Shapiro, T. A. Tombrello, D. E. Harrison, *Simulation of Isotopic Mass Effects in Sputtering.2.*, Nuclear Instruments & Methods in Physics Research Section B-Beam Interactions with Materials and Atoms **30**, 152 (1988).
- <sup>184</sup>K. Morishita, R. Sugano, B. D. Wirth, *Thermal Stability of Helium-Vacancy Clusters and Bubble Formation - Multiscale Modeling Approach for Fusion Materials development*, Fusion Science and Technology **44**, 441 (2003).
- <sup>185</sup>R. Smith, D. Bacorisen, B. P. Uberuaga, K. E. Sickafus, J. A. Ball, R. W. Grimes, *Dynamical Simulations of Radiation Damage in Magnesium Aluminate Spinel, MgAl<sub>2</sub>O<sub>4</sub>*, Journal of Physics-Condensed Matter **17**, 875 (2005).

- <sup>186</sup>B. P. Uberuaga, R. Smith, A. R. Cleave, G. Henkelman, R. W. Grimes, A. F. Voter, K. E. Sickafus, *Dynamical Simulations of Radiation Damage and Defect Mobility in MgO*, *Physical Review B* **71** (2005).
- <sup>187</sup>R. Devanathan, W. J. Weber, T. D. de la Rubia, *Computer Simulation of a 10 keV Si Displacement Cascade in SiC*, *Nuclear Instruments & Methods In Physics Research Section B-Beam Interactions With Materials And Atoms* **141**, 118 (1998).
- <sup>188</sup>T. D. delaRubia, *Irradiation-induced defect production in elemental metals and semiconductors: A review of recent molecular dynamics studies*, *Annual Review Of Materials Science* **26**, 613 (1996).
- <sup>189</sup>R. Smith, K. Beardmore, *Molecular Dynamics Studies of Particle Impacts with Carbon-based Baterials*, *Thin Solid Films* **272**, 255 (1996).
- <sup>190</sup>L. Van Brutzel, J. M. Delaye, D. Ghaleb, M. Rarivomanantsoa, *Molecular Dynamics Studies of Displacement Cascades in the Uranium Dioxide Matrix*, *Philosophical Magazine* **83**, 4083 (2003).
- <sup>191</sup>N. D. Morelon, D. Ghaleb, J. M. Delaye, L. Van Brutzel, *A New Empirical Potential for Simulating the Formation of Defects and Their Mobility in Uranium Dioxide*, *Philosophical Magazine* **83**, 1533 (2003).
- <sup>192</sup>L. Van Brutzel, M. Rarivomanantsoa, D. Ghaleb, *Displacement Cascade Initiated with the Realistic Energy of the Recoil Nucleus in UO<sub>2</sub> Matrix by Molecular Dynamics Simulation*, *Journal of Nuclear Materials* **354**, 28 (2006).
- <sup>193</sup>M. J. Norgett, M. T. Robinson, I. M. Torrens, *Proposed Method of Calculating Displacement Dose-Rates*, *Nuclear Engineering and Design* **33**, 50 (1975).

- <sup>194</sup>J. F. Ziegler, J. P. Biersak, U. Littmark, *The Stopping and Range of Ions in Matter* (Pergomon, New York, 1985).
- <sup>195</sup>R. Smith, *Atomic & Ion Collisions in Solids and at Surfaces* (Cambridge University Press, Cambridge, UK, 1997).
- <sup>196</sup>J. Fikar, R. Schaeublin, *Molecular Dynamics Simulation of Radiation Damage in bcc Tungsten*, Nuclear Instruments & Methods in Physics Research Section B-Beam Interactions with Materials and Atoms **255**, 27 (2007).
- <sup>197</sup>J. M. Delaye, D. Ghaleb, *Dynamic processes during displacement cascades in oxide glasses: A molecular-dynamics study*, Physical Review B **61**, 14481 (2000).
- <sup>198</sup>J. M. Delaye, D. Ghaleb, *Dynamic Processes during Displacement Cascades in Oxide Glasses: a Molecular Dynamics Study*, Physical Review B **61**, 14481 (2000).
- <sup>199</sup>L. Van Brutzel, M. Rarivomanantsoa, *Molecular Dynamics Simulation Study of Primary Damage in UO<sub>2</sub> Produced by Cascade Overlaps*, Journal of Nuclear Materials **358**, 209 (2006).
- <sup>200</sup>L. R. Corrales, A. Chartier, R. Devanathan, *Excess Kinetic Energy Dissipation in Materials*, Nuclear Instruments & Methods in Physics Research Section B-Beam Interactions with Materials and Atoms **228**, 274 (2005).
- <sup>201</sup>A. L. Garcia, *Numerical Methods for Physics* (Prentice-Hall, Inc., 2000).
- <sup>202</sup>Y. H. Hu, S. B. Sinnott, *Constant Temperature Molecular Dynamics Simulations of Energetic Particle-solid Collisions: Comparison of Temperature control methods*, Journal of Computational Physics **200**, 251 (2004).
- <sup>203</sup>F. Reif, *Fundamentals of Statistical and Thermal Physics* (McGraw-Hill, New York, 1965).
- <sup>204</sup>K. Huang, *Statistical Mechanics* (John Wiley & Sons Inc., New York, 1987).

- <sup>205</sup>H. J. C. Berendsen, J. P. M. Postma, W. F. Vangunsteren, A. Dinola, J. R. Haak, *Molecular-Dynamics with Coupling to an External Bath*, Journal of Chemical Physics **81**, 3684 (1984).
- <sup>206</sup>S. A. Adelman, J. D. Doll, *Generalized Langevin Equation Approach for Atom-Solid-Surface Scattering - General Formulation for Classical Scattering Off Harmonic Solids*, Journal of Chemical Physics **64**, 2375 (1976).
- <sup>207</sup>K. E. Sickafus, L. Minervini, R. W. Grimes, J. A. Valdez, M. Ishimaru, F. Li, K. J. McClellan, T. Hartmann, *Radiation Tolerance of Complex Oxides*, Science **289**, 748 (2000).
- <sup>208</sup>H. O. Pierson, *Handbook of Carbon, Graphite, Diamond and Fullerenes - Properties, Processing and Applications* (William Andrew Publishing/Noyes, 1993).
- <sup>209</sup>O. Auciello, J. Birrell, J. A. Carlisle, J. E. Gerbi, X. C. Xiao, B. Peng, H. D. Espinosa, *Materials Science and Fabrication Processes for a New MEMS Technology Based on Ultrananocrystalline Diamond Thin Films*, Journal of Physics-Condensed Matter **16**, R539 (2004).
- <sup>210</sup>M. H. Nazare, A. J. Neves, *Properties, Growth and Applications of Diamond* (Institution of Engineering and Technology, 2001).
- <sup>211</sup>T. Sato, K. Ohashi, T. Sudoh, K. Haruna, H. Maeta, *Thermal Expansion of a High Purity Synthetic Diamond Single Crystal at Low Temperatures*, Physical Review B **65** (2002).
- <sup>212</sup>G. A. Slack, S. F. Bartram, *Thermal-Expansion of Some Diamond-Like Crystals*, Journal of Applied Physics **46**, 89 (1975).
- <sup>213</sup>P. K. Schelling, S. R. Phillpot, P. Keblinski, *Comparison of atomic-level simulation methods for computing thermal conductivity*, Physical Review B **65**, 144306 (2002).

- <sup>214</sup>D. G. Onn, A. Witek, Y. Z. Qiu, T. R. Anthony, W. F. Banholzer, *Some Aspects of the Thermal-Conductivity of Isotopically Enriched Diamond Single-Crystals*, Physical Review Letters **68**, 2806 (1992).
- <sup>215</sup>S. von Alftan, P. D. Haynes, K. Kaski, A. P. Sutton, *Are the structures of twist grain boundaries in silicon ordered at 0 K?* Physical Review Letters **96**, 055505 (2006).
- <sup>216</sup>P. Shukla, T. Watanabe, J. C. Nino, J. S. Tulenko, S. R. Phillpot, *Thermal Transport Properties of MgO and Nd<sub>2</sub>Zr<sub>2</sub>O<sub>7</sub> Pyrochlore by Molecular Dynamics Simulation*, Journal of Nuclear Materials (2007).
- <sup>217</sup>H. K. Lyeo, D. G. Cahill, *Thermal conductance of interfaces between highly dissimilar materials*, Physical Review B **73**, 144301 (2006).
- <sup>218</sup>T. Watanabe, B. Ni, S. R. Phillpot, P. K. Schelling, P. Keblinski, *Thermal Conductance Across Grain Boundaries in Diamond from Molecular Dynamics Simulation*, Journal of Applied Physics **106**, 063503 (2007).
- <sup>219</sup>M. A. Angadi, T. Watanabe, A. Bodapati, X. C. Xiao, O. Auciello, J. A. Carlisle, J. A. Eastman, P. Keblinski, P. K. Schelling, S. R. Phillpot, *Thermal transport and grain boundary conductance in ultrananocrystalline diamond thin films*, Journal of Applied Physics **99** (2006).
- <sup>220</sup>R. Berman, in *The Properties of Diamond*, edited by J. E. Field (Academic Press, London, 1979).
- <sup>221</sup>J. Birrell, J. E. Gerbi, O. Auciello, J. M. Gibson, J. Johnson, J. A. Carlisle, *Interpretation of the Raman spectra of ultrananocrystalline diamond*, Diamond and Related Materials **14**, 86 (2005).
- <sup>222</sup>A. V. Sumant, A. R. Krauss, D. M. Gruen, O. Auciello, A. Erdemir, M. Williams, A. F. Artiles, W. Adams, *Ultrananocrystalline diamond film as a wear-resistant and protective coating for mechanical seal applications*, Tribology Transactions **48**, 24 (2005).

- <sup>223</sup>S. Bhattacharyya, O. Auciello, J. Birrell, J. A. Carlisle, L. A. Curtiss, A. N. Goyette, D. M. Gruen, A. R. Krauss, J. Schlueter, A. Sumant, P. Zapol, *Synthesis and Characterization of Highly Conducting Nitrogen-doped Ultrananocrystalline Diamond Films*, Applied Physics Letters **79**, 1441 (2001).
- <sup>224</sup>X. C. Xiao, J. Wang, L. Chao, J. A. Carlisle, B. Mech, R. Greenberg, D. Guven, R. Freda, M. Humayun, J. Weiland, O. Auciello, *In Vitro and In Vivo Evaluation of Ultrananocrystalline Diamond for Coating of Implantable Retinal Microchips*, Journal of Biomedical Materials Research Part B: Applied Biomaterials **77**, 273 (2006).
- <sup>225</sup>D. G. Cahill, K. Goodson, A. Majumdar, *Thermometry and thermal transport in micro/nanoscale solid-state devices and structures*, Journal of Heat Transfer-Transactions of the Asme **124**, 223 (2002).
- <sup>226</sup>J. Birrell, J. E. Gerbi, O. Auciello, J. M. Gibson, D. M. Gruen, J. A. Carlisle, *Bonding Structure in Nitrogen Doped Ultrananocrystalline Diamond*, Journal of Applied Physics **93**, 5606 (2003).
- <sup>227</sup>S. Ertl, M. Adamschik, P. Schmid, P. Gluche, A. Floter, E. Kohn, *Surface micromachined diamond microswitch*, Diamond and Related Materials **9**, 970 (2000).
- <sup>228</sup>D. G. Cahill, R. O. Pohl, *Thermal-Conductivity of Amorphous Solids above the Plateau*, Physical Review B **35**, 4067 (1987).
- <sup>229</sup>D. G. Cahill, M. Katiyar, J. R. Abelson, *Thermal-Conductivity of Alpha-Si<sub>3</sub>N<sub>4</sub> Thin-Films*, Physical Review B **50**, 6077 (1994).
- <sup>230</sup>A. V. Sumant, D. S. Grierson, J. E. Gerbi, J. Birrell, U. D. Lanke, O. Auciello, J. A. Carlisle, R. W. Carpick, *Toward the ultimate tribological interface: Surface chemistry and nanotribology of ultrananocrystalline diamond*, Advanced Materials **17**, 1039 (2005).

- <sup>231</sup>C. J. Morath, H. J. Maris, J. J. Cuomo, D. L. Pappas, A. Grill, V. V. Patel, J. P. Doyle, K. L. Saenger, *Picosecond Optical Studies of Amorphous Diamond and Diamond-Like Carbon - Thermal-Conductivity and Longitudinal Sound-Velocity*, Journal of Applied Physics **76**, 2636 (1994).
- <sup>232</sup>A. J. Bullen, K. E. O'Hara, D. G. Cahill, O. Monteiro, A. von Keudell, *Thermal conductivity of amorphous carbon thin films*, Journal of Applied Physics **88**, 6317 (2000).
- <sup>233</sup>J. E. Graebner, S. Jin, G. W. Kammlott, J. A. Herb, C. F. Gardinier, *Unusually High Thermal-Conductivity in Diamond Films*, Applied Physics Letters **60**, 1576 (1992).
- <sup>234</sup>D. T. Morelli, C. P. Beetz, T. A. Perry, *Thermal-Conductivity of Synthetic Diamond Films*, Journal of Applied Physics **64**, 3063 (1988).
- <sup>235</sup>J. Philip, P. Hess, T. Feygelson, J. E. Butler, S. Chattopadhyay, K. H. Chen, L. C. Chen, *Elastic, mechanical, and thermal properties of nanocrystalline diamond films*, Journal of Applied Physics **93**, 2164 (2003).
- <sup>236</sup>V. B. Efimov, L. P. Mezhov-Deglin, *Phonon scattering in diamond films*, Physica B **263**, 745 (1999).
- <sup>237</sup>J. E. Graebner, S. Jin, Journal of Applied Physics **76**, 3 (1994).
- <sup>238</sup>J. E. Graebner, M. E. Reiss, L. Seibles, T. M. Hartnett, R. P. Miller, C. J. Robinson, Physical Review B **50**, 6 (1994).
- <sup>239</sup>J. E. Graebner, V. G. Ralchenko, A. A. Smolin, E. D. Obraztsova, K. G. Korotushenko, V. I. Konov, *Diamond and Related Materials* **5**, 693 (1996).
- <sup>240</sup>O. W. Kading, E. Matthias, R. Zachai, H.-J. Fusser, P. Munzinger, *Diamond and Related Materials* **2**, 1185 (1993).
- <sup>241</sup>K. E. Goodson, O. W. Kading, R. Zachai, ASME HTD Proceedings **292**, 83 (1994).

<sup>242</sup>K. Plamann, D. Fournier, E. Anger, A. Gicquel, *Photothermal examination of the heat diffusion inhomogeneity in diamond films of sub-micron thickness*, *Diamond and Related Materials* **3**, 752 (1994).

<sup>243</sup>D. Fournier, K. Plamann, *Diamond and Related Materials* **4**, 809 (1995).

<sup>244</sup>J. Hartmann, P. Voigt, M. Reichling, *Measuring local thermal conductivity in polycrystalline diamond with a high resolution photothermal microscope*, *Journal of Applied Physics* **81**, 2966 (1997).

## BIOGRAPHICAL SKETCH

Taku Watanabe was born in Seiro, Niigata, Japan. He received the B.E. degree from the Department of Physics, Stevens Institute of Technology in Hoboken, NJ in 2000 and the M.S. degree from the Department of Physics, University of Florida in Gainesville, FL, in 2004. He then began his Ph.D. study in the Department of Materials Science and Engineering with Prof. Simon R. Phillpot as his advisor.